VYSOKÉ UČENÍ TECHNICKÉ V BRNĚ

Středoevropský technologický institut VUT

POJEDNÁNÍ

Brno, 2025

Xia Peng

BRNO UNIVERSITY OF TECHNOLOGY
VYSOKÉ UČENÍ TECHNICKÉ V BRNĚ

CENTRAL EUROPEAN INSTITUTE OF TECHNOLOGY BUT
STŘEDOEVROPSKÝ TECHNOLOGICKÝ INSTITUT VUT

MICRO AND NANOROBOTS BASED ON PHOTOCATALYTIC MATERIALS FOR ENVIRONMENTAL AND BIOMEDICAL APPLICATIONS

MIKRO A NANOROBOTI NA BÁZI FOTOKATALYTICKÝCH MATERIÁLŮ PRO ENVIRONMENTÁLNÍ A BIOMEDICÍNSKÉ APLIKACE

DOCTORAL THESIS TOPIC
POJEDNÁNÍ

AUTHOR
AUTOR PRÁCE
Xia Peng

SUPERVISOR
ŠKOLITEL
prof. RNDr. Martin Pumera, Ph.D.

BRNO 2025

Acknowledgement

As I began to write this section of acknowledgments, my mind and heart were filled with the love that I've received from so many people. I feel that, with my imperfect English, I cannot fully express my gratitude for all who have helped me along the way.

First of all, I would like to express my deepest gratitude to my supervisor Prof. Martin Pumera. I want to thank him that he gave me the valuable opportunity to work in such a big and international group four years ago when I was nobody, which definitely have a profound impact in my future career. I have gained comprehensive knowledge regarding the field of micro/nanorobots and learnt how to collaborate with other professionals. Inspired by Prof. Martin Pumera, I understood that you will never stop your step toward to success if you find the things you are truly loving, and then put most your attention and energy working on that.

Secondly, I want to thank my mentor Dr. Mario Urso and Dr. Martina Ussia for all the invaluable guidance and advice you provided me throughout my PhD. I really miss the time we spent in the lab, worked together, and shared all joys and depressions. I still remembered Mario rushed to C building and hug me thrilled when my first paper was accepted. I also remembered how heartbroken I was when I knew that you had to go back to Catania. Then I tried to be independent. You told me that I can call you whenever I want. Mario, you are not only my mentor, but you are my dearest friend. I believe our friendship will not vanish with time and distance, and it will exist as long as we are alive. I love you and Martina, of course Leo and Gio. I also want to sincerely thank Katka our coordinator, Cagatay and all colleagues in our group or from CEITEC for your continuous help.

I am deeply grateful to Prof. Dr. Oliver G. Schmidt for giving me the opportunity to carry out my internship in his group and for his invaluable guidance and support during my time in Germany. It was truly an amazing experience to collaborate with all the group members at the MAIN Research Center, Chemnitz University of Technology, in Chemnitz, Germany.

I want to thank my friends, because without their love and support, I couldn't imagine how I went through the whole PhD journal. I want to thank Zhengyue Zhang, who took me to travel everywhere and share all your emotions with me. I want to thank Sophie and Roshan, who always helped me in the lab and also outside of work. From you two, I learnt that I need to enjoy my work and life at this moment. I want to thank all Chinese friends who provided me help and showed your care to me.

I want to thank my parents, thank you for bringing me to this world and have such a great experience with so many great people I have worked with and so beautiful natural view I have seen. Your selfless love and support have always accompanied me on my journey, no matter where I am. I want to specially thank my beloved grandma and grandpa. Your kindness and integrity have had a profound and lasting impact on my views on life, values, and worldview—and continue to shape them. I want to thank my boyfriend. I used to think maybe I will be alone all the time, then I met you. We are partners, we are good friends, also.

In the end, I want to thank myself. Thank myself for the resilient, brave, and kind person I have become. You always are firmed and move forwards without any hesitation to the final goals. I believe that you will be a great woman in the future!

I want to thank all who showed your kindness to me during my PhD journey!

Bibliographic citation

Peng X., Micro and nanorobots based on photocatalytic materials for environmental and biomedical applications, Brno 2025, Brno University of Technology, Central European Institute of Technology BUT, 130 p., Supervisor: prof. RNDr. Martin Pumera, Ph.D..

DECLARATION

I certify, that I performed dissertation work independently, under the supervision of prof. RNDr. Martin Pumera, Ph.D.. All technical literature and other information sources presented in this work are properly cited in the text and listed in the reference list.

Brno 2025 Xia Peng, M.Sc.

Table of Contents

Author publications and academic outputs

Publications

- **Xia Peng**, Cagatay M. Oral, Mario Urso, Martina Ussia, Martin Pumera, Active Microrobots for Dual Removal of Biofilms via Chemical and Physical Mechanisms. *ACS Appl. Mater. Interfaces*. **2025**, *17*, 3608−3619. **(IF=8.3)**
- Xianghua Wu, **Xia Peng**, Long Ren, Jianguo Guan, Martin Pumera, Reconfigurable Magnetic Liquid Metal Microrobots: A Regenerable Solution for the Capture and Removal of Micro/Nanoplastics. *Adv. Funt. Mater.* **2024**, *34*, 2410167. **(IF=18.5)**
- Mario Urso, Martina Ussia, **Xia Peng**, Cagatay M. Oral, Martin Pumera, Reconfigurable self-assembly of photocatalytic magnetic microrobots for water purification. *Nat. Commun.* **2023**, *14*, 6969. **(IF=14.7)**
- **Xia Peng**, Mario Urso, Martina Kolackova, Dalibor Huska and Martin Pumera, Biohybrid magnetically-driven microrobots for sustainable removal of micro/nanoplastics from the aquatic environment. *Adv. Funt. Mater.* **2023**, *2307477*. **(IF=18.5)**
- **Xia Peng**, Mario Urso and Martin Pumera, Metal oxide single-component light-powered microrobots for photocatalytic degradation of nitroaromatic pollutants. *npj Clean Water* **2023**, *6*, 21. **(IF=12.2)**
- **Xia Peng**, Mario Urso, Jan Balvan, Michal Masarik, and Martin Pumera, Self-Propelled Magnetic Dendrite-Shaped Microrobots for Photodynamic Prostate Cancer Therapy. *Angew. Chem. Int. Ed.* **2022**, *61*, e202213505. **(IF=16.6)**

- **Xia Peng**, Mario Urso, Martina Ussia and Martin Pumera, Shape-Controlled Self-Assembly of Light- Powered Microrobots into Ordered Microchains for Cells Transport and Water Remediation. *ACS Nano* **2022**, *16*, 7615–7625. **(IF=15.8)**
- **Xia Peng**, Mario Urso and Martin Pumera, Photo-Fenton Degradation of Nitroaromatic Explosives by Light-Powered Hematite Microrobots: When Higher Speed Is Not What We Go For. *Small Methods* **2021**, *2100617*. **(IF=10.7)**

Grants and awards

- CSC scholarship from China, **57600 USD** (2021-2025)**;**
- KInG - internal grants 2022 of Brno University of Technology, “Visible-light-powered hematite microrobots with self-assembly and reconfigurable capabilities for efficient degradation of microplastics” (CEITEC VUT-K-22-7678) **480 000 CZK, Xia Peng (PI);**
- Specific Research Project 2024 of CEITEC BUT, “Self-propelling Janus microrobots for dual eradication of bacterial biofilm” (CEITEC VUT-J-24-8537) **200 000 CZK, Xia Peng (PI);**
- Winner of the Brno PhD Talent 2021 competition, “Autonomous self-propelled hematite micro robots with self-assembly and reconfigurable capabilities for the remediation of biological threats” **300 000 CZK** (2021-2025), **Xia Peng (PI)**.
- The Rector’s Award for outstanding results in doctoral studies 2024.

Conferences

- **Xia Peng**, Mario Urso and Martin Pumera, “Biohybrid magnetically-driven microrobots for sustainable removal of micro/nanoplastics”, NANOROBOTS International Conference--20th Anniversary, 5-8 June 2024, Barcelona, poster presentation;
- **Xia Peng**, Mario Urso, Martina Ussia and Martin Pumera, “Shape-Controlled Self-Assembly of Light- Powered Microrobots into Ordered Microchains for Cells Transport and Water Remediation”, X NyNA 2022: International Conference on Analytical Nanosciences and Nanotechnologies, 5-8 September 2022, Ciudad Real, poster and flash talk contribution;
- **Xia Peng**, Mario Urso, Martina Ussia and Martin Pumera, “Shape-Controlled Self-Assembly of Light- Powered Microrobots into Ordered Microchains for Cells Transport and Water Remediation”, CEITEC PhD Retreat, 20 September 2022, Telč, oral contribution;
- **Xia Peng**, Mario Urso and Martin Pumera, “Photo-Fenton Degradation of Nitroaromatic Explosives by Light-Powered Hematite Microrobots: When Higher Speed Is Not What We Go For”, CEITEC PhD Retreat, 21 September 2021, online, oral contribution;
- **Xia Peng**, Mario Urso, Martina Ussia and Martin Pumera, “Shape-Controlled Self-Assembly of Light- Powered Microrobots into Ordered Microchains for Cells Transport and Water Remediation”, the Falling Walls Lab competition, 21 September 2021, Wroclaw, online, oral contribution;

Student internship

May-Aug 2024: Research Center for Materials, Architectures and Integration of Nanomembranes, Chemnitz University of Technology, Chemnitz, Germany.

Abstract

A mere fraction below 1% of the total global freshwater reservoirs of the Earth is readily attainable. The escalating processes of industrialization, population expansion, and shifts in climate patterns are further exacerbating the clean water shortage. The existing methodologies for water purification and rectification exhibit partial efficacy in eliminating a majority of contaminants, often yielding toxic byproducts that are introduced into the surrounding environment. These issues are addressed by the employment of self-propelled, collective micro- and nanoscale artificial robots, presenting a promising and feasible alternative path to improve water monitoring and remediation by overcoming diffusion-limited reactions and enhancing the interactions with specific target pollutants, encompassing objects such as organic pollutants, biofilms and nano/microplastics.

The thesis explored self-propelled microrobots to address different environmental issues. Single-component WO_3 microrobots and Janus hematite/Pt microrobots were successively demonstrated that they are capable of effective degradation of explosive contaminants in water with enhanced propulsion and reusability without producing hazard by-products. Light-driven $ZnFe_2O_4$-based microrobots exhibited effective treatment of biofilms by photodegradation and physical erosion. Additionally, micro/nanoplastics have been emerging as a sever environmental issue that may propose threat to human health. Algae-based microrobots have been functionalized for efficient micro/nanoplastics removal via electrostatic interaction. Collective behavior of microrobots that surpass individual capabilities also plays a crucial role in cooperative endeavors for environmental remediation. Cubic hematite microrobots swarming into microchains is achieved for the first time due to off-axis orientation of the dipole moment. These intelligent microchains are successfully applied for object manipulation at small scales and breaking polymer chains. Although extensive investigations have been conducted on photocatalytic microrobots possessing light-induced wireless and controllable motion, their potential in the context of cancer treatment via photodynamic therapy (PDT) needs to be further studied. The heightened presence of antioxidants within the tumor microenvironment can exert a down-regulatory influence on the levels of reactive oxygen species (ROS), thereby impeding the efficacy of cancer therapeutic interventions. In this regard, dendrite-shaped microrobots composed of light-responsive hematite with phototaxis as a proficient agent are proposed here and demonstrated a capacity to induce apoptosis of prostate cancer cells, thus markedly amplifying the overall efficacy of PDT. Moreover, these hematite microrobots exhibit a versatile manipulation of their trajectory along a pre-defined path via the exertion of an external magnetic field, facilitating the contactless transport of micro-scale cells. The conceptualized dendrite-shaped hematite microrobots thus pave the way for the advancement of bimodal light and magnetic field-propelled microrobots, holding substantial promise for applications within the domain of biomedicine.

Keywords

Microrobots, micromotors, photocatalysis, self-propulsion, WO_3, hematite, Janus structure, collective behavior, phototaxis, environmental remediation, object manipulation, cancer therapy.

Abstrakt

Méně než 1 % z celkových světových zásob sladké vody na Zemi je snadno dostupných. Rostoucí industrializace, populační expanze a změny klimatických vzorců dále zhoršují nedostatek čisté vody. Stávající metody čištění a úpravy vody jsou jen částečně účinné při odstraňování většiny kontaminantů, přičemž často produkují toxické vedlejší produkty, které se dostávají do okolního prostředí. Tyto problémy lze řešit použitím samořízených kolektivních mikro- a nanoskopických umělých robotů, kteří představují slibnou a realizovatelnou alternativu ke zlepšení monitorování a čištěni vody. Tím překonávají limity difúzních reakcí a zvyšují interakce s konkrétními cílovými znečišťujícími látkami, včetně organických znečišťovatelů a nano-/mikroplastů.

Tato práce se zabývala samořízenými mikroroboty pro řešení různých environmentálních problémů. Jednosložkové WO_3 mikroroboty a Janus hematit/Pt mikroroboty byly postupně prokázány jako účinné při degradaci výbušných kontaminantů ve vodě díky zlepšenému pohonu a opakovatelnosti použití, aniž by produkovaly nebezpečné vedlejší produkty. Světlem řízené mikroboty na bázi $ZnFe_2O_4$ vykazovaly účinné ošetření biofilmů fotodegradací a fyzikální erozí. Mikro/nanoplasty se stávají vážným environmentálním problémem, který může ohrozit lidské zdraví. Mikrorobotí na bázi řas byly funkčně upraveny pro efektivní odstranění mikro-/nanoplastů prostřednictvím elektrostatické interakce. Kolektivní chování mikrorobotů, které překonává individuální schopnosti, také hraje klíčovou roli při spolupráci na environmentální sanaci. Poprvé bylo dosaženo rojení kubických hematitových mikrorobotů do mikrořetězců díky mimoosé orientaci dipólového momentu. Tyto inteligentní mikrořetězce byly úspěšně použity k manipulaci s objekty v malém měřítku a k rozpadu polymerních řetězců.

Ačkoliv byla provedena rozsáhlá šetření týkající se fotokatalytických mikrorobotů s bezdrátovým a kontrolovatelným pohybem indukovaným světlem, jejich potenciál v kontextu léčby rakoviny prostřednictvím fotodynamické terapie (PDT) je třeba dále studovat. Zvýšená přítomnost antioxidantů v mikroprostředí nádoru může snižovat hladinu reaktivních forem kyslíku (ROS), a tím omezovat účinnost terapeutických zásahů při léčbě rakoviny. V této souvislosti jsou zde navrženi dendriticky tvarovaní mikroroboti složení ze světlem řízeného hematitu s fototaxí jako efektivním prostředkem, kteří prokazují schopnost indukovat apoptózu buněk rakoviny prostaty, čímž významně zvyšují celkovou účinnost PDT. Kromě toho tyto hematitové mikroroboty umožňují všestrannou manipulaci své trajektorie podél předem definované dráhy prostřednictvím aplikace externího magnetického pole, což usnadňuje bezkontaktní transport mikroskopických buněk. Navržení dendriticky tvarovaní hematitoví mikroroboti tak otevírají cestu k rozvoji bimodálních mikrorobotů poháněných světlem a magnetickým polem, kteří mají značný potenciál pro aplikace v oblasti biomedicíny.

Klíčová slova

Mikroroboti, mikromotory, fotokatalýza, samořízení, WO_3, hematit, Janus struktura, kolektivní chování, fototaxe, environmentální sanace, manipulace s objekty, léčba rakoviny.

Organization of the thesis

This thesis is organized into eleven chapters. The introductory **Chapter 1** outlines the primary objectives and aims of the thesis. **Chapter 2** provides a broad overview of the research topic and its relevance to current scientific and technological advancements. In **Chapter 3**, a comprehensive literature review is presented, highlighting a theoretical foundation for the research and cutting-edge developments in the field of photocatalytic materials. A detailed description of the methodologies employed throughout the thesis was presented in **Chapter 4**. Following, **Chapters 5-10** include the published papers that corresponds to objectives of this thesis. Designing microrobots in terms of higher propulsion speed from single component WO_3 microrobots to Janus hematite and $ZnFe_2O_4$ based microrobots for degradation of pollutants and removal of biofilm are presented in **Chapters 5,6 and 7**. **Chapter 8 and 9** describes the collective behavior of cubic hematite and algae based microrobots and their environmental applications. Following that, the scope of microrobots into the biomedical domain for photodynamic cancer therapy by fabricating phototactic hematite microrobots is provided in **Chapter 10**. The final **Chapter 11** summarizes the main results of this research and provides an outlook on the prospective applications and developments of the materials and methods explored in the thesis.

1. Objectives of the thesis

The primary objective of this thesis is to develop advanced microrobot systems that address critical environmental and biomedical challenges through innovative designs and functionalities. First, the goal of the research is to design the structure of self-propelled microrobots, to study the motion behavior and mechanism of designed microrobots. Given that the global freshwater scarcity has been exacerbated by industrialization, population growth, and climate change, the second of goal of the thesis is to employ photocatalytic and magnetic microrobots capable of efficient water purification. These designed microrobots aims to degrade contaminants, eliminate biofilm, and remove micro/nanoplastics without generating toxic byproducts with enhanced propulsion and reusability. Apart from environmental applications, the thesis also expands the scope of microrobots into the biomedical domain for photodynamic cancer therapy. In this thesis, hematite, WO_3 etc. have been selected and fabricated as microrobots.

Based on the demonstration above, the goals of the thesis can be divided into three main points as follows:

1. To design advanced microrobots in terms of higher propulsion speed, programmable collective behaviors, response to environmental stimuli with phototaxis, and more.
    - Tailoring the metal thickness of Janus structure and surface modification of self-propelled microrobots and investigating the variation of propulsion speed.
    - Fabricating various morphologies of microrobots and investigating the collective and phototactic behavior of microrobots.
    - Providing the detailed motion mechanism of these studied microrobots.
2. To explore how these increasingly intelligent features allow advancement in environmental and biomedical applications, such as degradation of hazard pollutants, object handling at the micro/nanoscale, and photodynamic cancer therapy.

- Employing the designed microrobots to study the relationship between speed and degradation of pollutants.
- Investigating the performance of fabricated microrobots for environmental remediation and photodynamic cancer therapy.

3. To develop a cost-efficient, eco-friendly, mass-producible, and intelligent microrobot system for various practical applications in real-world settings.

2. Introduction

Water is indispensable for all living beings, but unfortunately, only a small fraction of Earth's freshwater, less than 1%, is readily accessible[1,2]. Moreover, its contamination poses a grave ecological threat. The situation is worsening due to the rising global demand for clean water, driven by population growth, industrialization, and climate change[3]. Various pollutants such as plastic waste, heavy metals, persistent organic pollutants (including pharmaceuticals and pesticides), and oil spills pose significant risks to ecosystems. Once these contaminants enter aquatic environments, they can lead to irreversible and cumulative harmful effects on aquatic plants and animals. The pollutants can also be carcinogenic, mutagenic, and have other detrimental effects. The risks are further amplified as these contaminants propagate through the food chain[4]. Advanced techniques such as water chlorination, desalination, advanced oxidation processes, and nanotechnologies have helped reduce the hazards and diseases related to contaminated drinking water distribution systems. However, despite these advancements, 75% of water bodies are still at risk ecologically. During the process of water remediation, most pollutants including micro/nanoplastics are not entirely removed from contaminated areas, and in some cases, they are only partially degraded, leading to the release of toxic by-products into the environment[5,6].

Meanwhile, with remarkable advancements in nanotechnology and nanomaterials within the biomedical field, various therapeutic approaches for cancer treatments have been established, including chemotherapy, gene therapy, radiotherapy, immunotherapy, and photodynamic therapy (PDT)[7]. Among these approaches, PDT has garnered significant attention as a drug-free and promising method for cancer treatment. PDT utilizes photocatalysts capable of converting oxygen molecules into reactive oxygen species (ROS), which can inflict permanent damage to cancer cells[8]. However, the therapeutic efficacy of PDT is hindered by the overexpression of antioxidants within cancer cells[9]. To overcome this challenge, it is essential to reduce the number of antioxidants in the microenvironment surrounding cancer cells, thereby elevating ROS levels and effectively destroying the cellular antioxidation defense system, leading to the synergistic killing of cancer cells. Moreover, object manipulation at the micro/nanoscale is the foundation for various applications, including biomedical development, single-cell analysis, and cell interaction studies[10]. However, these existing methods have their limitations. For example, atomic force microscopy (AFM) requires critical alignment and large apparatus, optical tweezers (OT) rely on intense lasers, and dielectrophoresis (DEP) involves strong electric fields[11]. These factors can affect both the maneuverability of the manipulation process and the viability of the cells involved. As a result, developing a single-cell manipulation technique that is biofriendly, cost-effective, and easy to operate while ensuring autonomous control remains a challenging task.

In nature, a series of vital life processes, such as cell division, DNA replication, and nutrient transport, rely on the activity of biomolecular robots within the cytoplasm[12]. These biomolecular robots efficiently convert biochemical energy within organisms into mechanical energy, enabling highly precise nanoscale assembly, transportation, and separation processes, which are essential for sustaining cellular metabolism. Inspired by these nanoscale, self-driven molecular robots with remarkable functionalities, researchers are actively exploring the fabrication of self-propelled artificial robots to power micro- and nanosystems, which represents a significant frontier in current nanomaterials research[13,14].

The development of artificial robots dates back to 2002, when the Whitesides group proposed and designed the first synthetic robot, a PDMS-based robot capable of converting chemical energy into mechanical energy[15]. Using platinum (Pt) as a catalyst and hydrogen peroxide (H_2O_2) as fuel, the robot generated oxygen (O_2) through a chemical reaction, enabling autonomous motion. This was the first centimeter-scale robot driven by a catalytic mechanism using H_2O_2 as fuel. The successful demonstration of autonomous motion in small-scale objects captured the interest of researchers worldwide, inspiring the subsequent development of numerous catalytic micro- and nanorobots, which are capable of propelling themselves by transforming surrounding energies into mechanical motion[14]. The motion mechanisms and applications of micro- and nanorobots have become increasingly diverse, allowing them to be broadly categorized into two main types: Externally powered micro- and nanorobots, which rely on external energy sources such as magnetic fields (magnetically driven robots), electric fields (electrically driven robots), ultrasonic waves (ultrasound-driven robots), or light (photocatalytic robots)[16]. Fuel-powered micro- and nanorobots, which utilize chemical fuels such as H_2O_2 or water to generate propulsion. In particular, light emerges as an immensely appealing energy source for empowering microrobots, given its potency, renewability, and abundance[17,18]. With advancement of nanoscience and nanotechnology, photoactive materials i.e., TiO_2, ZnO, Fe_2O_3 have been widely investigated and designed for various environmental and biological applications, for instance, effectively interact with target pollutants and tumor cells, further improving the remediation process and accelerating the apoptosis of cancer cells[19,20]. Therefore, light-powered micro/nanorobots offer great potential to enhance treatment efficiency by overcoming limitations caused by diffusion-limited reactions. Beyond the utilization of photocatalytic materials, microrobots composed of magnetic materials also represent a promising and innovative approach to address challenges by offering a targeted and minimally invasive way of biofilm disruption[21]. When subjected to an external magnetic field, these microrobots demonstrate controlled actuation, which enables them to maneuver precisely. The thesis mainly focuses on studying the motion behavior and the applications of self-propelled microrobots for efficient water purification and photodynamic cancer therapy. Through surface functionalization and morphology manipulation, self-driven microrobots exhibit higher propulsion speed, and intriguing collective behavior and nature-mimic phototactic actuation. Taking advantages of these properties of active microrobots, they were applied for the study of the relationship between motion speed and pollutant degradation efficiency; for breaking down hazard pollutants, elimination of biofilms, removal of micro/nanoplastics and synergistic micro-sized objects transport; for eventually photodynamic induced cancer cells apoptosis. In this thesis, photoactive and magnetic materials have been mainly explored from Brownian motion to active and controllable locomotion as microrobots, also further investigated for shedding light on of their potential in various fields, which hold great promise in real-world settings. Given that the thesis is mostly focused on photocatalytic microrobots, the mechanism of photocatalytic microrobots will be explained in details in Chapter 3.

3. Literature review

3.1. Theory and background

3.1.1 Photocatalysis: from fundamental principles to materials

Photocatalysis draws inspiration from the intricate process of photosynthesis, nature's way of converting sunlight into chemical energy[22]. A sophisticated energy transfer pathway involving two key complexes: photosystem II (PSII) and photosystem I (PSI). PSII captures light at a wavelength of 680 nm, triggering a cascade of reactions powered by water oxidation catalysts. These catalysts split water into oxygen, protons, and electrons. The liberated electrons travel to PSI, which absorbs light at 700 nm and boosts the electrons to an even higher energy state. This heightened energy drives the reduction of $NADP^+$ into NADPH, a critical molecule that powers subsequent processes like the fixation of carbon dioxide into hydrocarbons. This natural system showcases the remarkable efficiency with which sunlight can be harnessed to drive complex chemical processes.

Photocatalysis adapts this principle for human innovation, with its origins dating back to Edmond Becquerel's discovery in 1839[23]. While the materials used for the photocatalysis can be defined as photocatalysts, able to absorb light and induce chemical transformations. With the advancement of nanoscience and nanotechnology, a broad category of photocatalysts has been extensively explored and developed, including semiconductor particles (e.g., TiO_2, Fe_2O_3, WO_3, $BiVO_4$), 2D materials (e.g., g-C_3N_4, MoS_2, and MXene), and QDs (e.g., graphene dots and CdSe QDs) *etc*[24]. Among them, semiconductor materials represent one of the most popular and widely investigated photocatalysts used to establish photocatalytic microrobots, requiring facile fabrication methods, i.e., hydrothermal, microwave and sol–gel reactions. The photoactivation of semiconductors plays a pivotal role in photocatalysis, with its effectiveness influenced by the material's optical and structural characteristics, meanwhile the interactions at the solid-liquid interface also matters. One of the most important parameters influencing photocatalytic performance is the semiconductor's bandgap energy (E_{bg}). This energy gap dictates the minimum wavelength (λ) of light capable of initiating photocatalytic reactions, a relationship that can be expressed mathematically as follows:

$$\lambda\ (\text{nm}) = \frac{hc}{E_{bg}} = \frac{1240}{E_{bg}} \tag{3.1}$$

where h is Planck's constant (6.63×10^{-34} J·s), and c is the speed of light (3.00×10^{8} m/s)[25]. Semiconductors with different bandgap energies shown in Figure 3.1., exhibit distinct light absorption properties[26]. Wide-bandgap materials, for instance, are primarily responsive to high-energy ultraviolet (UV) light and are often utilized for applications requiring strong UV activation. On the other hand, intermediate and narrow-bandgap semiconductors are optimized for visible and near-infrared light absorption, respectively, enabling their use in the development of microrobots and devices tailored for these spectral regions. By selecting the appropriate semiconductor bandgap, photocatalytic systems can be designed that align with specific energy inputs and application requirements, enhancing the versatility and efficiency of photocatalysis.

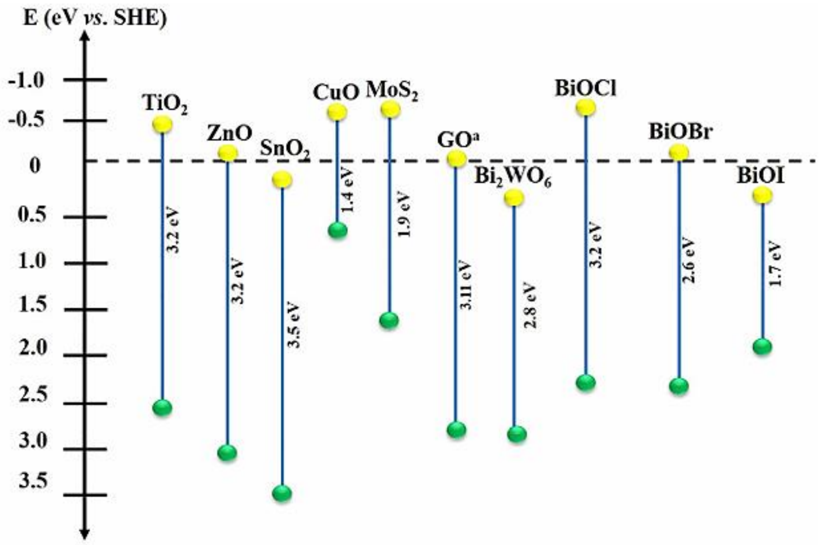

Figure 3.1. The energy band structure of various semiconductor materials, illustrating the valence band (green) and conduction band (yellow). Reproduced from Ref. 26.

Upon light irradiation, photons having energy equal to or higher than the semiconductor bandgap are absorbed, promoting electrons to the conduction band of the semiconductor, and leaving holes in the valence band, which refers to electron-hole pairs separation process.

Afterward, electrons and holes migrate to the surface site, further making contributions to reduction and oxidation reactions, respectively, as demonstrated in Figure 3.2[27]. To our best knowledge, photogenerated charge carriers are generated, trapped, and recombined within femtoseconds to nanoseconds, whereas interfacial surface reactions typically occur over milliseconds. As a result, the rapid recombination of electron–hole pairs represent the primary bottleneck, limiting the efficiency of photocatalytic processes[28].

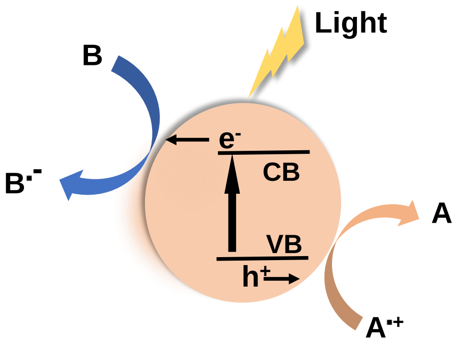

Figure 3.2. Photocatalytic mechanism illustrating the reactions taking place on a photocatalyst upon irradiation.

3.1.2 Design of photocatalytic microrobots

Photocatalytic microrobots, or called light-driven microrobots based on photoactive materials are capable to absorb light, perform photochemical reactions, and eventually convert light energy into kinetic energy, i.e., mechanical motion[29]. There are two primary strategies for constructing light-driven micro/nanorobots (MNRs) using photocatalytic materials. The first involves photocatalytic materials with carefully designed asymmetric micro/nanostructures. The second relies on inducing non-uniform light exposure on a photocatalyst. Both strategies enable photocatalytic materials to exhibit light-driven motion.

Asymmetric microrobots

Figure 3.3 highlights a widely adopted strategy for designing asymmetric microrobots. These designs often incorporate irregularly shaped photocatalytic micro/nanoparticles which inherently generate non-uniform distributions of photochemical reaction products[30]. For instance, Villa etc. proposed single component multifaceted $BiVO_4$ micromotors capable of self-propulsion under light irradiation[31]. Despite their potential, the practical implementation of such structures is limited by the rapid recombination of electron–hole pairs, which indicates weak propulsion forces and incapability in achieving precise motion control.

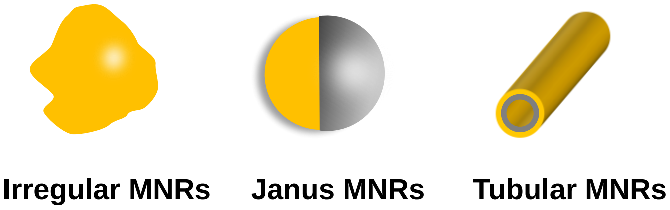

Figure 3.3. Design of asymmetric MNRs.

Among the most prominent designs for light-driven MNRs are based on Janus micro/nanostructures[32]. These particles possess anisotropic chemical and physical properties within a single structure, facilitating asymmetric surface photochemical reactions and photophysical effects that induce an uneven field distribution. Various fabrication techniques, including physical vapor deposition and encapsulation, are employed to create these structures. Another promising category is tubular micro/nanostructures, which leverage distinct photoactivities between their inner and outer surfaces or differential mass diffusion between their hollow interiors and the surrounding medium[33,34]. In 2008, light-activated tubular microrobots based on $g\text{-}C_3N_4$, a 2D material were demonstrated efficient bubble propulsion due to that photogenerated O_2 molecules accumulate and nucleate as bubbles within the interior of the micromotor[35]. These bubbles are subsequently ejected through one opening of the tubular structure, propelling the micromotor in the opposite direction. These features enable propulsion mechanisms such as bubble recoil and phoretic motion. Tubular structures are typically fabricated using methods like template-assisted layer-by-layer assembly or dry spinning[36,37].

Asymmetric photo-exposure

The second approach focuses on generating an asymmetric field by manipulating light exposure to create spatially non-uniform reactions. One effective method involves irregular light irradiation, where the angle of illumination leads to uneven light penetration within isotropic particles (Figure 3.4). This results in localized differences in photochemical activity across the particle's surface, causing asymmetric surface reactions. The resulting concentration gradient of reactants or products produces a driving force that propels the particle in a specific direction[38], as shown in Figure 3.4. An alternative method employs structured light patterns to achieve non-uniform photo-exposure. This technique can selectively activate certain regions of a particle or material, inducing asymmetric changes in surface chemistry or physical properties. For instance, light-responsive materials may deform asymmetrically when exposed to structured light, creating a mechanical force that drives directional motion. This light-induced deformation not only propels the MNR but also allows for more precise control over its trajectory[39]. Both strategies offer promising avenues for developing advanced light-driven MNRs.

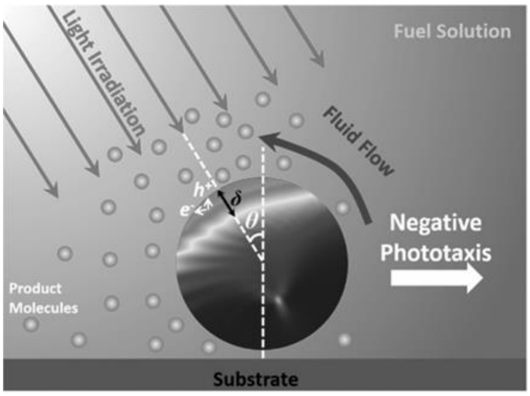

Figure 3.4. Schematic illustration of uneven light penetration within isotropic particles. Reproduced from Ref. 38.

3.1.3 Motion mechanism of photocatalytic microrobots

Under low Reynolds number conditions, the motion of a locomotive object is dominated by viscous forces and random Brownian effects[40]. For light-driven MNRs, overcoming the fluid's viscous drag requires a constant input of energy in the form of a driving force. To address this challenge, researchers have spent the last decade developing various strategies for designing such systems[30,41]. These strategies focus on creating an asymmetric field around photocatalysts, disrupting the uniformity of photogenerated products' distribution. Depending on how the driving force is generated, light-driven MNR propulsion mechanisms can be mainly divided into two categories: phoretic propulsion triggered by light, propulsion via bubble recoil.

3.1.3.1 Light-induced phoretic propulsion

Light-induced phoretic propulsion is a mechanism by which MNRs achieve motion in response to light-induced gradients within their surrounding environment. This phenomenon typically arises due to local variations in chemical concentration, temperature, or electric fields, which are generated upon the interaction of light with the material properties of the MNR or its surrounding medium. These gradients create asymmetric forces along the particle surface, breaking the equilibrium and resulting in directed motion. Depending on the specific gradient induced, light-induced phoretic propulsion can be further classified into light induced electrolyte, nonelectrolyte and temperature gradients. This versatile mechanism has garnered significant attention due to its remote controllability, high precision, and potential applications in targeted delivery, environmental remediation, and microscale robotics[42,43].

Light induced electrolyte gradient

Light-driven MNRs utilizing electrolyte gradients as their propulsion mechanism operate based on the interplay of ion-generating photochemical reactions and asymmetric ion distribution. These systems primarily rely on two distinct mechanisms: self-electrophoresis and self-diffusiophoresis, each offering a unique approach to generating motion[44].

In the case of self-electrophoresis, the propulsion arises from an electric field (E) that is self-generated by the asymmetric distribution of ions around the particle[45]. For example, photocatalytic reactions on the MNR surface can produce a gradient of protons (H^+), leading to an imbalance in ion concentration. This creates a local electric field, which propels the charged particle. The direction of movement depends on the surface charge of the MNR, as it determines how the particle interacts with the self-induced electric field.

Alternatively, self-diffusiophoresis is based on the creation of solute concentration gradients that induce particle motion. For light-driven MNRs, photochemical reactions can produce ions with significantly different diffusion rates. This disparity establishes a concentration gradient, which not only generates a diffusion-induced E but also propels the particle through electrophoresis. Additionally, this gradient induces fluid motion along charged surfaces via electroosmosis, which can move nearby passive particles depending on the substrate's charge polarity[46,47]. Moreover, the localized solute concentration near the MNR surface tends to be higher, resulting in chemophoretic flow (Figure 3.5)[48]. This flow directs particles toward regions of lower solute concentration, complementing the overall propulsion process. Together, these mechanisms demonstrate how light-induced electrolyte gradients enable MNRs to achieve controlled and efficient motion, providing valuable insights into designing advanced systems for targeted applications.

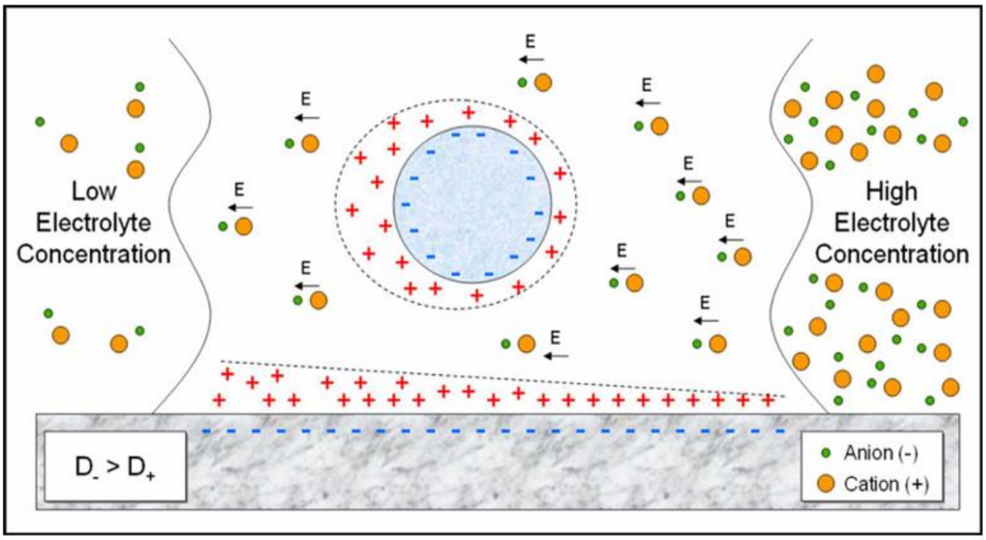

Figure 3.5. Illustration of electrolyte diffusiophoresis. Reproduced from Ref. 48.

Light-induced nonelectrolyte gradient

Light-induced nonelectrolyte gradient propulsion refers to the motion of micro/nanorobots driven by gradients of nonionic solutes, such as neutral molecules, that are generated through light-activated processes[49,50]. Unlike electrolyte gradients, which rely on charged species and electrostatic interactions, nonelectrolyte gradient propulsion is based on the asymmetric distribution of neutral molecules in the surrounding environment, leading to chemophoretic or thermophoretic forces. The underlying mechanism typically involves the interaction of light with the MNR surface or the surrounding medium, which triggers a localized photochemical or photothermal reaction. For example, light absorption by the MNR may induce the release or depletion of neutral solutes, creating a concentration gradient. Alternatively, light-induced heating can generate a temperature gradient in the medium. Both types of gradients disrupt the symmetry of the surrounding environment, resulting in directed motion of the MNR. In terms of chemophoretic propulsion, the concentration gradient of neutral solutes creates differences in chemical potential around the MNR. These differences exert a force on the particle surface, driving its motion toward regions of lower or higher solute concentration, depending on the solute-MNR interaction. Several light-driven nanomaterials have been developed upon the photodecomposition of H_2O_2 to generate O_2 under light irradiation in the presence of semiconducting photocatalysts, which include peanut-shaped Fe_2O_3[51], isotropic TiO_2 microparticles[52], and Janus Au-WO_3@C microrobots[53]. Regrading thermophoretic propulsion, the temperature gradient caused by light absorption induces a thermally-driven flow of the surrounding medium. This flow is often accompanied by the motion of the MNR, which moves either toward or away from the heat source depending on its thermophoretic properties[54,55]. Light-induced nonelectrolyte gradient propulsion offers several advantages for MNR design, including the ability to avoid ionic species, which may destabilize the system or interfere with specific applications. This propulsion mechanism is particularly promising for environments where ionic interference must be minimized, such as biological systems, and for tasks requiring precise and controllable movement at the microscale.

3.1.3.2 Bubble propulsion

Bubble propulsion was the pioneering mechanism for the movement of nano- and microrobots. This process occurs when a transition metal catalyst (such as platinum, manganese, nickel, or silver) decomposes a chemical fuel, producing oxygen bubbles[56]. Early versions of bubble-driven nano- and microrobots faced challenges, including limited movement efficiency due to ionic strength constraints. However, advances in robot design, such as optimizing geometry, have allowed researchers to overcome these limitations, enabling new movement patterns and enhancing the functionality of these robots at the nanoscale[57,58]. Compared to phoresis-driven robots, bubble-propelled robots offer notable advantages, including stronger thrust, faster speeds, and a longer operational lifespan. For instance, Mou et al. developed a light-driven, bubble-propelled microrobot using a TiO_2 tubular structure, achieving speeds up to 325 mm/s[36]. The mechanism relies on the photocatalytic decomposition of H_2O_2 under UV light, where the TiO_2 catalyst generates O_2 (Figure 3.6). The O_2 molecules then nucleate and grow into bubbles inside the TiO_2 tube. The confined space of the tube, which has a specific inner diameter and length, plays a crucial role in promoting bubble formation. The internal confinement accelerates the bubble nucleation and growth, enhancing the propulsion of the microrobot, which demonstrates that the confined environment inside the tube is key to significantly increasing the efficiency of the light-induced propulsion mechanism.

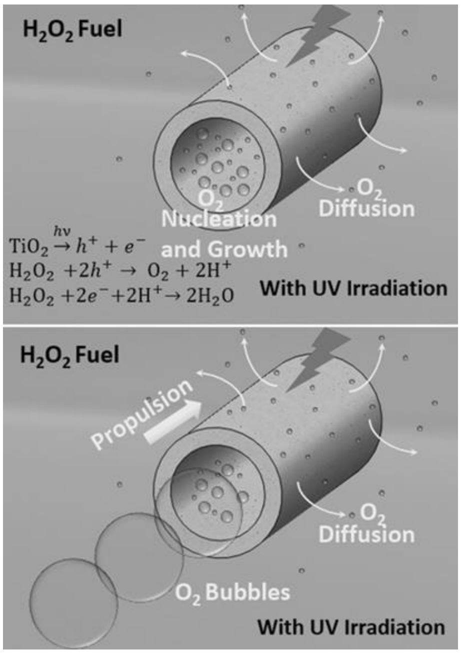

Figure 3.6. Motion mechanism of TiO_2 tubular microrobots in presence of H_2O_2. Reproduced from Ref. 36.

3.2 State of the art

3.2.1 Photocatalytic microrobots for environmental applications

To date, extensive research efforts have been dedicated to exploring the potential of photocatalysts for a plethora of application domains, including environmental remediation.[16] The initial reported PMNMs were comprised of plain TiO_2 microspheres[59]. Under a UV light intensity of 2.5 W/cm^2, they exhibited self-diffusiophoresis, propelling themselves at a speed of 10 ± 3μm/s in pure water. This groundbreaking work opened up novel opportunities for light-driven MNRs. Afterward, single-component light-driven microrobots have been extensively exploited. For instance, these graphene carbon nitride (GCN)-based microrobots have demonstrated their capabilities in simultaneously monitoring and removing heavy metal pollutants[35]. Nevertheless, the microrobots' motion required a high concentration of fuel (H_2O_2). In this thesis, single-component WO_3 microrobots capable of propelling in low concentrations of fuel were first demonstrated for the degradation of pollutants.

In order to further improve the photocatalytic efficiency of photocatalysts and promote the propulsion of photocatalytic MNRs, it is necessary to have an asymmetric structure, which in turn converts this asymmetry into motion[60,61] In this regard, "two-faced" Janus microrobots deserve special mention, featuring a design wherein a photocatalytic semiconductor (i.e., TiO_2, ZnO, and Cu_2O) is asymmetrically coated with a metal layer (Pt, Au, Fe, etc.), rendering them highly efficient in harnessing light as a driving force (Figure 3.7)[32,62–65]. Leveraging the self-electrophoretic mechanism, these microrobots exploit the asymmetric generation of charges upon light irradiation, thereby establishing a local electric field that induces their motion. The presence of the metal layer plays a pivotal role in enhancing charge separation at the semiconductor/metal interface, thus augmenting the microrobots' speed and photocatalytic properties. TiO_2−Au Janus photocatalytic microrobots with a novel approach aimed at improving photocatalytic efficiency for the rapid detection and “on-the-fly” degradation of dye pollutants (i.e., methyl blue) in aqueous environments have been developed[66]. These innovative microrobots can operate at a remarkably reduced activation UV light intensity of only 2.5 mW/cm^2 in pure water. Magnetic properties also play a crucial role in broadening the microrobot's application scope and recyclability, aiming to achieve greater efficiency for environmental remediation. For example, light-driven TiO_2-Fe Janus microrobots have been introduced, enabling highly efficient degradation of organic pollutants in water environments.

Advantageously, the TiO_2-Fe microrobots could be easily collected and reused by external permanent magnets[67].

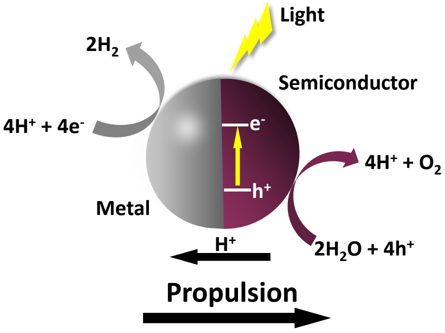

Figure 3.7. Schematic illustration of the photocatalytic activation of Janus microrobots and their self-propulsion mechanism.

In line with the reported TiO_2-based Janus microrobots, ZnO photocatalysts and metal Pt were skillfully combined to create a hybrid ZnO-Pt photocatalytic microrobots for efficient photodegradation of explosives (i.e., picric acid), which are more difficult to be degraded in comparison to dye pollutants[68]. These cases demonstrate that the ingenious combination of photocatalyst and metal in the Janus structure can significantly enhance propulsion while efficiently reducing the required light intensity and fuel concentration. However, the influence of metal layer thickness on the self-propulsion ability of light-driven Janus microrobots has not been reported yet. Additionally, the relationships between metal layer thickness and microrobots' speed and photocatalytic properties aiming at improving environmental remediation efficiencies remain to be studied and clarified. To address this issue, Janus hematite/Pt microrobots with different Pt layer thicknesses have been studied to demonstrate the relationship between metal layer thickness and photocatalytic properties, further investigating the differences in the degradation efficiencies of explosives and organic pollutants. Hematite has been selected as the most used semiconductor due to its narrow band gap, which can be activated by visible light, its low cost, biocompatibility, and for the catalyzed photo-Fenton reaction in the presence of light and H_2O_2, which increases the production of ROS to attack the target pollutants. Moreover, hematite is weakly magnetic, allowing the navigation of hematite-based microrobots using magnetic fields, which endows them with recyclability and navigation precision.

Compared to single robots, micro/nanorobot swarms offer enhanced efficiency, robustness, and flexibility. Integrating contaminant removal and degradation functions into robotic swarms holds great promise for future environmental applications[69,70]. Collective animal behavior encompasses tasks that go beyond the capabilities of individual animals. These collective behaviors have served as inspiration for artificial swarming micro- and nanorobots. Groups of robots can accomplish tasks faster and handle size-dependent operations, like transporting large cargoes that necessitate the cooperation of several robots. Swarms have a broader perception of environmental variations compared to single robots, and even in the event of a robot failure, the group can still complete the assigned task[11,71–74]. For example, Bi_2WO_6 microrobots with swarming behavior by forming swarms consisting of multiple microrobots were demonstrated to tackle textile contamination in water (Figure 3.8)[75]. These swarms of microrobots can collectively move together, leading to the formation of larger agglomerations. This swarming behavior is attributed to the chemical gradient concentration created by their photocatalytic activation, which induces osmotic and phoretic interactions among the microrobots. However, practical applications require swarms to adapt to environmental changes through self-organization and reconfigurability in shape and function, which still remains a challenge to be further investigated. Due to the asymmetric orientation of the dipolar moment in the crystal, cubic-shaped hematite microparticles have been illustrated that they possess the ability of self-organization and reconfigurability. Therefore, it is desirable to study the collective behavior of cubic hematite microrobots for tackling various problems in complex environments.

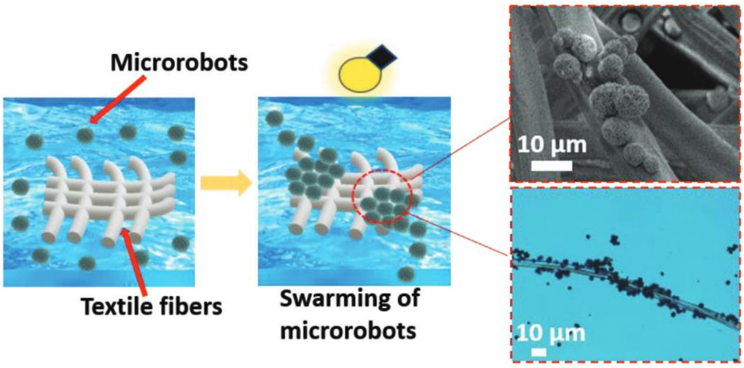

Figure 3.8. Swarming of Bi_2WO_6 microrobots under light irradiation and their further attachment onto the textile fibers. Reproduced from Ref. 75.

3.2.2 Photocatalytic microrobots for biomedical applications

Over the last decade, a significant amount of research has focused on the biomedical application of photocatalytic micro/nanorobots. These robots have been explored for various purposes, including disease treatment, photo-related cancer therapy, cell manipulation, and more. Villa *et al.* developed single-component $BiVO_4$ microrobots with precise micro/nanostructures capable of autonomous swimming both individually and as part of a collective assembly under visible-light irradiation. These microrobots can efficiently carry out cargo loading and transport of passive particles and living microorganisms without requiring any surface functionalization[31]. In order to solve the neurodegenerative disorders that can cause, for example, Parkinson's, Alzheimer's, and Huntington's diseases, concave $BiVO_4$ microspheres are used to disaggregate protein fibrils by the microrobots' intrinsic on-the-fly generation of ROS[76].

PDT, in particular, is a highly promising therapeutic technique that has been extensively studied in fundamental research and applied in clinical medicine[77,78]. The principle of PDT involves the transfer of energy from light-excited photosensitizers to surrounding oxygen molecules ($^3O_2$), generating cytotoxic/ ROS, particularly singlet oxygen ($^1O_2$), which effectively kills cancer cells (Figure 3.9)[79,80]. Despite significant progress in PDT research and clinical applications, certain physical limitations have hindered its therapeutic efficacy. Existing photosensitizer platforms still function as passive nanocarriers, and the generated $^1O_2$ can only reach the target organism through their own free diffusion, which may limit their effectiveness in reaching certain regions efficiently[81].

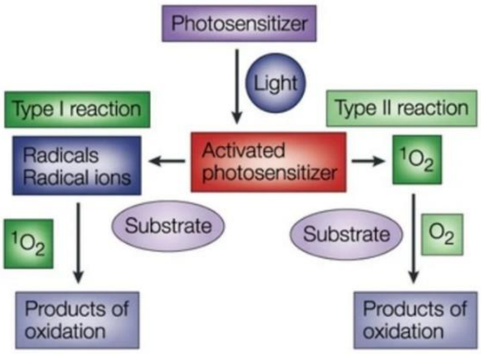

Figure 3.9 Two types of reaction during PDT.Reproduced from Ref. 43.

Nevertheless, photocatalytic microrobots can offer distinct advantages for photodynamic therapy, particularly due to their active actuation and excellent ability to generate ROS[82–84]. A multi-functionalized microrobot as a mobile photosensitizer platform was developed for treating bacterial infections[85]. In comparison to passive carriers operating under the same conditions, the active motion of the mobile photosensitizer led to a significant enlargement of the coverage area of the photodynamic therapy system by approximately 10 times, effectively spreading $^1O_2$ and resulting in a highly efficient photodynamic activity. However, the motion direction and magnitude of single light-powered microrobots cannot be precisely controlled in the absence of magnetite nanoparticle modification.

Certain microorganisms exhibit responses to light, causing them to change their orientation and swim either toward or away from the light source. This phenomenon is referred to as phototaxis[86]. The replication of such phototactic behaviors in artificial microrobots would enable these microrobots to adjust their orientation and position by simply manipulating the illumination conditions. Recent advancements have demonstrated phototactic reactions in microrobots controlled by light[87–89]. In a study by Chen *et al.*, they introduced a straightforward design for phototactic microrobots[38]. These microrobots utilized isotropic particles composed of a single semiconductor material like TiO_2, ZnO, or CdS, which were exposed to light from a specific direction. As the material absorbed the light, only the side of the particle facing the light became photocatalytically active. This non-uniform illumination of the isotropic particles effectively transformed them into microrobots resembling Janus particles, possessing an active chemical surface on one side and an inactive one on the other. Consequently, these isotropic microrobots, subjected to anisotropic illumination, moved in the direction of the incident light. Microrobots with phototaxis behavior have been exploited in the biomedical field, i.e., cell manipulation and target drug delivery[90]. However, light-powered microrobots with phototaxis that break the constraint of 2D motion for PDT still need to be uncovered. In the thesis, dendrite-shaped hematite microrobots have been demonstrated that exhibited phototaxis by changing the light source directions for efficient PDT and cell manipulation.

4. Methods

4.1 Microrobots fabrication

Single-component WO_3 microrobots

Initially, 50 mL of deionized (DI) water was placed in an 80 mL beaker, followed by dissolving 1 mmol Na_2WO_4 in the DI water with magnetic stirring. Subsequently, 25 mmol of glucose was added to the suspension. After thorough magnetic mixing, the solution was transferred to an autoclave, sealed, and heated in a preheated oven at 200 °C for 20 h. After cooling to room temperature, the precipitate was centrifuged using DI water and ethanol and then dried overnight. The dried products were sealed, and calcined at 550 °C in air, and the resulting green product was collected for further analysis.

Janus hematite/Pt microrobots

Hematite (α-Fe_2O_3) microspheres were synthesized via a hydrothermal route. $FeCl_3$ (Sigma Aldrich, 97%) was dissolved in ultra-pure water (18 MΩ cm) to create 1 M $FeCl_3$ solution under magnetic stirring. The solution was transferred to a 50 mL Teflon-lined stainless-steel autoclave, hydrothermally treated at 160 °C for 20 h, and cooled to room temperature. The product was collected by centrifugation, washed with DI water and ethanol, then vacuum-dried at 60 °C for 12 h. For hematite/Pt Janus microrobots, synthesized microspheres were dispersed in pure water (5 mg mL^{-1}), sonicated, drop-cast onto glass slides, and air-dried overnight. Asymmetric Pt layers (30, 60, and 90 nm) were sputter-deposited, as shown in Figure 4.1.

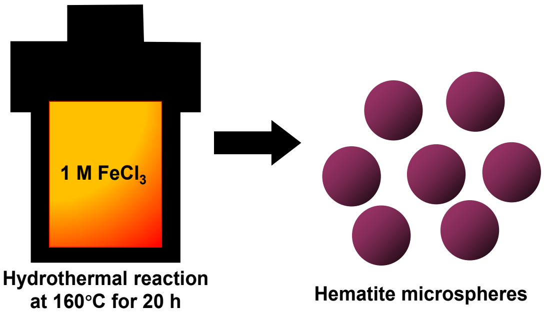

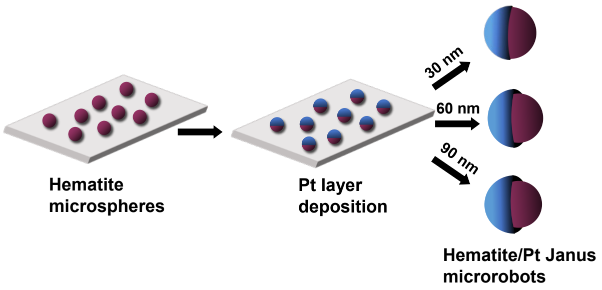

Figure 4.1 Schematic illustration of hematite microspheres synthesis and hematite/Pt Janus microrobots fabrication.

Self-assembled cubic hematite microrobots

For cubic hematite microparticles, in a typical synthesis, 0.5 M $FeCl_3$ (Alfa Aesar, 98%) and 1.2 g hexamethylenetetramine (Sigma Aldrich, 99.5%) were directly dissolved in a 30 mL mixture of ethanol and DI water (1:1 v/v) with vigorous magnetic stirring. Subsequently, 3 wt% of $CuCl_3$ (Alfa Aesar, 98%) was added to the above solution. After 30 min stirring, the mixture was transferred into a Teflon-lined stainless-steel autoclave and heated at 160 °C for 12 h. Asymmetric Pt layers (30 nm) were sputter-deposited to fabricate cubic hematite microrobots (Figure 4.2).

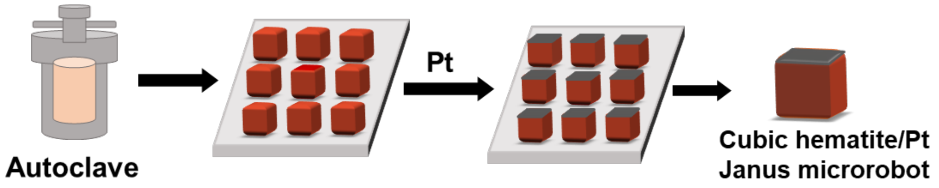

Figure 4.2 Schematic illustration of cubic hematite synthesis and hematite/Pt Janus microrobots fabrication.

Dendrite-shaped microrobots

Typically, 0.5 mmol $K_3[Fe(CN)_6]$ (Sigma Aldrich, 99%) was dissolved in DI water (18 MΩ cm) first, and 0.5 g of PEG-4000 (3500 - 4500 g/mol, Alfa Aesar) was included to the yellow aqueous solution. The composition remained strongly stirred for 30 min. The obtained solution was shifted into a Teflon-lined stainless autoclave with a volume of 50 mL. Afterward, the autoclave was placed in a preheated oven. The oven was set at 160 °C. The whole reaction time lasted for 6 h. When the process ended, DI water and ethanol were used to wash the final product by centrifuging. Finally, the obtained product was dehydrated at 70 °C overnight.

Janus ZFO/Pt microrobots

ZFO microspheres were synthesized via a hydrothermal method. A mixture of 30 mL isopropanol, 8 mL glycerol, 2 mmol $Fe(NO_3)_3$, and 1 mmol $Zn(CH_3COO)_2 \cdot 2H_2O$ was stirred for 30 min, transferred to a 50 mL Teflon-lined autoclave, and heated at 180 °C for 12 h. After cooling, the precipitate was centrifuged, washed, dried at 60 °C overnight, and calcined at 450 °C for 3 h. Janus microrobots were prepared by dispersing ZFO microspheres (3 mg mL^{-1}) in DI water, sonicating for 5 min, and depositing the suspension on glass slides to dry overnight. A 30 nm Pt layer was asymmetrically sputtered onto the microspheres, with thickness monitored by a quartz crystal microbalance. The microrobots were then detached using a scalpel.

4.2 Motion experiments

4.2.1 Optical measurements

The motion behavior of microrobots was studied using a Nikon ECLIPSE TS2R inverted microscope equipped with a Basler acA1920-155uc digital camera for high-resolution video recording. Experiments were conducted using aqueous suspensions of microrobots without the addition of surfactants to eliminate potential interference with their natural motion. The motility of the microrobots was evaluated under varying concentrations of hydrogen peroxide (H_2O_2) as a chemical fuel, prepared from a commercial 30% H_2O_2 solution (Sigma Aldrich).

To investigate the phototactic response of the microrobots, a fixed ultraviolet (UV) light source was utilized to illuminate the sample chamber from different directions. The UV intensity was calibrated to a constant value of 1.674 W cm^{-2} to ensure consistent exposure across experiments. The response to negative phototaxis, characterized by movement away from the light source, was recorded for subsequent analysis. Video recordings of the experiments were processed and analyzed using the NIS Elements Advanced Research software to extract quantitative data on microrobot speed, trajectory, and phototactic behavior.

4.2.2 Magnetic measurements

The magnetic navigation of microrobots was conducted using a custom-built magnetic controller system, designed to generate a transversal rotating magnetic field. The system comprised three orthogonal pairs of electromagnetic coils mounted on a 3D-printed polylactic acid (PLA) backbone, allowing precise manipulation of the magnetic field within the experimental setup. The experiments were performed under an applied magnetic field strength of 3 mT, with a rotational frequency of 10 Hz.

The microrobots were navigated within a confined environment, specifically a 100 µm-wide microfluidic channel, to mimic realistic microenvironments. Video footage of the microrobots' motion was captured using the Nikon ECLIPSE TS2R inverted microscope and recorded at 20 frames per second (fps) using Pylon Viewer software. This setup ensured accurate monitoring of the microrobots' magnetically guided trajectories, enabling detailed analysis of their navigation efficiency and responsiveness to the applied magnetic field.

4.3 Materials characterization

4.3.1 Morphology and composition analysis

Scanning electron microscopy (SEM) is a powerful imaging technique used in various scientific and industrial fields to obtain high-resolution, detailed images of the surface of a sample. It offers significantly greater magnification and depth of field compared to optical microscopy. In SEM, a focused beam of electrons is scanned over the surface of a sample. The interaction between the electrons in the beam and the atoms on the surface of the sample generates signals that are used to create an image[91]. SEM images of microrobots were obtained with a Tescan MIRA 3 XMU instrument. 100 µL of the suspended solution was placed on a glass slide under the microscope. The solution on the glass slide was quickly dried under irradiation of a LED lamp (100 W). Finally, this glass slide moved to the chamber of a Tescan MIRA 3 XMU instrument.

Energy-dispersive X-ray spectroscopy (EDS) is an analytical technique often used with electron microscopes to determine the elemental composition of materials. It functions by exposing a sample to an electron beam, which causes the emission of X-rays with characteristic energies from the sample's atoms. These emitted X-rays are captured by a detector and sorted by a spectrometer based on their energies[92]. The resulting X-ray spectrum displays peaks corresponding to the elements present in the sample. EDX mapping analysis of microrobots was performed using an Oxford EDX detector connected to the SEM.

X-ray Diffraction (XRD) is a versatile technique crucial for understanding crystalline materials' atomic arrangements. By directing X-rays onto a crystal, it generates a diffraction pattern that unveils the crystal's internal structure, driven by the interaction between X-rays and atoms' periodic arrangement[93].The X-ray diffraction (XRD) patterns of the synthesized products were analyzed using a Rigaku SmartLab 3 kW diffractometer. The instrument is equipped with a fine-focus Cu Kα radiation source, which operates at a voltage of 40 kV and a current of 30 mA, ensuring high-quality diffraction data with excellent resolution.

X-ray photoelectron spectroscopy (XPS) is a surface-sensitive analytical technique widely used to determine the elemental composition, chemical states, and electronic structures of materials[94]. XPS spectra were acquired using a Kratos Analytical Axis Supra™ instrument, ensuring high-resolution measurements. The acquired data were analyzed and fitted using CASA XPS software to extract detailed information on the surface chemistry.

4.3.2 Optical characterization

UV-Vis, short for Ultraviolet-Visible Spectroscopy, is a widely used analytical technique in chemistry and molecular biology. It involves shining ultraviolet (UV) and visible (Vis) light through a sample and measuring the absorbance or transmission of light as it interacts with the molecules in the sample. It passes light through a sample and gauges its absorption or transmission at different wavelengths. Components include a light source emitting UV and visible light, a monochromator for wavelength selection, a sample holder, and a detector measuring light intensity post-sample[95]. In this thesis, a UV-Vis spectrophotometer (Jasco V-750) was used to measure the absorbance spectra of the pollutant solutions. Microrobots, pollutant solution (i.e., picric acid, 4-nitrophenol and Rhodamine B), and different concentration of H_2O_2 were sequentially added to UV-transparent cuvettes. After certain time of UV exposure, suspensions were centrifuged, and the supernatants were analyzed using a Jasco V-750 UV-Vis spectrophotometer. Degradation efficiency of pollutants was calculated using the formula:

$$Degradation\ Efficiency = \frac{C_0 - C_1}{C_0} \times 100 \tag{4.1}$$

C_0 and C_1 represent the initial and final PA concentrations.

4.4 Electrochemical measurements

Electrochemical experiments were conducted to investigate the electrochemical properties of hematite and platinum electrodes under UV-light irradiation. A customized photoelectrochemical setup was utilized, incorporating a 365 nm UV LED (700 mA, model LZ4-04UV00, LedEngin Inc.) as the light source. The experiments were performed in a two-electrode configuration, employing either a hematite electrode or a platinum (Pt) electrode as the working electrode. An Ag/AgCl electrode was used in a dual role, functioning as both the reference and counter electrode, to simplify the setup while ensuring accurate measurements.

4.4.1 Electrode preparation

The hematite working electrodes were prepared by depositing 100 µL of a 5 mg mL^{-1} aqueous suspension of hematite microparticles onto commercial indium tin oxide (ITO)-coated glass slides (1×2 cm^2, Sigma Aldrich, surface resistance 8–12 Ω sq^{-1}). The hematite microparticles used in these experiments were synthesized in walnut-like or cubic morphologies. After deposition, the electrodes were dried at ambient conditions overnight to ensure proper adhesion and uniform particle distribution on the substrate.

The Pt working electrodes were fabricated by sputtering a 30 nm thin layer of platinum onto

ITO-coated glass slides, creating a conductive and catalytically active surface. Both hematite and Pt electrodes had an active immersion area of 1 × 1 cm^2 during the experiments.

4.4.2 Tafel measurements

Tafel measurements were conducted using a Metrohm AUTOLAB potentiostat. The electrochemical tests were performed in deionized (DI) water under continuous UV-light irradiation, ensuring consistent illumination of the working electrodes during measurements. The potential range was scanned from -0.2 V to 0.6 V versus the Ag/AgCl reference electrode at a constant scan rate of 5 mV s^{-1}. This scan rate was chosen to provide a balance between signal resolution and minimization of potential hysteresis effects.

4.5 In vitro cytotoxicity assessment

4.5.1 Cell culture and experimental setup

The in vitro cytotoxicity of the samples was evaluated using human PC-3 prostate cancer cells. This cell line, derived from a grade 4 prostatic adenocarcinoma of a 62-year-old male and originally obtained from a bone metastasis site, was sourced from HPA Culture Collections. The cells were cultured in Ham's F12 medium supplemented with 7% PBS and penicillin/streptomycin (100 U mL^{-1}). The cultures were maintained in a humidified incubator at 37°C with 5% CO_2 to ensure optimal cell growth.

To prepare for imaging and analysis, PC-3 cells were seeded in μ-Slide I Lauer Family flow chambers. During the experiments, the chambers were placed in a gas-controlled environment to maintain standard culture conditions, including a stable temperature (37°C), humidity (60%), and CO_2 levels (5%). Imaging experiments spanned 24 hours, with images captured from seven randomly selected fields of view to ensure statistically representative data. The observations were performed at a frame rate of 3 minutes per frame using a high-resolution imaging setup.

4.5.2 Imaging techniques and data analysis

Quantitative phase imaging (QPI) was performed using a Q-PHASE microscope, allowing for non-invasive assessment of cell morphology and dry mass. Holographic images were captured with a CCD camera, and fluorescence images were taken using an ANDOR Zyla 5.5 sCMOS camera. Specialized software was employed for image reconstruction, enabling precise measurement and visualization of cellular dry mass distribution. The dry mass values of individual cells were calculated using the following formula:

$$m = \frac{\varphi\lambda}{2\pi\alpha} \tag{4.2}$$

where m represents cell dry mass density (in pg μm^{-2}), φ is detected phase (in rad), λ is wavelength in μm (0.65 μm in Q-PHASE), and α is specific refraction increment (≈0.18 μm^{3} pg^{-1}). By measuring the integrated phase shift across the cells, their total dry mass was determined, providing insight into variations in mass distribution under different experimental conditions.

For hematite microrobots' activation, samples were exposed to blue light at 485 nm with controlled intensity and exposure duration, achieving a precise light dose. Viability of the cells during imaging was assessed using the fluorescent dyes Calcein AM and PI, which selectively stain live and dead cells, respectively. Fluorescence imaging was performed using a Q-PHASE microscope equipped with FITC and TRITC filters, ensuring accurate visualization of cellular viability.

Part 1: Self-propelled photocatalytic microrobots with enhanced propulsion for water purification

5. Metal oxide single-component light-powered micromotors for photocatalytic degradation of nitroaromatic pollutants

Published paper included in this chapter:

Xia Peng, Mario Urso and Martin Pumera*, Metal oxide single-component light-powered micromotors for photocatalytic degradation of nitroaromatic pollutants. *npj Clean Water* **2023**, *6*, 21.

5.1 Motivation of this study

Nitroaromatic compounds, widely utilized in industrial applications such as explosives, pesticides, and dyes, pose significant environmental challenges due to their recalcitrant nature and accumulation in water and soil systems, threatening human health. Traditional wastewater purification methods, including biological and physical approaches, are either inadequate or non-destructive, necessitating advanced strategies for effective pollutant degradation. While photocatalysis has emerged as a promising light-driven solution, current approaches often rely on passive diffusion or expensive noble metal coatings, limiting their practicality. This study aims to develop low-cost, efficient photocatalytic micromotors leveraging light-driven motion to enhance interactions with pollutants and address the limitations of existing technologies.

5.2 Paper conclusion

In this study, we successfully demonstrated the large-scale synthesis of precious metal-free, single-component WO_3 micromotors using a facile and scalable hydrothermal method combined with calcination. These micromotors exhibited light-responsive self-propulsion without the need for H_2O_2 fuel, achieving active motion under asymmetric UV illumination. Their remarkable photocatalytic activity was effectively utilized for the degradation of toxic nitroaromatic pollutants, such as PA and 4-NP, achieving 70% and 40% degradation, respectively, in water without external agitation. These results highlight the potential of WO_3

micromotors as a cost-effective, efficient, and sustainable solution for eliminating non-biodegradable and hazardous pollutants in industrial wastewater, paving the way for their practical application in environmental remediation.

5.3 Author contribution

For this study, I synthesized WO_3 micromotors by hydrothermal reaction, and characterized the micromotors by conducting SEM, EDX, XRD, and XPS. I evaluated the performance of the motion, conducted the degradation experiments, plotted and analyzed all data. I wrote the draft of the manuscript. All authors have given approval to the final version of the manuscript.

npj | clean water

www.nature.com/npjcleanwater

ARTICLE OPEN

Metal oxide single-component light-powered micromotors for photocatalytic degradation of nitroaromatic pollutants

Xia Peng[1], Mario Urso[1] and Martin Pumera[1,2,3,4]✉

Mass transfer is a key parameter in heterogeneous reactions. Micro/nanomachines, a promising technology for environmental applications, significantly enhance the performance of conventional purification treatments because of the active motion ability and thus enhanced diffusion (superdiffusion) of these photocatalysts, which in turn leads to dramatically improved mass transfer and higher degradation capability compared to stationary microparticles. However, the design of micromotors generally involves noble metals, for instance, Au and Pt, to achieve an effective autonomous motion. Considering the expensive fabrication cost and complicated steps, we present Pt-free single-component light-powered WO_3 micromotors capable of enhanced diffusion and effective degradation of nitroaromatic compounds in water. These microswimmers, synthesized by a hydrothermal method, which is highly scalable at low cost, followed by calcination, exhibit fuel-free light-driven motion due to asymmetric light irradiation. Picric acid (PA) and 4-nitrophenol (4-NP) were selected as representative nitroaromatic contaminants and photocatalytically decomposed by WO_3 micromotors thanks to the close contact with the micromotors promoted by their self-propulsion. This work provides a low-cost, sustainable, scalable method for enhancing mass transfer by creating moving catalysts with broad application potential for water cleanup.

npj Clean Water (2023)6:21 ; https://doi.org/10.1038/s41545-023-00235-z

INTRODUCTION

Nitroaromatic compounds are organic composites that comprise one or more nitro groups (-NO_2) connected to the aromatic ring[1]. Taking advantage of these groups, nitroaromatic compounds have been broadly applied to fabricate diverse industrial products, such as explosives, pesticides, and dyes[2]. Unfortunately, the nitro group also hinders the biodegradation of these compounds, resulting in continuous environmental accumulation. Indeed, their extensive employment has led to severe contamination of groundwater and soil, which is usually associated with drinking water quality, severely posing a threat to human health[3,4]. Traditional wastewater purification approaches mainly depend on biological oxidation and physical procedures (i.e., activated carbon adsorption, nano-filtration)[5–7]. The biological process is inadequate as these compounds are barely degraded due to their high constancy in the water system. Physical methods only transfer the pollutants instead of destructive removal, which indicates that further treatments are necessary. Advanced oxidation processes (AOPs) have been extensively explored in degrading organic contaminations in wastewater[8–10]. AOPs generally involve highly reactive oxygen species (ROS), for instance, hydroxyl radical (•OH) and superoxide radical (•O_2^-), which can oxidize hazardous chemical species in water[11]. Photocatalysis is a promising light-driven AOP technology, necessitating a photocatalyst and proper light irradiation to generate ROS that break down organic pollutants. Recently, nanostructured TiO_2, ZnO, and Fe_2O_3 photocatalysts have received great interest[12–17]. For instance, Reddy et al. proposed Cu-doped ZnO nanoparticles for RhB dye degradation under light irradiation[18]. Similarly, Z-scheme binary heterostructured nanocomposites (i.e., MoS_2/g-C_3N_4 and $ZnWO_4$/$NiFe_2O_4$) were employed for the efficient photocatalytic degradation of toxic organic pollutants[19,20]. However, these approaches are restricted because of the passive diffusion of photocatalytic materials, requiring constant agitation. Furthermore, most of them involved more than one component. Consequently, it is highly desirable to explore more facile and practical strategies to facilitate the removal of pollutants.

Light-powered micromotors, micro/nano-sized materials that exploit energy from a powerful, renewable, and abundant source, such as light, and convert it into motion, have received considerable interest[21–26]. Previous research has shown that the active locomotion of light-powered micromotors based on photocatalytic materials can overcome the limitation of passive diffusions of photocatalysts by enhancing the interactions with targeted pollutants[27–31]. For instance, Ma et al. developed tubular micromotors based on TiO_2, magnetic Fe_3O_4 nanoparticles, and Pt for the effective degradation of rhodamine 6G[30]. Moreover, light-powered ZnO/Pt micromotors with H_2O_2-free light-driven propulsion ability and hematite/Pt Janus microrobots were explored for nitroaromatic explosives decomposition[31,32]. However, a noble metal coating was required in both cases to unlock the self-propulsion ability, increasing fabrication costs and complexity. Therefore, low-cost and simpler micromotors remain to be explored for future practical applications.

Here, we demonstrate the photocatalytic degradation of nitroaromatic pollutants by noble metal-free single-component light-powered WO_3 micromotors. Compared to Au-WO_3@C Janus micromotors proposed by Ren et al. for the photodegradation of dye pollutants[25], single-component WO_3 micromotors without the need for additional noble-metal coating were prepared by a facile hydrothermal reaction followed by a calcination process. Once exposed to asymmetric light illumination, the micromotors

---

[1]Future Energy and Innovation Laboratory, Central European Institute of Technology, Brno University of Technology, Purkynova 123, 61200 Brno, Czech Republic. [2]Department of Medical Research, China Medical University Hospital, China Medical University, No. 91 Hsueh-Shih Road, TW-40402 Taichung, Taiwan. [3]Faculty of Electrical Engineering and Computer Science, VSB - Technical University of Ostrava, 17. listopadu 2172/15, 70800 Ostrava, Czech Republic. [4]Department of Chemical and Biomolecular Engineering, Yonsei University, 50 Yonsei-ro, Seodaemun-gu, Seoul 03722, Korea. ✉email: martin.pumera@ceitec.vutbr.cz

can exhibit fuel-free self-actuation in pure water, with remote control and rapid response over on/off switching of UV-light. Motion behavior in different conditions demonstrated that H_2O_2 enhanced the motion and diffusion of micromotors. Finally, these WO_3 micromotors were applied for the effective photodegradation of nitroaromatic compounds, among which picric acid (PA) and 4-nitrophenol (4-NP) were selected as models because of their hazardous nature and high stability in water. Such simple and low-cost micromotors capable of degrading toxic substances hold great potential in the micro/nanomotors systems for environmental remediation.

RESULTS

Characterization of WO_3 micromotors

WO_3 micromotors were successfully prepared via the combination of a simple hydrothermal method and a calcination process, as described in Fig. 1a. Specifically, a homogenous solution consisting of the tungsten precursor and glucose was sealed under the hydrothermal condition, followed by an annealing process in air to promote the formation of single-component WO_3 micromotors. Scanning electron microscopy (SEM) images in Fig. 1b illustrate the obtainment of WO_3 microspheres with sizes varying from 1 to 2 μm. A more detailed analysis displays a highly rough surface, ascribed to a hierarchical structure composed of assembled nanoparticles (Fig. 1c). Energy-dispersive X-ray spectroscopy (EDX) elemental mapping images validate the existence and even distribution of the W and O elements, as shown in Fig. 1d, e. The X-ray diffraction (XRD) pattern of WO_3 micromotors is displayed in Fig. 1f, which agrees with the standard monoclinic phase (JCPDS 83-0951)[33]. In fact, diffraction peaks are observed at $2\theta = 22.9°$, 23.4°, 24.1°, 26.4°, 28.1°, 32.8°, 33.1°, 41.6°, 50,43° and associated with the (002), (020), (200), (120), (112), (022), (202), (222), and (400) crystalline planes of WO_3. The chemical states of WO_3 micromotors were additionally determined by X-ray photoelectron spectroscopy (XPS). Figure 1g shows the main peaks ascribed to W 4*f* and O 1*s*, highlighted in the XPS wide spectrum. The high-resolution spectrum of W 4*f* demonstrates two distinguished peaks in Fig. 1g. The binding energies of W $4f_{7/2}$ and W $4f_{5/2}$, positioned at 35.3 eV and 37.3 eV, respectively, match well with reported values of the W^{6+} oxidation state for WO_3 microspheres. The high-resolution spectrum of O 1*s* displays two peaks at 531.8

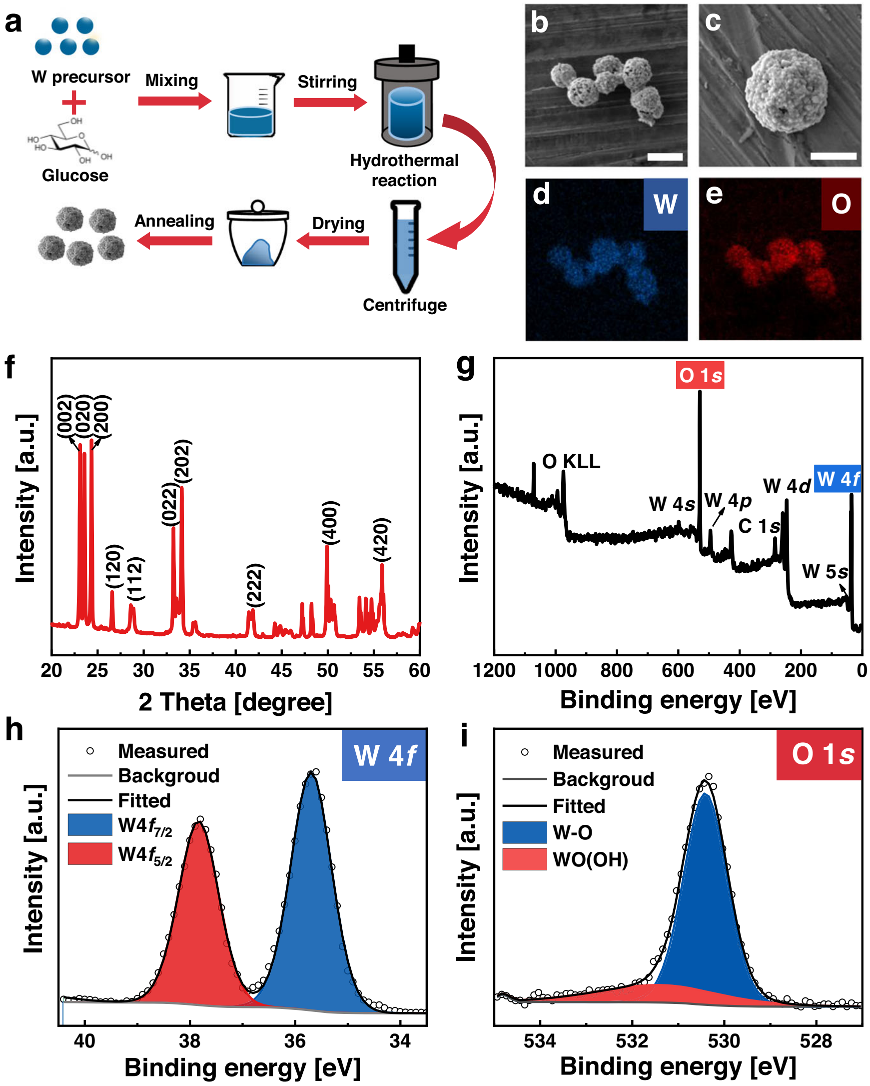

Fig. 1 The preparation process and characterization of WO_3 micromotors. **a** Schematic illustration of the preparation of WO_3 microspheres by hydrothermal and calcination processes. **b** (the scale bar is 2 μm) and **c** (the scale bar is 1 μm) SEM images of WO_3 micromotors. Elemental mapping images for **d** W and **e** O. **f** XRD pattern. **g** XPS wide spectrum. **h** High-resolution W 4*f* XPS spectrum. **i** High-resolution O 1*s* XPS spectrum.

and 530.3 eV binding energy (Fig. 1i)[34]. The peak at 531.8 eV is ascribed to OH groups on the WO_3 micromotors' surface, and the other peak agrees with the lattice oxygen in the crystal structure of WO_3 micromotors.

Motion behavior of WO_3 micromotors

The single-component WO_3 micromotors display autonomous motion when exposed to UV-light illumination both in fuel-free and H_2O_2 solutions. Previous research has elucidated the locomotion mechanism of single-constituent photocatalytic micromachines under light irradiation[35,36]. As illustrated in Fig. 2a, the incidence of photons with higher energy than the optical bandgap of WO_3 micromotors triggers the generation of electron-hole pairs. According to previous works[37–39], the edge of the conduction band (CB) of WO_3 micromotors ($E_{CB} = 0.77$ V_{NHE}, where E_{CB} is the conduction band edge at the normal hydrogen electrode (NHE)) lies below the photocatalytic hydrogen evolution threshold. The photogenerated electrons in the CB could not react with H^+ to generate H_2, whereas they can decompose H_2O or H_2O_2 in protons (H^+). Meanwhile, the photogenerated holes in the valence band (VB) can contribute to breaking down H_2O or H_2O_2 into •OH, O_2, and H^+. The non-uniform light exposure of WO_3 micromotors results in an asymmetrical generation of these chemical species, establishing a product gradient leading to their movement by self-phoresis[40,41]. An optical bandgap of 2.72 eV, representing the minimum energy to excite the electrons from the VB to the CB, was determined from the absorption spectrum of WO_3 micromotors (Fig. 2b) using the Tauc plot (inset in Fig. 2b)[42]. Figure 2c exhibits the time-lapse images of a WO_3 micromotor's trajectory at intervals of ~5 s in pure water and 1% H_2O_2 (Supplementary Videos 1 and 2). WO_3 micromotors exhibit Brownian motion without light and fuel-free propulsion when illuminated by UV-light. A longer trajectory can be observed when 1% H_2O_2 is introduced due to the more pronounced product gradient around the micromotor. The corresponding speeds of these micromotors are also depicted in Fig. 2d and Supplementary Fig. 1a, further indicating the light-controlled on/off movement in pure water and H_2O_2.

The motion of WO_3 micromotors under different conditions was further studied by calculating the mean squared displacement (MSD). As reported in Fig. 2e, the MSD of WO_3 micromotors in 1% H_2O_2 without UV-light irradiation follows a linear increase within 1 s, indicating merely Brownian motion. The same is observed for the micromotors in pure water (Supplementary Fig. 1b). When UV-light is involved, the MSD of micromotors in pure water and H_2O_2 manifests a parabolic increase with time owing to the light-induced micromotors' self-propulsion (Fig. 2e and Supplementary Fig. 1b)[32,43,44]. According to MSD analyses, the diffusion coefficients (D) of WO_3 micromotors were plotted and inserted in Fig. 2e. Under UV-light irradiation in pure water, D is up to $2.0 \pm 0.1\ \mu m^2\ s^{-1}$, whereas a tenfold increase is noted in 1% H_2O_2 ($20 \pm 1\ \mu m^2\ s^{-1}$). To study the parameters that regulate the photocatalytic locomotion of WO_3 micromotors, different concentrations of H_2O_2 were introduced, as depicted in Fig. 2f. The speed of micromotors was progressively increased from $5 \pm 1\ \mu m\ s^{-1}$ to $26 \pm 2\ \mu m\ s^{-1}$ as a higher concentration of H_2O_2 (1% H_2O_2) was added.

Nitroaromatic pollutants degradation

Water contamination caused by nitroaromatic compounds poses severe environmental hazards due to their wide usage for the manufacture of explosives, pesticides, and pharmaceuticals and their non-biodegradable nature with high persistence[2]. Recently, various environmentally friendly treatments that employ active propelled micro/nanomotors have been demonstrated for the degradation or absorption of nitroaromatic compounds[6,45–48]. Nevertheless, most micromotors involve a primary half-coating with expensive Pt or Au to achieve the asymmetrical structure for light-activated propulsion or chemically-driven motion based on H_2O_2 decomposition. There is a strong desire to develop easily fabricated, low-cost, and recyclable micromotors as candidates to facilitate their practical applications. Therefore, we employed the single-component WO_3 micromotors to degrade nitroaromatic compounds in water. PA and 4-NP (molecular structures in the insets in Figs. 3a and 4, respectively) were both selected as representative nitroaromatic contaminants. PA was also employed to investigate the reusability and photodegradation mechanism of WO_3 micromotors.

PA photocatalytic degradation capability of WO_3 micromotors was estimated under UV-light irradiation up to 2 h in 1% H_2O_2. Figure 3a shows the UV-Vis spectra of PA solutions at different reaction times. The intensity of the absorbance peak after the treatments with micromotors decreases with time, suggesting the degradation of PA. The degradation efficiency of micromotors was estimated according to Eq. (1)

$$\text{Degradation Efficiency} = \frac{C_0 - C_t}{C_0} \times 100\% \tag{1}$$

where C_0 represents the original PA concentration, while C_t is the PA concentration at the time t. Specifically, the decomposition efficiency of PA is 72% after 2 h treatment, as shown in Fig. 3c (red line). Additionally, several control experiments were accomplished to assess other contributions to the PA photocatalytic degradation using WO_3 micromotors: 1) PA + UV-light; 2) PA + UV-light + H_2O_2; 3) PA + H_2O_2; 4) PA + WO_3 + UV-light; 5) PA + WO_3 + H_2O_2. As shown in Supplementary Fig. 2a, negligible decreases in the peak intensity can be observed after 2 h photodegradation without micromotors. For fuel-free motion (PA + WO_3 + UV-light) and no motion (PA + WO_3 + H_2O_2), the degradation efficiencies are merely 28% and 5%, respectively, which are lower than the efficient motion with H_2O_2 (PA + WO_3 + UV-light + H_2O_2). These results suggest that UV-light and the addition of H_2O_2 are not sufficient to degrade PA. The reusability of materials has been considered one of the most critical factors for their practical applications. Figure 3b shows that the degradation efficiency still exhibits up to 55% after several consecutive degradation cycles (Supplementary Fig. 2b), which indicates that these micromotors preserved their high photocatalytic capability.

Photogenerated radicals (i.e., h^+, •OH, O_2^-) are crucial for degrading organic pollutants. Owing to the low CB position of WO_3 micromotors ($E_{CB} = 0.77$ V_{NHE}), the reduction of O_2 ($O_2 + e^- \rightarrow \bullet O_2^-$ (aq), -0.33 V_{NHE}) cannot happen under light irradiation[37]. Consequently, photogenerated h^+ and •OH are considered the main radicals that can break down PA. Upon UV-light irradiation, •OH radicals can be formed in two paths: the oxidation of water and reduction of H_2O_2 adsorbed on the surface of WO_3 micromotors as follows.

$$H_2O + h^+ \rightarrow \bullet OH + H^+ \tag{2}$$

$$H_2O_2 + e^- \rightarrow \bullet OH + OH^- \tag{3}$$

A suitable potential value for the reduction of H_2O_2 is $E_{CB} =$ 0.87 V_{NHE}[49]. WO_3 has a higher E_{CB} (0.77 V_{NHE}), so this reaction can happen due to being energetically favorable. Therefore, the enhanced photodegradation efficiency achieved by PA + WO_3 + UV-light + H_2O_2 relies on the photocatalytic capability of WO_3 micromotors and also the enhanced radical production on the surface of WO_3 micromotors because of the presence of H_2O_2. In order to further understand the degradation mechanism, radical trapping experiments were performed[50]. In this regard, EDTA ($10\ mg\ L^{-1}$) and isopropanol ($0.25\ \mu L\ mL^{-1}$) were chosen as typical scavengers to capture h^+ and •OH, respectively[51]. As shown in Fig. 3c, the involvement of isopropanol sharply decreased the photo-induced degradation efficiency of the micromotors,

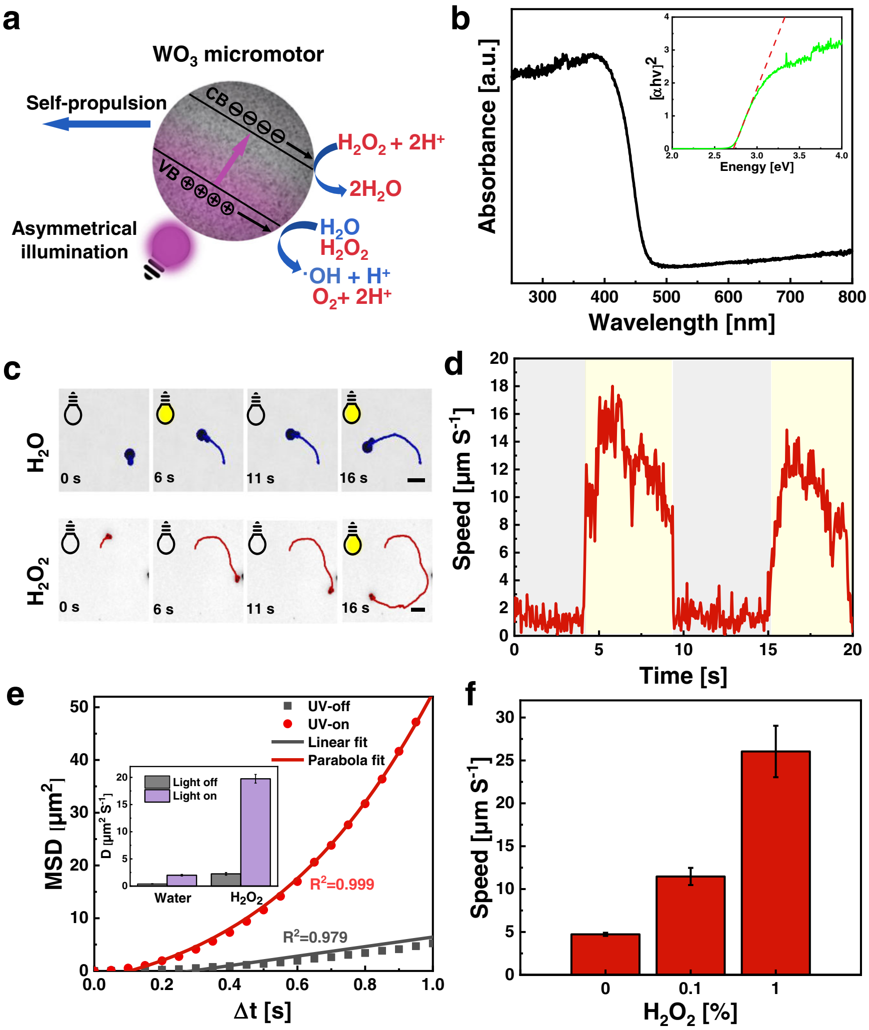

Fig. 2 Motion behavior of WO_3 micromotors. **a** Schematic illustration of the propulsion mechanism of light-powered WO_3 micromotors. **b** UV-Vis spectrum of WO_3 micromotors. The inset shows the bandgap estimation from the corresponding Tauc plot. **c** Time-lapse images of a WO_3 micromotor in 1% H_2O_2 at intervals of ~5 s. Scale bars are 5 μm. **d** Instantaneous speed values and **e** MSD plots of WO_3 micromotors in 1% H_2O_2 without/with UV-light irradiation. The inset shows the corresponding diffusion coefficients according to MSD plots fitting. **f** Comparison of micromotors' speed in different concentrations of H_2O_2. Error bars represent the standard deviation, $n = 5$ independent replicates.

resulting in 37% (Supplementary Fig. 3b). Therefore, the addition of isopropanol decreased the amount of free •OH species, resulting in a markable decrease in the PA photodegradation efficiency. On the contrary, the addition of EDTA accelerated the photodegradation process, enhancing the photoactivity of the micromotors after 2 h light exposure with 1% H_2O_2 (Supplementary Fig. 3a). On these bases, it can be concluded that the radicals •OH are the key photogenerated chemical species responsible for PA oxidation (Fig. 3d).

4-Nitrophenol (4-NP) is a poisonous and bio-rebellious nitroaromatic contaminant that can harm human health considerably[8]. In this work, WO_3 micromotors were also used to degrade 4-NP. Initially, control experiments were run to exclude the interference of other factors (UV-light, H_2O_2, and their combination). As depicted in Supplementary Fig. 4a, no noticeable decline in the absorbance intensity can be observed when micromotors are not involved in control experiments. Figure 4 demonstrates the 4-NP degradation after the treatment with WO_3 micromotors under light exposure in water (free-fuel motion) and in the presence of H_2O_2 (fuel-driven motion) for different durations. Obviously, micromotors powered by the fuel presented an enhanced degradation activity, resulting in an efficiency of 40%, higher than fuel-free motion (11%). This phenomenon can be explained by the lower propulsion speed of micromotors in pure water without any agitation.

DISCUSSION

Here, we reported the large-scale synthesis of precious metal-free single-component WO_3 micromotors via a facile hydrothermal method, which is easily scalable, combined with calcination. We demonstrated that such WO_3 micromachines exhibit self-propulsion upon light exposure, even without H_2O_2 fuel. Specifically, they displayed perceptive on/off motion capability with light exposure. From MSD analyses, it can be proved that micromotors showed pure Brownian motion without light, whereas self-propulsion was achieved under asymmetric UV illumination. The active motion and photocatalytic activity of WO_3 micromotors were applied to degrade toxic nitroaromatic pollutants, such as PA and 4-NP. The micromotors degraded 70% of PA and 40% of 4-NP in water without any external agitation. The photodegradation mechanism was also investigated through radical trapping experiments, which confirmed that •OH is the key ROS responsible for pollutant degradation. The obtained results indicate the possibility of using single-component

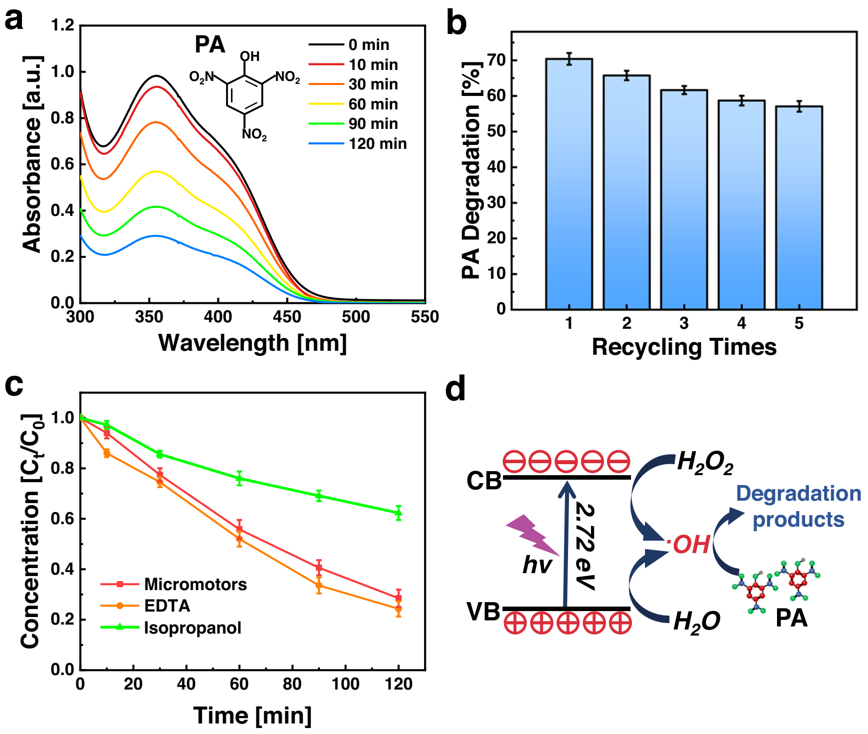

Fig. 3 Photocatalytic degradation of PA by WO_3 micromotors. a UV-Vis spectra of PA after photocatalytic degradation by WO_3 micromotors exposed to UV-light irradiation in 1% H_2O_2; **b** Reusability assessment of WO_3 micromotors under 5 successive cycles of PA degradation; **c** Radical scavenger experiments conducted by employing EDTA and isopropanol; **d** Proposed WO_3 photodegradation mechanism. Error bars represent the standard deviation, *n* = 3 independent replicates.

photocatalytic micromotors to eliminate non-biodegradable and hazardous pollutants from industrial sewages.

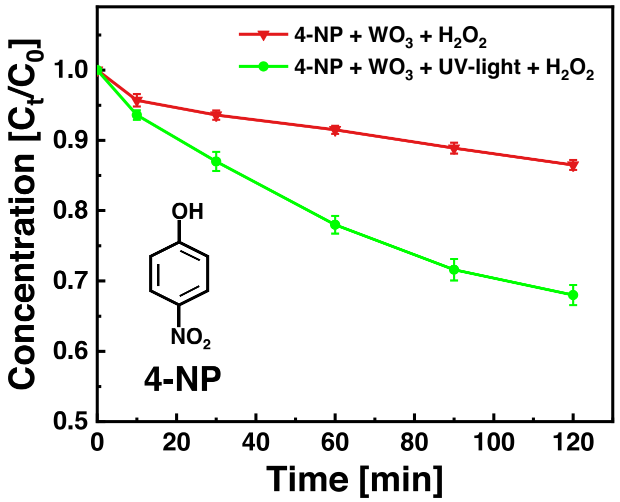

Fig. 4 Photocatalytic degradation of 4-NP using WO_3 micromotors under UV-light irradiation in 1% H_2O_2. Error bars represent the standard deviation, *n* = 3 independent replicates.

METHODS

Synthesis of WO_3 micromotors

Firstly, 50 mL of deionized (DI) water was placed in an 80 mL beaker. Then, 1 mmol Na_2WO_4 was dissolved in the prepared DI water with constant magnetic stirring. Afterward, 25 mmol of glucose was added to the prepared suspension. The final mixture was magnetically mixed until obtaining a homogeneous solution. Then, the solution was transferred into an autoclave. The autoclave was sealed and placed in a preheated oven at 200 °C and lasted for 20 h. When the reaction ended, the autoclave was taken out from the oven and naturally cooled down to room temperature. The precipitated product was cleaned using DI water and ethanol and dried in an oven overnight. Then, the dried products were sealed with aluminum foil and calcined at 550 °C in air. The obtained green-colored product was collected for further experiments.

Characterization of micromotors

SEM images of WO_3 micromotors were acquired by a Tescan MIRA 3 XMU instrument. EDX mapping analysis was conducted by an EDX detector (Oxford Instruments) coupled to the SEM. The chemical states of WO_3 micromotors were characterized by a Kratos Analytical Axis Supra instrument.

Motion experiments

The micromotors' motion was recorded by an inverted microscope (Nikon ECLIPSE Ts2R) and a camera (BASLER acA1920-155uc). Specifically, a 5 µL aqueous suspension containing WO_3 micromotors was used for motion experiments. Three concentrations of H_2O_2 (Merck, 30%) were mixed with the previous suspension, achieving final concentrations of 0, 0.1, and 1%, to observe and record the videos of micromotors' motion with a frame rate of 25 fps. No surfactants were involved in all experiments. The micromotors were exposed to a UV-light source (Cool LED pE-100, 1.6 W cm^{-2}) with a 365 nm wavelength. In order to observe the on/off behavior of micromotors, the light source was switched on/off at defined time intervals (~5 s). The WO_3 micromotors' velocities and trajectories were calculated from the recorded videos and tracked by the NIS Elements Advanced Research software. The diffusion coefficient of micromotors was calculated according to the following equations based on the results of MSD plot fitting:

$$\mathrm{MSD} = 4D\Delta t \tag{4}$$

$$\mathrm{MSD} = 4D\Delta t + v^2\Delta t^2 \tag{5}$$

Pollutants degradation experiments

In all experiments, 2 mg mL^{-1} of micromotors, 50 μM aqueous solution of picric acid (PA, Merck, 99%), and 1% H_2O_2 were consecutively placed in UV-transparent cuvettes. Once UV-light (356 nm, 9 W) was turned on, the cuvettes were put in a closed box for in total of 120 min. Control experiments without UV-light irradiation or H_2O_2 were performed to elucidate the contribution of micromotors. After a different light exposure time, the mixtures were centrifuged at a certain speed for 3 min to obtain the final solution without the micromotors. A UV-Vis spectrophotometer (Jasco V-750) was used to measure the absorbance spectra of the solutions. The absorbance peak at 354 nm was considered to calculate the degradation efficiency. The degradation of 150 μM 4-nitrophenol (4-NP, Sigma Aldrich, 99%) followed the same procedures as PA.

DATA AVAILABILITY

The data that support the findings of this study are available from the corresponding author upon reasonable request.

Received: 17 August 2022; Accepted: 20 February 2023;

REFERENCES

1. Kovacic, P. & Somanathan, R. Nitroaromatic compounds: environmental toxicity, carcinogenicity, mutagenicity, therapy and mechanism. *J. Appl. Toxicol.* **34**, 810–824 (2014).
2. Ju, K. S. & Parales, R. E. Nitroaromatic compounds, from synthesis to biodegradation. *Microbiol. Mol. Biol. Rev.* **74**, 250–272 (2010).
3. Tiwari, J., Tarale, P., Sivanesan, S. & Bafana, A. Environmental persistence, hazard, and mitigation challenges of nitroaromatic compounds. *Environ. Sci. Pollut. Res.* **26**, 28650–28667 (2019).
4. Cai, Q. Y., Mo, C. H., Wu, Q. T., Zeng, Q. Y. & Katsoyiannis, A. Occurrence of organic contaminants in sewage sludges from eleven wastewater treatment plants. *Chemosphere* **68**, 1751–1762 (2007).
5. Jurado-Sánchez, B. & Wang, J. Micromotors for environmental applications: a review. *Environ. Sci. Nano* **5**, 1530–1544 (2018).
6. Oral, C. M., Ussia, M. & Pumera, M. Self-propelled activated carbon micromotors for 'on-the-fly' capture of nitroaromatic explosives. *J. Phys. Chem. C* **125**, 18040–18045 (2021).
7. Chan, S. S., Khoo, K. S., Chew, K. W., Ling, T. C. & Show, P. L. Recent advances biodegradation and biosorption of organic compounds from wastewater: microalgae-bacteria consortium - a review. *Bioresour. Technol.* **344**, 126159 (2022).
8. Patial, S. et al. Recent advances in photocatalytic multivariate metal organic frameworks-based nanostructures toward renewable energy and the removal of environmental pollutants. *Mater. Today Energy* **19**, 100589 (2021).
9. Hasija, V. et al. Advanced activation of persulfate by polymeric G-C_3N_4 based photocatalysts for environmental remediation: a review. *J. Hazard. Mater.* **413**, 125324 (2021).
10. Sharma, S. et al. Tailoring cadmium sulfide-based photocatalytic nanomaterials for water decontamination: a review. *Environ. Chem. Lett.* **19**, 271–306 (2021).
11. Liu, H., Wang, C. & Wang, G. Photocatalytic advanced oxidation processes for water treatment: recent advances and perspective. *Chem. Asian J.* **15**, 3239–3253 (2020).
12. Zhao, B. et al. Degradation of 4-nitrophenol (4-NP) using Fe-TiO_2 as a heterogeneous photo-Fenton catalyst. *J. Hazard. Mater.* **176**, 569–574 (2010).
13. Ussia, M. et al. Light-propelled nanorobots for facial titanium implants biofilms removal. *Small* **18**, 2200708 (2022).
14. Hitam, C. N. C. & Jalil, A. A. A review on exploration of Fe_2O_3 photocatalyst towards degradation of dyes and organic contaminants. *J. Environ. Manag.* **258**, 110050 (2019).
15. Chen, X., Wu, Z., Liu, D. & Gao, Z. Preparation of ZnO photocatalyst for the efficient and rapid photocatalytic degradation of azo dyes. *Nanoscale Res. Lett.* **12**, 4–13 (2017).
16. Karthik, K. V. et al. Barium titanate nanostructures for photocatalytic hydrogen generation and photodegradation of chemical pollutants. *J. Mater. Sci. Mater. Electron.* **30**, 20646–20653 (2019).
17. Urso, M., Ussia, M. & Pumera, M. Smart micro- and nanorobots for water purification. *Nat. Rev. Bioeng.* https://doi.org/10.1038/s44222-023-00025-9 (2023).
18. Karthik, K. V. et al. Green synthesis of Cu-doped ZnO nanoparticles and its application for the photocatalytic degradation of hazardous organic pollutants. *Chemosphere* **287**, 132081 (2022).
19. Monga, D., Ilager, D., Shetti, N. P., Basu, S. & Aminabhavi, T. M. 2D/2d heterojunction of MoS_2/g-C_3N_4 nanoflowers for enhanced visible-light-driven photocatalytic and electrochemical degradation of organic pollutants. *J. Environ. Manag.* **274**, 111208 (2020).
20. Reddy, C. V. et al. Z-Scheme binary 1D $ZnWO_4$ nanorods decorated 2D $NiFe_2O_4$ nanoplates as photocatalysts for high efficiency photocatalytic degradation of toxic organic pollutants from wastewater. *J. Environ. Manag.* **268**, 110677 (2020).
21. Xu, L., Mou, F., Gong, H., Luo, M. & Guan, J. Light-driven micro/nanomotors: from fundamentals to applications. *Chem. Soc. Rev.* **46**, 6905–6926 (2017).
22. Vizsnyiczai, G. et al. Light controlled 3D micromotors powered by bacteria. *Nat. Commun.* **8**, 15974 (2017).
23. Dong, R. et al. Visible-light-driven BiOI-based Janus micromotor in pure water. *J. Am. Chem. Soc.* **139**, 1722–1725 (2017).
24. Peng, X., Urso, M., Ussia, M. & Pumera, M. Shape-controlled self-assembly of light-powered microrobots into ordered microchains for cells transport and water remediation. *ACS Nano* **16**, 7615–7625 (2022).
25. Zhang, Q. et al. Light-driven Au-WO_3@C Janus micromotors for rapid photodegradation of dye pollutants. *ACS Appl. Mater. Interfaces* **9**, 4674–4683 (2017).
26. Urso, M., Ussia, M., Novotný, F. & Pumera, M. Trapping and detecting nanoplastics by MXene-derived oxide microrobots. *Nat. Commun.* **13**, 3573 (2022).
27. Ussia, M. et al. Active light-powered antibiofilm ZnO micromotors with chemically programmable properties. *Adv. Funct. Mater.* **31**, 2101178 (2021).
28. Fernández-Medina, M., Ramos-Docampo, M. A., Hovorka, O., Salgueiriño, V. & Städler, B. Recent advances in nano- and micromotors. *Adv. Funct. Mater.* **30**, 1908283 (2020).
29. Urso, M., Ussia, M. & Pumera, M. Breaking polymer chains with self-propelled light-controlled navigable hematite microrobots. *Adv. Funct. Mater.* **31**, 2101510 (2021).
30. Liang, C. et al. Bilayer tubular micromotors for simultaneous environmental monitoring and remediation. *ACS Appl. Mater. Interfaces* **10**, 35099–35107 (2018).
31. Ying, Y. et al. Light-driven ZnO brush-shaped self-propelled micromachines for nitroaromatic explosives decomposition. *Small* **16**, 1902944 (2020).
32. Peng, X., Urso, M. & Pumera, M. Photo-Fenton degradation of nitroaromatic explosives by light-powered hematite microrobots: when higher speed is not what we go for. *Small Methods* **5**, 2100617 (2021).
33. Szilágyi, I. et al. WO_3 photocatalysts: Influence of structure and composition. *J. Catal.* **294**, 119–127 (2012).
34. Kalanur, S. S. Structural, optical, band edge and enhanced photoelectrochemical water splitting properties of tin-doped WO_3. *Catalysts* **9**, 456 (2019).
35. Hong, Y., Diaz, M., Córdova-Fteueroa, U. M. & Sen, A. Light-driven titanium-dioxide-based reversible microfireworks and micromotor/micropump systems. *Adv. Funct. Mater.* **20**, 1568–1576 (2010).
36. Villa, K., Děkanovský, L., Plutnar, J., Kosina, J. & Pumera, M. Swarming of perovskite-like Bi_2WO_6 microrobots destroy textile fibers under visible light. *Adv. Funct. Mater.* **30**, 2007073 (2020).
37. Mardare, C. C. & Hassel, A. W. Review on the versatility of tungsten oxide coatings. *Phys. Status Solidi A* **216**, 1900047 (2019).
38. Nguyen, T. T., Nam, S. N., Son, J. & Oh, J. Tungsten trioxide (WO_3)-assisted photocatalytic degradation of amoxicillin by simulated solar irradiation. *Sci. Rep.* **9**, 9349 (2019).
39. Xiao, T. et al. In situ construction of hierarchical WO_3/g-C_3N_4 composite hollow microspheres as a Z-scheme photocatalyst for the degradation of antibiotics. *Appl. Catal. B Environ.* **220**, 417–428 (2018).
40. Pourrahimi, A. M., Villa, K., Ying, Y., Sofer, Z. & Pumera, M. ZnO/ZnO_2 /Pt Janus micromotors propulsion mode changes with size and interface structure: enhanced nitroaromatic explosives degradation under visible light. *ACS Appl. Mater. Interfaces* **10**, 42688–42697 (2018).
41. Ibele, M., Mallouk, T. E. & Sen, A. Schooling behavior of light-powered autonomous micromotors in water. *Angew. Chem. Int. Ed.* **48**, 3308–3312 (2009).
42. Vemuri, R. S., Engelhard, M. H. & Ramana, C. V. Correlation between surface chemistry, density, and band gap in nanocrystalline WO_3 thin films. *ACS Appl. Mater. Interfaces* **4**, 1371–1377 (2012).
43. Hu, Y., Liu, W. & Sun, Y. Self-propelled micro-/nanomotors as 'on-the-move' platforms: cleaners, sensors, and reactors. *Adv. Funct. Mater.* **32**, 2109181 (2022).

44. Gao, C., Feng, Y., Wilson, D. A., Tu, Y. & Peng, F. Micro-nano motors with taxis behavior: principles, designs, and biomedical applications. *Small* **18**, 2106263 (2022).
45. Kong, L., Ambrosi, A., Nasir, M. Z. M., Guan, J. & Pumera, M. Self-propelled 3D-printed 'aircraft carrier' of light-powered smart micromachines for large-volume nitroaromatic explosives removal. *Adv. Funct. Mater.* **29**, 1903872 (2019).
46. Srivastava, S. K., Guix, M. & Schmidt, O. G. Wastewater mediated activation of micromotors for efficient water cleaning. *Nano Lett.* **16**, 817–821 (2016).
47. Mayorga-Martinez, C. C., Vyskočil, J., Novotný, F. & Pumera, M. Light-driven Ti_3C_2 MXene micromotors: Self-propelled autonomous machines for photodegradation of nitroaromatic explosives. *J. Mater. Chem. A* **9**, 14904–14910 (2021).
48. Kong, L., Mayorga-Martinez, C. C., Guan, J. & Pumera, M. Fuel-free light-powered TiO_2/Pt Janus micromotors for enhanced nitroaromatic explosives degradation. *ACS Appl. Mater. Interfaces* **10**, 22427–22434 (2018).
49. Kochergin, Y. S., Villa, K., Nemeškalová, A., Kuchař, M. & Pumera, M. Hybrid inorganic-organic visible-light-driven microrobots based on donor-acceptor organic polymer for degradation of toxic psychoactive substances. *ACS Nano* **15**, 18458–18468 (2021).
50. Hirakawa, T. & Nosaka, Y. Properties of $O_2•^-$ and •OH formed in TiO_2 aqueous suspensions by photocatalytic reaction and the influence of H_2O_2 and some ions. *Langmuir* **18**, 3247–3254 (2002).
51. Liu, T. et al. Comparative study of the photocatalytic performance for the degradation of different dyes by $ZnIn_2S_4$: Adsorption, active species, and pathways. *RSC Adv.* **7**, 12292–12300 (2017).

ACKNOWLEDGEMENTS

M.P. acknowledges the financial support of the Grant Agency of the Czech Republic (EXPRO: 19-26896X). X.P. was supported by the China Scholarship Council (CSC No. 202008320382). CzechNanoLab project LM2018110 funded by MEYS CR is gratefully acknowledged for the financial support of the measurements/sample fabrication at CEITEC Nano Research Infrastructure.

AUTHOR CONTRIBUTIONS

X.P. prepared, and characterized the micromotors, evaluated the performance of the motion, conducted the degradation experiments, and wrote the manuscript. M.U. designed the experiments and contributed to data interpretation. X.P. and M.P. originated the idea. M.U. and M.P. supervised the research. All authors have given approval to the final version of the manuscript.

COMPETING INTERESTS

The authors declare no competing interests.

ADDITIONAL INFORMATION

Supplementary information The online version contains supplementary material available at https://doi.org/10.1038/s41545-023-00235-z.

Correspondence and requests for materials should be addressed to Martin Pumera.

Reprints and permission information is available at http://www.nature.com/reprints

6. Photo-Fenton degradation of nitroaromatic explosives by light-powered hematite microrobots: when higher speed is not what we go for

Published paper included in this chapter:

Xia Peng, Mario Urso and Martin Pumera*, "Photo-Fenton Degradation of Nitroaromatic Explosives by Light-Powered Hematite Microrobots: When Higher Speed Is Not What We Go For", *Small Methods* **2021**, *2100617*.

6.1 Motivation of this study

The primary aim of this research is to investigate how the thickness of the metal layer affects the motion dynamics of light-powered Janus microrobots and its impact on their photocatalytic efficiency. Different from single component microrobots, Janus microrobot generally consist of one photocatalyst and half coated metal layer. The metal layer plays important role in the propulsion performance of microrobots due to that it improves the charge separation at the semiconductor/metal interface, enhancing the microrobots' speed and photocatalytic properties. However, the impact of metal layer thickness on the self-propulsion performance of light-driven Janus microrobots remains unexplored. Furthermore, the correlation between metal layer thickness, microrobot speed, and photocatalytic efficiency has yet to be thoroughly investigated and understood.

6.2 Paper conclusion

The research focused on investigating the influence of different thickness of metal layer on microrobots, employing hematite as the active photocatalyst and sputtering half Pt as metal layer. These microrobots, fabricated via hydrothermal synthesis and Pt sputtering (with 30, 60, and 90 nm Pt layers), leverage hematite's photocatalytic properties, low cost, and magnetism. A thicker Pt layer increased microrobot speed, as confirmed by Tafel measurements. However, while faster motion was observed, degradation efficiency of picric acid (PA), a model explosive pollutant, decreased with thicker Pt layers. This reduction was attributed to greater consumption of H_2O_2 for propulsion, leaving less available for the hematite-driven photo-Fenton degradation process. Interestingly, microrobots with a 30 nm Pt layer demonstrated the balance between speed and pollutant degradation, successfully degrading PA, 4-NP, and RhB, both individually and in mixtures. These findings highlight the need to balance motion and catalytic efficiency by optimizing Pt layer thickness for water pollutant remediation.

6.3 Author contribution

I performed the fabrication of microrobots, recorded, and analyzed their motion, carried out the degradation experiments, and interpreted the data. Then, I wrote the first version of the manuscript.

RESEARCH ARTICLE

small methods
www.small-methods.com

Photo-Fenton Degradation of Nitroaromatic Explosives by Light-Powered Hematite Microrobots: When Higher Speed Is Not What We Go For

*Xia Peng, Mario Urso, and Martin Pumera**

Self-powered micromachines are considered a ground-breaking technology for environmental remediation. Light-powered Janus microrobots based on photocatalytic semiconductors asymmetrically covered with metals have recently received great interest as they can exploit light to move and contemporarily degrade pollutants in water. Although various metals have been explored and compared to design Janus microrobots, the influence of the metal layer thickness on motion behavior and photocatalytic properties of microrobots have not been investigated yet. Here, light-driven hematite/Pt Janus microrobots are reported and fabricated by depositing Pt layers with different thickness on hematite microspheres produced by hydrothermal synthesis. It has been demonstrated that the thicker the metal layer the higher the microrobots speed. However, when employed for the degradation of nitroaromatic explosives pollutants through the photo-Fenton mechanism, higher rate of H_2O_2 consumption leads to higher propulsion speed of microrobots and lower pollutants degradation efficiencies owing to less H_2O_2 involved in the photo-Fenton reaction. This work presents new insights into the motion behavior of light-powered Janus micromotors and demonstrates that high speed is not what really matters for water purification via photo-Fenton reaction, which is important for the future environmental applications of micromachines.

1. Introduction

Micro/nanorobots are smart micro/nanomaterials that can efficiently convert the surrounding energy into autonomous motion, navigate, and perform desired actions.[1,2] They hold great prospects in various application fields from biomedicine to environmental remediation and sensing.[3–8] Over the past decades, tremendous efforts have been made toward the precise control of microrobots' motion mechanism, speed, and directionality, with the aim to accomplish specific tasks in complex environments.[9–11] The self-propulsion of these tiny machines can be induced by chemical fuels (H_2O_2, glucose, urea) or external stimuli such as light, magnetic fields, and ultrasound.[12–20] Light is a very attractive energy source to power microrobots because it is powerful, renewable, and abundant. Consequently, light-driven microrobots have recently attracted great attention and have been reported moving at the cellular level, overcoming the major limitation of toxic fuels such as H_2O_2, or degrading "on-the-fly" harmful pollutants in water.[21,22] "Two-faced" Janus microrobots, consisting of a photocatalytic semiconductor asymmetrically covered by a metal layer, represent the most efficient light-powered microrobots.[23–26] These microrobots can move via the self-electrophoretic mechanism due to the asymmetric generation of charges under light irradiation, establishing a local electric field that induces their motion.[27] The metal layer plays a crucial role as it improves the charge separation at the semiconductor/metal interface, enhancing the microrobots' speed and photocatalytic properties.[9] Different metals, especially noble metals like Au and Pt, have been combined with different photocatalysts (UV-light-activated TiO_2 and ZnO, visible light-activated Fe_2O_3 and BiOI)

X. Peng, M. Urso, M. Pumera
Future Energy and Innovation Laboratory
Central European Institute of Technology
Brno University of Technology
Brno 61200, Czech Republic
E-mail: martin.pumera@ceitec.vutbr.cz

M. Pumera
Center for Nanorobotics and Machine Intelligence
Department of Chemistry and Biochemistry
Mendel University in Brno
Brno 61300, Czech Republic

M. Pumera
Department of Medical Research
China Medical University Hospital
China Medical University
Taichung 40402, Taiwan

M. Pumera
Department of Chemical and Biomolecular Engineering
Yonsei University
Seodaemun-gu, Seoul 03722, Korea

The ORCID identification number(s) for the author(s) of this article can be found under https://doi.org/10.1002/smtd.202100617.

DOI: 10.1002/smtd.202100617

to fabricate light-driven Janus microrobots.[28–31] It has been demonstrated that the metal layer must be carefully chosen in order to achieve the highest speed. Moreover, the optimal metal layer may vary from one semiconductor to another. For instance, Maric et al. studied the speed in pure water of UV-powered metal/TiO_2 Janus microrobots with different metal coatings (Au, Ag, Pt, Cu, Fe), reporting that TiO_2/Pt microrobots showed the highest speed due to the largest electrochemical potential difference between Pt and TiO_2 compared to the other metals[29] while Au was found to be the best metal coating for visible light-driven metal/BiOI Janus microrobots.[28] The effect of bimetals (bilayers of Au and Ag on TiO_2 microparticles and bimetallic coatings of Pt-Pd and Au-Pd 80:20 on Fe_2O_3) has also been investigated, evidencing a remarkable enhancement in speed compared to single metals.[30] Nevertheless, the influence of metal layer thickness on the self-propulsion ability of light-driven Janus microrobots has not been reported yet. Additionally, the relationships between metal layer thickness and microrobots' speed and photocatalytic properties remain to be studied and clarified.

In this work, the role of metal layer thickness in the motion behavior of light-powered Janus microrobots was investigated and how it affects microrobots' photocatalytic properties was also illustrated by applying them for the photocatalytic degradation of pollutants in water. Hematite was selected as the semiconducting side due to its low cost, biocompatibility, catalyzed Fenton and photo-Fenton reaction, and intrinsic magnetism, which allows navigation through magnetic fields. Pt has been chosen as the metal side according to our previous paper.[30] Hematite/Pt Janus microrobots were fabricated by depositing Pt layers with different thickness (30, 60, and 90 nm) through sputtering on hematite microspheres synthesized by a hydrothermal method (**Scheme 1**). All microrobots show self-propulsion under UV-light irradiation in pure water and higher speed in the presence of small amounts of H_2O_2, with a rapid on/off response to light. With increasing Pt layer thickness, microrobots exhibit faster motion, which was explained by electrochemical potential measurements from Tafel experiments. In addition, the influence of metal layer thickness on pollutant degradation was investigated using picric acid (PA) as a typical high-energy nitroaromatic explosive pollutant in water. The photo-Fenton reaction in the presence of UV-light irradiation and 0.1% H_2O_2 was identified as the dominant degradation mechanism. Still, the higher speed achieved with the thicker Pt layer does not result in higher degradation efficiency, which was attributed to the higher consumption of H_2O_2 for motion, leading to less H_2O_2 available for photo-Fenton degradation. This work presents new important insights into the motion mechanism and speed of light-powered microrobots, and evidences the rise of a competition between microrobots speed and pollutant degradation efficiency when photo-Fenton processes are involved.

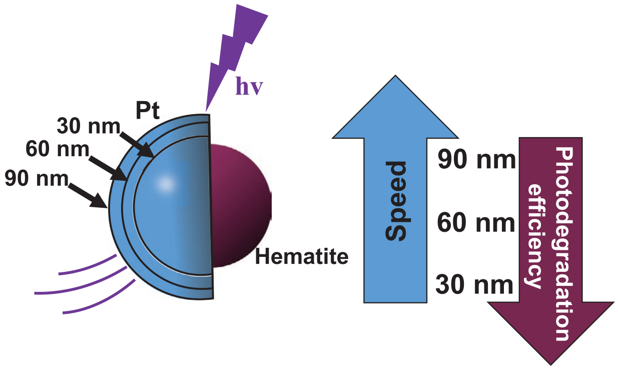

Scheme 1. Light-powered hematite/Pt Janus microrobots with different Pt layer thickness for photo-Fenton degradation of explosive pollutants in water. The higher Pt layer thickness results in higher microrobots speed but lower efficiency in PA degradation via the photo-Fenton mechanism.

2. Experimental Section

2.1. Synthesis of Hematite Microspheres

Hematite (α-Fe_2O_3) microspheres were synthesized by a facile hydrothermal reaction. In a typical synthesis, $FeCl_3$ (Sigma Aldrich, 97%) was added to ultra-pure water (18 MΩ cm) to form a 1 M $FeCl_3$ homogenous solution under magnetic stirring. Then the solution was transferred into a 50 mL Teflon-lined stainless-steel autoclave, heated at 160 °C for 20 h, and cooled down to room temperature naturally. Afterward, the product was collected by centrifugation and washed several times with deionized water and ethanol. Finally, it was dried in a vacuum oven at 60 °C for 12 h.

2.2. Preparation of Hematite/Pt Janus Microrobots

To prepare hematite/Pt Janus microrobots, the synthesized hematite microspheres were suspended in pure water (5 mg mL^{-1}) and dispersed by sonication. The suspension was dropped by a pipette on glass slides and dried overnight. Pt layers with different thickness (30, 60, and 90 nm) were asymmetrically deposited on hematite microspheres by sputtering method. The real-time thickness of the sputtered Pt layer was controlled by a quartz crystal microbalance. After the sputtering process, microrobots were released using a scalpel.

2.3. Microrobots Characterization

Scanning electron microscopy (SEM) images of hematite microspheres and hematite/Pt Janus microrobots were obtained with a Tescan MIRA 3 XMU instrument. Energy-dispersive X-ray spectroscopy (EDX) mapping analysis was performed using an Oxford EDX detector connected to the SEM. The magnetic hysteresis loop was carried out on a Cryogenic-free VSM magnetometer at 300 K in magnetic fields up to 10 kOe.

2.4. Motion Experiments

A Nikon ECLIPSE TS2R inverted microscope coupled with a Hamamatsu digital camera C13440-20CU was used to record the microrobots' motion. Briefly, a microrobot aqueous suspension was dropped on a glass slide. Different concentrations of H_2O_2

(Merck, 30%) were subsequently added to the drop in order to study microrobots motion in 0%, 0.1%, and 1% H_2O_2. All experiments were carried out in the absence of surfactants. Then, the microrobots were activated by a 365 nm UV LED (CoolLED pE-100) operated at different light intensities. Recorded videos were analyzed to observe microrobot tracks and calculate their speed through NIS Elements Advanced Research software.

2.5. Electrochemical Measurements

Tafel experiments were carried out using a customized photoelectrochemical setup with a 365 nm UV LED (700 mA powered LZ4-04UV00, LedEngin Inc.) in the two-electrode configuration with either hematite electrode or Pt electrode as working electrodes and an Ag/AgCl electrode as both reference and counter electrode. The hematite working electrode was made by dropping 100 µL of a 5 mg mL^{-1} aqueous suspension of hematite microspheres on a commercial indium tin oxide (ITO)-covered glass slide (1×2 cm^2, Sigma Aldrich, 8–12 Ω sq^{-1}) and drying overnight. Pt working electrodes with different Pt layer thickness were obtained by sputtering 30, 60, and 90 nm Pt on ITO-covered glass slides. Tafel measurements were recorded at a scan rate of 5 mV s^{-1} from 0 to 0.5 V versus Ag/AgCl under UV-light irradiation on the working electrodes (1×1 cm^2 immersed area) in pure water and 1% H_2O_2 solution using a Metrohm AUTOLAB potentiostat.

2.6. Pollutants Degradation Experiments

Microrobots (1 mg mL^{-1}), piric acid (PA, Merck, 99%) aqueous solution (50×10^{-6} M), and 0.1% H_2O_2 were successively added to UV-transparent cuvettes. A control experiment with bare hematite microspheres was also carried out. Cuvettes were exposed to UV-light irradiation (365 nm UV LED lamp, 4 W) for 2 h. Additional control experiments in the absence of UV-light irradiation or H_2O_2 were conducted to elucidate the degradation mechanism. At the end of the process, the suspensions were centrifuged (7000 rpm for 3 min) to separate the solution from the microrobots and UV-Vis absorption spectra were recorded using a Jasco V-750 UV-Vis spectrophotometer. PA degradation efficiency was calculated based on Equation (1)

$$\text{Degradation Efficiency} = \frac{C_0 - C_1}{C_0} \times 100 \qquad (1)$$

where C_0 is the initial PA concentration and C_1 is PA concentration after the treatment with microrobots, measured in correspondence of the maximum at 354 nm in the UV-vis spectrum. The same procedure was applied for the degradation of 4-nitrophenol (4-NP, Sigma Aldrich) aqueous solution (140×10^{-6} M) and Rhodamine B (RhB, Alfa Aesar) aqueous solution (200×10^{-6} M).

3. Results and Discussion

The aim of this work is to investigate the influence of metal layer thickness on the speed and explosive pollutant photodegradation ability of light-driven Janus microrobots based on photocatalytic semiconductors asymmetrically covered with a metal layer. For this purpose, among the different semiconductors, hematite (α-Fe_2O_3) has been selected due to its low cost, biocompatibility, excellent photocatalytic properties, catalyzed Fenton and photo-Fenton reaction, and magnetic field navigability. Based on our previous work, Pt has been chosen as the metal to fabricate Janus micromotors owing to its larger electrochemical potential difference with hematite compared to other single metals, leading to higher speed.[30] Specifically, hematite/Pt Janus microrobots were fabricated using a simple approach as illustrated in **Scheme 2**. Hematite microspheres were first synthesized via a facile hydrothermal method and subsequently coated with Pt layers with different thickness (30, 60, and 90 nm) by sputtering method to fabricate Janus microrobots. **Figure 1** shows SEM images and the corresponding elemental mapping images obtained by EDX of a bare hematite microsphere and microrobots with different Pt layer thickness. Hematite microspheres consist of self-assembled nanoparticles, resulting in a highly rough surface as shown in the region marked in red in Figure S1 in the Supporting Information, and exhibit a uniform distribution of Fe and O. After Pt layer deposition, microspheres exhibit the distinct asymmetrical structure of Janus microrobots. Furthermore, the atomic percentages of Fe, O, and Pt were obtained by EDX, finding the 2:3 ratio between Fe and O, as expected for hematite, and an increasing amount of Pt with increasing thickness of the Pt layer. In particular, the atomic percentages were estimated as: 41% Fe and 59% O for the bare hematite microsphere; 39% Fe, 60.3% O, and 0.7% Pt for 30 nm Pt microrobots; 36.8% Fe, 61% O, and 2.2% Pt for 60 nm Pt microrobots; and 41.7% Fe, 55.1% O, and 3.2% Pt for 90 nm Pt microrobots. It must also be noted that the ratio of Pt among the different samples is ≈1:2:3, which is in agreement with the selected sputtered thicknesses (30, 60, and 90 nm).

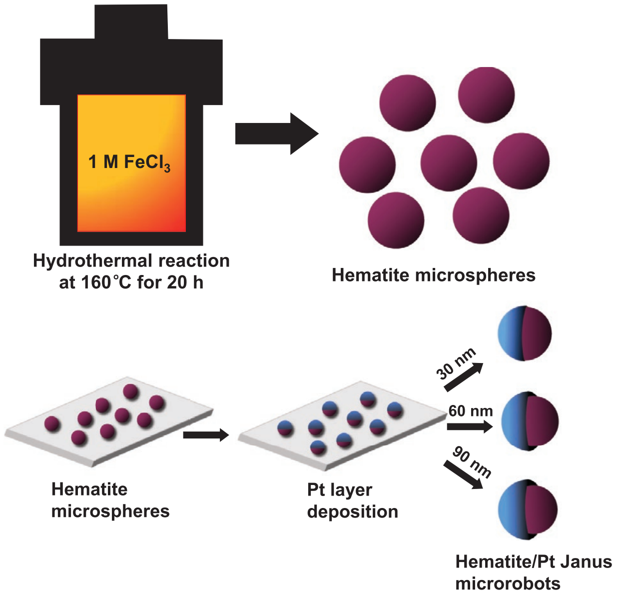

Scheme 2. Schematic illustration of hematite microspheres synthesis and hematite/Pt Janus microrobots fabrication.

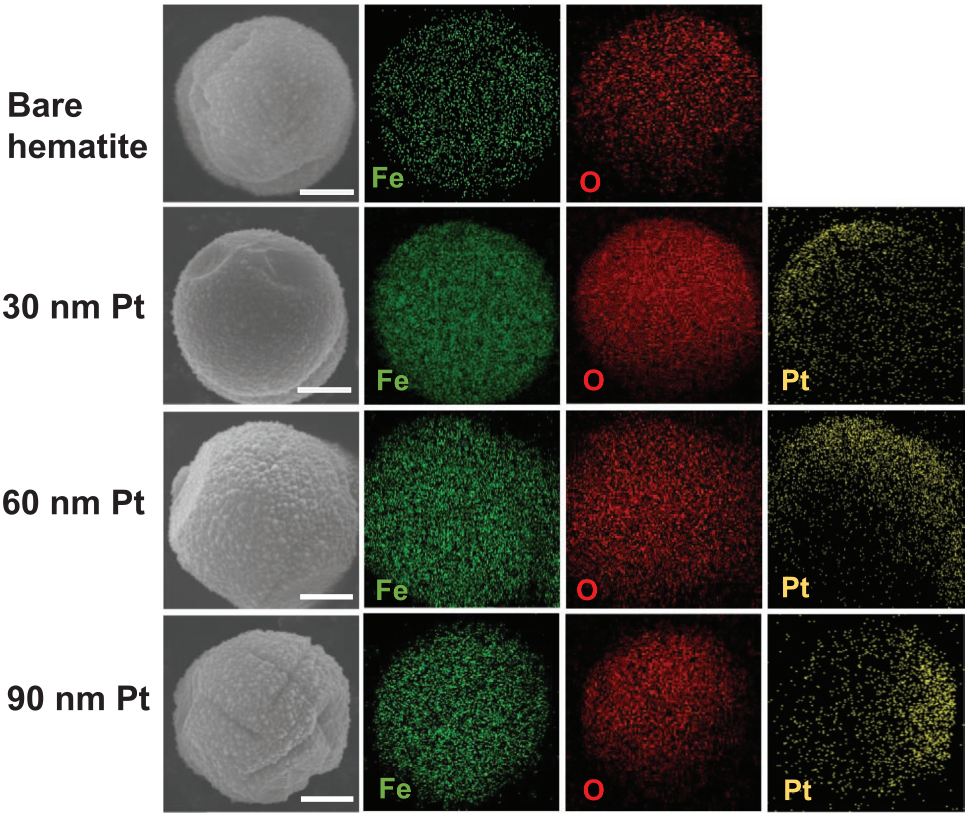

Figure 1. SEM and EDX elemental mapping images of a bare hematite microsphere and hematite/Pt Janus microrobots with different Pt layer thickness (scale bars are 1 µm).

The motion behavior of hematite/Pt microrobots with different Pt layer thickness was evaluated in pure water and in the presence of H_2O_2 under UV-light irradiation. **Figure 2**a reports 5 s long trajectories of microrobots in 0%, 0.1%, and 1% H_2O_2 (Movies S1–S3, Supporting Information). All microrobots show Brownian motion in the dark and fuel-free self-propulsion ability under UV-light irradiation, independently of the thickness of the Pt layer, which was not observed for bare hematite microspheres also in the presence of both H_2O_2 fuel and UV-light irradiation (Movie S4, Supporting Information). Moreover, at a fixed Pt layer thickness, a higher concentration of H_2O_2 facilitates longer navigation trajectories within the 5 s recording. The speed of 30, 60, and 90 nm Pt microrobots in different concentrations of H_2O_2 was also calculated from the average of more than 20 different microrobots (Figure 2b). From 0% to 1% H_2O_2, the speed increases from 5 ± 1 to 14 ± 2 $\mu m\ s^{-1}$ for 30 nm Pt microrobots, from 7 ± 0.7 to 21 ± 3 $\mu m\ s^{-1}$ for 60 nm Pt microrobots, and from 4 ± 0.7 to 27 ± 5 $\mu m\ s^{-1}$ for 90 nm Pt microrobots. In addition, a larger Pt layer thickness results in higher speed for the same concentration of H_2O_2 fuel. Only a small deviation from this behavior is noted for the 90 nm Pt microrobots in pure water as they display a lower speed compared to 60 nm Pt microrobots. Upon UV-light irradiation, separation of photogenerated electron–hole pairs in hematite occurs at the interface with Pt, and electrons are injected from the hematite conduction band into Pt. As a consequence, more protons are produced at the hematite side from the oxidation of water and H_2O_2, if present. This gradient of protons generates a powerful fluid flow toward Pt side and establishes an electric field which results in Janus microrobots self-propulsion via a self-electrophoretic mechanism.[9,23,24,28,30,32] The addition of small amount of H_2O_2 (0.1%) results in a much stronger gradient of charges and thus in a faster propulsion and higher speed. Furthermore, in the absence of light irradiation and in the presence of H_2O_2, microrobots can move via a self-diffusiophoretic mechanism due to the gradient of products resulting from the Pt-catalyzed decomposition of H_2O_2. In general, these findings suggest that increasing the metal layer thickness can significantly enhance the speed of light-powered Janus microrobots.

To further explore the parameters that control the light-powered motion of hematite/Pt microrobots, UV-light on/off switching experiments were performed. Figure 2c reports the speed of microrobots with different Pt layer thickness for on/off switching of UV-light irradiation at time intervals of ≈5 s in 1% H_2O_2. All microrobots display a perceptive on/off response to light. In addition, the influence of light intensity on microrobots' motion and speed was taken into consideration. When the UV-light source intensity was varied from 0.4 to 1.6 $W\ cm^{-2}$, the speed of 90 nm Pt microrobots nearly tripled, increasing from 10 ± 1 to 27 ± 5 $\mu m\ s^{-1}$ (Figure S2, Supporting Information).

The underlying reasons for the differences in the speed when different Pt layer thicknesses are deposited on the surface of hematite microspheres were investigated. According to previous reports, the speed of a light-powered Janus microrobot is

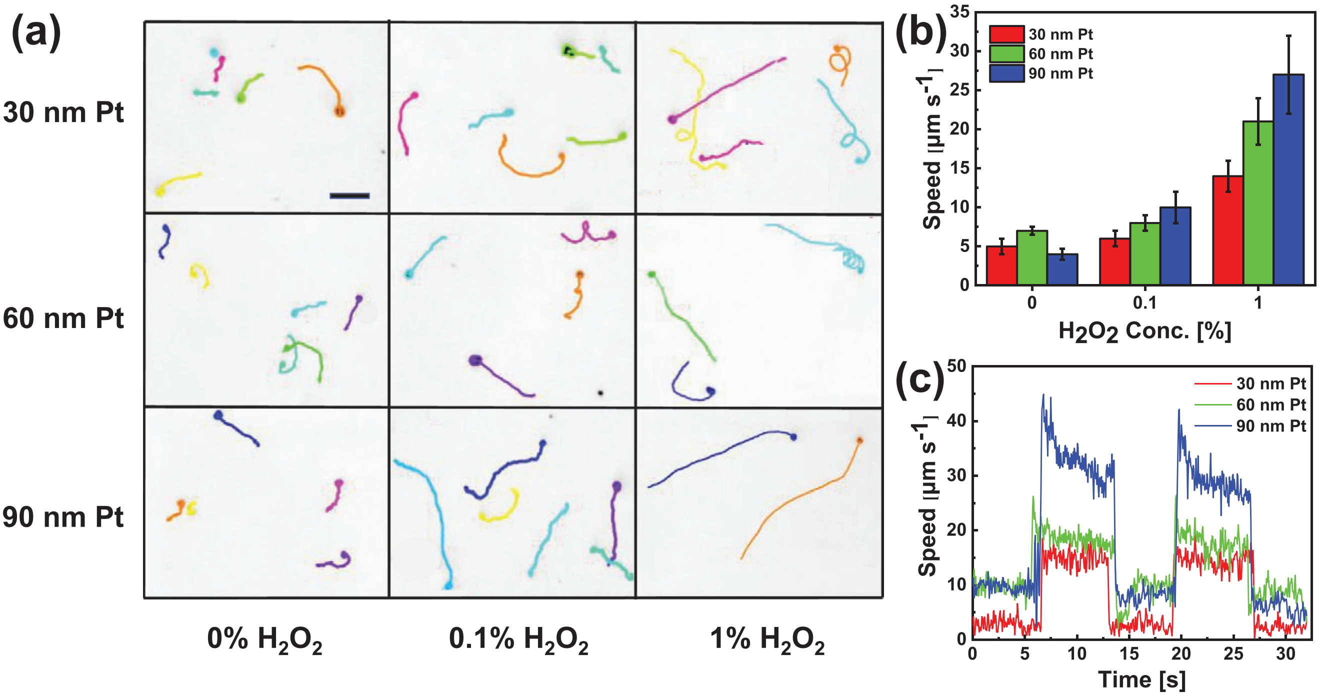

Figure 2. Motion behavior of hematite/Pt Janus microrobots in pure water and in different concentrations of H_2O_2. a) Micrographs showing 5 s long trajectories (scale bars are 20 µm). b) Comparison of microrobots speed. c) Microrobots speed in 1% H_2O_2 by on/off switching of UV-light irradiation at time intervals of ≈5 s.

correlated with the mixed potential difference between the two sides of the microrobot.[32–35] In particular, it has been demonstrated that the larger is such potential difference, the higher is the speed.[29,30] On these bases, the mixed potential difference between hematite and Pt electrodes with different thickness were measured in pure water and in 1% H_2O_2 under UV-light irradiation. As shown in **Figure 3**a, the lowest potential difference (132 mV) between hematite and 90 nm Pt electrodes is observed in pure water, which is consistent with the lowest speed of 90 nm Pt microrobots in pure water (Figure 2b). There is an exception, since a larger difference for 60 nm Pt microrobots was expected on the bases of speed measurements. However, in 1% H_2O_2, a thicker Pt layer results in a larger potential difference with hematite, which is exactly consistent with the trend observed for the speed.

The motion mechanism of hematite/Pt microrobots with different Pt layer thickness was studied by calculating the mean squared displacement (MSD) with and without UV-light irradiation for 30 and 90 nm Pt microrobots, which represent the two extreme conditions. As reported in Figure S3 in the Supporting Information, the MSD of 30 nm Pt microrobots in pure water and in dark (UV-off) increases linearly over time, indicating a Brownian behavior (Figure S3a, Supporting Information). The same is observed for 90 nm Pt microrobots. Under UV-light irradiation (UV-on), the MSD of both microrobots follows a parabola due to the light-induced self-electrophoretic motion of microrobots (Figure S3a, Supporting Information). The main differences between the two samples are observed in dark and in the presence of H_2O_2. In fact, without UV-light irradiation, 30 nm Pt microrobots displayed parabolic MSD

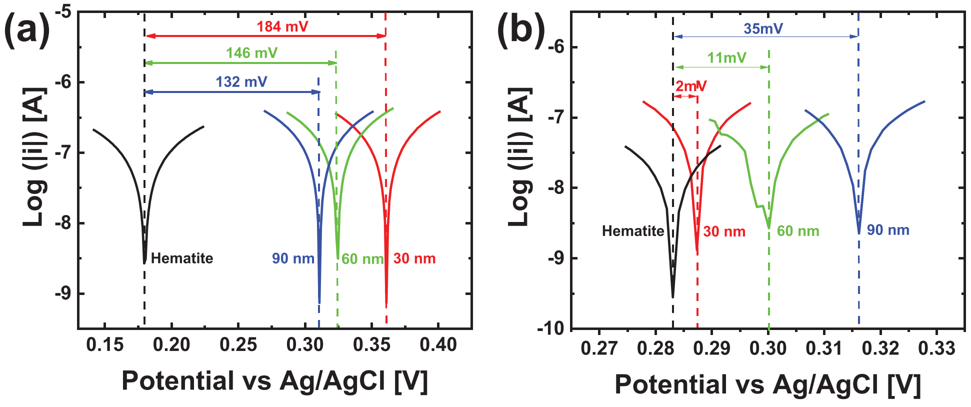

Figure 3. Tafel plots of hematite and 30, 60, and 90 nm thick Pt electrodes under UV-light irradiation a) in pure water and b) in 1% H_2O_2.

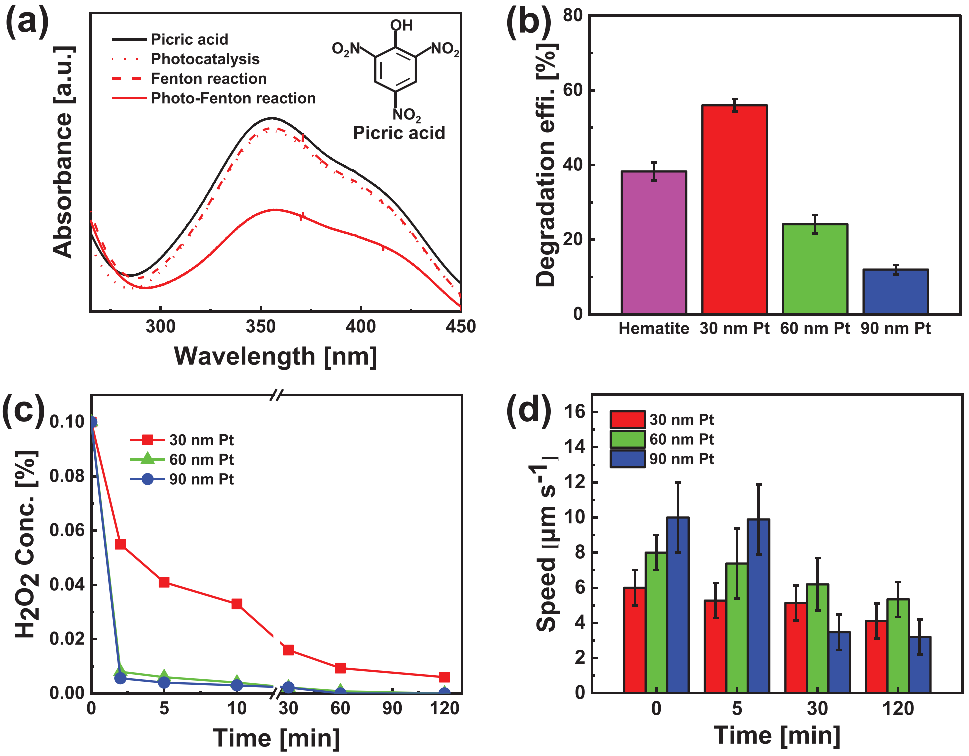

Figure 4. Investigation of PA degradation by light-driven hematite/Pt Janus microrobots with different Pt layer thickness. a) Absorbance spectra of PA treated for 2 h with 30 nm Pt microrobots under UV-light irradiation in pure water (photocatalysis) without UV-light irradiation in 0.1% H_2O_2 (Fenton reaction) and under UV-light irradiation in 0.1% H_2O_2 (photo-Fenton reaction). b) PA degradation efficiency of bare hematite and 30, 60, and 90 nm Pt microrobots after 2 h UV-light irradiation in 0.1% H_2O_2. c) Time-dependent H_2O_2 consumption by 30, 60, and 90 nm Pt microrobots under UV-light irradiation in 0.1% H_2O_2. d) Microrobots' speed at different stages of the degradation process.

only in 1% H_2O_2 (Figure S3b, Supporting Information). Therefore, it can be concluded that for 30 nm Pt microrobots, self-diffusiophoresis in 0.1% H_2O_2 is not powerful enough to overcome the Brownian motion, and it becomes dominant only at higher H_2O_2 concentrations. Contrarily, 90 nm Pt microrobots exhibit self-diffusiophoretic motion also at the lower concentration of 0.1% H_2O_2 (Figure S3c, Supporting Information). Thus, the strength of the diffusiophoresis increases with the amount of sputtered Pt, and plays a major role in the improved self-propulsion ability of 90 nm Pt microrobots in the presence of H_2O_2, in agreement with Tafel measurements. From MSD analysis, the diffusion coefficients of the microrobots were calculated and plotted in Figure S3d in the Supporting Information. The diffusion coefficient rises by increasing the Pt layer thickness and H_2O_2 concentration.

The improved light-powered motion of hematite/Pt microrobots with increasing Pt layer thickness was tested for the photocatalytic degradation of pollutants in water. PA (molecular structure in the inset in **Figure** 4a) was selected as a high-energy explosive representative contaminant. Initially, we investigated the mechanism of PA degradation using 30 nm Pt microrobots for 2 h under different conditions: 1) UV-light irradiation, no H_2O_2 (photocatalysis); 2) no UV-light irradiation, 0.1% H_2O_2 (Fenton reaction); and 3) UV-light irradiation, 0.1% H_2O_2 (photo-Fenton reaction). The absorbance spectra of PA solutions before and after treatments are shown in Figure 4a. A significant decline of PA absorbance intensity is observed only for the solution treated via photo-Fenton reaction, suggesting that photo-Fenton is the dominant degradation mechanism. This behavior is in agreement with previous reports.[20,36] In fact, it has been proven that photo-Fenton reaction generates stronger oxidative species, i.e., hydroxyl radicals and superoxide radicals required for the degradation of pollutants, compared to photocatalysis and Fenton reaction.[37]

After identifying the most effective degradation mechanism, bare hematite and microrobots with different Pt layer thickness were all employed to degrade PA under UV-light irradiation in 0.1% H_2O_2 for 2 h (the corresponding absorption spectra are reported in Figure S4, Supporting Information). As shown in Figure 4b, bare hematite displays a lower PA degradation efficiency (38%) than 30 nm Pt microrobots (56%) owing to their autonomous motion and enhanced diffusion. It should be noted that in the case of microrobots, half of the hematite area is, in principle, coated by Pt. Nonetheless, they still exhibit superior efficiency compared to bare, static hematite, indicating that self-propulsion plays a crucial role in the effective and rapid degradation of PA. A higher speed leading to a faster PA degradation was expected. Surprisingly, the degradation efficiency of 60 and 90 nm Pt microrobots is merely 24% and 12%, respectively, which is lower than 30 nm Pt microrobots and bare hematite. These results indicate that the higher thickness of Pt layer and, consequently, the higher speed of microrobots could not be beneficial for photo-Fenton degradation of pollutants. One possible explanation for this behavior is that

Pt overcoated the surface of hematite microspheres, leading to less exposed surface of hematite participating to the degradation process. Nevertheless, EDX elemental mapping (Figure 2) shows that the Janus structure of 60 and 90 nm Pt microrobots is preserved. An alternative explanation is that the higher thickness of the Pt layer could accelerate the decomposition of H_2O_2, leaving less H_2O_2 available for the photo-Fenton degradation. In order to verify this hypothesis, H_2O_2 consumption over time by microrobots under UV-light irradiation was evaluated as shown in Figure 4c. H_2O_2 was almost completely consumed by 60 and 90 nm Pt microrobots within only 5 min from the start of the process. In contrast, almost 50% of H_2O_2 was still present after 5 min treatment with 30 nm Pt microrobots and a not negligible amount was detected also after 2 h. The kinetics of the reaction with the thickness of the layer was successfully fitted only by using the third-order kinetics model[38]

$$\left(\frac{1}{C_t^2}\right)=\left(\frac{1}{C_0^2}\right)+2kt \tag{2}$$

where C_0 is the initial concentration of H_2O_2, C_t is the concentration of H_2O_2 at the time t [s], and k [$\text{mol}^{-2}\ \text{L}^2\ \text{S}^{-1}$] is the third-order rate constant. The plots of $\left(\frac{1}{C_t^2}\right)$as a function of t for hematite/Pt microrobots at varying Pt layer thickness are shown in Figure S5a in the Supporting Information. From the linear fitting of these plots, the rate constant k was calculated using Equation (2), finding that k increases with Pt layer thickness as $k_{30\ \text{nm Pt}} = 14\ \text{mol}^{-2}\ \text{L}^2\ \text{S}^{-1} < k_{60\ \text{nm Pt}} = 528\ \text{mol}^{-2}\ \text{L}^2\ \text{S}^{-1} < k_{90\ \text{nm Pt}} = 827\ \text{mol}^{-2}\ \text{L}^2\ \text{S}^{-1}$ (Figure S5b, Supporting Information). These k values demonstrate much faster H_2O_2 consumption of 90 nm Pt micromotors, which also confirms Tafel measurements results that in H_2O_2 a thicker Pt layer results in a larger potential difference with hematite and higher speed of microrobots, as shown in Figure 3b.

Microrobots speed at different stages of the degradation process was further investigated. Figure 4d shows that the speed of 90 nm Pt microrobots decreases dramatically after 30 min. Notably, the speed of 30, 60, and 90 nm Pt microrobots after 2 h UV-light irradiation is consistent with the trend of microrobots speed already illustrated in Figure 2b in pure water (0% H_2O_2). Based on these experimental results, it should be emphasized that the higher thickness of Pt, which significantly enhances the photocatalytic capacity of Janus microrobots, is generally preferable. However, when conducting photo-Fenton degradation experiments with such microrobots, the opposite trend is observed for the degradation efficiency.

The photo-Fenton degradation kinetics of PA using hematite/Pt Janus microrobots under UV-light irradiation in 0.1% H_2O_2 were also evaluated following the first-order kinetics model[39]

$$\ln\left(\frac{C_t}{C_0}\right)=-kt \tag{3}$$

where C_0 is the initial concentration of PA, C_t is the concentration of PA at the time t [min], and k [min^{-1}] is the first-order rate constant. The plots of $\ln(C_t/C_0)$ as a function of t for hematite/Pt microrobots at varying Pt layer thickness are shown in Figure S6a in the Supporting Information. From the linear fitting of these plots, the rate constant k was calculated using Equation (3), finding that k decreases with Pt layer thickness as $k_{30\ \text{nm Pt}} = 0.686 \times 10^{-2}\ \text{min}^{-1} > k_{60\ \text{nm Pt}} = 0.226 \times 10^{-2}\ \text{min}^{-1} > k_{90\ \text{nm Pt}} = 0.0975 \times 10^{-2}\ \text{min}^{-1}$ (Figure S6b, Supporting Information). The $k_{30\ \text{nm Pt}}$ is nearly seven times larger than $k_{90\ \text{nm Pt}}$ and three times larger than $k_{60\ \text{nm Pt}}$. It can be seen that the Pt layer thickness of hematite microrobots has a significant effect on the degradation rates, which further proves the superior degradation ability of 30 nm Pt hematite microrobots.

The degradation ability of the optimal 30 nm Pt microrobots against 4-nitrophenol (4-NP) and rhodamine B (RhB) pollutants was further investigated. 4-NP has been selected as a more toxic pollutant which can cause considerable damage to the ecosystem and human health.[40] Instead, RhB has been chosen to carry out selectivity test, since the UV-Vis absorption peak of PA (354 nm) and 4-NP (313 nm) are almost overlapped while RhB absorbs at higher wavelength (peak at 553 nm), allowing to discriminate it from PA. Both 4-NP and RhB degradation were carried out under UV-light irradiation in 0.1% H_2O_2 to exploit the photo-Fenton mechanism. The measured UV-Vis spectra for 4-NP and RhB degradation are shown in Figure S7a,b in the Supporting Information, respectively. The absorbance of the pollutant solution treated with microrobots decreases with UV-light irradiation time, which is indicative of the significant degradation of 4-NP and RhB. Specifically, the decomposition efficiencies of 4-NP and RhB are 63% and 38% after 120 min, as reported in Figure S7e in the Supporting Information. The mixture of pollutants with PA was also degraded by 30 nm Pt microrobots (Figure S7a,b, Supporting Information). Owing to the overlap between PA and 4-NP absorption peaks (Figure S7c, Supporting Information), the degradation of a mixture of PA and RhB (peak at 553 nm) was studied (Figure S7d, Supporting Information). It must be noted that the degradation efficiency of RhB (35%) is similar to the one of RhB (38%) when it is in mixture with PA. However, the degradation efficiency of PA (34%) in the mixture is lower than bare PA (56%). Still, the sum of the degradation efficiency of PA and RhB in the mixture is close to that of bare PA and bare 4-NP. Notably, the microrobots are not specific for PA degradation, but can degrade PA in mixture of pollutants such as RhB with a lower efficiency. This lower efficiency of PA can be explained by the larger size of RhB molecule compared to PA, hindering PA adsorption, and hence, degradation on microrobots surface.

Regarding these degradation results, it is worth noting that other microrobots have been used for degradation of PA, achieving higher efficiencies (84%) than 30 nm Pt microrobots (56%) in this work.[37] However, these values were achieved using an extremely powerful UV-light source (300 W) compared to merely 4 W UV-light lamp. Furthermore, Fe_3O_4 nanoparticles have been introduced to achieve navigable motion and magnetic collection. Here, hematite microspheres are intrinsically magnetic as previously demonstrated.[30] Magnetic hysteresis loop of hematite microspheres using vibrating sample magnetometer (VSM) was measured and plotted in Figure S8 in the Supporting Information. Hematite exhibits a coercivity of about 0.2 emu g^{-1} at about 1 kOe magnetic field, which is enough to induce the rotation of microrobots using small magnets and, in combination with UV-light irradiation, achieve precise navigation (Movie S5, Supporting Information).[41] Based on these considerations, 30 nm Pt microrobots hold great potential in pollutant photodegradation.

4. Conclusions

The influence of metal layer thickness on the motion and speed of light-powered Janus microrobots as well as on their application in environmental remediation was investigated. Hematite/Pt Janus microrobots with different Pt layer thickness (30, 60, and 90 nm) were fabricated by hydrothermal synthesis of hematite microspheres and Pt layer deposition via sputtering. Hematite was chosen among the photocatalytic semiconductors owing to its low cost, biocompatibility, catalyzed Fenton and photo-Fenton reactions, and intrinsic magnetism. A higher Pt layer thickness generally leads to a higher speed as confirmed by Tafel measurements. This result demonstrates that the speed of light-powered Janus microrobots can be greatly enhanced by increasing metal layer thickness. The enhanced speed of these microrobots for the degradation of picric acid (PA) as a model for explosive pollutants was tested in water. The photo-Fenton reaction proved to be the dominant mechanism. Surprisingly, by increasing the Pt layer thickness, a faster light-powered motion of microrobots in the presence of H_2O_2 and less degradation efficiency of PA were obtained, which is attributed to the higher consumption of H_2O_2 for microrobots motion based on the Pt-catalyzed decomposition of H_2O_2, resulting in less H_2O_2 available for the photo-Fenton degradation process on hematite side. Furthermore, successful degradation of 4-NP, RhB and in mixture with PA indicates superior capability of 30 nm Pt microrobots. This work presents a new approach to control the speed of Janus microrobots based on tailoring the metal layer thickness. The competition between H_2O_2 consumption for motion and photo-Fenton reaction must be carefully considered when using these microrobots for degradation of pollutants in water.

Supporting Information

Supporting Information is available from the Wiley Online Library or from the author.

Acknowledgements

M.P. was supported by Ministry of Education, Youth and Sports (Czech Republic) Grant LL2002 under the ERC CZ program. CzechNanoLab project LM2018110 funded by MEYS CR is gratefully acknowledged for the financial support of the measurements/sample fabrication at CEITEC Nano Research Infrastructure. X.P. was supported by the China Scholarship Council (CSC No. 202008320382).

Conflict of Interest

The authors declare no conflict of interest.

Author Contributions

X.P. performed the fabrication of microrobots, recorded, and analyzed their motion, carried out the degradation experiments, and interpreted the data. M.U. designed the experiments, performed SEM-EDX analysis and Tafel measurements, and contributed to data interpretation. M.P. originated the idea. M.P. and M.U. supervised the project. All authors contributed to writing the manuscript.

Data Availability Statement

Research data are not shared.

Keywords

micromotors, microrobots, photocatalysis, pollutants

Received: June 9, 2021
Revised: July 22, 2021

---

[1] F. Novotný, H. Wang, M. Pumera, *Chem* **2020**, *6*, 867.
[2] W. Gao, J. Wang, *ACS Nano* **2014**, *8*, 3170.
[3] J. Wang, W. Gao, *ACS Nano* **2012**, *6*, 5745.
[4] B. E. Ávila, P. Angsantikul, J. Li, M. A. Lopez-Ramirez, D. E. Ramírez-Herrera, S. Thamphiwatana, C. Chen, J. Delezuk, R. Samakapiruk, V. Ramez, M. Obonyo, L. Zhang, J. Wang, *Nat. Commun.* **2017**, *8*, 272.
[5] A. C. Hortelao, R. N. Carrascosa, M. T. Patino, S. Sánchez, *ACS Nano* **2019**, *13*, 429.
[6] L. Wang, A. Kaeppler, D. Fischer, J. Simmchen, *ACS Appl. Mater. Interfaces* **2019**, *11*, 32937.
[7] L. Kong, C. C. Mayorga-Martinez, J. Guan, M. Pumera, *ACS Appl. Mater. Interfaces* **2018**, *10*, 22427.
[8] Y. Zhang, K. Yuan, L. Zhang, *Adv. Mater. Technol.* **2019**, *4*, 1800636.
[9] R. Dong, Q. Zhang, W. Gao, A. Pei, B. Ren, *ACS Nano* **2016**, *10*, 839.
[10] K. Villa, F. Novotný, J. Zelenka, M. P. Browne, T. Ruml, M. Pumera, *ACS Nano* **2019**, *13*, 8135.
[11] H. Zhou, C. C. Mayorga-Martinez, S. Pané, L. Zhang, M. Pumera, *Chem. Rev.* **2021**, *121*, 4999.
[12] G. Zhao, S. Sanchez, O. G. Schmidt, M. Pumera, *Nanoscale* **2013**, *5*, 2909.
[13] W. Gao, A. Pei, R. Dong, J. Wang, *J. Am. Chem. Soc.* **2014**, *136*, 2276.
[14] X. Ma, X. Wang, K. Hahn, S. Sánchez, *ACS Nano* **2016**, *10*, 3597.
[15] B. E. Ávila, C. Angell, F. Soto, M. A. Lopez-Ramirez, D. F. Báez, S. Xie, J. Wang, Y. Chen, *ACS Nano* **2016**, *10*, 4997.
[16] B. E. Avila, A. Martin, F. Soto, M. A. Lopez-Ramirez, S. Campuzano, G. M. Va´squez-Machado, W. Gao, L. Zhang, J. Wang, *ACS Nano* **2015**, *9*, 6756.
[17] X. Peng, H. Zhu, H. Chen, X. Feng, R. Liu, Z. Huang, Q. Shen, Y. Ma, L. Wang, *New J. Chem.* **2019**, *43*, 12594.
[18] K. E. Peyer, S. Tottori, F. Qiu, L. Zhang, B. J. Nelson, *Chem. – Eur. J.* **2013**, *19*, 28.
[19] M. Ussia, M. Urso, K. Dolezelikova, H. Michalkova, V. Adam, M. Pumera, *Adv. Funct. Mater.* **2021**, *31*, 2101178.
[20] Q. Wang, C. Wang, R. Dong, Q. Pang, Y. Cai, *Inorg. Chem. Commun.* **2018**, *91*, 1.
[21] L. Xu, F. Mou, H. Gong, M. Luo, J. Guan, *Chem. Soc. Rev.* **2017**, *46*, 6905.
[22] Y. Hong, M. Diaz, U. M. Córdova-Fteueroa, A. Sen, *Adv. Funct. Mater.* **2010**, *20*, 1568.
[23] A. M. Pourrahimi, K. Villa, C. L. Palenzuela, Y. Ying, Z. Sofer, M. Pumera, *Adv. Funct. Mater.* **2019**, *29*, 1808678.
[24] Q. Zhang, R. Dong, X. Chang, B. Ren, Z. Tong, *ACS Appl. Mater. Interfaces* **2015**, *7*, 24585.
[25] K. Yuan, B. Jurado-Sánchez, A. Escarpa, *Angew. Chem., Int. Ed.* **2021**, *60*, 4915.

[26] R. María-Hormigos, A. Escarpa, B. Goudeau, V. Ravaine, A. Perro, A. Kuhn, *Adv. Mater. Interfaces* **2020**, *7*, 1902094.
[27] H. Wang, M. Pumera, *Chem. Soc. Rev.* **2020**, *49*, 3211.
[28] R. Dong, Y. Hu, Y. Wu, W. Gao, B. Ren, Q. Wang, Y. Cai, *J. Am. Chem. Soc.* **2017**, *139*, 1722.
[29] T. Maric, M. Z. Nasir, M. R. D. Webster, M. Pumera, *Adv. Funct. Mater.* **2020**, *30*, 1908614.
[30] M. Urso, M. Ussia, M. Pumera, *Adv. Funct. Mater.* **2021**, *31*, 2101510.
[31] Z. Xiao, J. Chen, S. Duan, X. Lv, J. Wang, X. Ma, J. Tang, W. Wang, *Chem. Commun.* **2020**, *56*, 4728.
[32] Y. Kim, D. D. Torres, P. K. Jain, *Catalysts* **2016**, *16*, 3399.
[33] S. Balasubramanian, D. Kagan, K. M. Manesh, P. Calvo-Marzal, G. U. Flechsig, J. Wang, *Small* **2009**, *5*, 1569.
[34] Y. Nakato, H. Tsubomura, *Isr. J. Chem.* **1982**, *22*, 180.
[35] A. M. Brooks, M. Tasinkevych, S. Sabrina, D. Velegol, A. Sen, K. Bishop, *Nat. Commun.* **2019**, *10*, 495.
[36] X. Cui, J. Li, D. Ng, J. Liu, Y. Liu, W. Yang, *Carbon* **2020**, *158*, 738.
[37] Y. Ying, J. Plutnar, M. Pumera, *Small* **2021**, *17*, 2100294.
[38] R. Serra-Maia, J. D. Rimstidt, F. M. Michel, *Catal. Lett.* **2021**, *151*, 138.
[39] M. Sundararajan, V. Sailaja, L. Kennedy, J. Vijaya, *Ceram. Int.* **2017**, *43*, 540.
[40] B. Zhao, G. Mele, I. Pio, J. Li, L. Palmisano, G. Vasapollo, *J. Hazard. Mater.* **2010**, *176*, 569.
[41] Z. Lin, X. Fan, M. Sun, C. Gao, Q. He, H. Xie, *ACS Nano* **2018**, *12*, 2539.

7. Active microrobots for dual removal of biofilms via chemical and physical mechanisms

Paper published in this Chapter:

Xia Peng, Cagatay M. Oral, Mario Urso, Martina Ussia, Martin Pumera, Active Microrobots for Dual Removal of Biofilms via Chemical and Physical Mechanisms. *ACS Appl. Mater. Interfaces* **2025**, *17*, 3608−3619.

7.1 Motivation of this study

The proliferation of bacterial biofilms is closely tied to the emergence of infectious diseases. Additionally, biofilms pose significant challenges in water distribution systems and industrial pipelines, such as water-cooling plants and municipal drinking water networks, represents a serious public health concern. Traditional antibiotics often fail to eliminate biofilms due to their protective EPS matrix and the presence of bacterial cells. In response, innovative approaches have emerged, such as active photocatalytic microrobots for chemically degrading biofilms and mechanical strategies for physically disrupting the biofilm structure. In this paper, photocatalytic $ZnFe_2O_4$ microrobots were employed to get insight into the removal of bacterial biofilm via photodegradation and collectively physical eradication.

7.2 Paper conclusion

This study introduced two effective strategies for bacterial biofilm removal using ZFO-based microrobots. Light-driven ZFO/Pt microrobots, with an asymmetric Pt coating, exhibited UV-activated motion via self-electrophoresis, effectively removing *E. coli* biofilms through active motion and ROS production in the presence of H_2O_2. Magnetically driven ZFO microrobots, leveraging their paramagnetic properties, achieved precise collective manipulation for mechanical biofilm disruption on open surfaces and within narrow channels. These approaches highlight the versatility of ZFO microrobots for biofilm treatment in various environments.

7.3 Author contribution

I prepared the microrobots and I performed morphological characterization using SEM and analyzed the elemental composition through EDS and XPS. I conducted motion experiments under light irradiation and under magnetic field. Finally, I conducted part of bacteria experiments and wrote the manuscript draft.

ACS APPLIED MATERIALS & INTERFACES

Active Microrobots for Dual Removal of Biofilms via Chemical and Physical Mechanisms

Xia Peng, Cagatay M. Oral, Mario Urso, Martina Ussia, and Martin Pumera*

Cite This: *ACS Appl. Mater. Interfaces* 2025, 17, 3608−3619

Read Online

ACCESS | Metrics & More | Article Recommendations | Supporting Information

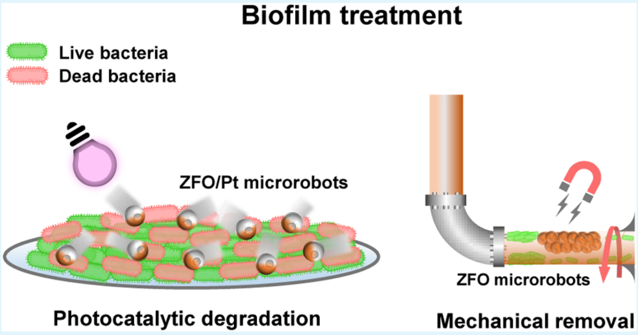

ABSTRACT: Bacterial biofilms are complex multicellular communities that adhere firmly to solid surfaces. They are widely recognized as major threats to human health, contributing to issues such as persistent infections on medical implants and severe contamination in drinking water systems. As a potential treatment for biofilms, this work proposes two strategies: (i) light-driven $ZnFe_2O_4$ (ZFO)/Pt microrobots for photodegradation of biofilms and (ii) magnetically driven ZFO microrobots for mechanical removal of biofilms from surfaces. Magnetically driven ZFO microrobots were realized by synthesizing ZFO microspheres through a low-cost and large-scale hydrothermal synthesis, followed by a calcination process. Then, a Pt layer was deposited on the surface of the ZFO microspheres to break their symmetry, resulting in self-propelled light-driven Janus ZFO/Pt microrobots. Light-driven ZFO/Pt microrobots exhibited active locomotion under UV light irradiation and controllable motion in terms of "stop and go" features. Magnetically driven ZFO microrobots were capable of maneuvering precisely when subjected to an external rotating magnetic field. These microrobots could eliminate Gram-negative *Escherichia coli* (*E. coli*) biofilms through photogenerated reactive oxygen species (ROS)-related antibacterial properties in combination with their light-powered active locomotion, accelerating the mass transfer to remove biofilms more effectively in water. Moreover, the actuation of magnetically driven ZFO microrobots allowed for the physical disruption of biofilms, which represents a reliable alternative to photocatalysis for the removal of strongly anchored biofilms in confined spaces. With their versatile characteristics, the envisioned microrobots highlight a significant potential for biofilm removal with high efficacy in both open and confined spaces, such as the pipelines of industrial plants.

KEYWORDS: *micromotors, microrobots, photocatalysis, magnetically driven, biofilm, collective motion*

1. INTRODUCTION

The emergence of infectious diseases has a strong connection with the proliferation of bacterial biofilms, intricate three-dimensional structures composed of microorganisms, and extracellular polymeric substances (EPS).[1,2] The process of biofilm formation unfolds through several stages.[3] Initially, planktonic cells attach on a surface, followed by rapid multiplication and the formation of a protective EPS matrix. This EPS matrix provides the structural foundation for the biofilm's architecture, accommodating bacterial cells. Moreover, it grants crucial adhesion capabilities to surfaces and enhances resistance against environmental interferences, such as antibiotics and mechanical forces.[4−6] Beyond the well-documented implications of biofilms for recurrent infections and various medical complications, such as their adhesion to implants and catheters,[7−9] biofilm formation presents a multifaceted challenge when extended to industrial pipelines and water distribution systems.[10−12] This issue is particularly pronounced in industrial water-cooling plants and municipal drinking water networks, which have emerged as a significant threat to public health.[13,14] Hence, the imperative to secure access to pathogen-free drinking water has become highly critical, emphasizing the importance of implementing effective biofilm control measures. Current disinfection methods, such as UV treatment and chemical disinfectants, face challenges like high energy consumption, harmful byproducts, and the risk of promoting resistant biofilms. Moreover, their effectiveness against emerging pathogens is uncertain and requires further evaluation. Novel technologies have recently emerged as a potential remedy, such as chemical removal strategies based on the utilization of photocatalytic nanoparticles to degrade biofilm or physical removal strategies based on the mechanical disruption of biofilm.[15] These approaches are capable of concurrently targeting the EPS matrix and dormant bacterial cells, holding particular promise for biofilm treatment.[16−19]

Received: October 24, 2024
Revised: December 13, 2024
Accepted: December 17, 2024
Published: January 2, 2025

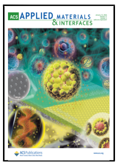

Scheme 1. Light-Driven and Magnetic ZFO-Based Microrobots for Effective Biofilm Treatment[a]

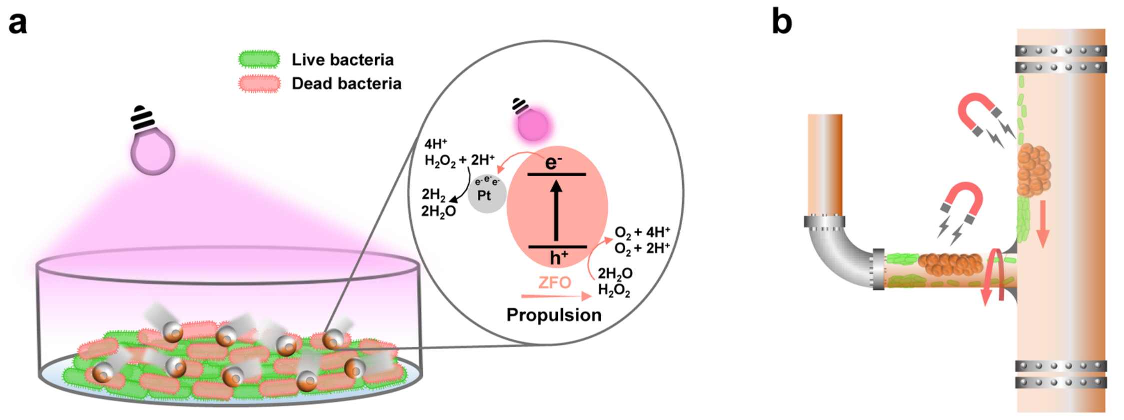

Photocatalytic degradation of biofilms via light-driven ZFO/Pt Janus microrobots

Mechanical removal of biofilms via magnetically driven ZFO microrobots

[a](a) Light-driven ZFO/Pt microrobots eliminate Gram-negative *E. coli* biofilms via photogenerated ROS-related antibacterial properties. (b) Magnetically driven ZFO microrobots are capable of mechanical removal of biofilms under manipulation by a permanent magnet.

In recent years, there has been a remarkable surge in research and development efforts aimed at leveraging microrobots as innovative tools for biofilm eradication.[20−22] Microrobots are miniature, self-propelled structures that can navigate within complex environments, making them particularly promising for tackling the challenges posed by biofilms.[15,23,24] One of the pioneering breakthroughs in this field involves the utilization of photocatalytic microrobots capable of propelling themselves under light irradiation.[25−27] Photocatalytic microrobots can produce highly concentrated reactive oxygen species (ROS) to target biofilm matrices, disrupting their structural integrity, and subsequently making them more susceptible to removal.[28,29] For example, we introduced a novel concept involving Pt-tubes having a biocompatible TiO_2 coating to harness light-induced ROS production, which plays a pivotal role in removing dental biofilm.[30] Alternatively, Ussia et al. demonstrated an effective strategy to eradicate biofilms from solid surfaces by employing light-driven Ag-doped ZnO microrobots, which boost anti-biofilm efficacy by increasing ROS production through the catalytic reaction of ZnO and enhancing the diffusion of antimicrobial nanosilver.[10] Beyond the utilization of photocatalytic materials, microrobots composed of magnetic materials also represent a promising and innovative approach to address biofilm-related challenges by offering a targeted and minimally invasive form of biofilm disruption.[31−33] When subjected to an external magnetic field, these microrobots demonstrate controlled actuation, which enables them to be maneuvered precisely within biofilm matrices, regardless of the complexity of the biofilm's architecture.[34,35] For instance, catalytic antimicrobial robots (CARs) with dual catalytic−magnetic functionality using iron oxide nanoparticles (NPs) were designed to kill, break down, and remove biofilms in a controlled manner. 3D-molded CARs, shaped like vanes or helicoids, targeted specific tasks in enclosed domains by eliminating biofilms and killing bacteria simultaneously.[36] Similarly, Dong et al. introduced magnetic microswarms with navigation capabilities that effectively eliminated targeted biofilms in both open and confined environments through a synergistic combination of the Fenton reaction and physical disruption.[37] The precise control and adaptability of magnetic microrobots, along with their ability to operate within the complex environment of biofilms, make them a promising tool for solving biofilm-related issues.[38−40] Although the different propulsion modes based on one material may provide advanced strategies applicable in daily scenarios associated with biofilms, only a few examples of such microrobots have been reported until now.

Here, we present $ZnFe_2O_4$ (ZFO)-based microrobots for biofilm treatment from solid surfaces. Previous studies faced challenges in controlling ZnO-based microrobots due to their lack of magnetic properties while Fe_3O_4 nanoparticles, despite their superparamagnetism, exhibited weak photocatalytic performance due to a narrow band gap.[10,36,37] In this work, we address these limitations by utilizing ZFO, which combines both photocatalytic and magnetic properties in one material to enhance the removal of bacterial biofilm through chemical and physical mechanisms. In particular, compared to Fe_2O_3, ZFO shows stronger magnetic properties, allowing easy collection of the microrobots using a permanent magnet.[41,42] This capability not only enables enhanced reusability but also facilitates the efficient isolation of the microrobots from the surrounding environment, thereby minimizing potential interference. Furthermore, ZFO can be considered to have biocompatible characteristics in the environment.[43,44] Light-driven ZFO particles were synthesized by a facile hydrothermal reaction, followed by a calcination process. Then, to obtain a Janus structure for light-powered self-propulsion, the ZFO microrobots were half-coated with a Pt layer through the sputtering technique, obtaining ZFO/Pt microrobots. When exposed to UV light, electrons (e^-) in the valence band of ZFO and promoted to the conduction band, leaving holes (h^+) within the valence band. Electrons migrate from the conduction band to Pt, while holes remain within ZFO, where they contribute to water or H_2O_2 decomposition. During this process, it establishes a H^+ concentration gradient, creating a localized electric field that drives the motion of the microrobots through self-electrophoresis, as depicted in Scheme 1. Their speed values were notably enhanced when subjected to low concentrations of H_2O_2 fuel, accompanied by a rapid modulation of their motion/no motion conditions in response to the on/off switch of the UV light source. Due to the intrinsic paramagnetic properties of ZFO microspheres, they can be precisely guided along predefined paths and demonstrate reconfigurable, collective

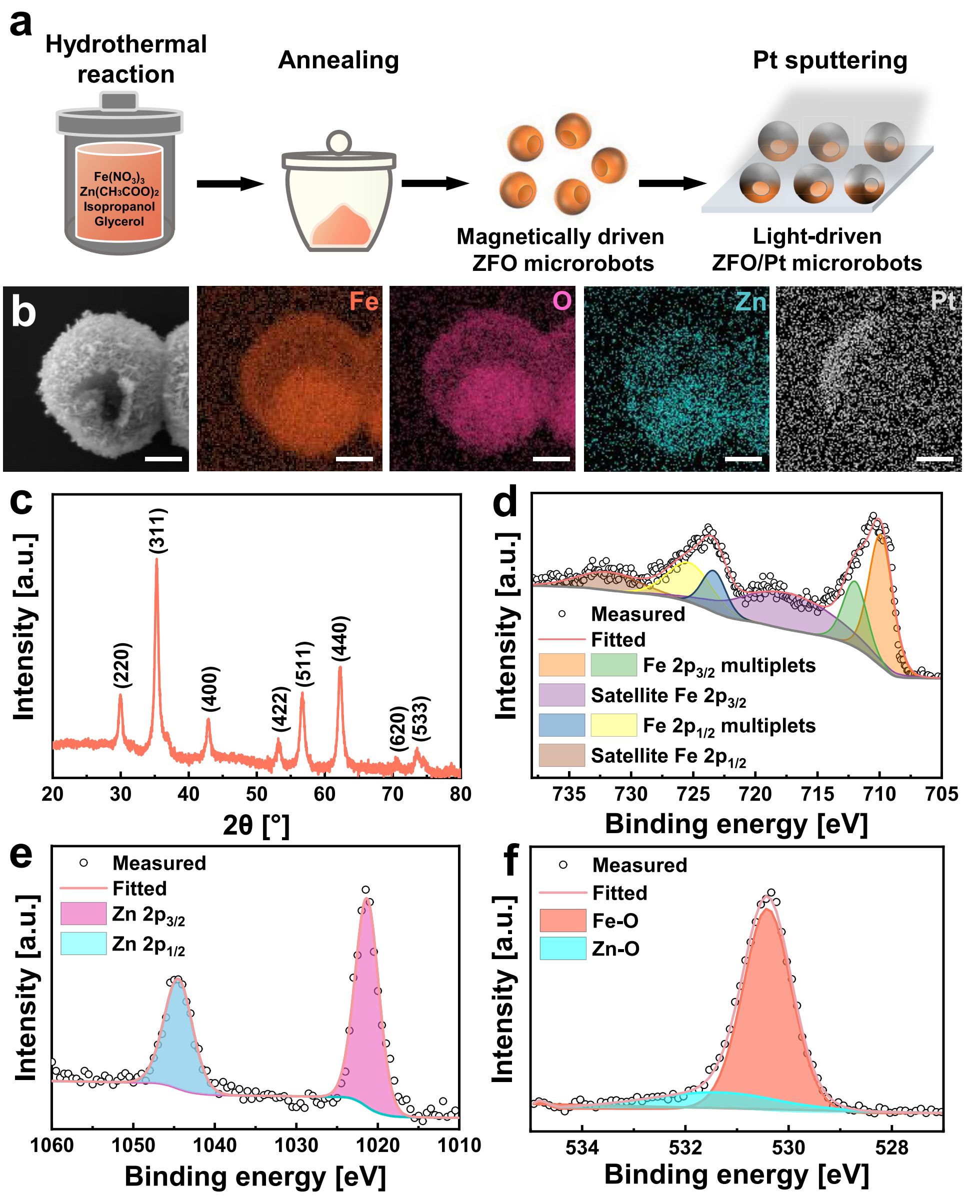

Figure 1. Fabrication and characterization of ZFO-based microrobots. (a) Schematic illustration of the preparation of magnetically driven ZFO microrobots and light-driven ZFO/Pt microrobots. (b) SEM and EDX mapping images of a light-driven ZFO/Pt microrobot showing the distribution of Fe, O, Zn, and Pt elements. Scale bars are 1 μm. (c) XRD spectrum of magnetically driven ZFO microrobots. (d−f) High-resolution XPS spectra of magnetically driven ZFO microrobots for Fe 2p, Zn 2p, and O 1s regions, respectively.

behavior under the influence of an external magnetic field. This functionality is achieved even without the Pt layer, earning them the designation of magnetically driven ZFO microrobots. Gram-negative *Escherichia coli* (*E. coli*) was selected as a model strain for the incubation of biofilm due to its extensive existence in the environment and then treated with light-driven ZFO/Pt microrobots or magnetically driven ZFO microrobots. Light-driven ZFO/Pt microrobots showed excellent performance in killing bacteria under UV light irradiation in the presence of a low concentration of H_2O_2, whereas the static microrobots demonstrated only minor removal of the biofilm, which further demonstrates the primary contribution of the dynamic locomotion of microrobots in achieving efficient biofilm removal. Furthermore, magnetically driven ZFO microrobots have been substantiated to effectively prevent biofilm formation from both open surfaces and inner parts of glass tubes having varying diameters, demonstrating that magnetic microrobots hold significant potential for biofilm disruption strategies in both open and confined spaces. This concept is schematically illustrated in Scheme 1. The proposed microrobots, having dual functionalities and scalable fabrication possibilities, hold significant promise for biofilm eradication, especially in addressing long-standing challenges in industrial applications.

2. RESULTS AND DISCUSSION

2.1. Fabrication and Characterization of ZFO-Based Microrobots. Magnetically driven ZFO microrobots were fabricated by a hydrothermal reaction, followed by a calcination process. Light-driven ZFO/Pt microrobots were prepared by asymmetrical Pt sputtering as schematically shown in Figure 1a, resulting in the half-coating of ZFO microrobots with a Pt layer. The morphology of ZFO-based microrobots was characterized and illustrated by scanning electron microscopy (SEM) images in Figures S1 and 1b. These micrographs display a spherical

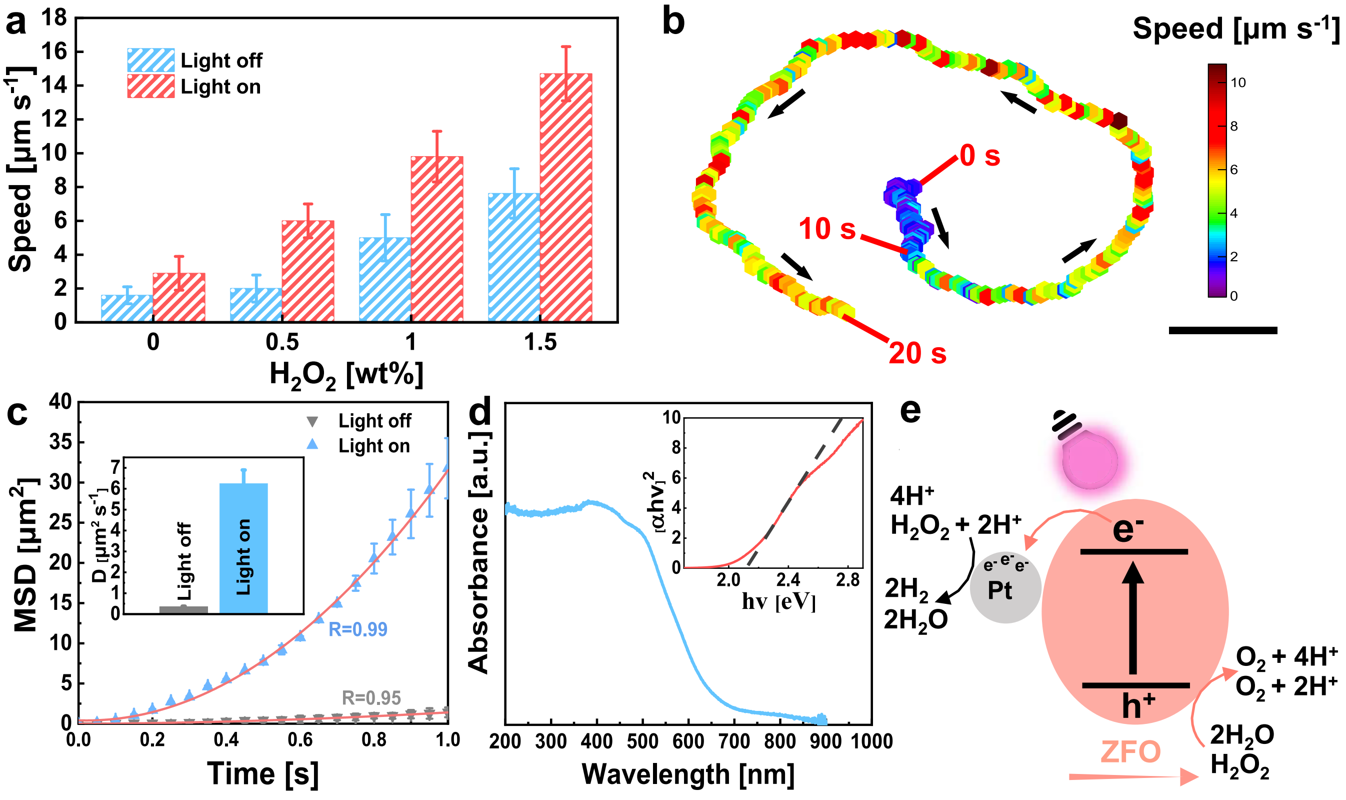

Figure 2. Motion behavior of light-driven ZFO/Pt microrobots. (a) Average speed values of the light-driven ZFO/Pt microrobots at various concentrations of H_2O_2 without (light off) or with (light on) UV light irradiation. Error bars represent the standard deviation with $n = 3$ independent replicates. (b) Trajectory and instantaneous speed (color-coded) of a microrobot in 0.5 wt % H_2O_2 without (0−10 s) and with (10−20 s) UV light irradiation. Scale bar = 10 μm. Black arrows represent the motion directions of the microrobot. (c) MSD plots of the light-driven ZFO/Pt microrobots in 0.5 wt % H_2O_2 without and with UV light irradiation. The inset shows the corresponding diffusion coefficients (D) calculated by fitting the MSD plots. (d) UV−vis absorbance spectrum of the light-driven ZFO/Pt microrobots. The inset reports the corresponding Tauc plot. (e) Schematic illustration of the proposed propulsion mechanism of the light-driven ZFO/Pt microrobots.

morphology with a hollow structure and a diameter of approximately 2.5 μm. This structure could be justified by the high temperature reached during the hydrothermal process (180 °C) and the formation of ZnFe-glycolate nuclei due to the solvent's high surface energy, which is responsible for its tendency to aggregate into a spherical structure, thereby reducing the free energy.[45] During the calcination process, the ZnFe-glycolate nuclei decompose into ZFO, which eventually results in the formation of hollow ZFO microspheres. In addition, the hollow spheres possess a notably rough surface composed of closely interconnected ZFO nanosheets. Elemental mapping images of ZFO were attained by energy-dispersive X-ray spectroscopy (EDX) to prove their elemental composition and effective deposition of the Pt layer. The EDX images in Figure S1 indicate a uniform distribution of Fe, O, and Zn elements of magnetically driven ZFO microrobots, while Figure 1b demonstrates the asymmetrical Pt layer deposition. To further prove the Janus structure of ZFO/Pt microrobots, SEM measurements using a backscattered electron (BSE) detector were conducted to determine the elemental distribution and clearer contrast between different elements, as shown in Figure S2. The SEM image on the right clearly distinguishes the half-coated Pt layer from the ZFO particles, confirming the Janus structure of the microrobots. Additionally, the EDX images in Figure S2b further validate the Pt layer distribution, which aligns with the SEM observations.

Structural analysis of the microrobots was performed by X-ray diffraction (XRD) within the 2θ range of 20−80°. As depicted in Figure 1c, the XRD pattern reveals consistency between all of the reflection peaks and the standard JCPDS card No. 22−1012, confirming the presence of the spinel ZFO phase.[46] Specifically, the diffraction peaks at 2θ values of 29.92, 35.28, 36.92, 42.88, 53.16, 56.72, 62.24, and 73.64 can be attributed to the (220), (311), (222), (400), (422), (511), (440), and (533) planes, respectively, which correspond to the cubic phase of spinel ZFO. The absence of any discernible peaks in the spectrum that correspond to ZnO and Fe_2O_3 highlights the crystalline purity of the resulting magnetically driven ZFO microrobots.

X-ray photoelectron spectroscopy (XPS) was carried out to investigate the surface composition and chemical states of the ZFO microrobots. The corresponding fitted data for the high-resolution Fe, Zn, and O regions are presented in Figure 1d−f, respectively. Fe 2p spectrum displays peaks at 710.8 (718.7) and 712.9 (725.0) eV binding energies, corresponding to Fe $2p_{3/2}$ (Fe $2p_{1/2}$), which are ascribed to tetrahedral and octahedral sites within ZFO, respectively, and signify the presence of Fe^{3+} in the microrobots.[47,48] In Figure 1e, the Zn 2p spectrum reveals fitting peaks at 1022.1 and 1045.0 eV, corresponding to the binding energy of Zn $2p_{1/2}$ and Zn $2p_{3/2}$, respectively, which suggests the presence of Zn^{2+} in the $ZnFe_2O_4$ structure. O 1s spectra exhibit a peak at ∼532 eV, which is attributed to typical lattice oxygen within the structure of Zn−O or Fe−O, while the peak at ∼530 eV designates the presence of adsorbed oxygen on the microrobot's surface.

2.2. Motion Behavior of Light-Driven ZFO/Pt Microrobots.

Motion analysis of light-driven ZFO/Pt microrobots

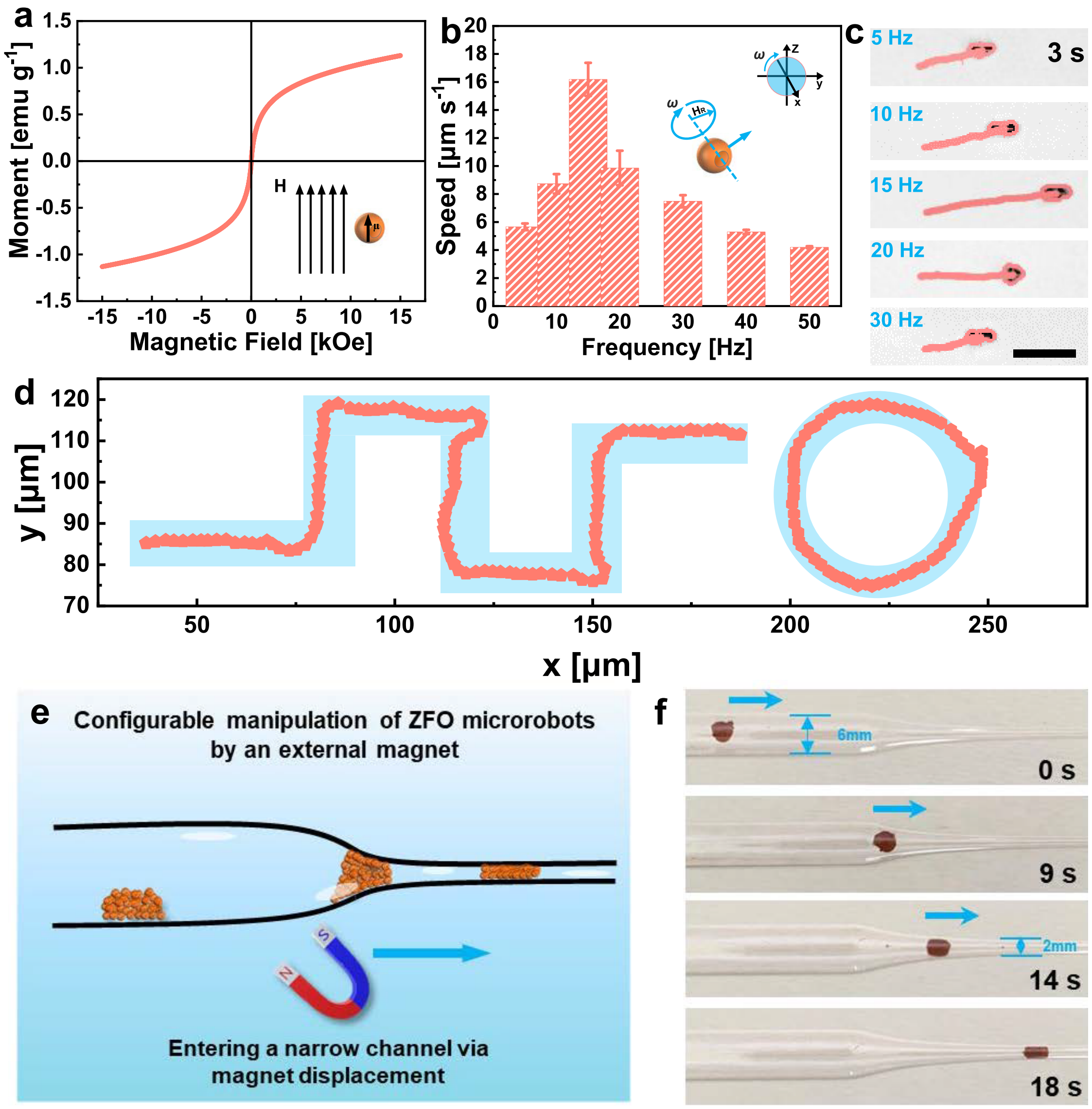

Figure 3. Magnetic motion of ZFO microrobots. (a) Magnetic hysteresis loop of magnetically driven ZFO microrobots. The inset depicts the magnetic dipole moment ($\boldsymbol{\mu}$) of a magnetically driven ZFO microrobot and how it aligns with the direction of an externally applied magnetic field (**H**). (b) Average speed values of magnetically driven ZFO microrobots under a transverse rotating magnetic field. Error bars represent the standard deviation with $n = 10$ independent replicates. (c) Trajectories of a magnetically driven ZFO microrobot under a transversal rotating magnetic field (5 mT) at different frequencies (5−30 Hz) for 3 s. (d) Trajectories of a ZFO microrobot along predefined paths under a transversal magnetic field of 5 mT at 15 Hz frequency. (e) Schematic illustration of configuration and external manipulation of a magnetically driven ZFO microrobot agglomerate. (f) Time-lapse digital images of the manipulation of a microrobot agglomerate inside a glass tube, showing its adaptability to the varying tube diameters.

was performed both under UV light illumination and under dark conditions. Different amounts of H_2O_2 were eventually employed as a fuel. As can be appreciated from Figure 2a, under UV light exposure, the microrobots exhibited free-fuel motion in water, registering a speed value of about 3 μm s^{-1}. The speed of the microrobots further increased up to 9.8 and 14.7 μm s^{-1} by adding 1 and 1.5 wt % of H_2O_2, respectively. Differently, in the dark, the microrobots did not show any significant displacement without H_2O_2 or in the presence of 0.5 wt % H_2O_2. When 1 and 1.5 wt % H_2O_2 were introduced under the dark condition, the speed of microrobots registered about 5.1 and 7.6 μm s^{-1}, respectively. Therefore, at high H_2O_2 concentrations, the microrobots could move, even without UV light irradiation. Figure 2b displays a characteristic trajectory and instantaneous speed (color-coded) of a single microrobot in the dark and under UV light irradiation (Supporting Movie 1). The instantaneous speed is ∼1.5 μm s^{-1} without UV light in the initial 10 s, which is in good agreement with Figure 2a. Afterward, UV light boosted the microrobot speed in a circular trajectory, demonstrating that light irradiation can make a noticeable difference in the speed and trajectory of ZFO/Pt microrobots.

To further analyze the motion behavior of the microrobots under different conditions, a mean squared displacement (MSD) analysis was conducted (Figure 2c). In the presence of 0.5 wt % H_2O_2, MSD values of ZFO/Pt microrobots exhibited a linear increase under the dark condition (gray pattern), indicating Brownian motion. However, when UV light was introduced, MSD values followed a parabolic relationship with time. This observation is attributed to the light-driven self-propulsion of ZFO/Pt microrobots.[49] Based on the analysis of MSD values, diffusion coefficients (D) of the microrobots were

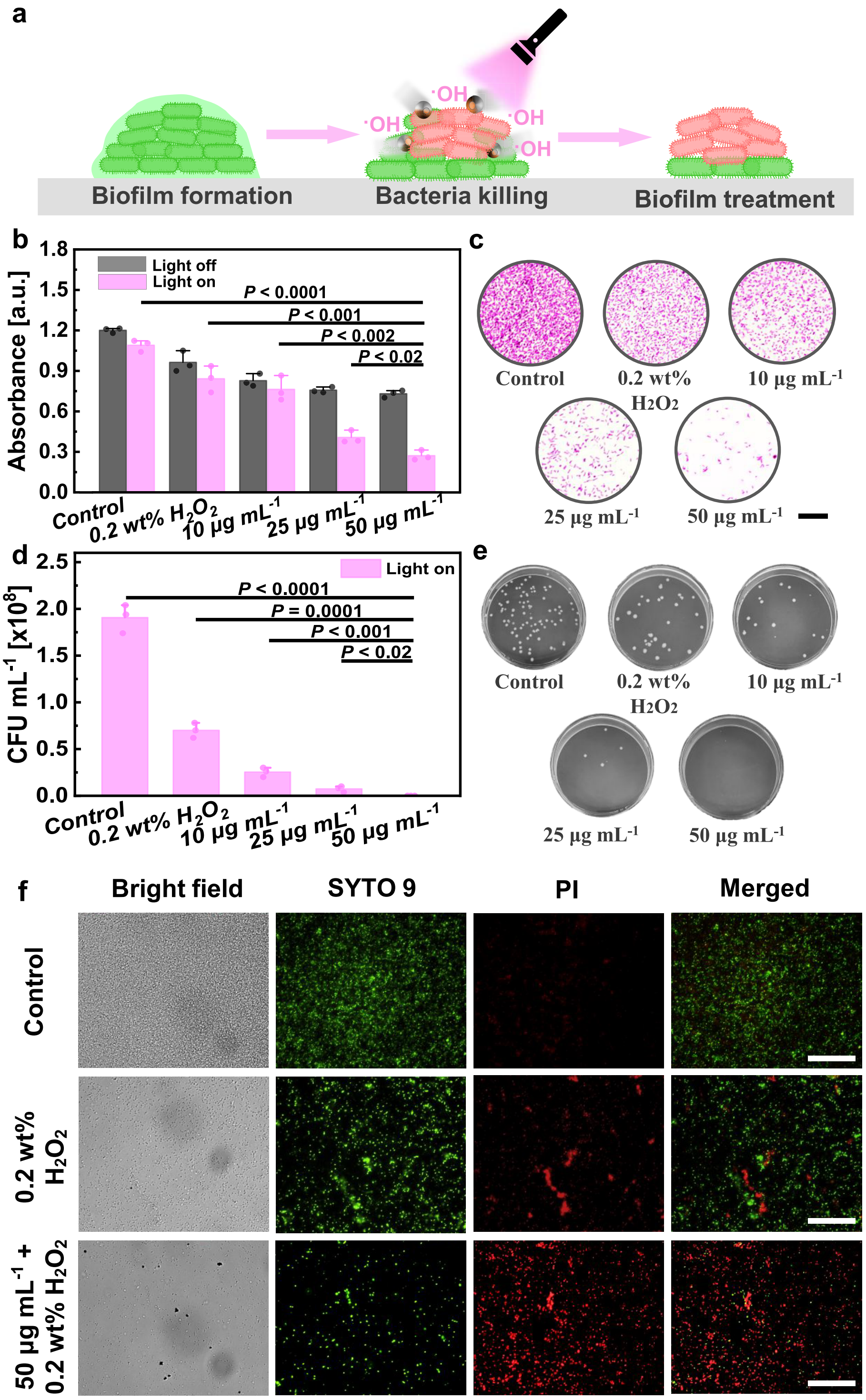

Figure 4. Biofilm removal via light-driven ZFO/Pt microrobots. (a) Schematic illustration of the biofilm removal process in the presence of light-driven ZFO/Pt microrobots, UV light irradiation, and H_2O_2 fuel. (b) Absorbance values for stained biofilms treated at different conditions (water, 0.2 wt % H_2O_2, or microrobots at 10, 25, and 50 μg mL^{-1} concentrations in the presence of 0.2 wt % H_2O_2) without (light off) or with (light on) UV light irradiation for 30 min. (c) Fluorescence images of stained living bacteria after the treatments under different conditions. Scale bar is 10 μm. (d) CFU counts for different groups (water, 0.2 wt % H_2O_2, or microrobots at 10, 25, and 50 μg mL^{-1} concentrations in the presence of 0.2 wt % H_2O_2) under UV light irradiation for 30 min and (e) the corresponding digital images. (f) LIVE/DEAD assay for biofilms treated for 30 min under UV light irradiation at different conditions (water, 0.2 wt % H_2O_2, microrobots 50 μg mL^{-1} concentration in the presence of 0.2 wt % H_2O_2). Scale bars: 100 μm. Error bars represent the standard deviation with $n = 3$ independent replicates.

also calculated (Figure 2c). D values significantly increased from 0.4 μm^2 s^{-1} under dark to 6.3 μm^2 s^{-1} under UV light irradiation in the presence of 0.5 wt % H_2O_2, thus highlighting the light-induced active motion of ZFO/Pt microrobots.

The optical band gap (E_g) for the microrobots was determined based on absorption measurements by UV−vis spectroscopy.[50] The Tauc plot presented in Figure 2d indicates an E_g value of 2.1 eV. The potential motion mechanism of light-driven ZFO/Pt microrobots is presented in Figure 2e. ZFO, as an n-type semiconductor with a band gap of 2.1 eV, exhibits light absorption capabilities. When subjected to UV light irradiation, electrons in the semiconductor's valence band are promoted to the conduction band, thereby leaving vacancies or holes within the valence band.[51] Electrons migrate from the conduction band to Pt while holes remain confined within the ZFO, where they actively participate in water decomposition reactions as illustrated in Figure 2e.

Notably, the protons (H^+) generated on the ZFO side are consumed at the Pt side, leading to the production of H_2. This process establishes a large H^+ concentration gradient, consequently generating a localized electric field that propels the microrobots through a mechanism known as self-electrophoresis.[52,53] To highlight the catalytic properties of ZFO/Pt microrobots, a comparison of the catalytic rates between Fe_3O_4, ZFO, and ZFO/Pt microrobots, using picric acid (PA) as a degradation model, was conducted (Figure S3). The rate constant, calculated using first-order kinetics, showed a trend of k (ZFO/Pt) > k (Fe_3O_4) > k (ZFO), clearly demonstrating the enhanced catalytic efficiency of ZFO/Pt microrobots.

2.3. Motion Behavior of Magnetically Driven ZFO Microrobots.

Magnetically driven ZFO microrobots could allow external magnetic control due to the presence of Fe within their structure. To analyze the magnetic properties of the ZFO microrobots, a vibrating sample magnetometer (VSM) was utilized. The magnetic hysteresis loop shown in Figure 3a presents the distinctive characteristics of a paramagnetic material.[54] The magnetic dipole moment is symmetrically located in the center of the spherical structure. After analysis of the magnetic features, the rolling motion of magnetically driven ZFO microrobots was investigated under the influence of a transverse rotating magnetic field. The magnetic field was kept constant (5 mT) during the experiments, while the frequency was varied from 5 to 50 Hz. As shown in Figure 3b, the average speed of the microrobots increased with the frequency, reaching its peak value of 16.2 μm s^{-1} at 15 Hz, commonly referred to as the "step-out" frequency.[55] Beyond this frequency, the average speed experienced a notable decrease until 4.3 μm s^{-1} at 50 Hz due to insufficient time to maintain synchronous alignment between the rotation of the magnetic field and the rotation of the magnetically driven ZFO microrobots. The dependency of average speed values on the magnetic field's frequency also affects the total distance covered by the microrobots. Figure 3c reports micrographs, captured from Supporting Movie 2, of a single microrobot's trajectory under different frequencies (5−30 Hz) for 3 s. As expected, the longest trajectory is observed at 15 Hz due to the higher speed of magnetically driven ZFO microrobots under this condition.

Magnetically driven ZFO microrobots also enabled precise control of their trajectory, creating intricate patterns, as demonstrated in Figure 3d and Supporting Movie 3. In addition to the manipulation of individual microrobots, the actuation of multiple microrobots and their adaptability to the surrounding environment are of great importance for implementing synchronized tasks, especially in narrow and varying spaces as requested by practical applications, including water remediation in industrial pipelines. To test magnetically driven ZFO microrobots' abilities in this regard, a glass tube with varying diameters (Figure S4) was selected to simulate their motion behaviors in a real-world setting. Microrobots were injected into the tube's narrow area as schematically illustrated in Figure 3e. Here, a neodymium−iron−boron (NdFeB) magnet was used to guide the magnetically driven ZFO microrobots instead of the transverse rotating magnetic field. Digital images in Figure 3f demonstrate the displacement of the microrobots from the wide part (6 mm) to the narrow part (2 mm) of the transparent tube in 14 s (Supporting Movie 4). The regulable locomotion performance of magnetically driven ZFO microrobots introduces a pivotal role in undertaking diverse tasks for biomedical applications as well as environmental remediation, such as precise drug delivery, clinical imaging, and the degradation of pollutants at target locations.[25,55−57] Considering the conventional approach to enable magnetic navigability (obtaining a Janus structure by Ni deposition or incorporating superparamagnetic nanoparticles on particle surfaces), magnetically driven ZFO microrobots present a significant advantage to obtaining magnetic features in a cost-effective and reproducible way due to their intrinsic magnetic properties.[58−60]

2.4. Biofilm Treatment by Light-Driven ZFO/Pt Microrobots.

Because the EPS, which is mainly composed of exopolysaccharides, proteins, lipids, and extracellular DNA (eDNA), protects the microorganism from desiccation, oxidation, antibiotics, etc., effective biofilm treatment is a challenging task.[5,61] As a potential remedy, light-driven ZFO/Pt microrobots, which can produce ROS under light irradiation, were proposed in this study to chemically disrupt the EPS barrier and further kill the protected bacteria cells. The photocatalytic motion of microrobots mainly contributes to the mixing and distribution of ROS rather than directly removing the biofilm, as depicted in Figure 4a. ROS generation by light-driven ZFO/Pt microrobots under light irradiation and in the presence of low concentrations of H_2O_2 (0.2%) was validated by fluorescence measurements. As demonstrated in previous work,[30] terephthalic acid was employed as a probe molecule, effectively trapping hydroxyl radicals and yielding strongly fluorescent 2-hydroxyterephthalic acid. The proportional increase in fluorescent intensity indicates the efficient generation of hydroxyl radicals by ZFO/Pt microrobots (Figure S5). For biofilm experiments, a strain of Gram-negative *E. coli* was selected to investigate the antibacterial performance of light-driven ZFO/Pt microrobots. *E. coli* represents a widely encountered bacteria that typically resides in the intestines of healthy humans and animals.[62] On the other hand, some strains of *E. coli* can pose health threats in contaminated water systems when ingested or come into contact with the body, causing diarrhea, nausea, and vomiting. More importantly, some *E. coli* strains have also developed resistance to antibiotics, making their eradication more challenging.[63]

In the experimental setup, the growth of *E. coli* biofilms was performed inside 96-well plates. To minimize the effect of H_2O_2 on biofilm removal, the lowest concentration of H_2O_2 for microrobots motion was investigated. As displayed in Figure S6, the microrobots still exhibited light-triggered motion compared to the dark condition in 0.2% H_2O_2 (Supporting Movie 5). These bacterial biofilms were subsequently subjected to different concentrations of light-driven ZFO/Pt microrobots dispersed in a water solution containing 0.2 wt % H_2O_2. Simultaneously, the well plates were exposed to 30 min of UV light irradiation to facilitate photocatalytic motion. The antibiofilm activity was compared with data obtained by using water or 0.2 wt % H_2O_2 without the presence of the microrobots, to discern the contribution of UV light exposure and H_2O_2 to the removal of bacterial biofilms. Biofilm viability was tested using the Crystal Violet (CV) assay by measuring the absorbance value of the dye at 590 nm for each of the aforementioned

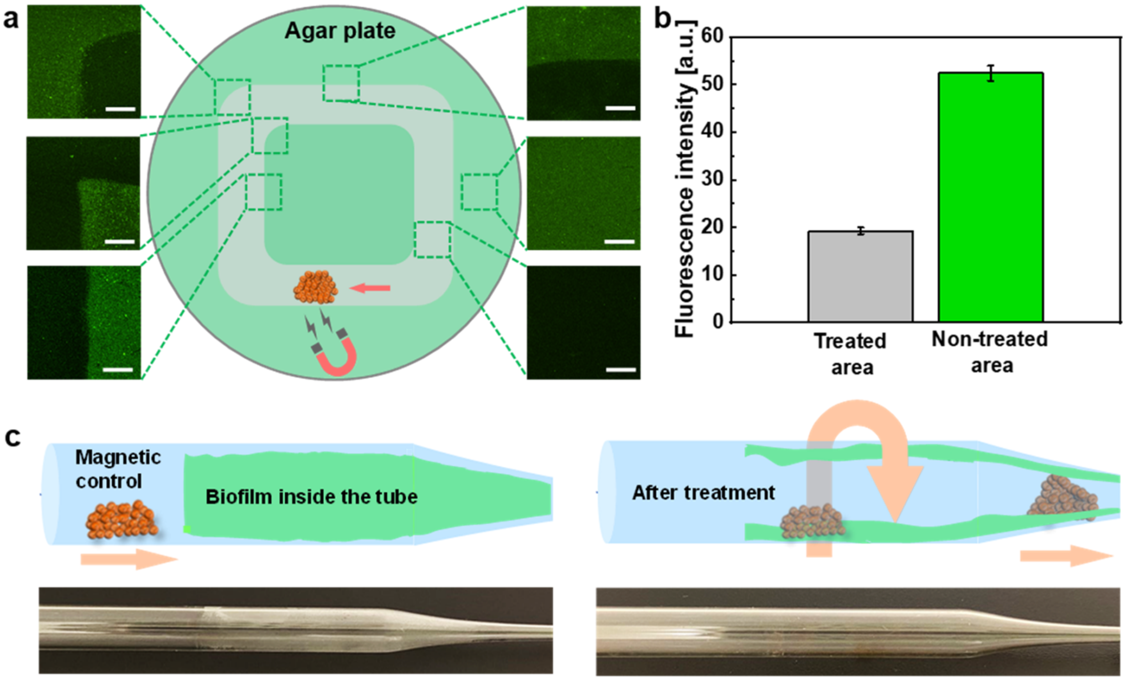

Figure 5. (a) Fluorescent images and (b) the corresponding fluorescence intensity values from different parts of an agar plate after mechanical biofilm disruption achieved by magnetically driven ZFO microrobots under the control of an external magnet. Scale bars are 100 μm. (c) Schematic illustration and digital images of mechanical biofilm disruption in a glass tube.

experimental conditions. As shown in Figure 4b, the absorbance values significantly decreased with higher concentrations of the microrobots during UV light irradiation (light on). The contribution of UV light irradiation or H_2O_2 in the absence of the microrobots reveals their limited effect on *E. coli* eradication, especially compared to the condition involving active microrobots at a concentration of 50 μg mL^{-1}. Furthermore, control experiments involving static ZFO/Pt microrobots (light off) demonstrated a partial removal of biofilms through Fenton reactions in the presence of ZFO and H_2O_2 fuel. The optical images of CV-stained well plates are reported in Figure S7 and further prove that 50 μg mL^{-1} of microrobots led to a much lighter purple color compared to all other conditions (control, 0.2 wt % H_2O_2, 10 and 25 μg mL^{-1}), indicating that most of the biofilm had been removed from the surface of the well plate. The effect of the duration of UV light exposure was also investigated by extending the irradiation time to 60 min. As illustrated in Figure S8, the results demonstrate that extended irradiation time has only a minimal impact on biofilm removal, indicating that optimal degradation efficiency is achieved within 30 min.

Optical images in Figures 4c and S9 illustrate that the number of stained living bacteria progressively decreased with the increasing concentrations of microrobots in the presence of H_2O_2 and UV light irradiation, which is in agreement with Figure 4b. To support these observations, the antimicrobial properties of the light-driven ZFO/Pt microrobots were further evaluated by calculating colony-forming units (CFU) based on a spread plate method as previously reported.[37] The results of the experiments performed with microrobot-treated groups were compared to the control groups (UV light irradiation and H_2O_2). As demonstrated in Figure 4d,e, the bacterial viability significantly decreased after treatment with the microrobots in the presence of UV light and H_2O_2, which supports the previous observations based on CV analysis. Finally, a LIVE/DEAD assay was used to validate the efficacy of light-driven ZFO/Pt microrobots against bacterial biofilms. SYTO 9 and propidium iodide (PI) were utilized to detect live (green) and dead (red) bacteria cells, respectively. These cells were initially treated with light-driven ZFO/Pt microrobots (50 μg mL^{-1}) under UV light irradiation in the presence of 0.2 wt % H_2O_2. Two control groups (only water and 0.2 wt % H_2O_2 without the microrobots) were also analyzed under UV light irradiation. The fluorescence microscopy images shown in Figure 4f demonstrate the promising features of the active microrobots toward effective biofilm removal by the significantly higher amount of dead bacteria for the treatment group and negligible effect of UV light or H_2O_2 in the absence of light-driven ZFO/Pt microrobots. The treatment of an older and matured biofilm was also taken into consideration by employing light-driven microrobots. Compared to the 24 h biofilm (Figure S10), the 72 h biofilm also exhibited a significant reduction in bacterial colonies, particularly under the optimal conditions of 50 μg mL^{-1} ZFO/Pt microrobots. However, the persistence of a small number of colonies at the highest microrobot concentration suggests that the catalytic efficiency of the microrobots requires further enhancement to effectively eradicate older and more mature biofilms.

2.5. Mechanical Removal of Biofilms by Magnetically Driven ZFO Microrobots. Different from the chemical disruption of biofilm by light-driven ZFO/Pt microrobots, the magnetic features of magnetically driven ZFO microrobots were utilized for the mechanical removal of the biofilms. For these experiments, a biofilm was successfully grown on an agar plate with 2 days of incubation at 37 °C as shown in Figure S11. An agglomerate of microrobots was then placed on the biofilm surface, followed by external manipulation via a permanent magnet in a predefined trajectory depicted in Figure 5a. Afterward, SYTO 9 was used to detect living bacteria. As evidenced by fluorescence images, mechanically treated areas presented significantly lower amounts of adhered bacteria compared to the areas without any treatment (Figure S12). The fluorescence intensity in Figure 5b decreased significantly after treatment with magnetically driven ZFO microrobots via physical erosion. A further detailed quantitative analysis was determined by comparing the fluorescence intensity in the designated triangular treatment area. From left to right across this region, a considerable decrease in the fluorescence intensity was also detected (Figure S13). Magnetically driven ZFO microrobots also allowed precise positioning for the treatment due to their strong response to external magnetic fields. It is worth mentioning that many areas of biofilm growth are difficult to reach for conventional microparticles, which typically could be observed in narrow plumbing systems or similar scenarios, making it a formidable task to address biofilm contamination.[4] In response to this requirement, a narrow tube (Figure S4) was used to simulate an enclosed and narrow environment that contains a biofilm on its surface. The magnet allowed easy manipulation of the microrobot agglomerate, leading to the mechanical scratching of the biofilm from the surface, as shown in Figure 5c. These results indicate that the intrinsic magnetic properties of magnetically driven ZFO microrobots can enable targeted biofilm removal even in confined spaces that can be encountered in different daily scenarios. Moreover, the possibility of irradiating UV light after the physical removal process allows for the definitive inactivation of the eradicated bacteria.

3. CONCLUSIONS

In this study, two effective approaches for the removal of bacterial biofilms were introduced based on light-driven ZFO/Pt microrobots and magnetically driven ZFO microrobots. To utilize the photocatalytic properties of the ZFO microrobots, an asymmetric structure was obtained by the sputtering deposition of Pt on ZFO microspheres synthesized by a hydrothermal method, followed by calcination. Light-driven ZFO/Pt microrobots demonstrated active light-induced motion via self-electrophoresis when exposed to UV light in a controllable way by switching the light on/off. Taking advantage of the paramagnetic properties of magnetically driven ZFO microrobots, they were manipulated collectively with high precision in both open surfaces and enclosed narrow channels. The dual propulsion mechanism of ZFO-based microrobots was utilized for biofilm removal by two strategies. Initially, the photocatalytic activity of light-driven ZFO/Pt microrobots was tested to treat *E. coli* biofilms. The microrobots, together with UV light irradiation and H_2O_2 fuel, demonstrated effective biofilm removal due to their active motion and simultaneous ROS production. Additionally, the collective movement of magnetically driven ZFO microrobots under an external magnetic field allowed the mechanical disruption of the biofilm structure inside the surface of a narrow glass tube as a representative example of confined environments. Given that the magnetic actuation of these microrobots could interfere with the stability of the self-electrophoresis mechanism that drives the light-induced motion, synergistic effects of dual motion on biofilm removal remain unconsidered in this work. Instead, the investigation of two motion modes independently for biofilm treatment promotes better insight into their individual contribution. To conclude, these microrobots offer a promising and versatile solution for biofilm treatment in both open surfaces or hard-to-reach confined areas of industrial environments. Owing to the wide variety of micro- and nanorobots that can be created by combining different properties, we focus our efforts on proof-of-concept studies for effective biofilm removal that will lay the foundation for the next generation of intelligent microrobots. In real-world applications, future studies should focus on investigating biofilm elimination using more efficient microrobots in simulated industrial pipelines or drinking water systems.

4. EXPERIMENTAL METHODS

4.1. Synthesis of Magnetically Driven ZFO Microrobots. In a typical synthesis, ZFO microspheres were obtained via a facile hydrothermal process. Briefly, 30 mL of isopropanol and 8 mL of glycerol were mixed in a beaker. Subsequently, 2 mmol of Fe $(NO_3)_3$ and 1 mmol of Zn $(CH_3COO)_2 \cdot 2H_2O$ were added to the mixture and further stirred for 30 min. The obtained homogeneous mixture was transferred into a Teflon-lined stainless-steel autoclave (50 mL) and kept in a heated oven at 180 °C for 12 h. After the natural cooling of the autoclave until room temperature, the precipitate was obtained by centrifugation at 4500 rpm and washed three times with deionized water and ethanol, followed by drying overnight at 60 °C. Finally, the as-prepared product was further treated via a calcination process in air inside a muffle furnace at 450 °C for 3 h with a heating rate of 5 °C/min. The final product was collected for further utilization.

4.1.1. Fabrication of Light-Driven ZFO/Pt Microrobots. To fabricate the Janus microrobots, the calcinated ZFO microspheres (3 mg mL^{-1}) were suspended in DI water and sonicated for 5 min. The suspension was dropped onto glass slides and dried overnight at room temperature. A 30-nm-thick Pt layer was asymmetrically deposited on ZFO microspheres by the sputtering technique. The real-time thickness of the sputtered Pt layer was controlled by a quartz crystal microbalance. Afterward, the microrobots were released from the glass slides using a scalpel.

4.2. Material Characterization. The morphology of magnetically driven ZFO and light-driven ZFO/Pt microrobots was assessed by using a Tescan MIRA 3 XMU SEM. EDX mapping analysis was conducted using an Oxford Instruments EDX detector connected to the SEM. XPS spectra were measured with the assistance of a Kratos Analytical Axis Supra instrument. To obtain the fitted data, XPS spectra were analyzed using CASA XPS software. Magnetic hysteresis loop measurements were performed at 300 K in magnetic fields up to 15 kOe using a Quantum Design PPMS VersaLab VSM magnetometer.

4.3. Motion Experiments. Microrobot motion was recorded with an inverted microscope (Nikon ECLIPSE TS2R) with a digital camera (Basler acA1920−155uc). The Pt/ZFO microrobots were suspended in DI water and sonicated for 3 min to properly disperse the particles. 0.3 wt % sodium dodecyl sulfate (SDS) was used as a surfactant during the motion experiments. Different concentrations of H_2O_2 (0, 0.5, 1, 1.5 wt %) were prepared to assess the speed of microrobots with/without UV light irradiation. The intensity of the light source was fixed at ∼1.5 W cm^{-2}. The magnetic motion of the ZFO microrobots was obtained by using a custom-built magnetic setup. The magnetic setup consists of three orthogonal coil pairs in a poly(lactic acid) (PLA) support to generate a transverse rotating magnetic field. Magnetically driven ZFO microrobots were navigated under different intensities of the magnetic field (3 or 5 mT) and different frequencies (5−50 Hz). The recorded videos were analyzed with NIS Elements Advanced Research software.

4.4. Biofilm Treatment by ZFO-Based Microrobots. The bacterial strain (*E. coli*, Migula 1895) employed for biofilm experiments was obtained from the Czech Collection of Microorganisms (CCM, Brno, Czech Republic). Initially, bacteria from the stock culture were inoculated onto nutrient agar plates and incubated overnight at 37 °C. Afterward, bacteria were collected in Luria−Bertani (LB) broth and then diluted with LB broth to reach an optical density of 0.15 absorbance units (AU) at 590 nm (OD_{590}). Then, the suspended bacteria (200 μL) were seeded into the wells of a 96-well plate. LB broth was refreshed after 1 h and the bacteria were further incubated for 24 h at 37 °C. Following the incubation period, bacterial biofilms were washed twice with phosphate-buffered saline (PBS). The efficacy of the microrobots toward biofilm removal was assessed by their utilization at various concentrations in the range of 10−50 μg mL^{-1}. The biofilm

https://doi.org/10.1021/acsami.4c18360

removal experiments were conducted in DI water containing 0.2 wt % H_2O_2 with or without exposure to UV light irradiation (UV LED at 365 nm, 9 W). Control experiments involved only DI water or H_2O_2 without the microrobots. After waiting 30 min, the wells were washed twice with PBS. The presence of biofilm was assessed by using a 1% CV solution. After waiting with CV solution for 15 min, the bacteria were washed twice with PBS. Finally, ethanol was added to dissolve CV and absorbance values were measured at 590 nm using a microplate reader. To further evaluate the efficacy of biofilm killing by the light-driven ZFO/Pt microrobots, CFU assay was conducted. After the treatments, the wells were washed once with PBS. Subsequently, the remaining bacteria were collected by pipet and transferred to centrifuge tubes. The suspension was serially diluted 5 times in PBS. 50 μL of the final bacterial suspension was seeded on agar plates followed by incubation for 24 h at 37 °C. After incubation, the CFUs were counted and averaged. Each experiment was repeated 3 times. Lastly, to obtain fluorescent images, a LIVE/DEAD BacLight bacterial viability kit, involving SYTO-9 and PI, was used according to the manufacturer's specifications.

ASSOCIATED CONTENT

Supporting Information

The Supporting Information is available free of charge at https://pubs.acs.org/doi/10.1021/acsami.4c18360.

SEM and EDS images of magnetic ZFO microrobots; optical images of the glass tube with varying diameters; fluorescence intensity of 2-hydroxyterephthalic acid; speed of light-driven ZFO/Pt microrobots in 0.2% H_2O_2; crystal violet staining of biofilm after treatment; absorbance changes for *E. coli* biofilm with different groups; microscope images of living bacteria after treatment; CFU images for different groups; and fluorescent image of the treated region on the agar plate (PDF)

Motion behavior of ZFO/Pt microrobots with on/off switching of UV light irradiation in 0.5 wt % H_2O_2 (Movie 1) (AVI)

Magnetic motion of ZFO microrobots at different frequencies of a transversal rotating magnetic field (Movie 2) (AVI)

Trajectories of a single ZFO microrobot along a predefined path under the control of a transversal rotating magnetic field (Movie 3) (AVI)

Reconfiguration and actuation of the collective microrobots swarm under the control of a permanent magnet (Movie 4) (AVI)

Motion behavior of light-driven ZFO/Pt microrobots in 0.2% H_2O_2 (Movie 5) (AVI)

AUTHOR INFORMATION

Corresponding Author

Martin Pumera − *Future Energy and Innovation Laboratory, Central European Institute of Technology, Brno University of Technology, 61200 Brno, Czech Republic; Department of Medical Research, China Medical University Hospital, China Medical University, TW-40402 Taichung, Taiwan; Advanced Nanorobots & Multiscale Robotics Laboratory, Faculty of Electrical Engineering and Computer Science, VSB—Technical University of Ostrava, 70800 Ostrava, Czech Republic;* orcid.org/0000-0001-5846-2951;
Email: martin.pumera@ceitec.vutbr.cz

Authors

Xia Peng − *Future Energy and Innovation Laboratory, Central European Institute of Technology, Brno University of Technology, 61200 Brno, Czech Republic*

Cagatay M. Oral − *Future Energy and Innovation Laboratory, Central European Institute of Technology, Brno University of Technology, 61200 Brno, Czech Republic*

Mario Urso − *Future Energy and Innovation Laboratory, Central European Institute of Technology, Brno University of Technology, 61200 Brno, Czech Republic*

Martina Ussia − *Future Energy and Innovation Laboratory, Central European Institute of Technology, Brno University of Technology, 61200 Brno, Czech Republic;* orcid.org/0000-0002-3248-6725

Complete contact information is available at:
https://pubs.acs.org/10.1021/acsami.4c18360

Author Contributions

X.P. prepared and characterized the microrobots, conducted motion experiments, and wrote the manuscript draft. X.P. and C.M.O. conducted bacteria experiments. C.M.O. obtained fluorescence images. M.Ur. and M.Us. contributed to experimental design and data interpretation. X.P. and M.P. originated the idea. M.P. supervised the project. All authors have approved the final version of the manuscript.

Notes

The authors declare no competing financial interest.

ACKNOWLEDGMENTS

This work was supported by ERDF/ESF project TECHSCALE (No. CZ.02.01.01/00/22_008/0004587). This research was cofunded by the European Union under the REFRESH—Research Excellence For REgion Sustainability and High-tech Industries project number CZ.10.03.01/00/22_003/0000048 via the Operational Programme Just Transition. X.P. was supported by the China Scholarship Council (CSC No. 202008320382) and acknowledges grant CEITEC-VUT-J-24-8537, realized within the Specific CEITEC Junior Project and Brno Ph.D. Talent scholarship funded by the Brno City Municipality. C.M.O. acknowledges the financial support of BUT (CEITEC VUT-J-22-8091). CzechNanoLab project LM2023051, funded by MEYS CR, is gratefully acknowledged for the financial support of the measurements/sample fabrication at CEITEC Nano Research Infrastructure.

REFERENCES

(1) Blair, K. M.; Turner, L.; Winkelman, J. T.; Berg, H. C.; Kearns, D. B. A Molecular Clutch Disables Flagella in the Bacillus Subtilis Biofilm. *Science* **2008**, *320*, 1636−1638.

(2) Mah, T. F.; Pitts, B.; Pellock, B.; Walker, G. C.; Stewart, P. S.; O'Toole, G. A. A Genetic Basis for Pseudomonas Aeruginosa Biofilm Antibiotic Resistance. *Nature* **2003**, *426*, 306−310.

(3) Arnaouteli, S.; Bamford, N. C.; Stanley-Wall, N. R.; Kovács, Á. T. Bacillus Subtilis Biofilm Formation and Social Interactions. *Nat. Rev. Microbiol.* **2021**, *19*, 600−614.

(4) Liu, Y.; Shi, L.; Su, L.; Van der Mei, H. C.; Jutte, P. C.; Ren, Y.; Busscher, H. J. Nanotechnology-Based Antimicrobials and Delivery Systems for Biofilm-Infection Control. *Chem. Soc. Rev.* **2019**, *48*, 428−446.

(5) Peterson, B. W.; He, Y.; Ren, Y.; Zerdoum, A.; Libera, M. R.; Sharma, P. K.; van Winkelhoff, A. J.; Neut, D.; Stoodley, P.; van der Mei, H. C.; Busscher, H. J. Viscoelasticity of Biofilms and Their Recalcitrance to Mechanical and Chemical Challenges. *FEMS Microbiol. Rev.* **2015**, *39*, 234−245.

(6) Dieltjens, L.; Appermans, K.; Lissens, M.; Lories, B.; Kim, W.; Van der Eycken, E. V.; Foster, K. R.; Steenackers, H. P. Inhibiting Bacterial Cooperation Is an Evolutionarily Robust Anti-Biofilm Strategy. *Nat. Commun.* **2020**, *11*, No. 107.

(7) Chauhan, A.; Ghigo, J. M.; Beloin, C. Study of in Vivo Catheter Biofilm Infections Using Pediatric Central Venous Catheter Implanted in Rat. *Nat. Protoc.* **2016**, *11*, 525−541.

(8) Arciola, C. R.; Campoccia, D.; Montanaro, L. Implant Infections: Adhesion, Biofilm Formation and Immune Evasion. *Nat. Rev. Microbiol.* **2018**, *16*, 397−409.

(9) Sun, M.; Chan, K. F.; Zhang, Z.; Wang, L.; Wang, Q.; Yang, S.; Chan, S. M.; Chiu, P. W. Y.; Sung, J. J. Y.; Zhang, L. Magnetic Microswarm and Fluoroscopy-Guided Platform for Biofilm Eradication in Biliary Stents. *Adv. Mater.* **2022**, *34*, No. 2201888.

(10) Ussia, M.; Urso, M.; Dolezelikova, K.; Michalkova, H.; Adam, V.; Pumera, M. Active Light-Powered Antibiofilm ZnO Micromotors with Chemically Programmable Properties. *Adv. Funct. Mater.* **2021**, *31*, No. 2101178.

(11) Chan, S.; Pullerits, K.; Keucken, A.; Persson, K. M.; Paul, C. J.; Rådström, P. Bacterial Release from Pipe Biofilm in a Full-Scale Drinking Water Distribution System. *npj Biofilms Microbiomes* **2019**, *5*, No. 9.

(12) Farh, H. M. H.; El Amine Ben Seghier, M.; Taiwo, R.; Zayed, T. Analysis and Ranking of Corrosion Causes for Water Pipelines: A Critical Review. *npj Clean Water* **2023**, *6*, No. 65.

(13) Gomes, I. B.; Simões, M.; Simões, L. C. An Overview on the Reactors to Study Drinking Water Biofilms. *Water Res.* **2014**, *62*, 63−87.

(14) Villa, K.; Sopha, H.; Zelenka, J.; Motola, M.; Dekanovsky, L.; Beketova, D. C.; Macak, J. M.; Ruml, T.; Pumera, M. Enzyme-Photocatalyst Tandem Microrobot Powered by Urea for *Escherichia coli* Biofilm Eradication. *Small* **2022**, *18*, No. 2106612.

(15) Urso, M.; Ussia, M.; Pumera, M. Smart Micro- and Nanorobots for Water Purification. *Nat. Rev. Bioeng.* **2023**, *1*, 236−251.

(16) Liu, Y.; Naha, P. C.; Hwang, G.; Kim, D.; Huang, Y.; Simon-Soro, A.; Jung, H. I.; Ren, Z.; Li, Y.; Gubara, S.; Alawi, F.; Zero, D.; Hara, A. T.; Cormode, D. P.; Koo, H. Topical Ferumoxytol Nanoparticles Disrupt Biofilms and Prevent Tooth Decay in Vivo via Intrinsic Catalytic Activity. *Nat. Commun.* **2018**, *9*, No. 2920.

(17) Chen, Z.; Wang, Z.; Ren, J.; Qu, X. Enzyme Mimicry for Combating Bacteria and Biofilms. *Acc. Chem. Res.* **2018**, *51*, 789−799.

(18) Benoit, D. S. W.; Sims, K. R.; Fraser, D. Nanoparticles for Oral Biofilm Treatments. *ACS Nano* **2019**, *13*, 4869−4875.

(19) Hu, Y.; Ruan, X.; Lv, X.; Xu, Y.; Wang, W.; Cai, Y.; Ding, M.; Dong, H.; Shao, J.; Yang, D.; Dong, X. Biofilm Microenvironment-Responsive Nanoparticles for the Treatment of Bacterial Infection. *Nano Today* **2022**, *46*, No. 101602.

(20) Wang, Z.; Klingner, A.; Magdanz, V.; Misra, S.; Khalil, I. S. M. Soft Bio-Microrobots: Toward Biomedical Applications. *Adv. Intell. Syst.* **2023**, *6*, No. 2300093.

(21) Soto, F.; Wang, J.; Ahmed, R.; Demirci, U. Medical Micro/Nanorobots in Precision Medicine. *Adv. Sci.* **2020**, *7*, No. 2002203.

(22) Zhang, Z.; Wang, L.; Chan, T. K. F.; Chen, Z.; Ip, M.; Chan, P. K. S.; Sung, J. J. Y.; Zhang, L. Micro-/Nanorobots in Antimicrobial Applications: Recent Progress, Challenges, and Opportunities. *Adv. Healthcare Mater.* **2022**, *11*, No. 2101991.

(23) Wu, R.; Zhu, Y.; Cai, X.; Wu, S.; Xu, L.; Yu, T. Recent Process in Microrobots: From Propulsion to Swarming for Biomedical Applications. *Micromachines* **2022**, *13*, No. 1473.

(24) Zhang, F.; Zhuang, J.; Li, Z.; Gong, H.; de Ávila, B. E. F.; Duan, Y.; Zhang, Q.; Zhou, J.; Yin, L.; Karshalev, E.; Gao, W.; Nizet, V.; Fang, R. H.; Zhang, L.; Wang, J. Nanoparticle-Modified Microrobots for in Vivo Antibiotic Delivery to Treat Acute Bacterial Pneumonia. *Nat. Mater.* **2022**, *21*, 1324−1332.

(25) Liu, D.; Wang, T.; Lu, Y. Untethered Microrobots for Active Drug Delivery: From Rational Design to Clinical Settings. *Adv. Healthcare Mater.* **2022**, *11*, No. 2102253.

(26) Rojas, D.; Kuthanova, M.; Dolezelikova, K.; Pumera, M. Facet Nanoarchitectonics of Visible-Light Driven Ag_3PO_4 Photocatalytic Micromotors: Tuning Motion for Biofilm Eradication. *NPG Asia Mater.* **2022**, *14*, No. 63.

(27) Ussia, M.; Urso, M.; Kment, S.; Fialova, T.; Klima, K.; Dolezelikova, K.; Pumera, M. Light-Propelled Nanorobots for Facial Titanium Implants Biofilms Removal. *Small* **2022**, *18*, No. 2200708.

(28) Guix, M.; Mayorga-martinez, C. C.; Merkoc, A. Nano/Micromotors in (Bio) Chemical Science Applications. *Chem. Rev.* **2014**, *114*, 6285−6322.

(29) Hu, D.; Li, H.; Wang, B.; Ye, Z.; Lei, W.; Jia, F.; Jin, Q.; Ren, K. F.; Ji, J. Surface-Adaptive Gold Nanoparticles with Effective Adherence and Enhanced Photothermal Ablation of Methicillin-Resistant Staphylococcus Aureus Biofilm. *ACS Nano* **2017**, *11*, 9330−9339.

(30) Villa, K.; Viktorova, J.; Plutnar, J.; Ruml, T.; Hoang, L.; Pumera, M. Chemical Microrobots as Self-Propelled Microbrushes against Dental Biofilm. *Cell Rep. Phys. Sci.* **2020**, *1*, No. 100181.

(31) Yuan, K.; Jurado-Sánchez, B.; Escarpa, A. Dual-Propelled Lanbiotic Based Janus Micromotors for Selective Inactivation of Bacterial Biofilms. *Angew. Chem., Int. Ed.* **2021**, *60*, 4915−4924.

(32) Mayorga-Martinez, C. C.; Zelenka, J.; Klima, K.; Mayorga-Burrezo, P.; Hoang, L.; Ruml, T.; Pumera, M. Swarming Magnetic Photoactive Microrobots for Dental Implant Biofilm Eradication. *ACS Nano* **2022**, *16*, 8694−8703.

(33) Dong, Y.; Wang, L.; Zhang, Z.; Ji, F.; Chan, T. K. F.; Yang, H.; Chan, C. P. L.; Yang, Z.; Chen, Z.; Chang, W. T.; Chan, J. Y. K.; Sung, J. J. Y.; Zhang, L. Endoscope-Assisted Magnetic Helical Micromachine Delivery for Biofilm Eradication in Tympanostomy Tube. *Sci. Adv.* **2022**, *8*, No. eabq8573.

(34) Zhou, H.; Mayorga-Martinez, C. C.; Pané, S.; Zhang, L.; Pumera, M. Magnetically Driven Micro and Nanorobots. *Chem. Rev.* **2021**, *121*, 4999−5041.

(35) Wang, L.; Meng, Z.; Chen, Y.; Zheng, Y. Engineering Magnetic Micro/Nanorobots for Versatile Biomedical Applications. *Adv. Intell. Syst.* **2021**, *3*, No. 2000267.

(36) Hwang, G.; Paula, A. J.; Hunter, E. E.; Liu, Y.; Babeer, A.; Karabucak, B.; Stebe, K.; Kumar, V.; Steager, E.; Koo, H. Catalytic Antimicrobial Robots for Biofilm Eradication. *Sci. Robot.* **2019**, *4*, No. eaaw2388.

(37) Dong, Y.; Wang, L.; Yuan, K.; Ji, F.; Gao, J.; Zhang, Z.; Du, X.; Tian, Y.; Wang, Q.; Zhang, L. Magnetic Microswarm Composed of Porous Nanocatalysts for Targeted Elimination of Biofilm Occlusion. *ACS Nano* **2021**, *15*, 5056−5067.

(38) Sun, B.; Sun, M.; Zhang, Z.; Jiang, Y.; Hao, B.; Wang, X.; Cao, Y.; Chan, T. K. F.; Zhang, L. Magnetic Hydrogel Micromachines with Active Release of Antibacterial Agent for Biofilm Eradication. *Adv. Intell. Syst.* **2023**, *6*, No. 2300092, DOI: 10.1002/aisy.202300092.

(39) Huang, S.; Gao, Y.; Lv, Y.; Wang, Y.; Cao, Y.; Zhao, W.; Zuo, D.; Mu, H.; Hua, Y. Applications of Nano/Micromotors for Treatment and Diagnosis in Biological Lumens. *Micromachines* **2022**, *13*, No. 1780.

(40) Ji, H.; Hu, H.; Tang, Q.; Kang, X.; Liu, X.; Zhao, L.; Jing, R.; Wu, M.; Li, G.; Zhou, X.; Liu, J.; Wang, Q.; Cong, H.; Wu, L.; Qin, Y. Precisely Controlled and Deeply Penetrated Micro-Nano Hybrid Multifunctional Motors with Enhanced Antibacterial Activity against Refractory Biofilm Infections. *J. Hazard. Mater.* **2022**, *436*, No. 129210.

(41) Urso, M.; Ussia, M.; Pumera, M. Breaking Polymer Chains with Self-Propelled Light-Controlled Navigable Hematite Microrobots. *Adv. Funct. Mater.* **2021**, *91*, No. 2101510, DOI: 10.1002/adfm.202101510.

(42) Urso, M.; Ussia, M.; Novotný, F.; Pumera, M. Trapping and detecting nanoplastics by MXene-derived oxide microrobots. *Nat. Commun.* **2022**, *13*, No. 3573, DOI: 10.1038/s41467-022-31161-2.

(43) Manjura Hoque, S.; Sazzad Hossain, Md.; Choudhury, S.; Akhter, S.; Hyder, F. Synthesis and Characterization of $ZnFe_2O_4$ Nanoparticles and its Biomedical Applications. *Mater. Lett.* **2016**, *162*, 60−63.

(44) Huang, Y.; Liang, Y.; Rao, Y.; Zhu, D.; Cao, J.; Shen, Z.; Ho, W.; Lee, S. C. Environment-Friendly Carbon Quantum Dots/$ZnFe_2O_4$ Photocatalysts: Characterization, Biocompatibility, and Mechanisms for NO Removal. *Environ. Sci. Technol.* **2017**, *51*, 2924−2933.

(45) F Fang, Z.; Zhang, L.; Qi, H.; Yue, H.; Zhang, T.; Zhao, X.; Chen, G.; Wei, Y.; Wang, C.; Zhang, D. Nanosheet Assembled Hollow

$ZnFe_2O_4$ Microsphere as Anode for Lithium-Ion Batteries. *J. Alloys Compd.* **2018**, *762*, 480−487.

(46) Köseoğlu, Y.; Baykal, A.; Toprak, M. S.; Gözüak, F.; Başaran, A. C.; Aktaş, B. Synthesis and Characterization of $ZnFe_2O_4$ Magnetic Nanoparticles via a PEG-Assisted Route. *J. Alloys Compd.* **2008**, *462*, 209−213.

(47) Manohar, A.; Vijayakanth, V.; Kim, K. H. Influence of Ca Doping on $ZnFe_2O_4$ Nanoparticles Magnetic Hyperthermia and Cytotoxicity Study. *J. Alloys Compd.* **2021**, *886*, No. 161276.

(48) Sundararajan, M.; Sukumar, M.; Dash, C. S.; Sutha, A.; Suresh, S.; Ubaidullah, M.; Al-Enizi, A. M.; Raza, M. K.; Kumar, D. A Comparative Study on $NiFe_2O_4$ and $ZnFe_2O_4$ Spinel Nanoparticles: Structural, Surface Chemistry, Optical, Morphology and Magnetic Studies. *Phys. B* **2022**, *644*, No. 414232.

(49) Khezri, B.; Villa, K. Hybrid Photoresponsive/Biocatalytic Micro- and Nanoswimmers. *Chem. - Asian J.* **2022**, *17*, No. e202200596.

(50) Villa, K.; Novotný, F.; Zelenka, J.; Browne, M. P.; Ruml, T.; Pumera, M. Visible-Light-Driven Single-Component $BiVO_4$ Micromotors with the Autonomous Ability for Capturing Microorganisms. *ACS Nano* **2019**, *13*, 8135−8145.

(51) Peng, X.; Urso, M.; Pumera, M. Photo-Fenton Degradation of Nitroaromatic Explosives by Light-Powered Hematite Microrobots: When Higher Speed Is Not What We Go For. *Small Methods* **2021**, *5*, No. 2100617.

(52) Lyu, X.; Liu, X.; Zhou, C.; Duan, S.; Xu, P.; Dai, J.; Chen, X.; Peng, Y.; Cui, D.; Tang, J.; Ma, X.; Wang, W. Active, Yet Little Mobility: Asymmetric Decomposition of H_2O_2 Is Not Sufficient in Propelling Catalytic Micromotors. *J. Am. Chem. Soc.* **2021**, *143*, 12154−12164.

(53) Brooks, A. M.; Tasinkevych, M.; Sabrina, S.; Velegol, D.; Sen, A.; Bishop, K. J. M. Shape-Directed Rotation of Homogeneous Micromotors via Catalytic Self-Electrophoresis. *Nat. Commun.* **2019**, *10*, No. 495.

(54) Navidpour, A. H.; Fakhrzad, M. Photocatalytic and Magnetic Properties of $ZnFe_2O_4$ Nanoparticles Synthesised by Mechanical Alloying. *Int. J. Environ. Anal. Chem.* **2022**, *102*, 690−706.

(55) Lin, Z.; Fan, X.; Sun, M.; Gao, C.; He, Q.; Xie, H. Magnetically Actuated Peanut Colloid Motors for Cell Manipulation and Patterning. *ACS Nano* **2018**, *12*, 2539−2545.

(56) Oral, C. M.; Ussia, M.; Urso, M.; Salat, J.; Novobilsky, A.; Stefanik, M.; Ruzek, D.; Pumera, M. Radiopaque Nanorobots as Magnetically Navigable Contrast Agents for Localized In Vivo Imaging of the Gastrointestinal Tract. *Adv. Healthcare Mater.* **2023**, *12*, No. 2202682.

(57) Jurado-Sánchez, B.; Wang, J. Micromotors for Environmental Applications: A Review. *Environ. Sci. Nano* **2018**, *5*, 1530−1544.

(58) Shen, H.; Cai, S.; Wang, Z.; Ge, Z.; Yang, W. Magnetically Driven Microrobots: Recent Progress and Future Development. *Mater. Des.* **2023**, *227*, No. 111735.

(59) Fu, D.; Jiang, J.; Fu, S.; Xie, D.; Gao, C.; Feng, Y.; Liu, S.; Ye, Y.; Liu, L.; Tu, Y.; Peng, F. Real-Time Micromotor Probe for Immune Neutrophil Activation State. *Adv. Healthcare Mater.* **2023**, *12*, No. 2300737.

(60) Valdez-Garduño, M.; Leal-Estrada, M.; Oliveros-Mata, E. S.; Sandoval-Bojorquez, D. I.; Soto, F.; Wang, J.; Garcia-Gradilla, V. Density Asymmetry Driven Propulsion of Ultrasound-Powered Janus Micromotors. *Adv. Funct. Mater.* **2020**, *30*, No. 2004043.

(61) Muhammad, M. H.; Idris, A. L.; Fan, X.; Guo, Y.; Yu, Y.; Jin, X.; Qiu, J.; Guan, X.; Huang, T. Beyond Risk: Bacterial Biofilms and Their Regulating Approaches. *Front. Microbiol.* **2020**, *11*, No. 928.

(62) Wasiński, B. Extra-Intestinal Pathogenic *Escherichia Coli* − Threat Connected with Food-Borne Infections. *Ann. Agric. Environ. Med.* **2019**, *26*, 532−537.

(63) Zhang, S.; Abbas, M.; Rehman, M. U.; Wang, M.; Jia, R.; Chen, S.; Liu, M.; Zhu, D.; Zhao, X.; Gao, Q.; Tian, B.; Cheng, A. Updates on the Global Dissemination of Colistin-Resistant *Escherichia Coli*: An Emerging Threat to Public Health. *Sci. Total Environ.* **2021**, *799*, No. 149280.

Part 2. Collective behavior of microrobots for environmental treatments at the small scale

8. Shape-controlled self-assembly of light powered microrobots into ordered microchains for cells transport and water remediation

Paper published in this chapter:

Xia Peng, Mario Urso, Martina Ussia and Martin Pumera, Shape-Controlled Self-Assembly of Light- Powered Microrobots into Ordered Microchains for Cells Transport and Water Remediation. *ACS Nano* **2022**, *16*, 7615–7625.

8.1 Motivation of this study

After investigation of single movement, the development of autonomous microrobotic systems capable of synchronized operation in complex environments holds immense potential for addressing challenges in environmental remediation, biomedical applications. While significant progress has been made in designing microrobots with swarm-like behaviors, achieving self-assembly and coordinated motion without external stimuli remains a major challenge. Inspired by nature's ability to organize complex systems through simple interactions, this work seeks to explore the collective behaviors of light-driven microrobots, emphasizing their self-assembly into reconfigurable microchains powered by dipolar interactions.

8.2 Paper conclusion

This study demonstrated that cubic hematite/Pt microrobots, due to their asymmetrical magnetic dipole moment, can self-assemble into microchains, which was visualized by SEM measurements. These light-powered microchains, driven by UV-light in low H_2O_2 concentrations, exhibit various propulsion modes based on microrobot orientation and can be reconfigured using external magnetic fields. Their collective behavior enables tasks such as yeast cell capture and transport, removal of suspended matter from water, and degradation of polymers, offering a low-cost, versatile solution for multimodal applications.

8.3 Author contribution

I performed the fabrication of the microrobots, recorded and analyzed their motion, performed SEM-EDX analysis and Tafel measurements, carried out the cargo transportation experiments, and interpreted the data. I wrote the manuscript.

ACS NANO

www.acsnano.org

Shape-Controlled Self-Assembly of Light-Powered Microrobots into Ordered Microchains for Cells Transport and Water Remediation

Xia Peng, Mario Urso, Martina Ussia, and Martin Pumera*

Cite This: *ACS Nano* 2022, 16, 7615−7625

Read Online

ACCESS | Metrics & More | Article Recommendations | Supporting Information

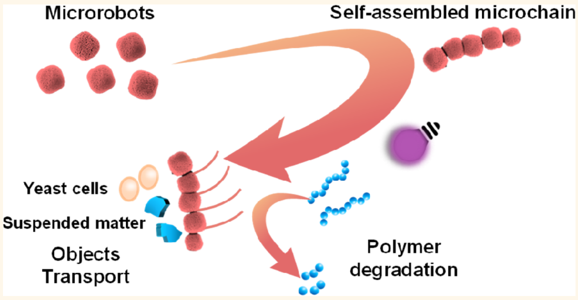

ABSTRACT: **Nature presents the collective behavior of living organisms aiming to accomplish complex tasks, inspiring the development of cooperative micro/nanorobots. Herein, the spontaneous assembly of hematite-based microrobots with different shapes is presented. Autonomous motile light-driven hematite/Pt microrobots with cubic and walnut-like shapes are prepared by hydrothermal synthesis, followed by the deposition of a Pt layer to design Janus structures. Both microrobots show a fuel-free motion ability under light irradiation. Because of the asymmetric orientation of the magnetic dipole moment in the crystal, cubic hematite/Pt microrobots can self-assemble into ordered microchains, contrary to the random aggregation observed for walnut-like microrobots. The microchains exhibit different synchronized motions under light irradiation depending on the mutual orientation of the individual microrobots during the assembly, which allows them to accomplish multiple tasks, including capturing, picking up, and transporting microscale objects, such as yeast cells and suspended matter in water extracted from personal care products, as well as degrading polymeric materials. Such light-powered self-assembled microchains demonstrate an innovative cooperative behavior for small-scale multitasking artificial robotic systems, holding great potential toward cargo capture, transport, and delivery, and wastewater remediation.**

KEYWORDS: *micromotors, swarming, collective behavior, self-assembly, cargo transport, photo-Fenton degradation*

INTRODUCTION

Ranging from ant colonies to bird flocking, nature provides a plethora of intriguing collective phenomena in biological systems, self-assembled in a synchronized manner to accomplish desired tasks and goals that individual capabilities cannot achieve. For example, a colony of ants can cooperate on the basis of achievable local information to transport food, construct nests, and self-assemble into sophisticated structures when encountering rugged terrain;[1] vast groups of starlings can twist, turn, swoop, and swirl across the sky in beautiful shape-shifting clouds, known as starling murmurations, to scare and repel natural enemies. Such ingenious behaviors in the absence of any external influences exhibit superior advantages to complete tasks in a highly efficient and robust way or to survive in complex environments, fascinating researchers, especially from the field of micro/nanorobotics. Inspired by the cooperative actions of living organisms, various artificial swarm robotic systems consisting of relatively simple robots have been developed, capable of complex task sequencing and communal formations relying on operator inputs or artificial intelligent software.[2,3]

Artificial micro/nanorobots, a relatively young field of research that has seen significant growth, becoming one of the most attractive research topics nowadays, are autonomously self-propelled micro/nanomaterials able to harvest and convert energy from their surrounding environment into autonomous movement with distinct capabilities for accomplishing various tasks.[4−9] Various energy sources, including chemical fuels (H_2O_2, glucose, urea) or external stimuli such as light, magnetic fields, and ultrasound, have been exploited to activate the self-propulsion of micro/nanorobots.[10−19] Partic-

Received: December 15, 2021
Accepted: April 8, 2022
Published: April 22, 2022

https://doi.org/10.1021/acsnano.1c11136

ularly, light is a very attractive energy source to power microrobots because it is powerful, renewable, and abundant. To obtain an active moving particle, it is necessary to have an asymmetric structure, which in turn converts this asymmetry into motion.[20,21] In this regard, the "two-faced" Janus microrobots consisting of a photocatalytic semiconductor (UV-light-activated TiO_2 and ZnO, visible light-activated Fe_2O_3 and BiOI) asymmetrically covered by a metal layer (Pt, Au, Ag) represent the most efficient light-powered self-motile microrobots.[22−31] Owing to their powerful motion, micro/nanorobots can accomplish numerous and different tasks, holding excellent prospects in various application fields from biomedicine to environmental remediation and sensing.[32−35] Still, further improvements are expected from rudimentary communication between individual microrobots (e.g., micro/nanorobotic swarms), allowing synchronized operation and high adaptability to different complex conditions.[36−38] On the basis of this consideration, the careful selection of the constituent materials plays a crucial role in micro/nanorobots' organization manners. In fact, self-propelled micro/nanorobots composed of colloids can exhibit swarm behaviors via physical or chemical interactions, such as dipole−dipole interactions, capillary forces, van der Waals forces, etc., rather than informatic communication in macro-robotic systems.[39−45] For instance, Bi_2WO_6 microrobots present swarms of multiple microrobots under continuous light exposure due to the release of ionic species.[46] Another case of microrobotic assembly is provided by peanut-shaped hematite colloids. With a combination of oscillating and rotating magnetic fields, swarms can be formed in the state of chains, vortices, and ribbons.[14] Similarly, helical swimmers consisting of polymeric helical structures covered with ferromagnetic thin films can be assembled into straight chains and various other configurations, such as bent chains, crosses, and more.[47] Furthermore, Au/Ru nanorods have been forced by acoustic standing waves into various configurations, such as chains or rings.[48] Nevertheless, microrobots that can self-assemble into microchains without any external influences with a reconfigurable capability and exhibit light-driven propulsion in a synchronized way with different motion modes remain to be explored.

In this work, we demonstrate the intriguing collective behavior of light-powered cubic hematite microrobots different from that of walnut-like hematite microrobots (Scheme 1).

Scheme 1. Shape-Controlled Self-Assembly Capabilities of Light-Powered Hematite/Pt Janus Microrobots under UV-Light Irradiation

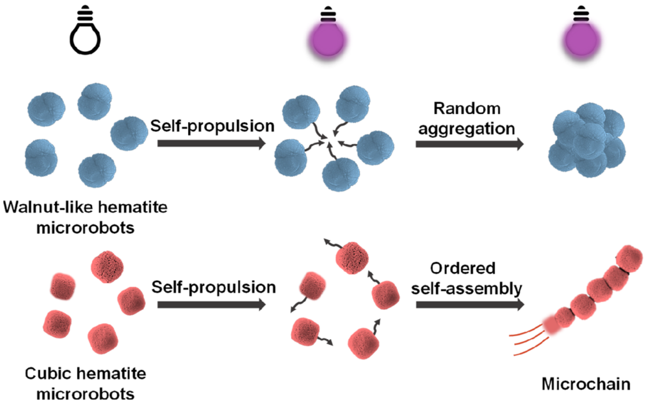

The microrobots are fabricated by asymmetrically depositing a 30 nm thin Pt layer on the surface of walnut-like and cubic-shaped hematite microparticles synthesized by facile and low-cost hydrothermal processes. All microrobots show self-propulsion under UV-light irradiation in pure water. Cubic microrobots display faster locomotion than walnut-like ones, agreeing with the larger mixed potential differences observed from Tafel measurements.

Moreover, cubic hematite microrobots can self-assemble into microchains exhibiting three types of autonomous motion under UV-light irradiation, according to the orientation of microrobots during the formation of the microchains. The self-assembled microchains can address multitasking requirements when environmental variations are encountered, including capturing, picking up, and transporting micro-objects, such as cells and suspended matter in water resulting from the contamination with personal care products, or photocatalytic degradation of polymer chains. This work offers self-assembled light-powered microchains based on dipolar interactions between individual cubic hematite/Pt Janus microrobot, which promise cargo transportation and degradation of pollutants in water, including plastic materials.

RESULTS AND DISCUSSION

Janus Microrobots Fabrication. The different shapes of micro/nanorobots play a crucial role in their self-assembly or collective behaviors. In this work, we investigate the influence of microrobots' shape on their collective behavior using self-propelled light-driven walnut-like and cubic hematite/Pt Janus microrobots.

As illustrated in Figure 1a, different shapes of hematite microparticles have first been synthesized by facile hydrothermal reactions. To fabricate Janus microrobots, 30 nm Pt films are physically deposited on the surface of hematite microparticles by the sputtering method. Scanning electron microscopy (SEM) images and the corresponding elemental mapping images obtained by energy-dispersive X-ray spectroscopy (EDX) of the two hematite shapes are presented in Figure 1b,c. Figure 1b shows walnut-like hematite microparticles with a diameter of 2−3 μm and a hierarchical porous structure resulting from the random arrangement of hematite nanoparticles (approximately 100 nm). As shown in Figure 1c, hematite microcubes display a round-edged morphology and a relatively rough surface with an average size of about 2 μm. EDX images manifest a uniform distribution of Fe and O for both hematite microparticles. After Pt layers deposition, both hematite microrobots exhibit the distinct asymmetrical structure of Janus microrobots, as indicated by the uneven Pt distribution.

X-ray diffraction (XRD) has been performed to assess hematite microparticles' crystalline structure, as shown in Figure S1. The recorded XRD patterns correspond to the characteristic α-Fe_2O_3 pattern (PDF card # 00-001-1053). The peaks appearing at the following 2θ values ≈24.12°, 33.12°, 35.61°, 40.88°, 49.51°, 54.22°, 57.63°, 62.45°, and 64.11°, correspond to the (012), (104), (110), (113), (024), (116), (018), (214), and (300) planes, respectively. These peaks agree with the distinctive rhombohedral centered hexagonal structure of the α-Fe_2O_3 crystal, commonly called hematite.[28]

Single Microrobots Propulsion. The hematite/Pt Janus microrobots display autonomous propulsion abilities in water and low amounts of H_2O_2 fuel when irradiated with UV light on the basis of a light-induced self-electrophoretic mechanism.

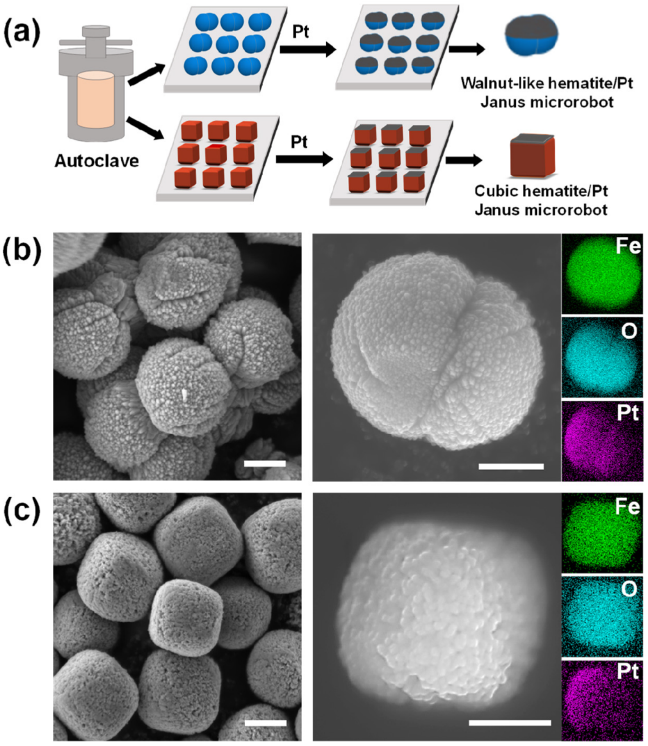

Figure 1. (a) Fabrication scheme of hematite/Pt Janus microrobots with different shapes. SEM and EDX elemental mapping images of (b) walnut-like and (c) cubic hematite/Pt Janus microrobots. Scale bars are 1 μm.

Upon exposure to UV light, charge separation occurs within hematite, and electrons from the hematite conduction band are transferred to the Pt layer. Consequently, protons are produced at the hematite side from water oxidation and consumed at the Pt side, establishing a proton gradient. This generates an electroosmotic flow, causing a net displacement of the particles and propelling the Janus microrobots with hematite as the forward side.[35] The addition of a small amount of H_2O_2 can result in a much stronger gradient of charges and more powerful propulsion, as illustrated in Figure S2. Figure 2a reports the speed of the walnut-like and cubic microrobots in different concentrations of H_2O_2, calculated from the average of more than 10 different microrobots. In pure water (0% H_2O_2), the speed of walnut-like microrobots (5 ± 1 μm s^{-1}) is slightly higher than cubic hematite microrobots (4.2 ± 0.8 μm s^{-1}). However, the addition of a small amount of H_2O_2 (0.1%) results in a huge increase in the speed of cubic hematite microrobots (19 ± 1 μm s^{-1}), while the speed of walnut-like ones is merely 6 ± 1 μm s^{-1}. Figure 2b shows the trajectories of walnut-like and cubic microrobots in 0.1% H_2O_2 under UV-light irradiation after 5 s of recording, demonstrating the much longer navigation within 5 s of the cubic ones (Supplementary Movie 1). When a higher concentration of H_2O_2 is applied (1% H_2O_2), there is an 8-fold increase in the speed of cubic microrobots (32 ± 3 μm s^{-1}) compared to pure water, while it is just tripled for walnut-like ones (14 ± 2 μm s^{-1}).

To better understand the underlying reasons for the differences in the speed of microrobots with different shapes, the mixed potential difference between walnut-like and cubic hematite microparticles and a Pt electrode has been evaluated in 1% H_2O_2 under UV-light irradiation. According to previous works,[28,31] a Tafel measurement is used to obtain the potentials established at different segments of the Janus microrobots (hematite and Pt) under UV-light illumination in H_2O_2. Tafel plots indicate that the variation in the mixed potentials between the electrodes is larger for cubic microrobots and consistent with the observed higher speed. As shown in Figure 2c, cubic hematite microrobots show a more negative mixed potential under UV-light illumination than walnut-like hematite microrobots, indicating that more electrons migrate from the cubic hematite electrode to the Pt electrode. The potential difference between cubic hematite microparticles and Pt electrodes (47 mV) is much larger than that for walnut-like hematite (4 mV), consistent with the trend of microrobots' speed in Figure 2a. This phenomenon can be explained by the photoabsorption and charge transport properties of different faces in the hematite crystal structure. As evidenced by previous papers,[49,50] it has been demonstrated that the (110) surface of hematite is more active than the (104) surface for photoelectrochemistry. As shown in Figure S1, the normalized XRD pattern illustrates that the ratio of peaks corresponding to (110) and (104) faces for cubic hematite is larger than that for walnut-like hematite, which is consistent with the result of the Tafel measurement.

Collective Behavior of Self-Assembled Microchains. We have discovered that the different microrobots' shapes give rise to different interactions. Figure 3a displays the temporal evolution of systems of walnut-like and cubic microrobots. In the beginning, walnut-like and cubic microrobots are randomly dispersed in water. After 10 min of observation, walnut-like

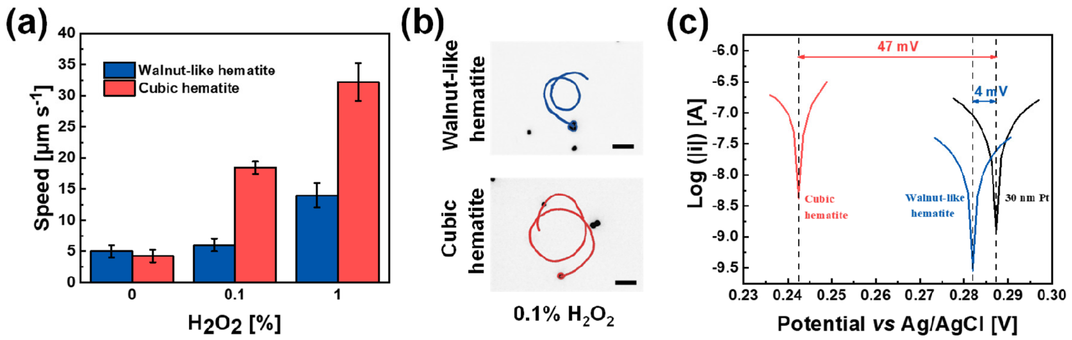

Figure 2. (a) Comparison of microrobots' speed in pure water and at different concentration of H_2O_2. (b) Micrographs showing walnut-like and cubic microrobots trajectories in 0.1% H_2O_2 under UV-light irradiation. Scale bars are 5 μm. (c) Tafel plots of walnut-like and cubic hematite electrodes and 30 nm Pt electrode in 1% H_2O_2 under UV-light irradiation.

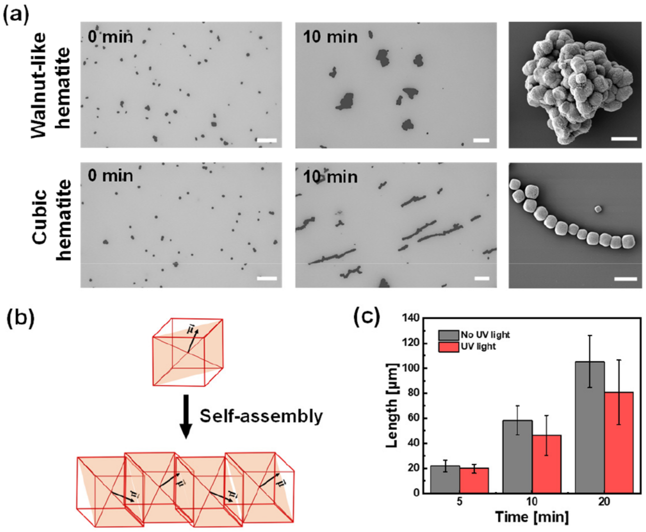

Figure 3. (a) Self-assembly of walnut-like and cubic microrobots in pure water in the absence of UV-light irradiation and the corresponding SEM images after 10 min of observation. Scale bars for SEM are 5 *μ*m. (b) The magnetic dipole moment orientation in a hematite cube and the alignment of a chain. (c) Length of the self-assembled microchains formed in pure water in the absence and presence of UV-light irradiation as a function of time.

microrobots display a random aggregation into large disordered clusters. As shown in Figure S3a, the direction of the magnetic dipole moment is perpendicular to its long axis.[14] According to previous research, walnut-like hematite microrobots can assemble into chains cooperating with the magnetic field.[51] In contrast, only two-particle chains are found in the absence of a magnetic field, and mostly random aggregations are observed, as displayed in Figure S3b. Rod-shaped hematite microparticles with a long axis of approximately 1 *μ*m and a short axis of approximately 500 nm have also been fabricated to study their collective behavior without any external influence (Figure S4a). After 5 min observation under the microscope in the absence of UV-light irradiation and H_2O_2, rod-shaped hematite microparticles form random aggregates (Figure S5a), the same behavior as walnut-like hematite microparticles. On the contrary, cubic microrobots self-assemble into ordered microchains, which can be observed from optical microscopy and SEM. The live formation of the microchains is also presented in Supplementary Movie 2 and Supplementary Movie 3, while several other microchains are reported in Figure S6. As SEM images show in Figure S7, we observe that cubic hematite microrobots self-assemble into microchains with different lengths in pure water without UV-light irradiation. The time-lapse images captured from Supplementary Movie 3 further reveal the live formation process of self-assembled microchains in pure water and in the absence of UV light. As shown in Figure S8a, most

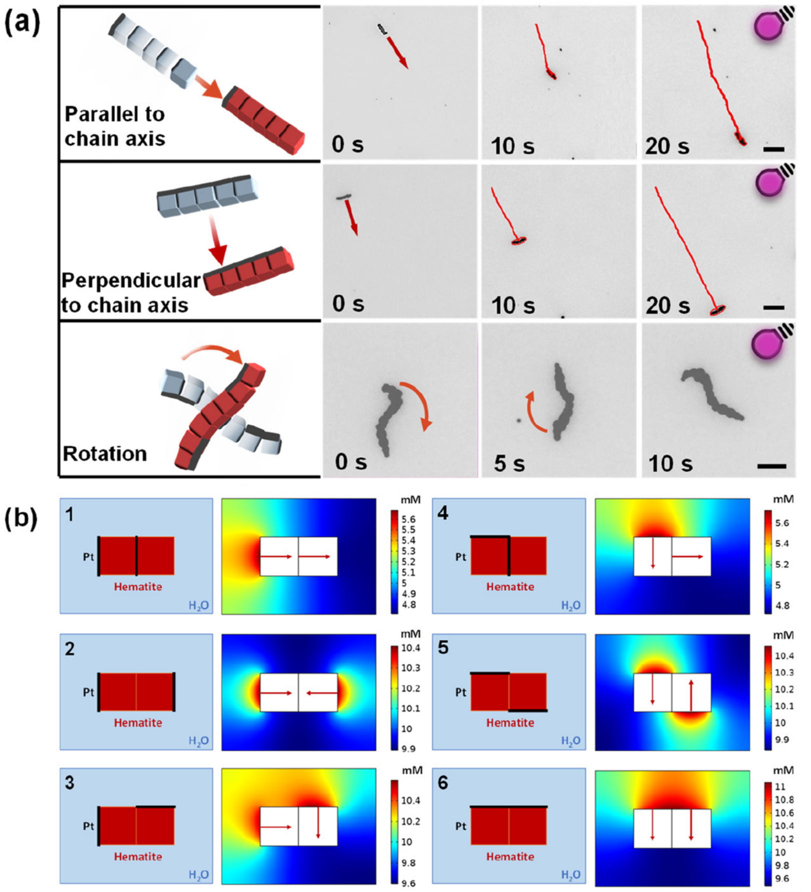

Figure 4. (a) Different motion modes of self-assembled microchains formed by cubic microrobots in 0.1% H_2O_2 under UV-light irradiation. Scale bars are 5 *μ*m. (b) Simulation of the 2D spatial distribution of H_2O resulting from the reaction at the Pt/H_2O_2 interface for different configurations of a two-microrobot microchain. The arrows indicate the direction of the driving force.

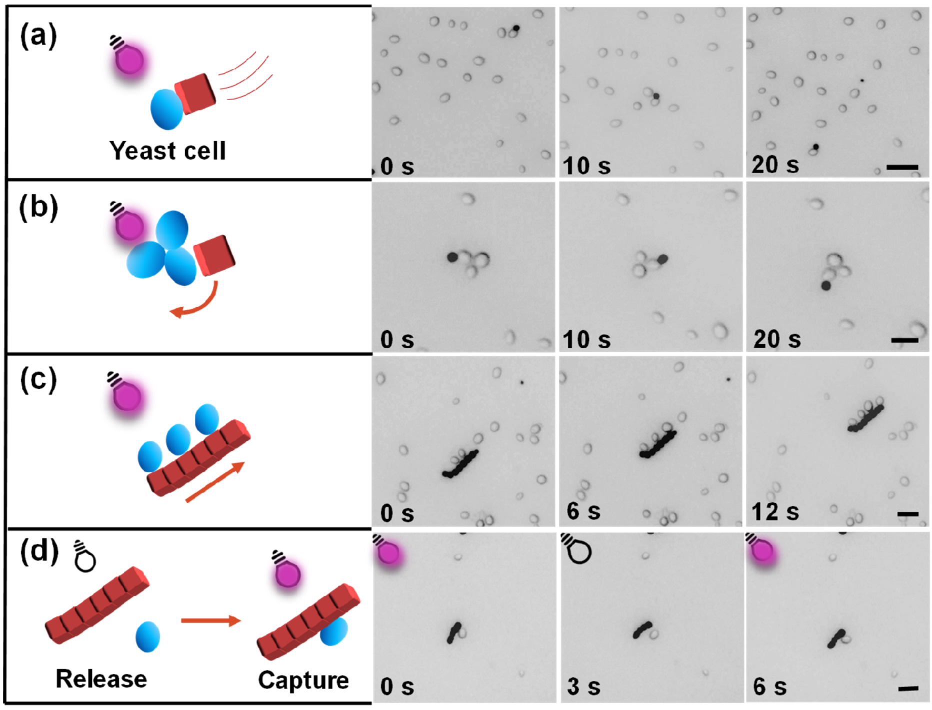

Figure 5. Interaction of cubic microrobots and self-assembled microchains with yeast cells in 0.1% H_2O_2 under UV-light irradiation. Time-lapse images of (a) a single microrobot transporting a yeast cell and (b) a single microrobot rotating with yeast cells, (c) a microchain capturing multiple yeast cells, and (d) controlled capture/release of the yeast cell by a microchain by turning on/off the UV light. Scale bars are 5 μm.

microrobots are well-dispersed in water. After 20 s, several microrobots gradually self assemble into longer microchains, as marked by the red circles. Figure S8b demonstrates the long-range assembling process, which requires a longer time. After 2 min, the most noticeable microchain marked by the red rectangle varies from a four-microrobot configuration to an eight-microrobot configuration, whose length changes from approximately 6 μm to more than 10 μm. This intriguing phenomenon is due to the orientation of the magnetic dipole moment in the crystal of cubic hematite, as illustrated in Figure 3b. For cubic hematite, the magnetic dipole moment is not aligned along a particle symmetry axis. As explained in a previous work,[52] the competing anisotropic interactions between the cube shape and dipole moment orientation are crucial for the formation of these microchains. Moreover, cubic hematite displays a fixed and permanent dipole moment, even in the absence of a magnetic field, which is strong enough to induce the formation of self-assembled microchains.[53] It is worth noting that the presence of the Pt layer does not influence the active interaction between individual hematite microrobots, also as shown in Figure S6 and Figure S7. The length of the self-assembled microchains has been measured both in the dark and under UV-light irradiation and plotted as a function of the time, finding that it increases from 20 ± 3 to 100 ± 20 μm in the dark and from 18 ± 4 to 80 ± 16 μm in the presence of UV light when the time changes from 5 to 20 min (Figure 3c). We assume that the light-induced motion of microrobots influences the formation of microchains to a certain degree, leading to shorter lengths under light irradiation. On the basis of these results, it can be concluded that the absence of external disturbances favors the self-assembly of the microrobots. Considering that reducing the size of cubic hematite particles may affect the self-assembly capability, nanosized cubic hematite, whose size is reduced nearly 4 times compared to that of cubic hematite microparticles (Figure S4b), can self-assemble into microchains, as shown in Figure S5b, demonstrating that the permanent magnetic dipole moment in the crystal structure is still strong enough to overcome the Brownian motion of nanosized cubic hematite in water.

The motion of the self-assembled microchains under UV-light irradiation has then been investigated. The microchains exhibit three main motion modes in 0.1% H_2O_2 under UV-light irradiation that are associated with a self-propulsion direction (1) parallel or (2) perpendicular to the microchain axis or (3) a rotational behavior (Supplementary Movie 4). Figure 4a presents a series of time-lapse images, which illustrate the autonomous locomotion of microchains with different propulsion modes.

The peculiar and varying motility of the microchains is ascribed to the distribution of the microrobots' Pt layers along the microchains, which depends on the microrobots' mutual orientation during the self-assembly process. To corroborate this hypothesis, a numerical simulation of the 2D spatial distribution of H_2O resulting from the reaction at the Pt/H_2O_2 interface between H_2O_2, photogenerated electrons transferred from hematite to Pt, and H^+ produced at the hematite side has been conducted. Despite its simplicity, this simulation provides an idea of the reaction at the Pt surface responsible for establishing a products' spatial gradient and, in turn, for the microchains' self-propulsion modes. At a first approximation, a microchain formed by only two adjacent microrobots is considered to simplify the calculation. The different orientations of the Pt layers in the two microrobots give rise to different configurations, as shown in Figure 4b (Pt layers parallel to the plane are excluded). In configurations 1 and 2, the Pt layers are on the small side of the microchains. However, configuration 1 results in the movement of the microchain along its axis. In contrast, configuration 2 leads to a static microchain as the driving forces of the two microrobots are equal and oppositely directed. Configurations 3 and 4 are a combination of translation and rotation, while configuration 5 is responsible for the pure rotation of the microchain. Finally, configuration 6, where the two Pt layers are adjacent and placed on the longer lateral side of the microchain, enables the locomotion of the microchain along the direction perpendicular to its axis. It is important to point out that cubic hematite can arrange in longer microchains. However, the chains with more cubes could occur in hundreds of combinations, making their simulation and interpretation difficult. In this regard, we have conducted simulations for microchains formed by six microrobots (Figure S9), selecting three different combinations of the configurations illustrated in Figure 4b. This study demonstrates that the motion behavior of longer microchains can be traced back to the ideal two-particle microchains model. Unfortunately, these propulsion modes and the moving direction of microchains cannot be precisely controlled at the present stage due to the random configuration of hematite microrobots and different orientations of their Pt layers during the self-assembly with or without UV-light irradiation.

Microchains also exhibit reconfigurable capability when an external magnetic field is applied. First, the magnetic hysteresis loop of hematite microrobots is measured using a vibrating sample magnetometer (VSM). Figure S10a demonstrates that hematite microrobots exhibit ferromagnetic behavior. Then, the suspended solution of hematite microrobots is injected into a microfluidic channel. Time-lapse optical microscopy images in Figure S10b, captured from Supplementary Movie 5, illustrate that hematite microrobots rotate and move toward the upside direction along the channel under a transversal rotating magnetic field of 3 mT and 10 Hz, which results in the deformation of microchains. When the external magnetic field is removed, these microrobots spontaneously reconfigure into microchains. Such emerging collective behavior, leading to a synchronized motion of the microchains and reconfigurable capability, is promising for completing tasks like the transport of cells or suspended matter as an example of possible contamination in water.

Yeast Cells Capture, Transport, And Release. Light-driven microrobots that can generate a local electric field and chemical gradients have demonstrated diverse interactions with surrounding passive particles, which is of great importance for performing desirable tasks such as cargo transport, object manipulation, and sensing.[54−56] The self-assembly of cubic microrobots into autonomous motile microchains has inspired their use for cargo transport applications using yeast cells as a model for living microorganisms, owing to their relatively big size (approximately 2−3 μm for haploids) that can be easily visualized by optical microscopy. Figure 5 displays the interaction between a cubic microrobot and yeast cells under UV-light irradiation in 0.1% H_2O_2 (Supplementary Movie 6 and Supplementary Movie 7). The time-lapse images in Figure 5a demonstrate the long-distance transportation of a yeast cell by a single cubic microrobot. Besides, the rotation of multiple yeast cells can be realized by a single microrobot, as shown in Figure 5b. The transportation capability of self-assembled microchains has also been evaluated. The self-assembled microchain in Figure 5c shows an autonomous motion parallel to the microchain axis, capturing four yeast cells, proving how the cooperation of several microrobots allows capturing and transporting several cells simultaneously in the absence of a magnetic field. We have further investigated the controlled release of yeast cells by switching on/off the UV light in 0.1% H_2O_2 using the self-assembled microchains. As illustrated in Figure 5d, the microchain captures one yeast cell under UV-light irradiation owing to the photogenerated local chemical gradients, which induces a phoretic attraction of the surrounding yeast cells. By turning off the UV light, the yeast cell is immediately released, which is attributed to the hindered self-propulsion of the microchain and consequently the stopped generation of a chemical gradient around it. When UV light is turned on again, the microchain produces photogenerated local chemical gradients, picks up again the yeast cell, and continues to transport it.

Removal of Suspended Matter in Water. Autonomous moving self-assembled microchains composed of synchronized microrobots hold great potential in separating microplastics and suspended matter from water. The removal of suspended matter (Figure S11) extracted from commercial toothpaste has been accomplished by the shoveling effect of microchains under UV-light irradiation in 0.1% H_2O_2 (Supplementary Movie 8). The artificially colored time-lapse images in Figure 6a (original images in Figure S12) demonstrate the motion of a microchain that was cleaning water by collecting suspended matter "on-the-fly". In fact, it can be observed that the removal area increases along the propulsion trajectory of the microchain, and within 60 s, a considerable number of pieces are quantitively accumulated on the forward side of the micro-

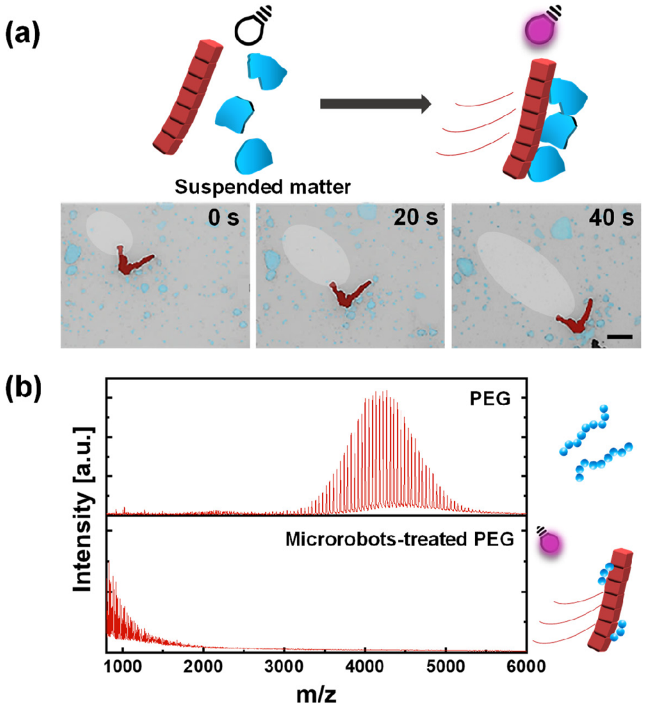

Figure 6. (a) Artificially colored time-lapse images of a self-assembled microchain for the removal of suspended matter under UV-light irradiation in 0.1% H_2O_2. White circles represent the area of suspended matter removal, blue areas are suspended matter pieces, and red areas are microchains. The scale bar is 5 μm. (b) PEG chain photodegradation. From top to bottom, MALDI-MS of untreated PEG and PEG treated with microchains under 24 h of UV-light irradiation in 1% H_2O_2.

chain, which further proves robust binding force between the single microrobots of the microchain. Compared to other light-driven micromotors, most agents can exhibit swarming behavior in a random aggregation form under light irradiation[46,57] rather than regular microchains, which shows superior capability toward the removal of microplastics.[58] Furthermore, intrinsic hematite magnetism without any surface functionalization can be used to navigate the microchains with captured microplastics using an external magnetic field, completing the remediation process. In addition to precise wireless positioning using an external magnetic field, microchains can also navigate to regions difficult to access, such as industrial tubes that are hard to reach with conventional strategies, providing an alternative solution for environmental applications in the future.[58−60]

PEG Photodegradation. To demonstrate the ability of the self-assembled microchains to degrade pollutants in water, PEG 4000 has been chosen as a model for polymeric materials like plastics, whose degradation can be monitored by Matrix-Assisted Laser Desorption/Ionization Mass Spectrometry (MALDI-MS). A higher concentration of H_2O_2 (1% H_2O_2) has been employed in this experiment to exploit a higher self-propulsion speed and enhanced photocatalytic activity required to break the strong covalent bonds in polymer chains. The PEG is exposed to UV-light irradiation for 24 h in the presence of the cubic microrobots leading to the self-assembled microchains. Figure 6b reports MALDI spectra of bare PEG and microrobots-treated PEG solution. Signals corresponding to PEG macromolecular chains around 4000 mass completely disappear after treatment with microchains upon exposure to UV light and H_2O_2, which is attributed to the combination of photocatalysis and catalyzed photo-Fenton reaction producing photogenerated ROS to attack C−O bonds in PEG backbone.[61] Several control experiments have been performed to corroborate the effectiveness of the chain-like structure toward the degradation of PEG. It is worth noting that cubic hematite can form microchains under motion and no-motion conditions, i.e., with or without exposure to UV light. Thus, it is difficult to establish the contribution of the microchain formation in this specific case. Due to this, PEG was treated with 1% H_2O_2 and UV-light irradiation separately and together to exclude secondary effects during the photodegradation process. As it is possible to appreciate in Figure S13, it is clearly shown that PEG treated with UV light and H_2O_2 separately remains stable or only partially degraded after 24 h of treatment, while, when UV light and H_2O_2 are applied in combination, the PEG photodegradation is notable but significantly lower than that for cubic hematite microchains. In agreement with previous studies about photodegradation of PEG mediated by microrobots, it is possible to conclude that the photo-Fenton reaction due to the simultaneous presence of iron-based microstructures, UV light, and H_2O_2 is more effective.[28] On the other hand, as already discussed before and as evidenced in Figure S6, the hematite microcubes are able to self-assemble into microchains both with or without UV light and in the absence or presence of H_2O_2. Thus, it is not possible to compare their photodegradation abilities with those of the single microrobots. Nevertheless, we retain that single microrobots can spontaneously aggregate without peculiar configurations in contaminated water solutions, thus partially reducing the surface area available and making it difficult to understand the different performances between single or aggregated systems.[62] Regarding the use of H_2O_2, previous research has demonstrated that the concentrations of 1% H_2O_2 decreased from 10 000 ppm to less than 2 ppm after 24 h long treatment with hematite microrobots, which is lower than 8 ppm, the allowed limit of H_2O_2 in drinking water. Consequently, it can be concluded that H_2O_2 does not introduce new pollution to the water system.[28]

CONCLUSION

In summary, we have demonstrated the influence of hematite/Pt microrobots shapes on their self-assembly behaviors. Because of the asymmetrical magnetic dipole moment orientation in the crystal, cubic hematite/Pt microrobots can self-assemble into regular microchains with morphologies different from those of walnut-like microrobots, which solely display random aggregation. Taking advantage of the intriguing collective behavior, we have also developed light-powered microchains composed of individual cubic hematite/Pt microrobots, exhibiting autonomous locomotion under UV-light irradiation in a low concentration of H_2O_2. These microchains demonstrate different types of self-propulsion depending on the various possible mutual orientations of the microrobots during the self-assembly, as well as reconfigurable capability after an external magnetic field was employed to break the formation of self-assembled chains. To prove the exceptional benefits of a collective behavior compared to that of individual microrobots, these light-powered self-assembled microchains are employed for yeast cells' capture, release, and transport, for the capture and removal of suspended matter in water originated from personal care products, and for the definitive degradation of polymeric materials. This work offers a different perspective on the collective behavior of photocatalytic microrobots with the benefits of easy batch fabrication, low-cost, and a broad range of multimodal applications.

EXPERIMENTAL SECTION

Synthesis of Walnut-like Hematite Microparticles. Walnut-like hematite microparticles were prepared by a one-step hydrothermal reaction. In brief, $FeCl_3$ (Alfa Aesar, 98%) was added to deionized water (DI water, 18 MΩ cm) to form a 1 M homogeneous solution under magnetic stirring. Then, the solution was transferred into a 50 mL Teflon-lined stainless-steel autoclave, heated at 160 °C for 20 h, and cooled to room temperature naturally. Afterward, the product was collected by centrifugation and washed with DI water and ethanol several times. Finally, it was dried in a vacuum oven at 60 °C for 12 h.

Synthesis of Cubic-Shaped Hematite Particles. For cubic hematite microparticles, in a typical synthesis, 2.45 g $FeCl_3$ (Alfa Aesar, 98%) and 1.2 g of hexamethylenetetramine (Sigma-Aldrich, 99.5%) were directly dissolved in a 30 mL mixture of ethanol and DI water (1:1 v/v) with vigorous magnetic stirring. Subsequently, 3 wt % $CuCl_3$ (Alfa Aesar, 98%) was added to the above solution. After 30 min of stirring, the mixture was transferred into a Teflon-lined stainless-steel autoclave and heated at 160 °C for 12 h. After that, the autoclave was cooled naturally to room temperature. The resultant precipitate was collected by centrifugation, washed several times with DI water and ethanol, and then dried at 80 °C in a vacuum oven for 8 h. For nanosized cubic hematite, 2.45 g $FeCl_3$ (Alfa Aesar, 98%) and 1.2 g of hexamethylenetetramine (Sigma-Aldrich, 99.5%) were directly dissolved in a 30 mL mixture of ethanol and DI water (1:1 v/v) with vigorous magnetic stirring. After 30 min of stirring, the mixture was transferred into a Teflon-lined stainless-steel autoclave and heated at 160 °C for 10 h. After that, the autoclave was cooled naturally to room temperature. The resultant precipitate was collected by centrifugation, washed several times with DI water and ethanol, and then dried at 80 °C in a vacuum oven for 8 h.

Synthesis of Rod-Shaped Hematite Microparticles. An NaOH solution (90 mL of 6 N) was added to 100 mL of a well-stirred 2 M $FeCl_3$ solution in a 200 mL Pyrex bottle for 5 min, followed by the addition of 10 mL of 0.6 M Na_2SO_4 solution, and the agitation was continued for additional 10 min. The tightly stoppered bottle containing the $Fe(OH)_3$ gel, which consisted nominally of 0.9 mol dm^{-3} $Fe(OH)_3$, 0.1 mol dm^{-3} Fe^{3+}, and 10^{-2} mol dm^{-3} SO_4^{2-}, was placed in an oven preheated to 100 °C, and the gel was aged for 8 days.

Preparation of Hematite/Pt Janus Microrobots. The synthesized hematite microparticles were suspended in DI water (5 mg mL^{-1}) and dispersed by sonication. The suspension was dropped by a pipette on glass slides and dried overnight. A 30 nm thin Pt layer was asymmetrically deposited on hematite microparticles by the sputtering method. The real-time thickness of the sputtered Pt layer was controlled by a quartz crystal microbalance. After the sputtering process, microrobots were released using a scalpel.

Microrobots Morphological, Chemical, And Structural Characterization. Scanning electron microscopy (SEM) images of hematite microparticles and hematite/Pt Janus microrobots were obtained with a Tescan MIRA 3 XMU instrument. For SEM imaging of self-assembled microchains, hematite microrobots were dispersed in DI water, and sonicated for 5 min. Then, 100 μL of the suspended solution was placed on a glass slide under the microscope. After hematite microrobots were observed to assemble into microchains, the solution on the glass slide was quickly dried under irradiation of a LED lamp (100 W). Finally, this glass slide was moved to the chamber of a Tescan MIRA 3 XMU instrument. Energy-dispersive X-ray spectroscopy (EDX) mapping analysis was performed using an Oxford EDX detector connected to the SEM. The XRD patterns of the products were examined by a Rigaku SmartLab 3 kW diffractometer, equipped with a fine focus Cu sealed tube operating at 40 kV and 30 mA.

Motion Experiments. A Nikon ECLIPSE TS2R inverted microscope coupled with a Basler digital camera acA1920-155uc was used to record the microrobots' motion. Briefly, a microrobot aqueous suspension was dropped on a glass slide. Different concentrations of H_2O_2 (Merck, 30%) were subsequently added to the drop to study microrobot motion in 0, 0.1, and 1% H_2O_2. All experiments were carried out in the absence of surfactants. Then, the microrobots were activated by a 365 nm UV LED (Cool LED pE-100) operated at a measured light intensity of 1.6 W cm^{-2}. Videos were recorded at 20 fps and analyzed to obtain microrobot tracks and calculate their speed through NIS Elements Advanced Research software.

Electrochemical Measurements. Tafel experiments were carried out using a customized photoelectrochemical setup with a 365 nm UV LED (700 mA powered LZ4−04UV00, LedEngin Inc.) in the two-electrode configuration with either hematite electrode or Pt electrode as working electrodes and an Ag/AgCl electrode as both the reference and counter electrode. The hematite working electrode was made by dropping 100 μL of a 5 mg mL^{-1} aqueous suspension of walnut-like or cubic hematite microparticles on commercial ITO-covered glass slides (1×2 cm^2, Sigma-Aldrich, 8−12 Ω sq^{-1}) and overnight drying. The Pt working electrode was obtained by sputtering a 30 nm thin Pt layer on an ITO-covered glass slide. Tafel measurements were recorded at a scan rate of 5 mV s^{-1} from −0.2 to 0.6 V vs Ag/AgCl under UV-light irradiation on the working electrodes (1×1 cm^2 immersed area) in DI water using a Metrohm AUTOLAB potentiostat.

Numerical Simulation. The numerical simulation was performed using the transport of the diluted species module of the COMSOL Multiphysics software for the cross-section of two (or six) adjacent hematite/Pt Janus microrobots. Each microrobot was designed as a square with a size of 2 μm × 2 μm. The H_2O generation at the interface between Pt and H_2O_2 due to the photogenerated electron−hole pairs in hematite was simulated. For this purpose, one of the four sides of each square was considered the generation one to emulate the face of the microrobot coated by the Pt layer. The most significant configurations of the two microrobots have been taken into account in the simulation (or their combinations for the simulation with six microrobots). To calculate the H_2O diffusion for 0.1 s light irradiation, an H_2O diffusion coefficient in water at 25 °C of 2.99×10^{-9} m^2 s^{-1} was used, while the photogeneration rate was set to 1 mmol m^{-2} s^{-1}.

Magnetic Experiment. Magnetic field-controlled navigation experiments were performed using a homemade magnetic controller system consisting of three orthogonal coil pairs in a 3D-printed polylactic acid (PLA) backbone, which generates a transversal rotating magnetic field. Navigation experiments were performed with an applied magnetic field of 3 mT at the frequency of 10 Hz inside a 100 μm wide microfluidic channel. Videos were recorded by using a Nikon ECLIPSE TS2R inverted microscope and Pylon Viewer software at 20 fps.

Yeast Cells Transport. Five grams of commercial yeast extract was suspended in 200 mL of distilled water under magnetic stirring for 10 min. Then, the solution was moved to an autoclave and heated at 121 °C for 15 min. After that, the broth was vortexed briefly to disperse yeast cells and immediately moved to a temperature-controlled shaking incubator at 300 rpm for 4 h at 37 °C. Yeast cells were centrifuged at 5000 rpm for 5 min to remove the culture media and then transferred in DI water (see the referenced protocol in the Supporting Information). An aqueous diluted yeast suspension (5 μL) and a suspension of the cubic hematite microrobots (5 μL, 1 mg mL^{-1}) were placed onto a glass slide to record the videos at a final concentration of 0.1% H_2O_2.

Removal of Suspended Matter in Water. One gram of commercial toothpaste was dissolved in 200 mL water. Then, a vacuum filtration device was used to filter the solution. A membrane (Whatman membrane filter) with 0.2 μm holes was used. After the filtration, the extracts were washed with distilled water three times. The final products were obtained after drying in a vacuum oven for 5 h. For the removal of suspended matter, 5 μL of the resulting solution (2 mg mL^{-1}), 5 μL cubic hematite microrobots (3 mg mL^{-1}), and 5 μL 0.1% H_2O_2 (the final concentration) were mixed to a clean glass slide to record videos.

PEG Photodegradation. The photocatalytic degradation ability of microrobots was evaluated through the degradation of polyethylene glycol (PEG, M_w 4000, Alfa Aesar) under UV-light irradiation. One milligram of PEG 4000 and 1 mg of microrobots were added to 1 mL of 1% H_2O_2 solution in a disposable cuvette. The cuvette was irradiated for 24 h using a 365 nm UV LED lamp (9 W) as the light source. Similarly, three control samples were prepared: (i) without the addition of microrobots; (ii) UV-light irradiation without H_2O_2 and microrobots; (iii) 1% H_2O_2 without UV-light irradiation and microrobots. After the degradation experiments, all solutions were centrifugated at 3500 rpm for 5 min to separate the solution from the microrobots for further analyses. The PEG 4000 degradation was evaluated by UltrafleXtreme Matrix-Assisted Laser Desorption/Ionization Mass Spectrometry (MALDI-MS, Bruker Daltonics, Bremen, Germany) operated in linear positive detection mode following the protocol of a previous paper.[25]

ASSOCIATED CONTENT

Supporting Information

The Supporting Information is available free of charge at https://pubs.acs.org/doi/10.1021/acsnano.1c11136.

> Normalized XRD patterns of hematite microparticles with walnut-like and cubic shapes; schematic illustration of the photocatalytic activation and their self-propulsion mechanism; the magnetic dipole moment orientation in a walnut-like hematite microparticle; SEM images after 10 min of observation; SEM and EDX elemental mapping images of rod-shaped and nanosized cubic hematite particles; collective behavior of rod-shaped and nanosized cubic microrobots in pure water in the

absence of UV-light irradiation after 5 min observation; snapshots showing the formation process of self-assembled microchains with time in pure water in the presence and absence of UV-light irradiation; self-assembly of cubic hematite microparticles in water without light irradiation; simulation of the 2D spatial distribution of H_2O; magnetic hysteresis loop of bare hematite microcubes; optical images showing the behavior of microchains under a transversal rotating magnetic field inside a microfluidic channel; SEM images of suspended matter extracted from a commercial toothpaste; original time-lapse images of a self-assembled microchain for the removal of suspended matter under UV-light irradiation in 0.1% H_2O_2; MALDI-MS spectra of PEG treated for 24 h under UV-light irradiation and 1% H_2O_2, in 1% H_2O_2 and no UV light, and in UV-light irradiation with no H_2O_2 (PDF)

Hematite/Pt microrobots in 0.1% H_2O_2 under UV-light irradiation (AVI)

Collective behaviors of walnut-like and cubic microrobots (AVI)

Self-assembly process of cubic hematite microrobots (AVI)

Different motion modes of cubic hematite microchains under UV-light irradiation in 0.1% H_2O_2 (AVI)

Reconfigurable capability of cubic hematite microrobots (AVI)

Interactions of single cubic hematite microrobots and yeast cells under UV-light irradiation in 0.1% H_2O_2 (AVI)

Interactions of self-assembled microchains and yeast cells under UV-light irradiation in 0.1% H_2O_2 (AVI)

Self-assembled microchain for removal of suspended matter under UV-light irradiation in 0.1% H_2O_2 (AVI)

AUTHOR INFORMATION

Corresponding Author

Martin Pumera − *Future Energy and Innovation Laboratory, Central European Institute of Technology, Brno University of Technology, 61200 Brno, Czech Republic; Department of Medical Research, China Medical University Hospital, China Medical University, Taichung, Taiwan 40402, ROC; Department of Chemical and Biomolecular Engineering, Yonsei University, 03722 Seoul, Korea;* orcid.org/0000-0001-5846-2951; Email: martin.pumera@ceitec.vutbr.cz

Authors

Xia Peng − *Future Energy and Innovation Laboratory, Central European Institute of Technology, Brno University of Technology, 61200 Brno, Czech Republic*

Mario Urso − *Future Energy and Innovation Laboratory, Central European Institute of Technology, Brno University of Technology, 61200 Brno, Czech Republic*

Martina Ussia − *Future Energy and Innovation Laboratory, Central European Institute of Technology, Brno University of Technology, 61200 Brno, Czech Republic*

Complete contact information is available at: https://pubs.acs.org/10.1021/acsnano.1c11136

Author Contributions

X.P. performed the fabrication of the microrobots, recorded and analyzed their motion, performed SEM-EDX analysis and Tafel measurements, carried out the cargo transportation experiments, and interpreted the data. M. Urso designed the experiments, performed the numerical simulation, and contributed to data interpretation. M. Ussia contributed to the degradation experiment and analyzed the data. M.P. originated the idea. M.P. and M. Urso supervised the project. All authors contributed to writing the manuscript.

Notes

The authors declare no competing financial interest.

ACKNOWLEDGMENTS

M.P. was supported by the Ministry of Education, Youth and Sports (Czech Republic) grant LL2002 under the ERC CZ program and by the Ministry of Health of the Czech Republic (NU21-08-00407). X.P. was supported by the China Scholarship Council (CSC No. 202008320382) and acknowledges the grant CEITEC VUT-K-22-7678, financed from Quality Internal Grants of BUT Reg. No. CZ.02.2.69/0.0/0.0/19_073/0016948. M. Urso acknowledges the financial support by the European Union's Horizon 2020 research and innovation program under the Marie Skłodowska-Curie grant agreement No. 101038066. The CzechNanoLab project LM2018110 funded by MEYS CR is gratefully acknowledged for the financial support of the measurements/sample fabrication at CEITEC Nano Research Infrastructure. CIISB, Instruct-CZ Centre of Instruct-ERIC EU consortium, funded by MEYS CR infrastructure project LM2018127, is gratefully acknowledged for the financial support of the measurements at the CEITEC Proteomics Core Facility.

REFERENCES

(1) Jin, D.; Yu, J.; Yuan, K.; Zhang, L. Mimicking the Structure and Function of Ant Bridges in a Reconfigurable Microswarm for Electronic Applications. *ACS Nano* **2019**, *13*, 5999−6007.

(2) Garattoni, L.; Birattari, M. Autonomous Task Sequencing in a Robot Swarm. *Sci. Robot.* **2018**, *3*, No. eaat0430.

(3) Rubenstein, M.; Cornejo, A.; Nagpal, R. Programmable Self-assembly in a Thousand-robot Swarm. *Science* **2014**, *345*, 795−800.

(4) Soto, F.; Karshalev, E.; Zhang, F.; Avila, B.; Wang, J. Smart Materials for Microrobots. *Chem. Rev.* **2022**, *122*, 5365−5403.

(5) Wang, H.; Moo, J.; Pumera, M. From Nanomotors to Micromotors: The Influence of the Size of an Autonomous Bubble-Propelled Device upon Its Motion. *ACS Nano* **2016**, *10*, 5041−5050.

(6) Ussia, M.; Pumera, M. Towards Micromachine Intelligence: Potential of Polymers. *Chem. Soc. Rev.* **2022**, *51*, 1558−1572.

(7) Zhou, H.; Mayorga-Martinez, C.; Pané, S.; Zhang, L.; Pumera, M. Magnetically Driven Micro and Nanorobots. *Chem. Rev.* **2021**, *121*, 4999−5041.

(8) Llopis-Lorente, A.; García-Fernandez, A.; Murillo-Cremaes, N.; Hortelao, A.; Patiño, T.; Villalonga, R.; Sancenon, F.; Martínez-Mañez, R.; Sanchez, S. Enzyme-Powered Gated Mesoporous Silica Nanomotors for On-Command Intracellular Payload Delivery. *ACS Nano* **2019**, *13*, 12171−12183.

(9) Pané, S.; Wendel-Garcia, P.; Belce, Y.; Chen, X.; Puigmartí-Luis, J. Powering and Fabrication of Small-Scale Robotics Systems. *Curr. Robot. Rep.* **2021**, *2*, 427−440.

(10) Li, J.; Yu, X.; Xu, M.; Liu, W.; Sandraz, E.; Lan, H.; Wang, J.; Cohen, M. Metal-organic Frameworks as Micromotors with Tunable Engines and Brakes. *J. Am. Chem. Soc.* **2017**, *139*, 611−614.

(11) Wang, Q.; Dong, R.; Wang, C.; Xu, S.; Chen, D.; Liang, Y.; Ren, B.; Gao, W.; Cai, Y. Glucose-Fueled Micromotors with Highly

Efficient Visible-Light Photocatalytic Propulsion. *ACS Appl. Mater. Interfaces* **2019**, *11*, 6201−6207.

(12) Ma, X.; Wang, X.; Hahn, K.; Sánchez, S. Motion Control of Urea-Powered Biocompatible Hollow Microcapsules. *ACS Nano* **2016**, *10*, 3597−3605.

(13) Pourrahimi, A. M.; Villa, K.; Palenzuela, C. L.; Ying, Y.; Sofer, Z.; Pumera, M. Catalytic and Light-Driven ZnO/Pt Janus Nano/Micromotors: Switching of Motion Mechanism via Interface Roughness and Defect Tailoring at the Nanoscale. *Adv. Funct. Mater.* **2019**, *29*, 1808678.

(14) Lin, Z.; Fan, X.; Sun, M.; Gao, C.; He, Q.; Xie, H. Magnetically Actuated Peanut Colloid Motors for Cell Manipulation and Patterning. *ACS Nano* **2018**, *12*, 2539−2545.

(15) Xu, T.; Soto, F.; Gao, W.; Garcia-Gradilla, V.; Li, J.; Zhang, X.; Wang, J. Ultrasound-Modulated Bubble Propulsion of Chemically Powered Microengines. *J. Am. Chem. Soc.* **2014**, *136*, 8552−8555.

(16) Urso, M.; Iffelsberger, C.; Mayorga-Martinez, C. C.; Pumera, M. Nickel Sulfide Microrockets as Self-Propelled Energy Storage Devices to Power Electronic Circuits 'On-Demand. *Small Methods* **2021**, *5*, 2100511.

(17) Oral, C. M.; Ussia, M.; Pumera, M. Self-Propelled Activated Carbon Micromotors for 'on-the-Fly' Capture of Nitroaromatic Explosives. *J. Phys. Chem. C* **2021**, *125*, 18040−18045.

(18) Muñoz, J.; Urso, M.; Pumera, M. Self-Propelled Multifunctional Microrobots Harboring Chiral Supramolecular Selectors for 'Enantiorecognition-on-the-Fly'. *Angew. Chemie - Int. Ed.* **2022**, *61*, e202116090.

(19) Oral, C. M.; Ussia, M.; Yavuz, D. K.; Pumera, M. Shape Engineering of TiO_2 Microrobots for 'On-the-Fly' Optical Brake. *Small* **2022**, *18*, 2106271.

(20) Gao, W.; D'Agostino, M.; Garcia-Gradilla, V.; Orozco, J.; Wang, J. Multi-fuel Driven Janus Micromotors. *Small* **2013**, *9*, 467−471.

(21) Eskandarloo, H.; Kierulf, A.; Abbaspourrad, A. Light-harvesting Synthetic Nano- and Micromotors: A Review. *Nanoscale* **2017**, *9*, 12218−12230.

(22) Jurado-Sánchez, B.; Pacheco, M.; Maria-Hormigos, R.; Escarpa, A. Perspectives on Janus Micromotors: Materials and Applications. *Appl. Mater. Today* **2017**, *9*, 407−418.

(23) Jurado-Sánchez, B.; Pacheco, M.; Rojo, J.; Escarpa, A. Magnetocatalytic Graphene Quantum Dots Janus Micromotors for Bacterial Endotoxin Detection. *Angew. Chemie - Int. Ed.* **2017**, *56*, 6957−6961.

(24) Dong, R.; Zhang, Q.; Gao, W.; Pei, A.; Ren, B. Highly Efficient Light-Driven TiO_2-Au Janus Micromotors. *ACS Nano* **2016**, *10*, 839−844.

(25) Ussia, M.; Urso, M.; Dolezelikova, K.; Michalkova, H.; Adam, V.; Pumera, M. Active Light-Powered Antibiofilm ZnO Micromotors with Chemically Programmable Properties. *Adv. Funct. Mater.* **2021**, *31*, 2101178.

(26) Pourrahimi, A. M.; Villa, K.; Ying, Y.; Sofer, Z.; Pumera, M. ZnO/ZnO_2 /Pt Janus Micromotors Propulsion Mode Changes with Size and Interface Structure: Enhanced Nitroaromatic Explosives Degradation under Visible Light. *ACS Appl. Mater. Interfaces* **2018**, *10*, 42688−42697.

(27) Peng, X.; Zhu, H.; Chen, H.; Feng, X.; Liu, R.; Huang, Z.; Shen, Q.; Ma, Y.; Wang, L. Eco-friendly Porous Iron(III) Oxide Micromotors for Efficient Wastewater Cleaning. *New J. Chem.* **2019**, *43*, 12594−12600.

(28) Urso, M.; Ussia, M.; Pumera, M. Breaking Polymer Chains with Self-Propelled Light-Controlled Navigable Hematite Microrobots. *Adv. Funct. Mater.* **2021**, *31*, 2101510.

(29) Dong, R.; Hu, Y.; Wu, Y.; Gao, W.; Ren, B.; Wang, Q.; Cai, Y. Visible-Light-Driven BiOI-Based Janus Micromotor in Pure Water. *J. Am. Chem. Soc.* **2017**, *139*, 1722−1725.

(30) Xiao, Z.; Chen, J.; Duan, S.; Lv, X.; Wang, J.; Ma, X.; Tang, J.; Wang, W. Bimetallic Coatings Synergistically Enhance the Speeds of Photocatalytic TiO_2 Micromotors. *Chem. Commun.* **2020**, *56*, 4728−4731.

(31) Maric, T.; Nasir, M. Z.; Webster, R. D.; Pumera, M. Tailoring Metal/TiO_2 Interface to Influence Motion of Light-Activated Janus Micromotors. *Adv. Funct. Mater.* **2020**, *30*, 1908614.

(32) Kong, L.; Rohaizad, N.; Nasir, M.; Guan, J.; Pumera, M. Micromotor-Assisted Human Serum Glucose Biosensing. *Anal. Chem.* **2019**, *91*, 5660−5666.

(33) Gao, W.; Dong, R.; Thamphiwatana, S.; Li, J.; Gao, W.; Zhang, L.; Wang, J. Artificial Micromotors in the Mouse's Stomach: A Step toward in Vivo Use of Synthetic Motors. *ACS Nano* **2015**, *9*, 117−123.

(34) Mayorga-Martinez, C.; Zelenka, J.; Grmela, J.; Michalkova, H.; Ruml, T.; Mareš, J.; Pumera, M. Swarming Aqua Sperm Micromotors for Active Bacterial Biofilms Removal in Confined Spaces. *Adv. Sci.* **2021**, *8*, 2101301.

(35) Peng, X.; Urso, M.; Pumera, M. Photo-Fenton Degradation of Nitroaromatic Explosives by Light-Powered Hematite Microrobots: When Higher Speed Is Not What We Go For. *Small Methods* **2021**, *5*, 2100617.

(36) Jin, D.; Yuan, K.; Du, X.; Wang, Q.; Wang, S.; Zhang, L. Domino Reaction Encoded Heterogeneous Colloidal Microswarm with On-Demand Morphological Adaptability. *Adv. Mater.* **2021**, *33*, 2100070.

(37) Vaghasiya, J.; Mayorga-Martinez, C.; Matějková, S.; Pumera, M. Pick up and Dispose of Pollutants from Water via Temperature-Responsive Micellar Copolymers on Magnetite Nanorobots. *Nat. Commun.* **2022**, *13*, 1026.

(38) Wang, H.; Pumera, M. Coordinated Behaviors of Artificial Micro/Nanomachines: From Mutual Interactions to Interactions with the Environment. *Chem. Soc. Rev.* **2020**, *49*, 3211−3230.

(39) Lu, C.; Tang, Z. Advanced Inorganic Nanoarchitectures from Oriented Self-Assembly. *Adv. Mater.* **2016**, *28*, 1096−1108.

(40) Yan, J.; Bloom, M.; Bae, S. C.; Luijten, E.; Granick, S. Linking Synchronization to Self-assembly Using Magnetic Janus Colloids. *Nature* **2012**, *491*, 578−581.

(41) Yu, J.; Yang, L.; Zhang, L. Pattern Generation and Motion Control of a Vortex-like Paramagnetic Nanoparticle Swarm. *Int. J. Rob. Res.* **2018**, *37*, 912−930.

(42) Snezhko, A.; Aranson, I. S. Magnetic Manipulation of Self-assembled Colloidal Asters. *Nat. Mater.* **2011**, *10*, 698−703.

(43) Breen, T. L.; Tien, J.; Scott, R.; Hadzic, T.; Whitesides, G. M. Design and Self-Assembly of Open, Regular, 3D Mesostructures. *Science* **1999**, *284*, 948−951.

(44) Gobre, V. V.; Tkatchenko, A. Scaling Laws for Van Der Waals Interactions in Nanostructured Materials. *Nat. Commun.* **2013**, *4*, 2341.

(45) Miele, E.; Raj, S.; Baraissov, Z.; Král, P.; Mirsaidov, U. Dynamics of Templated Assembly of Nanoparticle Filaments within Nanochannels. *Adv. Mater.* **2017**, *29*, 1702682.

(46) Villa, K.; Děkanovský, L.; Plutnar, J.; Kosina, J.; Pumera, M. Swarming of Perovskite-Like Bi_2WO_6 Microrobots Destroy Textile Fibers under Visible Light. *Adv. Funct. Mater.* **2020**, *30*, 2007073.

(47) Tottori, S.; Zhang, L.; Peyer, K. E.; Nelson, B. J. Assembly, Disassembly, and Anomalous Propulsion of Microscopic Helices. *Nano Lett.* **2013**, *13*, 4263−4268.

(48) Wang, W.; Castro, L. A.; Hoyos, M.; Mallouk, T. E. Autonomous Motion of Metallic Microrods Propelled by Ultrasound. *ACS Nano* **2012**, *6*, 6122−6132.

(49) Kment, S.; Schmuki, P.; Hubicka, Z.; Machala, L.; Kirchgeorg, R.; Liu, N.; Wang, L.; Lee, K.; Olejnicek, J.; Cada, M.; Gregora, I.; Zboril, R. Photoanodes with Fully Controllable Texture: The Enhanced Water Splitting Efficiency of Thin Hematite Films Exhibiting Solely (110) Crystal Orientation. *ACS Nano* **2015**, *9*, 7113−7123.

(50) Zhang, X.; Klaver, P.; Santen, R.; Sanden, M. C.; Bieberle-Hütter, A. Oxygen Evolution at Hematite Surfaces: The Impact of Structure and Oxygen Vacancies on Lowering the Overpotential. *J. Phys. Chem. C* **2016**, *120*, 18201−18208.

(51) Lee, S. H.; Liddell, C. M. Anisotropic Magnetic Colloids: A Strategy to Form Complex Structures Using Nonspherical Building Blocks. *Small* **2009**, *5*, 1957−1962.

(52) Rossi, L.; Donaldson, J.; Meijer, J.; Petukhov, A.; Kleckner, D.; Kantorovich, S.; Irvine, W.; Philipsec, A.; Sacanna, S. Self-organization in Dipolar Cube Fluids Constrained by Competing Anisotropies. *Soft Matter* **2018**, *14*, 1080−1087.

(53) Meijer, J. M.; Rossi, L. Preparation, Properties, and Applications of Magnetic Hematite Microparticles. *Soft Matter* **2021**, *17*, 2354−2368.

(54) Villa, K.; Novotný, F.; Zelenka, J.; Browne, M. P.; Ruml, T.; Pumera, M. Visible-Light-Driven Single-Component $BiVO_4$ Micromotors with the Autonomous Ability for Capturing Microorganisms. *ACS Nano* **2019**, *13*, 8135−8145.

(55) Hong, Y.; Diaz, M.; Cordova-Figueroa, U. M.; Sen, A. Light-Driven Titanium-Dioxide-Based Reversible Microfireworks and Micromotor/Micropump Systems. *Adv. Funct. Mater.* **2010**, *20*, 1568−1576.

(56) Wang, Y.; Zhou, C.; Wang, W.; Xu, D.; Zeng, F.; Zhan, C.; Gu, J.; Li, M.; Zhao, W.; Zhang, J.; Guo, J.; Feng, H.; Ma, X. Photocatalytically Powered Matchlike Nanomotor for Light-Guided Active SERS Sensing. *Angew. Chem., Int. Ed.* **2018**, *57*, 13110.

(57) Yuan, K.; Pacheco, M.; Jurado-Sánchez, B.; Escarpa, A. Design and Control of the Micromotor Swarm Toward Smart Applications. *Adv. Intell. Syst.* **2021**, *3*, 2100002.

(58) Wang, L.; Kaeppler, A.; Fischer, D.; Simmchen, J. Photocatalytic TiO_2 Micromotors for Removal of Microplastics and Suspended Matter. *ACS Appl. Mater. Interfaces* **2019**, *11*, 32937−32944.

(59) Jurado-Sánchez, B.; Wang, J. Micromotors for Environmental Applications: A Review. *Environ. Sci.: Nano* **2018**, *5*, 1530−1544.

(60) Urso, M.; Pumera, M. Nano/Microplastics Capture and Degradation by Autonomous Nano/Microrobots: A Perspective. *Adv. Funct. Mater.* **2022**, 2112120.

(61) Ussia, M.; Urso, M.; Miritello, M.; Bruno, E.; Curcuruto, G.; Vitalini, D.; Condorelli, G.; Cantarella, M.; Priviterab, V.; Carroccio, S. C. Hybrid Nickel-Free Graphene/Porphyrin Rings for Photodegradation of Emerging Pollutants in Water. *RSC Adv.* **2019**, *9*, 30182−30194.

(62) Shahzad, K.; Aeken, W. V.; Mottaghi, M.; Kamyab, V. K.; Kuhn, S. Aggregation and Clogging Phenomena of Rigid Microparticles in Microfluidics. *Microfluid. Nanofluid.* **2018**, *22*, 104.

9. Biohybrid magnetically driven microrobots for sustainable removal of micro/nanoplastics from the aquatic environment

Paper published in this chapter:

Xia Peng, Mario Urso, Martina Kolackova, Dalibor Huska and Martin Pumera, Biohybrid magnetically-driven microrobots for sustainable removal of micro/nanoplastics from the aquatic environment. *Adv. Funt. Mater.* **2023**, *2307477*.

9.1 Motivation of this study

Microplastics, as one of the main environmental pollutants, are defined as fragments less than 5 mm in size, which do not easily sediment and frequently pass by filtration systems, holding potential threats even for marine organisms and human beings. Recently, microplastics also have been found in human stools proving that the threat is ubiquitous, not only endangering to the marine organisms. Taking advantage of active movement, it is interesting to investigate the capture and removal of microplastics by microrobots. This study aims to establish the microrobot platform for efficient and dynamic removal of micro/nanoplastics from the aquatic environment.

9.2 Paper conclusion

This study developed eco-friendly algae-based microrobots for efficient capture and removal of micro- and nanoplastics from aquatic environments. The microrobots are based on *Chlorella vulgaris*—a widely used microalga with negatively charged surfaces. By incorporating positively charged Fe_3O_4 nanoparticles, these microrobots achieved precise actuation and collective manipulation under an external magnetic field, enhancing electrostatic attraction for targeted plastic capture. The MARs (micro-algae robots) demonstrated removal efficiencies of approximately 92% for nanoplastics and 70% for microplastics. They retained ≈80% efficiency for nanoplastics and ≈54% for microplastics even after five reuse cycles. To assess their practical applicability, MARs were tested in various real-world water samples, including tap water, rainwater, and lake water.

9.3 Author contribution

I prepared and characterized the microrobots. I captured and analyzed their motion under a magnetic field, evaluating their responsiveness and performance. Additionally, I conducted experiments to test their efficiency in capturing micro- and nanoplastics in various water samples. Finally, I interpreted the data and wrote the draft of the manuscript.

RESEARCH ARTICLE

ADVANCED FUNCTIONAL MATERIALS
www.afm-journal.de

Biohybrid Magnetically Driven Microrobots for Sustainable Removal of Micro/Nanoplastics from the Aquatic Environment

*Xia Peng, Mario Urso, Martina Kolackova, Dalibor Huska, and Martin Pumera**

The proliferation of micro/nanoplastics derived from the fragmentation of plastic waste released in the environment represents an increasingly alarming issue with adverse implications for aquatic ecosystems worldwide. Conventional approaches for mitigating such contamination are inadequate in removing plastic fragments with exceptionally tiny sizes. Therefore, it is highly urgent to develop efficient strategies to address the threats posed by micro/nanoplastics. Here, biohybrid microrobots, integrating the magnetic properties of Fe_3O_4 nanoparticles, are investigated for the dynamic removal of micro/nanoplastics from various aquatic environments via high-precision magnetic actuation and reliable electrostatic interactions. After the surface decoration with Fe_3O_4 nanoparticles, algae cells can achieve precise locomotion and wireless manipulation by regulating an external magnetic field. Taking advantage of this active movement, magnetic algae robots (MARs) display considerable capture and removal efficiencies for micro/nanoplastics in water with extensive application scenarios. The reusability of MARs is also investigated, proving great recyclable performance. The growth and cell viability experiments elucidate that the presence of Fe_3O_4 nanoparticles may result in hormesis stimulation of algae growth. Such recyclable microrobots with eco-friendly and low-cost characteristics offer an attractive strategy for sustainably tackling micro/nanoplastics pollution.

1. Introduction

Plastics are synthetic polymers composed of hundreds to thousands of organic subunits known as monomers, which are interconnected through robust covalent bonds.[1] Their exceptional properties, characterized by high chemical and thermal stability, have led to widespread utilization, while simultaneously presenting a significant obstacle in terms of their environmental management and elimination. Nowadays, the rampant abuse of plastics coupled with inadequate disposal measures has led to a dire situation.[2,3] Undesirably, large plastic waste can disintegrate into minute pieces, microplastics (<5 mm in size) and nanoplastics (<1000 nm in size), which have become a growing global concern due to their harmful effects on aquatic organisms and human beings.[4–6] Microplastics tend to settle and accumulate on the seafloor. Nanoplastics, due to their buoyancy, remain suspended in water and disperse rapidly under the influence of

---

X. Peng, M. Urso, M. Pumera
Future Energy and Innovation Laboratory
Central European Institute of Technology
Brno University of Technology
Purkynova 123, Brno 61200, Czech Republic
E-mail: martin.pumera@ceitec.vutbr.cz

M. Kolackova, D. Huska
Department of Chemistry and Biochemistry
Mendel University in Brno
Zemedelska 1, Brno 61300, Czech Republic

M. Pumera
Department of Medical Research
China Medical University Hospital
China Medical University
No. 91 Hsueh-Shih Road, Taichung TW-40402, Taiwan

M. Pumera
Advanced Nanorobots & Multiscale Robotics Laboratory
Faculty of Electrical Engineering and Computer Science
VSB – Technical University of Ostrava
17. listopadu 2172/15, Ostrava 70800, Czech Republic

M. Pumera
Department of Chemical and Biomolecular Engineering
Yonsei University
50 Yonsei-ro, Seodaemun-gu, Seoul 03722, South Korea

The ORCID identification number(s) for the author(s) of this article can be found under https://doi.org/10.1002/adfm.202307477

DOI: 10.1002/adfm.202307477

marine currents.[7] In the marine realm, the ingestion of micro/nanoplastics by fish and other aquatic organisms can result in physical harm and impede their digestive and reproductive processes. The unfortunate consequence of this phenomenon is the suffering and eventual death of these creatures.[8,9] Furthermore, the absorption of toxic substances by micro/nanoplastics, due to their high surface-to-volume ratio, can pose a risk to human health by transferring these harmful chemicals up the food chain.[4,8–11] Thus, there is a pressing need to address the pervasiveness of plastic pollution, specifically the proliferation of micro/nanoplastics in the environment. In light of this, conventional methods, such as physical removal methods (i.e., filtration and sedimentation)[12–14] and chemical degradation methods (i.e., chemical oxidation and photodegradation)[15–18] have been explored for the treatment of micro/nanoplastics in the environment, which are generally limited by low efficiencies and lack of accessible and cheap characterization means because of the tiny size of micro/nanoplastics.

The advent of micro/nanorobots, which synergistically integrate the exceptional physical–chemical attributes of micro/nanomaterials with powerful locomotion and allow exactitude in positional control,[19–22] is transforming a plethora of application domains, such as biomedicine,[23–25] sensing,[26–28] imaging,[29,30] and environmental remediation.[31–34] In the past decades, diverse micro/nanorobots actuated by light,[35,36] chemical fuels,[37] and magnetic fields[38,39] have been developed to tackle the threats posed by micro/nanoplastics. Photocatalytic Au@Ni@TiO_2 micromotors could remove microplastics via phoretic interaction by individual micromotors in a low amount of H_2O_2 or shoveling interaction due to the assembled microchains of several micromotors under the control of magnetic fields.[35] Light-powered multi-layered TiO_2/Pt microrobots display negative photogravitaxis, leading to a strong, fuel-free motion in three dimensions when exposed to light. With a distinctive blend of self-propulsion and adjustable Zeta potential, these microrobots swiftly draw and capture nanoplastics on their surfaces, even within the gaps among stacked layers.[40] Moreover, the bubble separation of microplastics was achieved by chemically driven core–shell MnO_2-based micromotors in the presence of H_2O_2.[37] Recently, autonomous magnetorobots consisting of ion-exchange resin spheres and paramagnetic Fe_3O_4 nanoparticles were demonstrated for removing or separating micro/nanoplastics from nonmarine waters.[38] Similarly, well-designed adhesive PDA@Fe_3O_4 MagRobots demonstrated robust adhesion to microplastic pollutants in moist aquatic environments, facilitating efficient capture, transport, and retrieval of microplastic contaminants under the influence of an external rotating magnetic field.[39] Nevertheless, the involvement of chemical fuels may lead to secondary contamination of the environment, and the fabrication cost of microrobots comprising noble metals such as Au and Pt is relatively expensive, making it unfavorable for large-scale production and viable implementation. More importantly, exploring inexhaustible resources from the natural world to address micro/nanoplastics elimination represents a research topic worthy of investigation.

Here, we demonstrate biohybrid microrobots integrating algae platforms and magnetic nanoparticles for active capture and removal of micro/nanoplastics from aquatic environments with excellent sustainability and ease of scaling, as illustrated in **Figure 1**. *Chlorella vulgaris* (*C. vulgaris*), which represents one of the most important microalgae in various biotechnology fields,[41] was selected as the structural platform of the microrobots. Through decorating the algae surface with Fe_3O_4 nanoparticles , the resulting MARs exhibited active motion under wireless magnetic manipulation with a rapid on/off response to the applied magnetic field, without the involvement of chemical fuel and noble metals. The enhanced replication capability of algae with 0.3 $mg{\bullet}mL^{-1}$ Fe_3O_4 nanoparticles revealed the hormesis effect on the algae growth rather than higher toxicity. Biohybrid MARs were applied to capture and remove micro/nanoplastics thanks to their active movement and electrostatic interactions. Improved efficiency for capturing nanoplastics than microplastics was demonstrated and attributed to the much smaller surface area of nanoplastics, allowing MARs to capture a larger number of plastic particles. Such magnetic microrobots also display practical utilization in different aquatic environments, endowing them as promising candidates for real-world applications in the future.

2. Results and Discussion

2.1. Fabrication and Characterization of MARs

The proposed construction process of magnetic algae robots (MARs) is conceptually illustrated in **Figure 2**a. Taking advantage of negative surface charges resulting from the carboxylic (—COOH) group on the algae cytomembrane,[42] the algae surface was partially decorated with oppositely charged magnetic Fe_3O_4 nanoparticles, leading to MARs. The morphology of bare algae and MARs was investigated and characterized by scanning electron microscopy (SEM) and energy-dispersive X-ray (EDX) spectroscopy mapping images. As shown in Figure 2b, the original alga cell possesses the characteristic spheroidal micro-sized structure, and the diameter is ≈3–5 μm. After mixing the algae and Fe_3O_4 nanoparticles suspensions (Figure S1a, Supporting Information), the SEM image depicted in Figure 2c suggests that the MAR preserved the original structural feature of the alga cell, while a small amount of Fe_3O_4 nanoparticles asymmetrically bound to its surface. The distribution of the element Fe confirmed that MARs were successfully decorated with Fe_3O_4 nanoparticles. To further confirm the successful contact between Fe_3O_4 nanoparticles and bare algae cells, X-ray diffraction (XRD) patterns of Fe_3O_4 nanoparticles and MARs were measured. The peaks in the XRD pattern of Fe_3O_4 nanoparticles in Figure 2d correspond to the (220), (311), (400), (422), (511), and (440) crystalline planes of Fe_3O_4 inverse spinel structure (PDF No. 89–0691).[43] As expected, these characteristic peaks can also be appreciated in the XRD pattern of MARs. Zeta potential measurements validated the electrostatic interaction between algae and Fe_3O_4 nanoparticles. Fe_3O_4 nanoparticles exhibit a positive charge due to the interaction between Fe-OH sites on the surface of Fe_3O_4 nanoparticles and H^+ ions in the medium, resulting in the generation of positive (Fe-OH^{2+}) surface charges.[44,45] As depicted in Figure 2e, the zeta potential of algae varies from −27 to −8 mV after being integrated with Fe_3O_4 nanoparticles (18 mV).

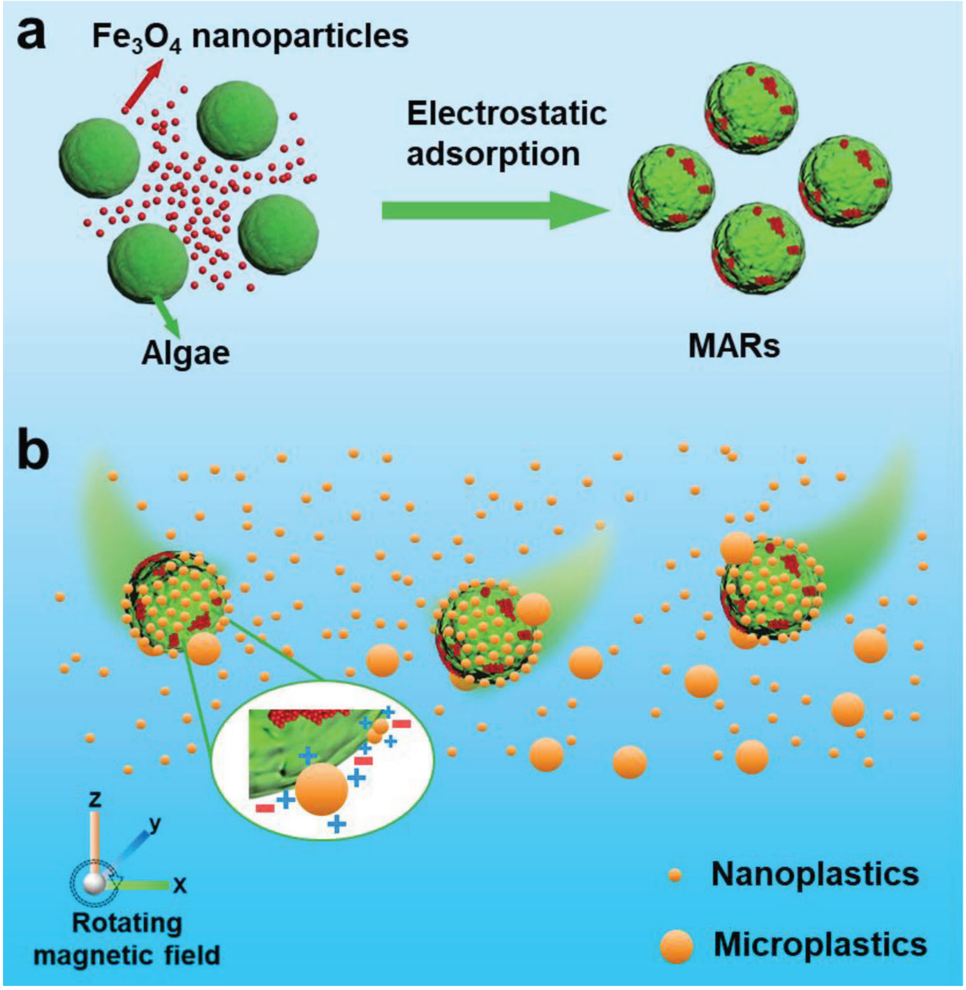

Figure 1. Biohybrid MARs for effective removal of micro/nanoplastics from water. a) Bare algae cells integrated Fe_3O_4 nanoparticles on the surface via electrostatic absorption. b) Utilizing magnetic actuation and electrostatic interactions, MARs facilitate the removal of micro/nanoplastics from water by drawing them to their surface.

2.2. Motion Behavior of MARs

Precise and controllable locomotion of microrobots is of great significance for the capture and removal of micro/nanoplastics.[34] The original *C. vulgaris* cells exhibit uncontrollable Brownian motion, as shown in Figure S2 and Movie S1 (Supporting Information). On the contrary, extracellular deposition of Fe_3O_4 nanoparticles constitutes an attractive strategy to endow the algae with excellent magnetic properties, as schematically illustrated in **Figure 3**a. The optimal concentration of Fe_3O_4 nanoparticles loading on the microalgae cells' surface was investigated as shown in Figure S3 and Movie S2 (Supporting Information). The Fe_3O_4 nanoparticles concentration of 0.3 mg mL^{-1} was identified as the optimal one for the preparation of MARs because only a few Fe_3O_4 nanoparticles-free microalgae were left in the mixture, while higher concentrations led to microalgae overloading or unbound Fe_3O_4 nanoparticles. The magnetic properties of Fe_3O_4 nanoparticles (Figure S1b, Supporting Information) and MARs were investigated by the hysteresis loop measured by a VSM. Figure 3b shows the measured magnetization curve for MARs, exhibiting 20.4 emu g^{-1} with zero coercivity, which indicates a superparamagnetic behavior.[46] In addition to being easily separated from water, untethered magnetic manipulation of MARs can be achieved by the magnetic field generated by a permanent magnet, as displayed in Figure 3c and Movie S3 (Supporting Information). Using a rotating magnetic field generated by a homemade set of orthogonal coil pairs allows exploiting several parameters to tune MARs actuation precisely, such as the magnetic field intensity and rotation frequency. MARs speed shows remarkable variation under different intensities and frequencies. In particular, Figure 3d provides the evidence that the MARs speed increases proportionally with the frequency until reaching 35 μm s^{-1} when exposed to a magnetic field intensity of 5 mT and a frequency of 30 Hz, which is commonly known as the "step-out" frequency,[47] followed by a decline since MARs cannot follow the rotation of the magnetic field at higher frequencies. The motion behavior of MARs can be easily recognized by switching on/off the magnetic field, as evidenced by the distinctive changes in the instantaneous speed over time reported in Figure 3e. The time-lapse images in Figure 3f also corroborate the controllable

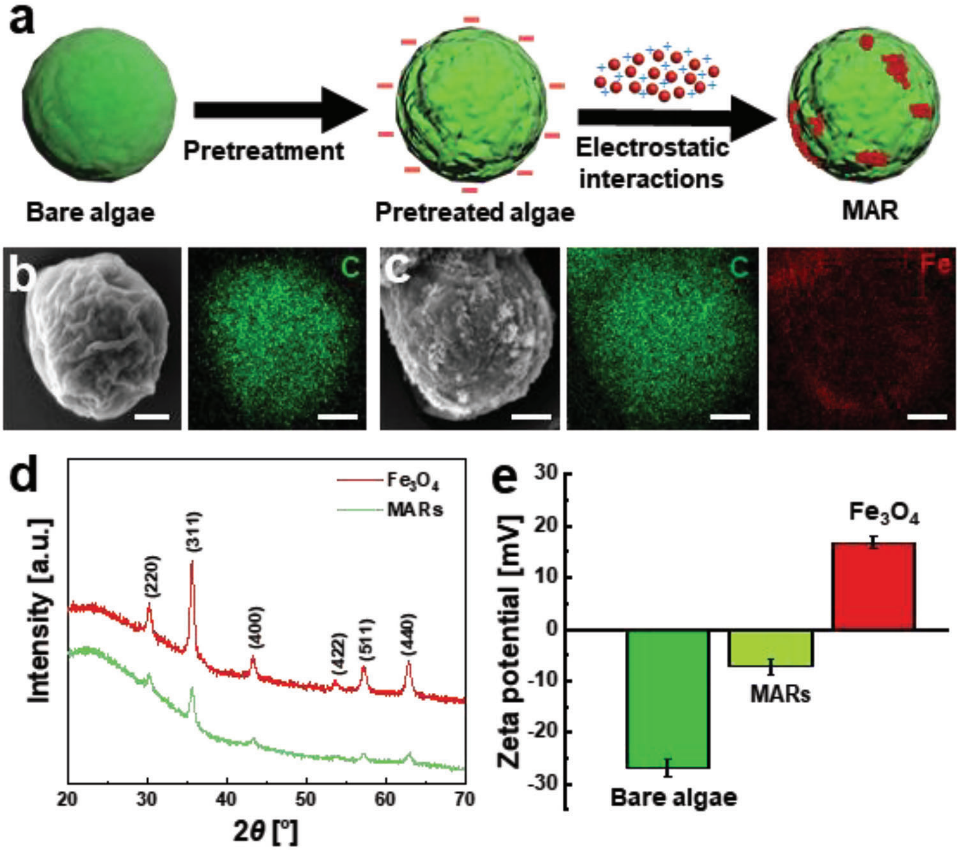

Figure 2. Preparation and characterization of MARs. a) Schematic diagram of the fabrication process. SEM and EDX elemental mapping images of: b) (a) a bare alga and c) a MAR. Scale bars are 1 µm. d) XRD patterns of Fe_3O_4 nanoparticles and MARs. e) Zeta potential of bare algae, Fe_3O_4 nanoparticles, and MARs.

actuation of MARs manipulated by the external magnetic field (Movie S4, Supporting Information).

2.3. Cell Viability of Microalgae

The growth of *C. vulgaris* cells under Fe_3O_4 nanoparticles exposure at the concentrations of 0.3 and 0.6 mg•mL^{-1} was studied. First, the growth was observed and expressed as OD750, a typical growth evaluation parameter.[48] In fact, *C. vulgaris* absorbed some Fe_3O_4, which caused interference in the measurement, resulting in false-negative results. Concurrently, it showed and confirmed the excellent capacity of *C. vulgaris* for metal accumulation, similar to previous works.[49,50] Therefore, the growth was then evaluated gravimetrically by comparing dry mass (DW) after treatment. As shown in **Figure 4**a, the dry mass of both Fe_3O_4 nanoparticles-treated *C. vulgaris* was comparable with the control. Notably, the treatment with 0.3 mg•mL^{-1} concentration of Fe_3O_4 nanoparticles significantly favored the growth process. Indeed, Fe_3O_4 nanoparticles may trigger the hormesis stimulation of *C. vulgaris*. Contrarily, a slightly reduced growth can be observed in the presence of 0.6 mg•mL^{-1} concentration of Fe_3O_4 nanoparticles, which indicates that higher doses can be more toxic, hindering the growth of microalgae.[51] To explain this behavior, different aspects and properties of the materials need to be considered since iron plays a crucial role in the cell division process.[52] Additionally, the morphology of nanoparticles or selected microalgal species may be also considered.[53] For instance, a reduced growth of *C. vulgaris*. was previously demonstrated in the presence of 0.1 mg•mL^{-1} and a higher concentration of Fe_3O_4 nanoparticles.[49] Another study revealed the highest tolerant/sublethal dose of Fe_3O_4 nanoparticles, specifically 0.05 mg•mL^{-1}, using microalgae *Coelastrella terrestris*.[54] Figure 4b, as a photo documentation supplement of the growth process, also displays the color change over time for the control sample and the Fe_3O_4 nanoparticles concentration of 0.3 mg•mL^{-1}, consistent with the results in Figure 4a. On the contrary, the color of the sample with a concentration of Fe_3O_4 nanoparticles of 0.6 mg•mL^{-1} is darker even at 0 h. Consequently, the higher amount of Fe_3O_4 nanoparticles does not allow a straightforward comparison between the results in Figure 4a and the photos in Figure 4b for the 0.6 mg•mL^{-1} Fe_3O_4 nanoparticles concentration. Although the morphology of nanoparticles may affect their toxicity in microalgal growth,[55,56] the results indicate minimal toxicity of selected Fe_3O_4 nanoparticles despite using relatively high concentrations on the growth of *C. vulgaris*. It is worth noting that the 0.3 mg•mL^{-1} Fe_3O_4 nanoparticles concentration corresponds to the growth condition of MARs whose motion and micro/nanoplastics removal has been investigated in this work.

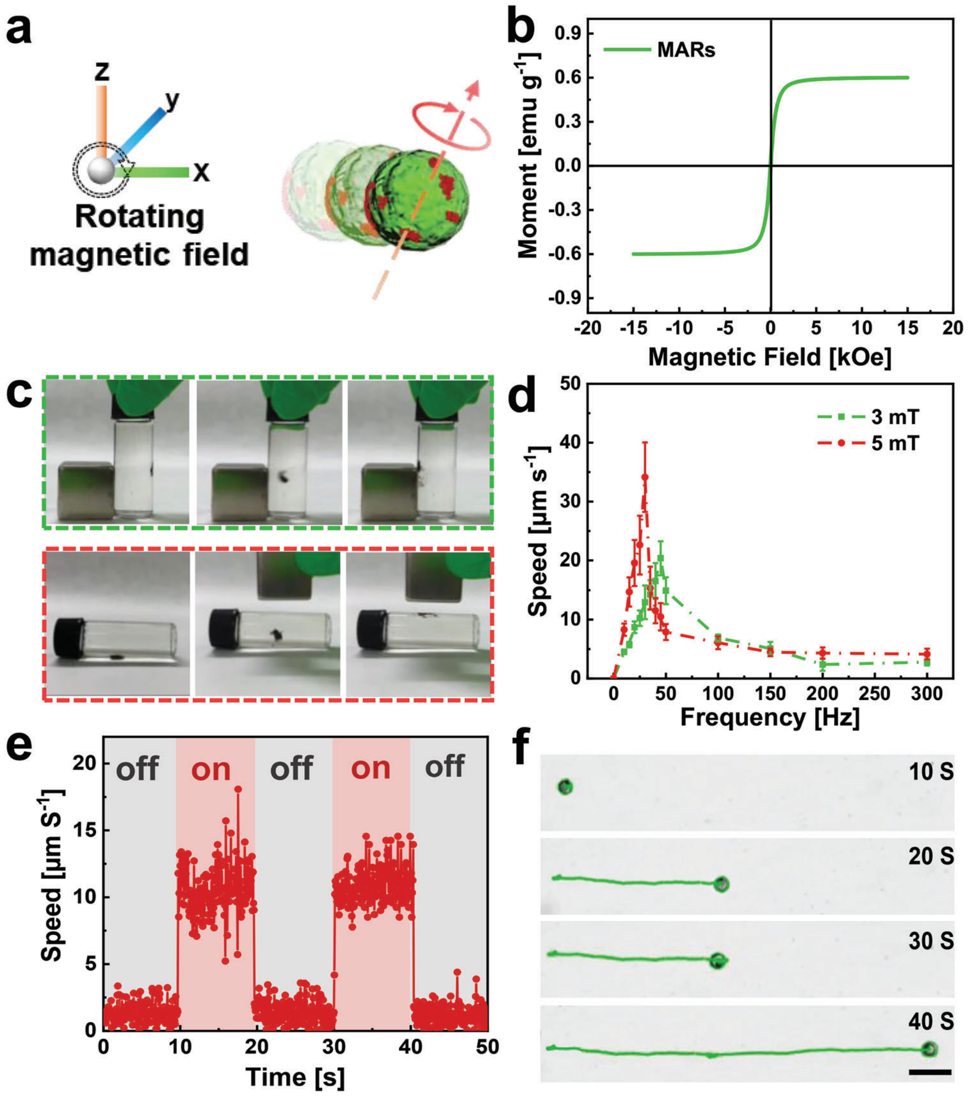

Figure 3. Magnetic motion of MARs. a) Schematic diagram of the motion principle of MARs under a rotating magnetic field. b) Magnetic hysteresis loop of MARs. c) Magnetic property of MARs using a permanent magnet promises precise manipulation by utilizing an external magnetic field. d) MARs speed at different intensities and frequencies of the applied rotating magnetic field. Error bars represent the standard deviation, $n = 10$ independent replicates. e,f) MARs on/off response in terms of instantaneous speed and time-lapse micrographs by on/off switching of the applied rotating magnetic field. The scale bar is 10 μm.

2.4. Micro/Nanoplastics Capture

The escalating presence of hazardous micro/nanoplastics in aquatic ecosystems poses an emergent challenge to the health of aquatic organisms and human beings.[57] Microrobots, the ground-breaking technology that integrates active interaction and precise orientation, represent a practical approach to addressing this issue.[58–60] Here, magnetically actuated MARs promise sustainable removal of micro/nanoplastics in water from different sources.

Amino-modified polystyrene (PS) micro- and nanoparticles with diameters of 1.5 μm and 50 nm were used as representative microplastics and nanoplastics (**Figure** 5a,b). The size distribution of the micro/nanoplastics was also determined by dynamic light scattering, whose results are consistent with the size indicated by SEM analysis, as illustrated in Figure 5c,d. The measured Zeta potential of micro/nanoplastics is shown in Figure 5e. Both types of plastic particles are positively charged because of the amino-modified surface. In particular, the Zeta potential values for nanoplastics and microplastics are +44 and +38 mV, respectively. In comparison, the Zeta potential of MARs is −8 mV, facilitating the electrostatic attraction between MARs and micro/nanoplastics. Based on the information provided by the manufacturer, the micro/nanoplastics exhibit blue fluorescence. Taking advantage of this property, micro/nanoplastics removal was monitored by a spectrofluorometer, which allows for examining the treated solutions. To assess this method, serial dilutions of the as-received micro/nanoplastic suspensions (6×10^9 microplastics mL^{-1} and 4×10^{14} nanoplastics mL^{-1}) were performed, and the corresponding fluorescence intensities are

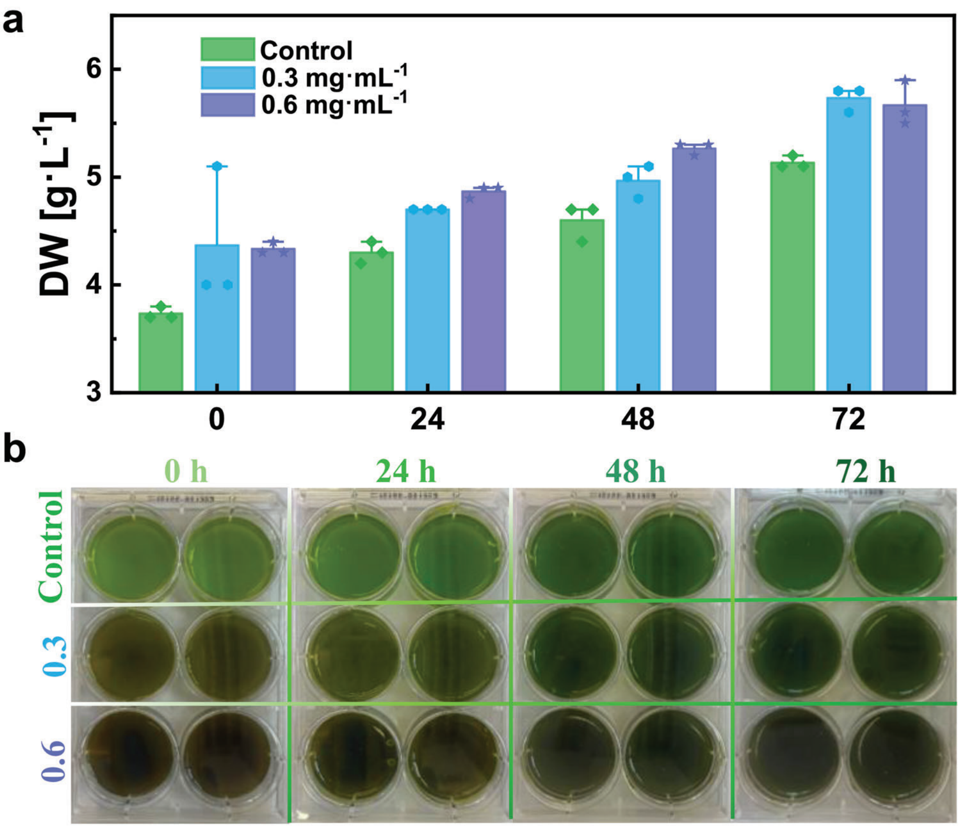

Figure 4. Cell viability of algae in the presence of Fe_3O_4 nanoparticles. a) Growth of *C. vulgaris* without (control) and with Fe_3O_4 nanoparticles at 0.3 and 0.6 mg•mL^{-1} concentrations. Every sample was taken daily, dried, and recalculated to dry weight (DW, g•L^{-1}). Error bars represent the standard deviation, $n = 3$ independent replicates. b) Photographs of *C. vulgaris* during the experimental testing without (control) and with Fe_3O_4 nanoparticles at 0.3 and 0.6 mg•mL^{-1} concentrations.

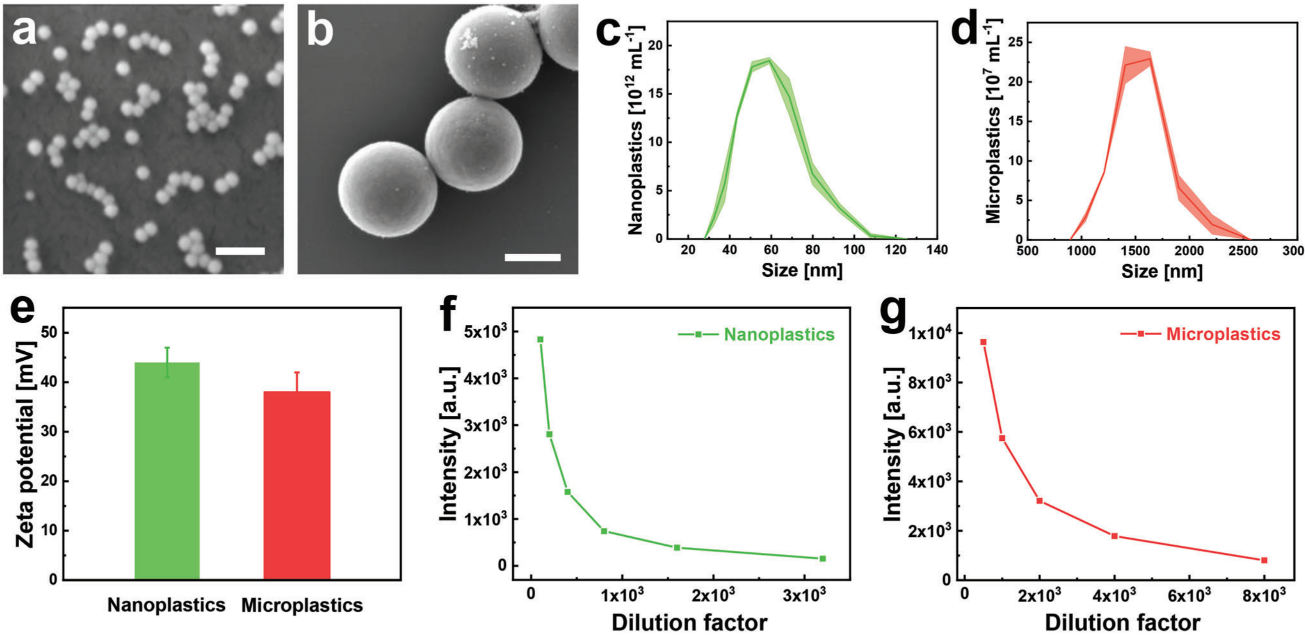

Figure 5. Micro/nanoplastics characterization. a,b) SEM images of nanoplastics (the scale bar is 200 nm) and microplastics (the scale bar is 1 µm) in water. c,d) Size distribution of the nanoplastic and microplastic suspensions. The shaded region represents the standard error for $n = 3$ replicates, substituting the discrete error bars. e) Zeta potential of nanoplastics and microplastics. f,g) Fluorescence intensities variation for serial dilutions of nanoplastic and microplastic suspensions.

shown in Figure 5f,g. It was noted that the fluorescence intensity significantly decreased with the increasing dilution factor, as expected. Considering that 50 nm large nanoparticles cannot be visualized under an optical microscope, only the optical images of microplastic suspensions after serial dilutions were captured and reported in Figure S4 (Supporting Information), evidencing a good agreement with the variation of fluorescence intensities reported in Figure 5g. Additionally, a detection limit of 1.8×10^6 microplastics mL^{-1} and 5×10^{10} nanoplastics mL^{-1} were determined.

The micro/nanoplastics capture mechanism is schematically illustrated in **Figure 6**a. MARs effectively remove micro/nanoplastics due to their powerful motion, induced by a transversal rotating magnetic field (Figure S5, Supporting Information) at 3 mT intensity and 50 Hz frequency, resulting in an average speed of MARs of 7.5 $\mu\text{m s}^{-1}$, promoting electrostatic interactions with targeted plastics. Micro/nanoplastics removal by MARs was evaluated in square-shaped cuvettes under magnetic motion along a predefined trajectory (Figure S6, Supporting Information) or no motion conditions for different treatment periods (0, 5, 10, 20, 30, and 40 min). The fluorescence spectra in Figure S7 (Supporting Information) show the variation of micro/nanoplastics concentrations before and after treatments by MARs without/with applying the rotating magnetic field, respectively, indicating the successful removal of micro/nanoplastics from water. The removal efficiency was calculated based on Equation (1):

$$\text{Removal Efficiency} = \frac{C_0 - C_t}{C_0} \times 100\% \tag{1}$$

where micro/nanoplastics concentrations at time t (C_t) and 0 min (C_0) were determined by measuring the fluorescence intensity at 418 nm, corresponding to the highest peak. Specifically, the removal efficiencies of nanoplastics (Figure 6b) are 92% and 71% for active motion and no motion, respectively, calculated from Figure S7a,b (Supporting Information), demonstrating the contribution of the MARs' active motion in accelerating nanoplastics removal. Figure 6c reports the microplastic removal efficiencies, which are 70% for active motion and 41% for static condition (Figure S7c,d, Supporting Information). In order to explain the removal efficiency difference between nanoplastics and microplastics, SEM images of MARs after interactions with micro/nanoplastic suspensions for 40 min under the rotating magnetic field were collected and shown in Figure 6d. Nanoplastics exhibit a remarkable affinity to the entire surface of MARs due to the much smaller size compared to microplastics and sufficient electrostatic interactions. In contrast, microplastics, though still minute in size, encounter challenges in occupying the surfaces of MARs due to their similar order of magnitude in size as microalgae cells. Hence, the comparable size between microplastics and algae restricts the microplastics' ability to effectively cover a significant portion of the MARs surface, limiting their removal efficiency. Consequently, MARs show higher potential in the removal of nanoplastics. Fluorescence images in Figure S8 (Supporting Information) also demonstrate that nanoplastics covered the surfaces of MARs after the treatment. Microplastics removal by the MAR was also observed at an optical microscope (Figure 6e). The time-lapse images captured from Movie S5 (Supporting Information) illustrate the successful capture and transport of microplastics that interacted with the MAR in water, which also elucidates that Fe_3O_4 nanoparticles remained on the surface of the microalgae during the active capture and removal of micro/nanoplastics and barely caused secondary contamination under control of the rotating magnetic field at 3 mT intensity and 50 Hz frequency. On the contrary, thanks to the presence of Fe_3O_4 nanoparticles, MARs empowered with active motion exhibited better performance in removal of micro/nanoplastics than bare algae cells, as illustrated in Figure S9 (Supporting Information). For real world settings it is important to investigate the effect on the removal efficiency of the micro/nanoplastics shape. However, this aspect goes beyond this present study due to limitations in acquiring fluorescent micro/nanoplastics with different shapes at a fixed size. Of note, according to the previous research, different shapes of microplastics show negligible effects on the removal efficiency.[38]

The reusable and low-cost characteristics of microrobots are considered the crucial feature that influences their long-term and sustainable applications for environmental remediation.[38] Figure 6f shows that MARs preserved electrostatic attraction capability over five cycles of treatment, guaranteeing ≈80% removal efficiency for nanoplastics and ≈54% for microplastics after the cycles. Through the cycle process, the magnetic response of MARs became weaker due to the vigorous agitation required to release the plastic particles from the robots' surface, which is ascribed to the loss of Fe_3O_4 nanoparticles from the algae surface, as shown in Figure S10 (Supporting Information). On the other hand, the navigation speed of MARs decreased during the recycling experiments (Figure S11, Supporting Information), which also results in the declined removal efficiencies. Nonetheless, the magnetic properties of MARs can be revived by mixing them with freshly prepared Fe_3O_4 nanoparticles again. The microalgae cells preserved their original shape and green color after recycling experiments, as shown in Figure S12 (Supporting Information), which elucidates their high viability.[61] To prove the practical utilization of MARs, Figure 6g reports the removal efficiencies of nanoplastics by MARs in different aquatic environments, such as tap water, rainwater, and lake water (Figure S13, Supporting Information), confirming the MARs excellent operation not only in DI water samples but also in real contaminated water samples. The removal efficiencies in tap water, rainwater, and lake water were 90%, 86%, and 89%, respectively. MARs performance was also evaluated against the mixture of nano- and microplastics, finding a slight decrease (84%), owing to surface take-up competition between the two classes of plastic particles. These experiments validate the applicability of the proposed strategy in natural settings.

3. Conclusion

In conclusion, we have presented eco-friendly and magnetic field-driven algae-based microrobots for effective capture and removal of micro/nanoplastics from the aquatic environment. The type of algae *C. vulgaris*, one of the most important microalgae in various biotechnology fields, was chosen as the platform for formulating biohybrid microrobots with a negatively charged surface. After decoration with positively charged Fe_3O_4 nanoparticles, microalgae realized precise actuation and collective manipulation rather

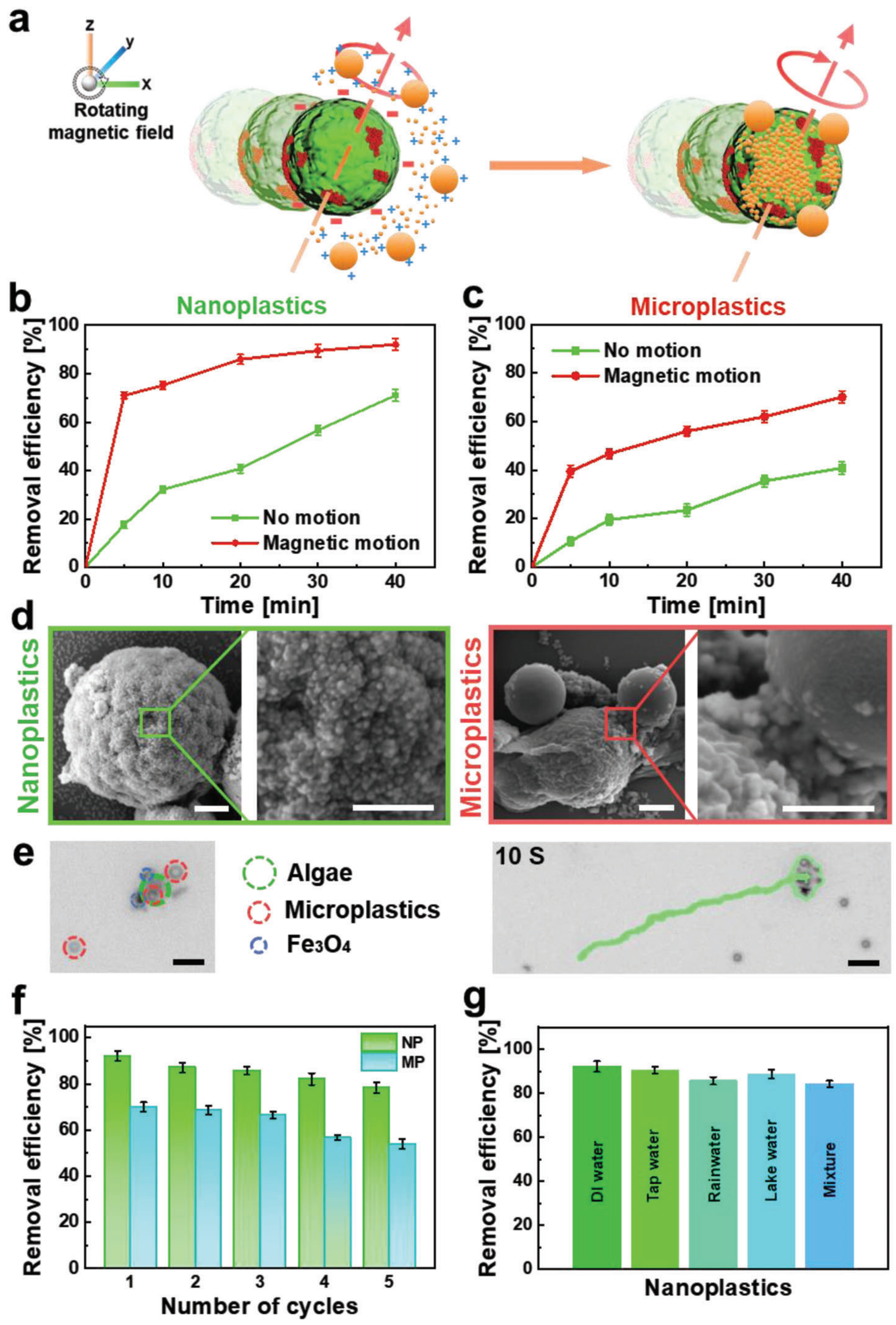

Figure 6. Micro/nanoplastics capture by MARs. a) Schematic diagram of the dynamic removal of micro/nanoplastics by MARs under the rotating magnetic field. b) Nanoplastics and c) microplastics removal efficiencies by MARs as a function of time varying from 0 to 40 min. d) SEM images depicting MARs after being exposed to the suspensions of micro/nanoplastics. Scale bars are 1 µm. e) Time-lapse images showing the transport of microplastics by a MAR. Scale bars are 5 µm. f) Reusability of MARs for nanoplastics (NP) and microplastics (MP) removal from water over five cycles. g) Removal efficiencies of MARs from DI water, tap water, rainwater, lake water, and the mixture of nanoplastics and microplastics. Error bars represent the standard deviation, *n* = 3 independent replicates.

than uncontrollable Brownian motion. To investigate the toxicity of Fe_3O_4 nanoparticles for microalgae, biomass experiments were conducted, which demonstrated that the exposure to 0.3 mg•mL^{-1} Fe_3O_4 nanoparticles resulted in the hormesis stimulation of algae cells growth. The capture of micro/nanoplastics by MARs in water was performed under the control of an external magnetic field to promote the electrostatic attraction of targeted micro/nanoplastics. Taking advantage of their active motion, MARs exhibited considerable efficiencies of 92% for nanoplastics and 70% for microplastics. The reusability of MARs was also tested over five cycles, preserving ≈80% removal efficiency for nanoplastics and ≈54% for microplastics. Considering the complexity of real aquatic environments, different water samples (tap water, rainwater, lake water) were collected and examined to validate the applicability of MARs. The introduced biohybrid microrobots, originating from naturally existing microalgae integrated with magnetic Fe_3O_4 nanoparticles, hold considerable promise for addressing environmental challenges associated with micro/nanoplastics in a sustainable and cost-effective manner.

4. Experimental Section

Model Organism: *C. vulgaris* (SAG 211-11b), a strain of green microalgae, was obtained from the Department of Experimental Phycology and Culture Collection of Algae (EPSAG) at Georg-August-Universität Göttingen (Göttingen, Germany). The microalgae were cultivated in Tris-acetate-phosphate (TAP) medium, using Erlenmeyer flasks, and shaking at 120 rpm under mixotrophic conditions. The cultures were grown at 23 ± 1 °C with illumination at 130 µmol m^{-2} s^{-1} in 12-h light and 12-h dark photoperiods.

Synthesis of Fe_3O_4 Nanoparticles: Briefly, 0.6 g $CaCl_2$ (Sigma Aldrich, ACS reagent, 99%) and 0.6 g $FeSO_4$ (Sigma Aldrich, ACS reagent, 99%) were dissolved in 21 mL deionized (DI) water (18 MΩ cm), respectively, to form uniform solutions. Then, two solutions were mixed under magnetic stirring for 5 min at room temperature. Subsequently, 1.1 g $FeCl_3$ (Alfa Aesar, 97%) was added to the mixture under continuous magnetic stirring for 15 min at 60 °C in an oil bath. Afterward, NaOH solution (Merck, 25%) was added to the mixture slowly until the mixture's pH value reached ≈11, and the solution turned into a uniform black suspension. After oil bath treatment for another 15 min under magnetic stirring, the resulting product was isolated using a permanent magnet and washed three times with DI water and ethanol, respectively. Finally, the Fe_3O_4 nanoparticles were naturally dried in a fume hood at room temperature.

Synthesis of MARs: The green algae were washed using DI water several times to eliminate the TAP medium from the surface. Then, they were suspended in DI water. 0.3 mg•mL^{-1} (final concentration) Fe_3O_4 nanoparticles solution was sonicated for 15 min, mixed with the algae suspension (V_{Fe3O4}:V_{algae} = 1:1), and vortexed for 10 min at 1000 rpm. A permanent magnet was applied to primarily assess the magnetic performance of MARs.

Characterization of MARs: To perform SEM characterization, MARs were initially treated with 2.5% glutaraldehyde for an overnight fixation at 4 °C, followed by washing with DI water to remove residues. After overnight drying, MARs were characterized by scanning electron microscopy (SEM, MIRA3-XMU) with an energy-dispersive X-ray (EDX) detector (Oxford Instruments) after coating with 10 nm gold/palladium. X-ray diffraction (XRD) was used to measure the crystal structure (Rigaku SmartLab 3 kW diffractometer, Cu Kα radiation). The same methodology was used to treat and examine bare algae. The magnetic hysteresis loop was measured using a Quantum Design VersaLab cryogen-free VSM at 300 K, with an applied magnetic field ranging from −15 to 15 kOe at 10 Oe s^{-1} steps. Micro/nanoplastics and MARs were diluted in DI water, respectively, and then 1 mL solution was transferred into a cuvette. Then, size distribution and Zeta potential measurements were carried out using a Malvern Panalytical Zetasizer Ultra instrument, where the cuvette was placed inside. The measurements were repeated three times to produce the error bars.

Motion Analysis: The magnetic movement of MARs was evaluated and recorded using an inverted Nikon ECLIPSE TS2R microscope coupled with a BASLER acA1920-155uc digital camera. No surfactant was utilized during the experiments. A homemade magnetic setup composed of three orthogonal coil pairs positioned on a polylactic acid (PLA) support was employed to regulate the magnetic motion. The setup created a transversal rotating magnetic field. The microrobots were steered under magnetic fields of 3 and 5 mT at various frequencies ranging from 0 to 300 Hz. The captured videos were analyzed using NIS Elements Advanced Research software.

The components of the transversal rotating magnetic field, B_x, B_y, B_z, are expressed by the following equations:

$$B_x = B_0 \cos(\omega t) \sin(\alpha) \tag{2}$$

$$B_y = B_0 \cos(\omega t) \cos(\alpha) \tag{3}$$

$$B_z = B_0 \sin(\omega t) \tag{4}$$

In these equations, B_0 denotes the magnetic field's magnitude, which bears a direct proportionality to the current flowing through the coils. Additionally, $\omega = 2\pi f$, where f is the frequency in Hertz [Hz], t is the time in seconds [s], and α is the navigation angle, spanning a comprehensive range from 0 to 360°. It is pertinent to note that by adjusting the value of α, a remarkable degree of control is achievable to empower the manipulation of the microrobots' trajectory confined within the XY plane, further ensuring high precision over their navigation.

The magnetic field assessments were conducted at the center of the coil holder, wherein a sample holder can be well positioned and the magnetic field was measured by using an A1302 Hall effect sensor.

Microalgal Growth Test: Toxicological assays were performed according to OECD guidelines, TG 201, employing 72 h of exposure. In brief, *C. vulgaris* cells in the exponential growth phase were inoculated into sterile TAP media with/without adding 0.3 and 0.6 mg•mL^{-1} Fe_3O_4 nanoparticles. The experiments were conducted in 6-well culture plates with 5 mL of medium, and the cultures were maintained under the aforementioned conditions for 72 h. During experimental windows, every sample was taken daily, dried for 24 h, and analyzed gravimetrically.

Micro/Nanoplastics Capture Experiments: Fluorescence spectroscopy was used for micro/nanoplastics quantification. Two stocks of micro/nanoplastics were prepared by diluting the commercial suspension, respectively. Specifically, 1.5 mL of MARs and 1.5 mL micro/nanoplastics solutions were transferred in cuvettes. Then, the cuvettes were put in the center of the rotating magnetic setup, set at 3 mT intensity and 50 Hz frequency. Following the treatment, MARs were isolated from the solution by employing a permanent magnet. The MARs and the treated solutions were preserved for subsequent analysis. The experiments were replicated a minimum of three times.

To evaluate the reusability of MARs, they were separated by an external magnet from the purified water after the treatment and subjected to vigorous shaking in water for 5 min to dislodge the micro/nanoplastics from their surface. After shaking, MARs were collected again and applied for following cycles. Each cycle was repeated three times to calculate the error bars.

Supporting Information

Supporting Information is available from the Wiley Online Library or from the author.

Acknowledgements

M.P. acknowledges the financial support of the Grant Agency of the Czech Republic (EXPRO: 19–26896X). X.P. was supported by the China Scholarship Council (CSC No. 202008320382) and acknowledges the Brno Ph.D. Talent scholarship funded by the Brno City Municipality. Czech Nano Lab project LM2023051 funded by MEYS CR is gratefully acknowledged for the financial support of the measurements/sample fabrication at CEITEC Nano Research Infrastructure.

Conflict of Interest

The authors declare no conflict of interest.

Author Contributions

X.P. prepared, and characterized the microrobots, evaluated the performance of the motion, conducted the micro/nanoplastics capture experiments, and wrote the manuscript. M.U. designed the experiments and contributed to data interpretation. M.K. and D.H. conducted microalgal preparation, growth testing, and related data interpretation. X.P. and M.P. originated the idea. M.U. and M.P. supervised this project. M.P. led the research. All the authors have approved the final version of the manuscript.

Data Availability Statement

The data that support the findings of this study are available from the corresponding author upon reasonable request.

Keywords

environment, micromotors, microplastics, nanorobots, water

Received: July 2, 2023
Revised: August 24, 2023
Published online: October 9, 2023

[1] R. Geyer, J. R. Jambeck, K. L. Law, *Sci. Adv.* **2017**, *3*, 25.
[2] M. MacLeod, H. P. H. Arp, M. B. Tekman, A. Jahnke, *Science* **2021**, *373*, 61.
[3] A. A. Horton, *J. Hazard. Mater.* **2022**, *422*, 126885.
[4] X. Chang, Y. Xue, J. Li, L. Zou, M. Tang, *J. Appl. Toxicol.* **2020**, *40*, 4.
[5] S. Reynaud, A. Aynard, B. Grassl, J. Gigault, *Curr. Opin. Colloid Interface Sci.* **2022**, *57*, 101528.
[6] M. Kumar, H. Chen, S. Sarsaiya, S. Qin, H. Liu, M. K. Awasthi, S. Kumar, L. Singh, Z. Zhang, N. S. Bolan, A. Pandey, S. Varjani, M. J. Taherzadeh, *J. Hazard. Mater.* **2021**, *409*, 124967.
[7] H. El Hadri, J. Gigault, B. Maxit, B. Grassl, S. Reynaud, *NanoImpact* **2020**, *17*, 100206.
[8] J. M. Gonçalves, M. J. Bebianno, *Environ. Pollut.* **2021**, *273*, 116426.
[9] L. Peng, D. Fu, H. Qi, C. Q. Lan, H. Yu, C. Ge, *Sci. Total Environ.* **2020**, *698*, 134254.
[10] J. L. Xu, X. Lin, J. J. Wang, A. A. Gowen, *Sci. Total Environ.* **2022**, *851*, 158111.
[11] B. Toussaint, B. Raffael, A. Angers-Loustau, D. Gilliland, V. Kestens, M. Petrillo, I. M. Rio-Echevarria, G. Van den Eede, *Food Addit. Contam. Part A Chem. Anal. Control. Expo Risk Assess* **2019**, *36*, 639.
[12] P. R. Rout, A. Mohanty, A. S. Aastha, M. Miglani, D. Liu, S. Varjani, *J. Hazard Mater. Adv.* **2022**, *6*, 100070.
[13] Y. Zhang, A. Diehl, A. Lewandowski, K. Gopalakrishnan, T. Baker, *Sci. Total Environ.* **2020**, *720*, 137383.
[14] S. M. Patil, N. R. Rane, P. O. Bankole, P. Krishnaiah, Y. Ahn, Y. K. Park, K. K. Yadav, M. A. Amin, B. H. Jeon, *Chem. Eng. J.* **2022**, *430*, 132913.
[15] A. Kundu, N. P. Shetti, S. Basu, K. Raghava Reddy, M. N. Nadagouda, T. M. Aminabhavi, *Chem. Eng. J.* **2021**, *421*, 129816.
[16] R. M. Blair, S. Waldron, V. Phoenix, C. Gauchotte-Lindsay, *Springer Sci. Rev.* **2017**, *5*, 19.
[17] A. Bratovcic, *J. Nanosci. Nanotechnol. Appl.* **2019**, *3*, 304.
[18] Y. K. Song, S. H. Hong, S. Eo, G. M. Han, W. J. Shim, *Environ. Sci. Technol.* **2020**, *54*, 11191.
[19] F. Soto, E. Karshalev, F. Zhang, B. E. Fernandez de Avila, A. Nourhani, J. Wang, *Chem. Rev.* **2022**, *122*, 5365.
[20] W. Wang, W. Duan, S. Ahmed, T. E. Mallouk, A. Sen, *Nano Today* **2013**, *8*, 531.
[21] H. Wang, M. Pumera, *Chem. Soc. Rev.* **2020**, *49*, 3211.
[22] B. Wang, S. Handschuh-Wang, J. Shen, X. Zhou, Z. Guo, W. Liu, M. Pumera, L. Zhang, *Adv. Mater.* **2023**, *35*, 2205732.
[23] J. Li, B. E. F. De Ávila, W. Gao, L. Zhang, J. Wang, *Sci Robot* **2017**, *2*, eaam6431.
[24] C. K. Schmidt, M. Medina-Sánchez, R. J. Edmondson, O. G. Schmidt, *Nat. Commun.* **2020**, *11*, 5618.
[25] T. Pan, Y. Shi, N. Zhao, J. Xiong, Y. Xiao, H. Xin, B. Li, *Adv. Funct. Mater.* **2022**, *32*, 2111038.
[26] L. Cai, D. Xu, Z. Zhang, N. Li, Y. Zhao, *Research* **2023**, *6*, 0044.
[27] T. Patino, A. Porchetta, A. Jannasch, A. Lladó, T. Stumpp, E. Schäffer, F. Ricci, S. Sánchez, *Nano Lett.* **2019**, *19*, 3440.
[28] R. María-Hormigos, Á. Molinero-Fernández, M. Á. López, B. Jurado-Sánchez, A. Escarpa, *Anal. Chem.* **2022**, *94*, 5575.
[29] X. Du, Q. Wang, D. Jin, P. W. Y. Chiu, C. P. Pang, K. K. L. Chong, L. Zhang, *IEEE Robot. Autom. Lett.* **2022**, *7*, 7668.
[30] C. M. Oral, M. Ussia, M. Urso, J. Salat, A. Novobilsky, M. Stefanik, D. Ruzek, M. Pumera, *Adv. Healthcare Mater.* **2022**, *12*, 2202682.
[31] M. Urso, M. Ussia, M. Pumera, *Nat. Rev. Bioeng.* **2023**, *1*, 236.
[32] H. Huang, J. Li, M. Yuan, H. Yang, Y. Zhao, Y. Ying, S. Wang, *Angew. Chem. Int. Ed.* **2022**, *61*, 202211163.
[33] J. Kim, C. C. Mayorga-Martinez, M. Pumera, *Nat. Commun.* **2023**, *14*, 935.
[34] M. Urso, M. Pumera, *Adv. Funct. Mater.* **2022**, *32*, 2200711.
[35] L. Wang, A. Kaeppler, D. Fischer, J. Simmchen, *ACS Appl. Mater. Interfaces* **2019**, *11*, 3293.
[36] X. Peng, M. Urso, M. Ussia, M. Pumera, *ACS Nano* **2022**, *16*, 7615.
[37] H. Ye, Y. Wang, X. Liu, D. Xu, H. Yuan, H. Sun, S. Wang, X. Ma, *J. Colloid Interface Sci.* **2021**, *588*, 510.
[38] W. Li, C. Wu, Z. Xiong, C. Liang, Z. Li, B. Liu, Q. Cao, J. Wang, J. Tang, D. Li, *Sci. Adv.* **2022**, *8*, eade1731.
[39] H. Zhou, C. C. Mayorga-Martinez, M. Pumera, *Small Methods* **2021**, *5*, 2100230.
[40] M. Urso, F. Novotný, M. Pumera, *Nat. Commun.* **2022**, *13*, 3573.
[41] K. Pooja, V. Priyanka, B. C. S. Rao, V. Raghavender, *Energy Nexus* **2022**, *7*, 100122.
[42] N. Li, P. Wang, S. Wang, C. Wang, H. Zhou, S. Kapur, J. Zhang, Y. Song, *J. Environ. Chem. Eng.* **2022**, *10*, 107516.
[43] V. A. J. Silva, P. L. Andrade, M. P. C. Silva, A. D. Bustamante, L. De Los Santos Valladares, J. Albino Aguiar, *J. Magn. Magn. Mater.* **2013**, *343*, 138.
[44] Q. Ai, Z. Yuan, R. Huang, C. Yang, G. Jiang, J. Xiong, Z. Huang, S. Yuan, *J. Mater. Sci.* **2019**, *54*, 4212.
[45] E. Illés, E. Tombácz, *Colloids Surfaces A Physicochem. Eng. Asp.* **2003**, *230*, 99.
[46] O. U. Rahman, S. C. Mohapatra, S. Ahmad, *Mater. Chem. Phys.* **2012**, *132*, 196.
[47] Z. Lin, X. Fan, M. Sun, C. Gao, Q. He, H. Xie, *ACS Nano* **2018**, *12*, 2539.
[48] Y. Jiang, T. Yoshida, A. Quigg, *Plant Physiol. Biochem.* **2012**, *54*, 70.
[49] T. E. Yazdanabdad, A. A. Forghaniha, M. Emtyazjoo, M. Ramezani, *Arch. Environ. Contam. Toxicol.* **2022**, *83*, 155.
[50] N. Mallick, *World J. Microbiol. Biotechnol.* **2003**, *19*, 695.
[51] V. Subramaniyam, S. R. Subashchandrabose, P. Thavamani, Z. Chen, G. S. R. Krishnamurti, R. Naidu, M. Megharaj, *J. Appl. Phycol.* **2016**, *28*, 2767.
[52] M. S. Rana, S. K. Prajapati, *Algal Res.* **2021**, *59*, 102458.
[53] M. Samei, M. H. Sarrafzadeh, M. A. Faramarzi, *Environ. Sci. Pollut. Res.* **2019**, *26*, 2409.

[54] P. Saxena, V. Sangela Harish, *Environ. Sci. Pollut. Res.* **2020**, *27*, 19650.
[55] A. Mahana, O. I. Guliy, S. K. Mehta, *Ecotoxicol. Environ. Saf.* **2021**, *208*, 111662.
[56] J. Hou, Y. Wu, X. Li, B. Wei, S. Li, X. Wang, *Chemosphere* **2018**, *193*, 852.
[57] Z. Hou, R. Meng, G. Chen, T. Lai, R. Qing, S. Hao, J. Deng, B. Wang, *Sci. Total Environ.* **2022**, *838*, 155811.
[58] J. Parmar, D. Vilela, K. Villa, J. Wang, S. Sánchez, *J. Am. Chem. Soc.* **2018**, *140*, 9317.
[59] M. Urso, M. Pumera, *Adv. Funct. Mater.* **2022**, *32*, 2112120.
[60] H. Zhou, C. C. Mayorga-Martinez, M. Pumera, *Small Methods* **2021**, *5*, 2100230.
[61] A. Abo Markeb, J. Llimós-Turet, I. Ferrer, P. Blánquez, A. Alonso, A. Sánchez, J. Moral-Vico, X. Font, *Water Res.* **2019**, *159*, 490.

Part 3. Self-propelled microrobots with phototaxis for cancer therapy

10. Self-propelled magnetic dendrite-shaped microrobots for photodynamic prostate cancer therapy

Paper published in this chapter:

Xia Peng, Mario Urso, Jan Balvan, Michal Masarik, and Martin Pumera, Self-Propelled Magnetic Dendrite-Shaped Microrobots for Photodynamic Prostate Cancer Therapy. *Angew. Chem. Int. Ed.* **2022**, *61*, e202213505.

10.1 Motivation of this study

Photocatalytic materials offer a promising avenue for drug-free therapies, particularly in cancer treatment where drug usage can be minimized. Photocatalysts generate reactive oxygen species (ROS), disrupting the antioxidant environment, and enhancing cytotoxicity against cancer cells. However, the efficiencies of cancer therapy remain limitations, ascribed to passive diffusion of photocatalysts. Microrobots that consist of photosensitizers can exhibit active actuation, overcoming the hindrance of inert motion. Meanwhile, microrobots exhibiting phototaxis have found utility within the realm of biomedicine, specifically in applications such as cellular manipulation and targeted drug delivery. Nonetheless, there remains an unexplored frontier in the domain of light-driven microrobots with phototaxis, where liberation from the confines of two-dimensional motion for photodynamic therapy (PDT) and non-contact cell manipulation remains a promising pursuit.

10.2 Paper conclusion

This study demonstrated that the increasing intelligence of photocatalytic microrobots was further realized by exploring the tactic behavior of dendrite-shaped microrobots, fabricated by a low cost and one-step hydrothermal method to realize the on-site generation of ROS to trigger prostate cancer cell therapy. Transportation of micro-sized targets in a non-contact way, such as cells, was demonstrated by manipulating the movement of a single microrobot, which produced a powerful fluid flow pushing the targeted cell. Moreover, the hematite microrobots presented good biocompatibility. In vitro experiments proved that hematite microrobots can induce apoptosis of prostate cancer cells upon reaction with the ROS generated by the photo-Fenton reaction, enhancing PDT efficacy.

10.3 Author contribution

I prepared and characterized the microrobots, optimized their integration with Fe_3O_4 nanoparticles, and analyzed their photocatalytic and magnetic motion under a magnetic field. I also interpreted the data, assessed their efficiency and reusability, and drafted the manuscript.

How to cite: *Angew. Chem. Int. Ed.* **2022,** *61,* e202213505
International Edition: doi.org/10.1002/anie.202213505
German Edition: doi.org/10.1002/ange.202213505

Micromachines

Self-Propelled Magnetic Dendrite-Shaped Microrobots for Photodynamic Prostate Cancer Therapy

*Xia Peng, Mario Urso, Jan Balvan, Michal Masarik, and Martin Pumera**

Abstract: Photocatalytic micromotors that exhibit wireless and controllable motion by light have been extensively explored for cancer treatment by photodynamic therapy (PDT). However, overexpressed glutathione (GSH) in the tumor microenvironment can downregulate the reactive oxygen species (ROS) level for cancer therapy. Herein, we present dendrite-shaped light-powered hematite microrobots as an effective GSH depletion agent for PDT of prostate cancer cells. These hematite microrobots can display negative phototactic motion under light irradiation and flexible actuation in a defined path controlled by an external magnetic field. Non-contact transportation of micro-sized cells can be achieved by manipulating the microrobot's motion. In addition, the biocompatible microrobots induce GSH depletion and greatly enhance PDT performance. The proposed dendrite-shaped hematite microrobots contribute to developing dual light/magnetic field-powered micromachines for the biomedical field.

Introduction

Inspired by the extensive photosynthesis process in nature, artificial microrobots consisting of "smart materials" with intrinsic capacity or functionalized integration can similarly convert light sources into energy for autonomous motion induced by diverse mechanisms, for instance, bubble thrust and self-phoretic propulsion.[1–3] These light-powered self-propelled microrobots have obtained considerable attention over the past years because of the remote and controllable motion by an external renewable and abundant energy source such as light and their potential applications in various fields, i.e., sensing, imaging, and environmental remediation.[4–8] Plenty of photocatalytic materials (TiO_2, ZnO, Fe_2O_3, BiOI) have been exploited as the main constituent for the fabrication of innovative light-powered microrobots.[9–15] Breaking the material's symmetry by the uneven deposition of a noble metal coating represents a promising strategy to endow them with an effective motion by light irradiation. For instance, the TiO_2 microparticles with Au half-coating exhibited motion behavior once exposed to UV light by self-electrophoresis, i.e., in charge of a localized electric field induced by the asymmetrical generation of a charged products gradient.[2] In addition, light-powered fuel-free spherical ZnO/Pt micromotors displayed the capability of positioning themselves to the light-exposure direction and exhibiting phototactic behavior at considerable velocities.[16] However, the dependence on expensive noble metals remains a challenge in the micro/nanorobotics field, not only for light-powered but also for fuel-driven micro/nanorobots.[17,18] On the other hand, magnetic materials are extensively integrated on the surface of microrobots in order to achieve precisely controllable motion for biomedical applications.[19–23] Consequently, simple, single-component, inherently magnetic, and low-cost light-driven microrobots are highly desired for real-world applications.

Given the tremendous progress in nanotechnology and nanomaterials in the biomedical field, many therapeutic approaches have been established for tumor treatments, for instance, chemotherapy, gene therapy, radiotherapy, immunotherapy, and PDT.[24] Among them, PDT has received extensive attention as an emergent and promising drug-free cancer treatment method.[25–27] PDT employs photocatalysts that can convert oxygen molecules into ROS, which can cause permanent damage to cancer cells.[28–30] However, overexpression of GSH existing in cancer cells critically impedes the therapeutic effect of PDT. Reducing the GSH amount in the microenvironment of cancer cells and, in turn,

---

[*] X. Peng, M. Urso, M. Pumera
Future Energy and Innovation Laboratory, Central European Institute of Technology, Brno University of Technology
Purkynova 123, 61200 Brno (Czech Republic)
E-mail: martin.pumera@ceitec.vutbr.cz

J. Balvan, M. Masarik
Department of Physiology, Faculty of Medicine, Masaryk University
Kamenice 5, 62500 Brno (Czech Republic)
and
Department of Pathological Physiology, Faculty of Medicine, Masaryk University
Kamenice 5, 62500 Brno (Czech Republic)

M. Masarik
BIOCEV, First Faculty of Medicine, Charles University
Prumyslova 595, 25250 Vestec (Czech Republic)

M. Masarik
Department of Chemistry and Biochemistry, Mendel University
Zemedelska 1, 61300 Brno (Czech Republic)

M. Pumera
Department of Medical Research, China Medical University Hospital, China Medical University
No. 91 Hsueh-Shih Road, 40402 Taichung (Taiwan)
and
Faculty of Electrical Engineering and Computer Science, VSB, Technical University of Ostrava
17. listopadu 2172/15, 70800 Ostrava (Czech Republic)
and
Department of Chemical and Biomolecular Engineering, Yonsei University
50 Yonsei-ro, Seodaemun-gu, Seoul 03722 (Korea)

boosting ROS level is very important to destroy the cellular antioxidation defense system, synergistically killing cancer cells.[31] The employment of photocatalytic materials to develop light-powered microrobots capable of active propulsion and producing ROS provides an emerging and promising tool to oxidize GSH and maximize the benefit of cancer treatment.

In this work, we propose single-component dendrite-structured hematite microrobots with dual magnetic/optical propulsion modes for effective GSH depletion, increasing the cytotoxicity against prostate cancer cells. Dendrite-structured hematite microparticles were synthesized in one step by a simple and facile hydrothermal reaction. The single-component hematite microrobots exhibit negative phototaxis when exposed to light irradiation by self-diffusiophoresis, as well as the magnetic motion under a rotating magnetic field. These single-component hematite microrobots provide two actuation modes that can both control the direction of their movement. Taking advantage of these features, the non-contact transportation of targeted microscale objects, such as cells, can be achieved using hematite microrobots by generating a localized fluid flow. The prostate cancer cells were selected to examine the PDT capacity of hematite microrobots. Under exposure to light in the presence of H_2O_2, the hematite microrobots based on the photo-Fenton reaction produce abundant ROS to induce GSH depletion and greatly enhance the PDT efficiency against prostate cancer cells. These results demonstrate that the dendrite-structured hematite microrobots can be an adjuvant for augmenting cancer therapeutic efficacy and a promising alternative for future biomedical applications.

Result and Discussion

Figure 1 reveals the fabrication process and characterization of hematite microrobots. A one-step low-cost hydrothermal reaction was employed to produce single-constituent hematite microrobots, as schematically shown in Figure 1A. Scanning electron microscopy (SEM) images at different magnifications of hematite microrobots are displayed in Figure 1B. The low-magnification SEM image reveals the hematite microrobots' uniform and symmetric dendrite-like structure (Figure 1B). The dimensions of the main trunks are approximately 8–10 μm. The high-resolution SEM image shows an attractive dendrite-like structure. The highly arranged branches are allocated on two sides of the central trunk. This asymmetrical dendrite-like structure can facilitate the migration of diverse chemical species beneficial for the motion of microrobots and their potential applications, owing to abundant active catalytic spots provided by the appreciable edges of the branches. Energy-dispersive X-ray spectroscopy (EDX) elemental mapping images validate the existence and uniform distributions of Fe and O elements, as shown in Figure 1B. The X-ray diffraction (XRD) spectrum of hematite microrobots is manifested in Figure 1C, indicating that pre-synthesized microrobots are well evidenced in the hexagonal phase (JCPDS no. 33-0664).[32] The chemical states of hematite microrobots were characterized by X-ray photoelectron spectroscopy (XPS). Figure 1D displays the high-resolution spectrum of Fe 2*p*. Two peaks at binding energies of ~711 eV for Fe $2p_{3/2}$ and ~724 eV for Fe $2p_{1/2}$ with the corresponding satellite peaks at ~719 and ~733 eV binding energies can be distinguished. These are characteristics of Fe^{3+} ions in hematite.[33] The high-resolution O 1s spectrum in Figure 1E shows two contributions at ~532 eV and ~530 eV binding energy, assigned to Fe–O within Fe_2O_3, and hydroxyl groups attached to FeO, respectively.

The motion behavior of hematite microrobots was evaluated under light exposure. The actuation mechanism of single-component light-powered microrobots has been elucidated in previous works.[34,35] As demonstrated in Figure 2A, the electrons excited by the light jump to the conduction

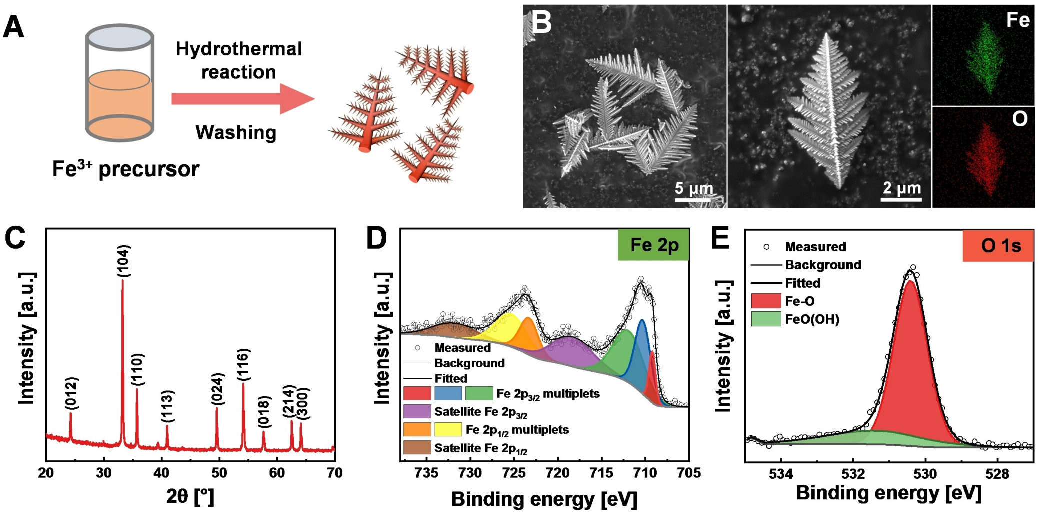

Figure 1. Preparation and characterization of hematite microrobots. A) Schematic illustration of the synthetic procedure. B) SEM images at two magnifications and EDX mapping images. C) XRD spectrum. D) Fe 2*p* XPS spectrum. E) O 1s XPS spectrum.

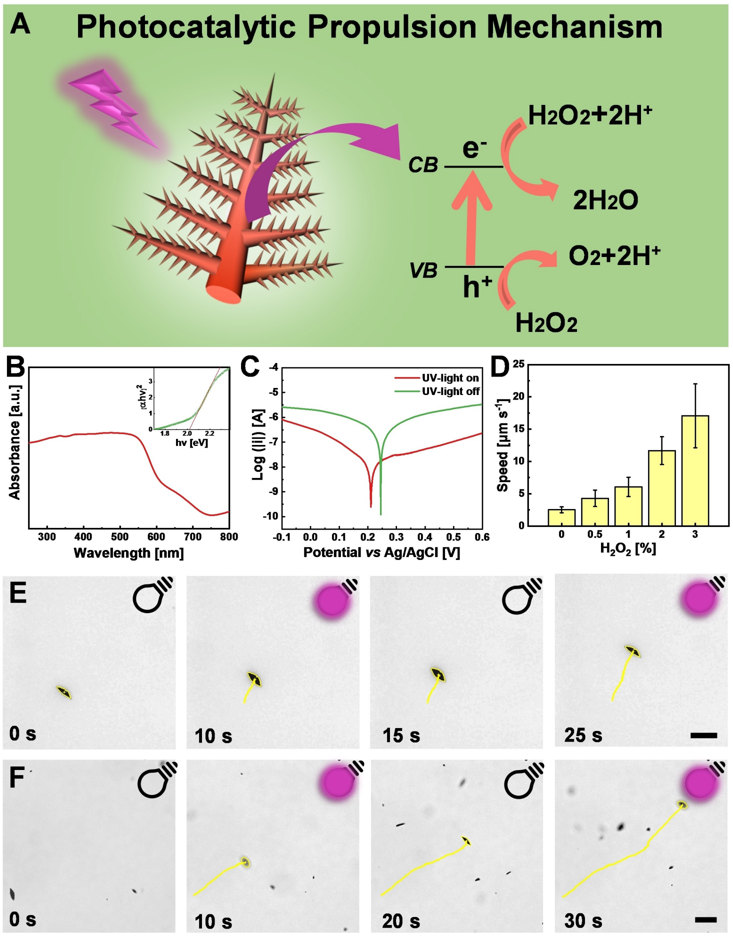

Figure 2. A) Schematic illustration of the motion mechanism of hematite microrobots. B) UV-Vis absorbance spectrum of the hematite microrobots. The inset reports the accorded Tauc plot. C) Tafel plot of the hematite microrobots with/without light irradiation in water. D) Average speed at various concentrations of H_2O_2 under light exposure. Trajectories of hematite microrobots in E) 0.5% H_2O_2 and F) 1% H_2O_2. Scale bars are 10 µm.

band (CB) of hematite microrobots, leaving holes in the valence band (VB). The electron-hole pairs will produce O_2 molecules and protons by H_2O_2 decomposition.[34] A chemical gradient of O_2 molecules and protons will be asymmetrically created, prompting the motion of microrobots based on self-diffusiophoresis. The optical band gap (E_g) of hematite microrobots in Figure 2B was obtained using the Tauc plot according to the measured UV/Vis absorption spectrum.[36] The estimated E_g value is 2.02 eV, proving that hematite microrobots can absorb light in the visible range. To elucidate the photocatalytic activity of hematite microrobots upon light exposure, the mixed potential was measured from the Tafel plot of the hematite microrobots under dark/light circumstances in water. As shown in Figure 2C, the mixed potential of hematite transfers to a more negative value with light exposure, which shows a difference of 40 mV between dark and light, indicating that hematite microrobots generated electron-hole pairs under light irradiation.[37] The speed of microrobots in pure water was merely $2.5\pm0.5\ \mu m\,s^{-1}$, but it progressively increased to $18\pm5\ \mu m\,s^{-1}$ when a higher concentration of H_2O_2 solution was introduced (Figure 2D). Photocatalytic decomposition of H_2O_2 proceeds according to the reaction scheme in Equation (1):[32]

$$\begin{aligned} &\alpha\text{-}Fe_2O_3 + h\nu \rightarrow e^- + h^+ \\ &H_2O_2 + 2\,h^+ \rightarrow 2H^+ + O_2 \\ &H_2O_2 + 2e^- + 2H^+ \rightarrow 2H_2O \end{aligned} \qquad (1)$$

As shown in Figure 2E, captured from Supplementary Movie 1, an enhanced wall-bound 2D motion of the microrobots rather than Brownian motion can be observed at a low H_2O_2 concentration when UV light is irradiated from the bottom. Interestingly, when the higher H_2O_2 concentration was employed, the time-frame images in Figure 2F manifest that the microrobots can exhibit powerful propulsion and move upwards against gravity, away from the bottom wall. They immediately swim out of focus, showing negative phototaxis (Supplementary Movie 1).[38–41] When the light is turned off, the microrobots gradually move back to the glass wall plane and get focused again. Control experiments with different light directions were also conducted to study further the negative phototactic motion

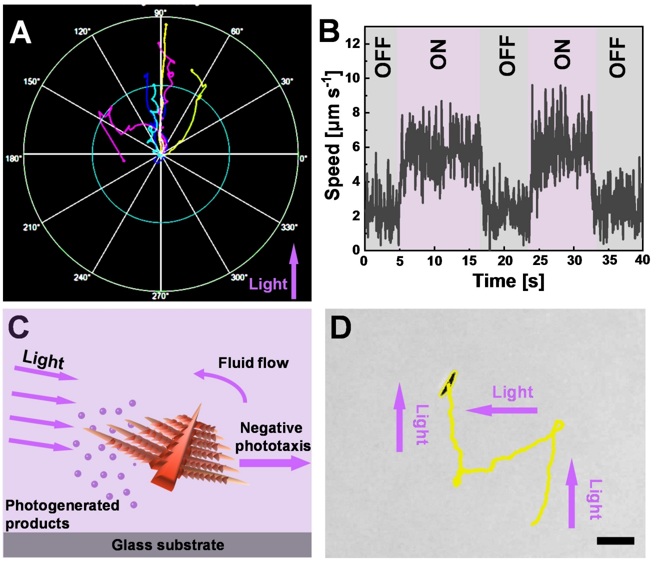

Figure 3. A) Polar graph showing the trajectories of hematite microrobots. B) The speed of the hematite microrobot with the light on/off responses. C) Schematic illustration of the negative phototaxis of hematite microrobots. D) Light-controlled steering of a single hematite microrobot by negative phototaxis in 1% H_2O_2. The scale bar is 10 µm.

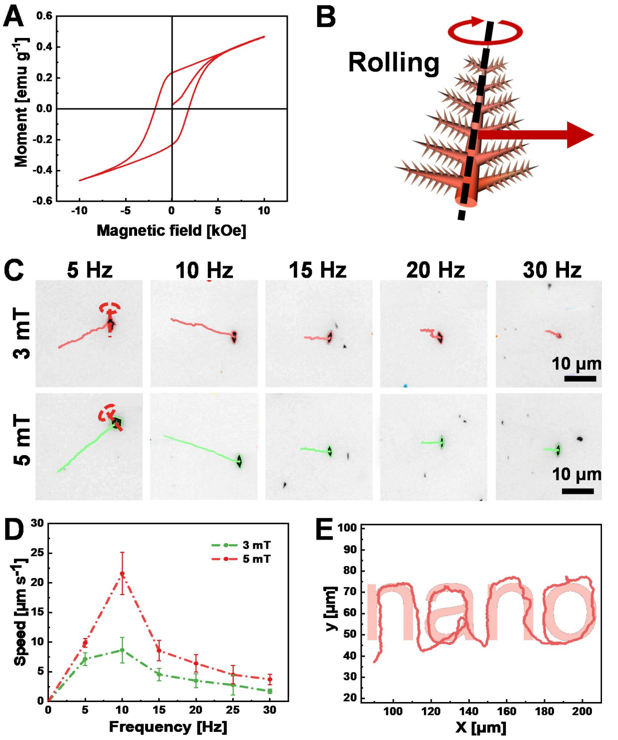

Figure 4. Magnetic actuation of hematite microrobots. A) Magnetic hysteresis loop of hematite microrobots. B) The scheme of a hematite microrobot in a rolling behavior under a rotating magnetic field. C) Representative tracking trajectories of hematite microrobots under a rotating magnetic field of 3 mT and 5 mT at different frequencies for 5 s. Dashed lines represent the long axis of hematite microrobots and the sense of revolution. D) Corresponding speeds of microrobots under a rotating magnetic field. E) Trajectory of a hematite microrobot following a predesigned "nano" track.

(Supplementary Movie 2). In the polar graph shown in Figure 3A, it can be seen that the trajectories of most microrobots tend to move away from the light source when UV light is placed in a tangential direction. The light on/off switching experiment also was included and shown in Figure 3B, demonstrating that the microrobots exhibit distinct light on/off responses. As evidenced by previous works,[42,43] single-component isotropic microrobots that exhibit negative phototaxis under light irradiation are propelled by self-diffusiophoresis. The produced products gradient could originate a directed local fluid flow, propelling the hematite microrobots toward the low product concentration area, as schematically shown in Figure 3C. Furthermore, a light-guided hematite microrobot is shown in Figure 3D, captured from Supplementary Movie 3. By changing the light source direction, the controlled movement of dendrite-shaped hematite microrobots can be achieved.

A previous paper has elucidated the inherent magnetic property of hematite microparticles.[44] The magnetic hysteresis loop of hematite microrobots was plotted in Figure 4A, suggesting a ferromagnetic behavior. Hematite microrobots can perform a rolling motion along their long axis when applying a transversal rotating magnetic field, moving in the perpendicular direction, as depicted in Figure 4B. Time-frame images (Figure 4C, Supplementary Movie 4 and 5) demonstrate that a hematite microrobot rotated along its central trunk and moved toward the orthogonal direction under a rotating magnetic intensity of 3 and 5 mT at different frequencies, varying from 5 Hz to 30 Hz. The propulsion trajectories of hematite microrobots exhibited a significant decline in a predefined time as the magnetic field frequency was higher. Figure 4D shows that the speed of microrobots linearly increases with the frequency up to the highest velocity of 22 µm s^{-1} at the frequency of 10 Hz and 5 mT, known as the "step-out" frequency. Above this frequency, the speed significantly decreases because the magnetic torque is inadequate to keep a synchronous association between the rotating magnetic field and the magnetic moment existing in hematite microrobots.[44,45] This behavior agrees with the previously reported peanut motors that are transversely magnetized and is consistent with the trajectories shown in Figure 4C.[45] In addition, Figure 4E shows that the hematite microrobot swims along a predefined "nano" track in a rolling mode (Supplementary Movie 6), which indicates that hematite microrobots can be precisely controlled and navigated to specific locations, holding tremendous potential for biological applications.

Controllable and precise cell transportation is of significant interest concerning desirable therapy, for example, targeted cell study and transport, for which two methods, contact and non-contact, can be realized.[46,47] In order to accomplish a flexible operation in the defined surroundings, the non-contact manipulation of microrobots holds great advantages in non-contamination and remote control for biological applications. By regulating the parameters of the external rotating magnetic field, the locomotion of hematite microrobots possesses the feature of flexible and remote control. Moreover, the rotation of the peculiar dendrite-like structure impels the adjacent fluid to produce a local hydrodynamic flow field to manipulate targeted cells without contact.[48] Yeast cells were selected as a cell model. As shown in Figure 5A, captured from Supplementary Movie 7, the yeast cell is synchronously moved along with the microrobots, exhibiting a linear trajectory. Considering the complex bio-microenvironments, we also control the locomotion of microrobots to transport the cell in a circular trajectory (Figure 5B), demonstrating that hematite microrobots can realize controllable non-contact cell transportation in arbitrary trajectories. Figure 5C displays the synchronized locomotion trajectories of the microrobot and the yeast cell under magnetic field navigation. By employing the actuation of the single microrobot along a predesigned trajectory, the selected yeast cell was effectively steered along a parallel route, showing a mean moving velocity of $\approx 3\ \mu m\,s^{-1}$, as displayed in Figure 5D. Furthermore, it is highlighted that there is no overlap between these two trajectories, which further indicates that hematite microrobots can realize the non-contact transportation of targeted objects along desired paths, enabling a significant benefit for future biomedical applications.

Drug-free therapy based on photocatalytic materials is highly desirable, being considered a beneficial method for cancer treatment where no drugs are involved.[31] The ROS produced by the photocatalyst can oxidize GSH into oxidized glutathione (GSSG) to destroy the antioxidant microenvironment and increase cytotoxicity against cancer cells. The effect of hematite microrobots in eliminating GSH was examined using 5,5′-dithiobis (2-nitrobenzoic acid) (DTNB) as an indicator since it reacts with GSH to form a 5-thio-2-nitrobenzoic acid anion, which was monitored by UV/Vis spectroscopy.[49] As shown in Figure S1A, DTNB exhibits an absorption peak at 323 nm. The combination of GSH results in the disappearance of the peak at 323 nm. Instead, an absorption peak at 408 nm appeared, representing the successful formation of the 5-thio-2-nitrobenzoic acid anion. Initially, we investigated GSH consumption using hematite microrobots under different conditions: 1) microrobots + GSH; 2) microrobots + GSH + blue light; 3) micro-

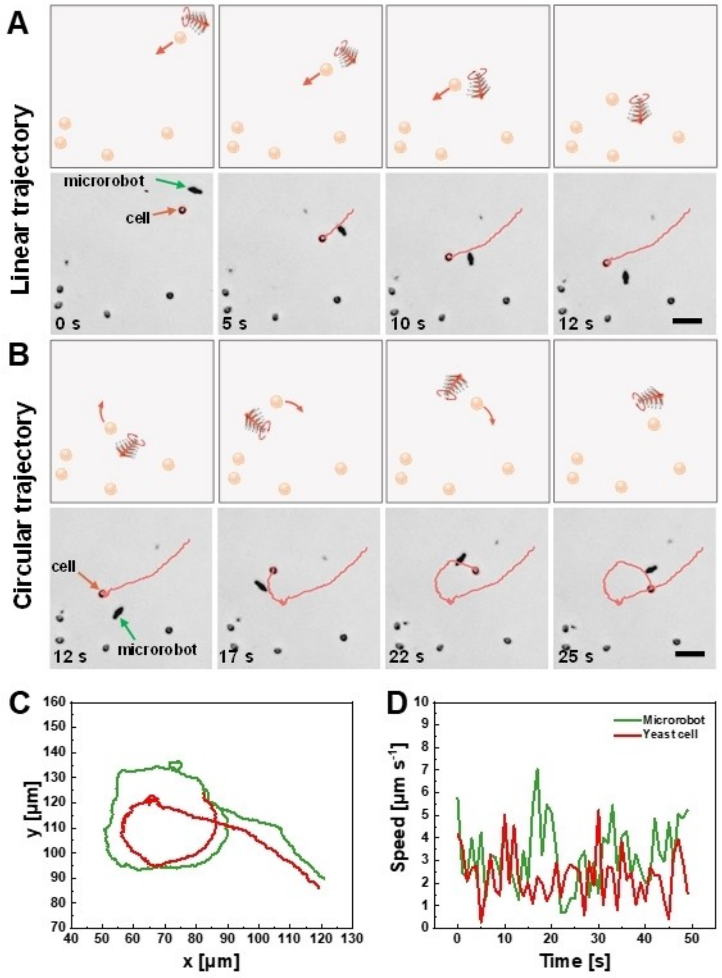

Figure 5. Controllable non-contact cell transportation by a hematite microrobot. A) Linear transport of the yeast cell and B) circular transport of the yeast cell under a rotating magnetic field of 5 mT at 10 Hz. Red curves show the trajectory of the targeted cell. Red arrows beside the cell indicate the transport direction. Scale bars are 20 µm. C) Trajectories of the microrobot and transported yeast cell. D) Speed of the microrobot and transported yeast cell along the circular path.

orobots + GSH + magnetic stirring; 4) microrobots + GSH + fuel (0.05 % H_2O_2); 5) microrobots + GSH + fuel (0.05 % H_2O_2) + blue light (Figure S1). As shown in Figure 6A, GSH content significantly decreased to 22 % after the treatment with hematite microrobots under light illumination in H_2O_2 fuel. The microrobots can consume a relatively high amount of GSH thanks to the photo-Fenton reaction that enhances ROS production to oxidize GSH in the solution. Figure 6B displays the variation of GSH concentration over time. After 60 min treatment, microrobots can consume 8 mM GSH. In order to investigate the main ROS responsible for GSH consumption, radical trapping experiments were carried out, as shown in Figure 6C. In this regard, ethylenediaminetetraacetic acid (EDTA, 10 $mg\,L^{-1}$), isopropanol (0.25 $\mu L\,mL^{-1}$), and nitro-blue tetrazolium (NBT, 10 $mg\,L^{-1}$) were chosen as typical scavengers to capture h^+, $^\bullet OH$, and $^\bullet O^{2-}$, respectively.[50] The involvement of isopropanol and NBT significantly increase the photocatalytic performance of hematite microrobots, leading to higher efficiencies of 86 % and 88 %, respectively. On the contrary, the addition of EDTA decreased the GSH consumption, indicating that the scavenging of holes by EDTA inhibits GSH oxidation. On this basis, it was concluded that the photogenerated holes are the key active photo-induced product responsible for GSH depletion and may boost the microrobots' cytotoxicity for cancer cell treatment (Figure 6D).

Since hematite microrobots can increase ROS production and oxidize GSH, they were applied for "proof of concept" in vitro PDT therapy of prostate cancer cells. The cytotoxicity of hematite microrobots was investigated first. From Figure 6F, the hematite microrobots have no effect on the viability of prostate cancer cells without fuel (H_2O_2) and light exposure. After 9 h incubation, no apparent cytotoxicity was noted at a 1 $mg\,mL^{-1}$ concentration of microrobots (Figure S3), suggesting the high biocompatibility of hematite microcatalysts. The effect of fuel (0.05 % H_2O_2) and light exposure (485 nm, 48 $mW\,cm^{-2}$) on the viability of prostate cancer cells were also conducted to exclude other potential contributions, demonstrating just a mild decrease (88 %), whereas, in the simultaneous presence of hematite microrobots, the cell viability significantly decreases down to 24 % (Figure 6F and Figure S2). To visualize cell killing efficiency,

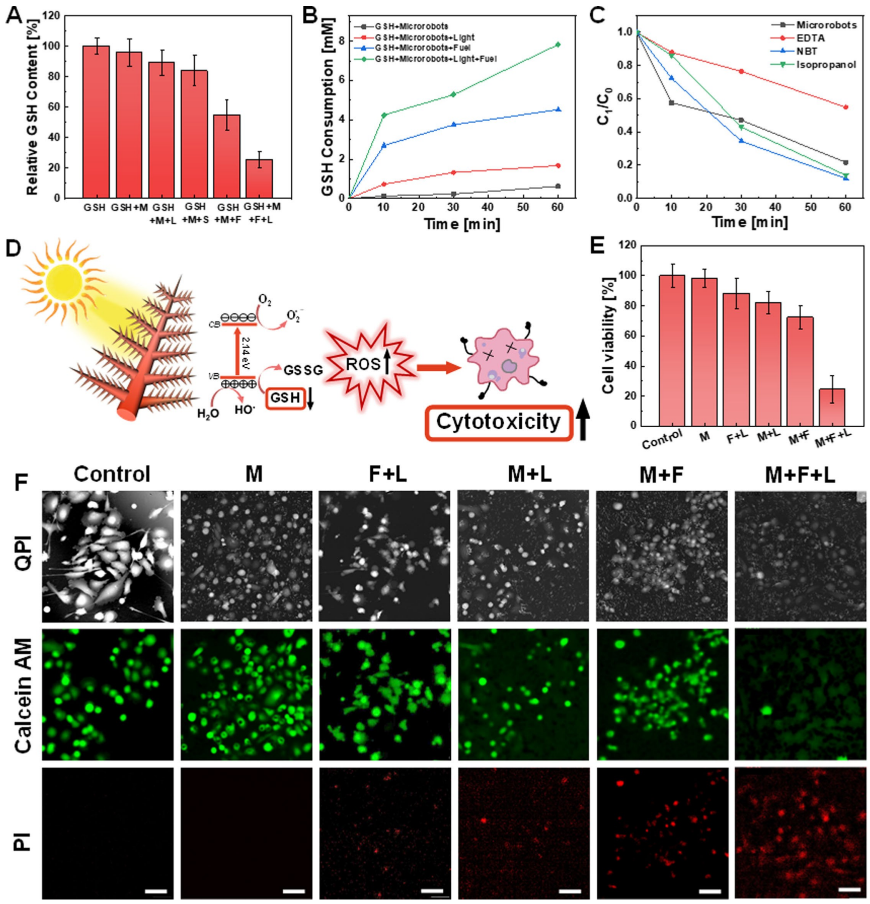

Figure 6. A) GSH consumption under different conditions (GSH + M: GSH + Microrobots; GSH + M + L: GSH + Microrobots + Light; GSH + M + S: GSH + Microrobots + Stirring; GSH + M + F: GSH + Microrobots + Fuel; GSH + M + F + L: GSH + Microrobots + Fuel + Light). B) GSH consumption as a function of time. C) Radical trapping experiments conducted using hematite microrobots with the involvement of EDTA, NBT, and isopropanol. D) The proposed mechanism and scheme for therapy performances based on hematite microrobots. E) Cell viability after treatment at different conditions (F + L: Fuel + Light; M: Microrobots; M + L: Microrobots + Light; M + F: Microrobots + Fuel; M + F + L: Microrobots + Fuel + Light). F) Calcein AM and PI staining method to investigate the death of prostate cancer cells caused by different conditions after 9 h treatment. Scale bars are 50 μm.

Calcein AM and propidium iodide (PI) co-staining experiments were conducted to validate the obtained results. The cell viability and morphology of the prostate cancer cells were observed under the fluorescent microscope, as shown in Figure 6F. Virtually no red-stained cells in the control group can be observed, elucidating that only a few cells were killed. In the microrobots-free treated group (fuel + light) and microrobots + light treated group, a few cells were stained in red, indicating a weak PDT effect. In contrast, the number of dead cells observed in treatments involving microrobots + fuel + light was significantly increased, demonstrating once again that the microrobots show enhanced cytotoxicity by the photo-Fenton reaction to kill the majority of cancer cells.

Conclusion

In summary, we developed dendrite-shaped photocatalytic magnetic hematite microrobots by a low-cost and one-step hydrothermal method to realize the on-site generation of ROS to trigger prostate cancer cell therapy by GSH depletion. These microrobots exhibited dual light /magnetic-driven propulsion without integrating multiple components, undergoing negative phototaxis under light irradiation and controllable actuation along a predefined path subjected to an external rotating magnetic field. Transportation of micro-sized targets in a non-contact way, such as cells, was demonstrated by manipulating the movement of a single microrobot, which produced a powerful fluid flow pushing the targeted cell. Moreover, the hematite microrobots presented good biocompatibility. In vitro experiments proved that hematite microrobots can induce GSH oxidation upon reaction with the ROS generated by the photo-Fenton reaction, enhancing the PDT efficacy toward prostate cancer cells. Future efforts will be focused on evaluating the performance of microrobots in vivo using animal models, including biocompatibility tests of microrobots and additional experiments to assess undesirable side effects that may be caused by microrobots. In addition, the therapeutic efficacy may be further increased by coating the microrobots with pH-responsive polymeric layers encapsulating drugs. These evaluations of microrobots in vitro/vivo experiments will contribute to broadening the horizon for biological applications of microrobots. Overall, the proposed drug-free PDT by dendrite-shaped hematite microrobots holds excellent potential for future clinical applications.

Authors Contributions

X.P. conducted the preparation and characterization of the microrobots, analyzed their motion, and interpreted the data. M.U. designed the experiments and contributed to data interpretation. J.B. and M.M. performed the biological experiments. M.P. initiated the idea. M.P. and M.U. supervised the project. All authors contributed to writing the manuscript.

Acknowledgements

M.P. acknowledges the financial support of Grant Agency of the Czech Republic (EXPRO: 19-26896X). X.P. was supported by the China Scholarship Council (CSC No. 202008320382) and acknowledges the Brno Ph.D. Talent scholarship funded by the Brno City Municipality, and the project Quality Internal Grants of BUT (KInG BUT), reg. no. CZ.02.2.69/0.0/0.0/19_073/0016948, which is financed from the OP RDE. M.U. acknowledges the financial support by the European Union's Horizon 2020 research and innovation program under the Marie Skłodowska-Curie grant agreement No. 101038066. J.B. and M.M. were supported by the Ministry of Health of the Czech Republic (NU21-08-00407). CzechNanoLab project LM2018110 funded by MEYS CR is gratefully acknowledged for the financial support of the measurements/sample fabrication at CEITEC Nano Research Infrastructure. CIISB, Instruct-CZ Centre of Instruct-ERIC EU consortium, funded by MEYS CR infrastructure project LM2018127, is gratefully acknowledged for the financial support of the measurements at the CEITEC Proteomics Core Facility.

Conflict of Interest

The authors declare no conflict of interest.

Data Availability Statement

The data that support the findings of this study are available from the corresponding author upon reasonable request.

Keywords: Cargo Transportation · Micromachines · Micromotors · Photocatalysis · Tumor Cells

---

[1] C. Chen, S. Tang, H. Teymourian, E. Karshalev, F. Zhang, J. Li, F. Mou, Y. Liang, J. Guan, J. Wang, *Angew. Chem. Int. Ed.* **2018**, *57*, 8110–8114.
[2] R. Dong, Q. Zhang, W. Gao, A. Pei, B. Ren, *ACS Nano* **2016**, *10*, 839–844.
[3] a) Y. Ji, X. Lin, H. Zhang, Y. Wu, J. Li, Q. He, *Angew. Chem. Int. Ed.* **2019**, *58*, 4184–4188; b) M. Ussia, M. Pumera, *Chem. Soc. Rev.* **2022**, *51*, 1558–1572.
[4] a) M. Fernández-Medina, M. A. Ramos-Docampo, O. Hovorka, V. Salgueiriño, B. Städler, *Adv. Funct. Mater.* **2020**, *30*, 1908283; b) C. C. Mayorga-Martinez, J. Vyskočil, F. Novotný, P. Bednar, D. Ruzek, O. Alduhaish, M. Pumera, *Appl. Mater. Today* **2022**, *26*, 101337.
[5] M. Zhou, Y. Xing, X. Li, X. Du, T. Xu, X. Zhang, *Small* **2020**, *16*, 2003834.
[6] B. A. Darmawan, D. Gong, H. G. Park, S. Jeong, G. Go, S. J. Kim, S. Zheng, M. Nan, V. D. Nguyen, D. Bang, C. Kim, H. Kim, J. Park, E. Choi, *J. Mater. Chem. B* **2022**, *10*, 4509–4518.
[7] a) B. Jurado-Sánchez, J. Wang, *Environ. Sci. Nano* **2018**, *5*, 1530–1544; b) J. V. Vaghasiya, C. C. Mayorga-Martinez, S. Matějková, M. Pumera, *Nat. Commun.* **2022**, *13*, 1026.
[8] M. Urso, M. Pumera, *Adv. Funct. Mater.* **2022**, *32*, 2112120.

[9] X. Peng, M. Urso, M. Ussia, M. Pumera, *ACS Nano* **2022**, *16*, 7615–7625.

[10] M. J. Esplandiu, A. A. Farniya, A. Bachtold, *ACS Nano* **2015**, *9*, 11234–11240.

[11] S. Fu, D. Fu, D. Xie, L. Liu, B. Chen, Y. Ye, D. A. Wilson, F. Peng, *Appl. Mater. Today* **2022**, *26*, 101348.

[12] a) R. Dong, Y. Hu, Y. Wu, W. Gao, B. Ren, Q. Wang, Y. Cai, *J. Am. Chem. Soc.* **2017**, *139*, 1722–1725; b) M. Ussia, M. Urso, K. Dolezelikova, H. Michalkova, V. Adam, M. Pumera, *Adv. Funct. Mater.* **2021**, *31*, 2101178; c) K. Villa, H. Sopha, J. Zelenka, M. Motola, L. Dekanovsky, D. C. Beketova, J. M. Macak, T. Ruml, M. Pumera, *Small* **2022**, *18*, 2106612.

[13] C. M. Oral, M. Ussia, D. K. Yavuz, M. Pumera, *Small* **2022**, *18*, 2106271.

[14] Q. Zhang, R. Dong, Y. Wu, W. Gao, Z. He, B. Ren, *ACS Appl. Mater. Interfaces* **2017**, *9*, 4674–4683.

[15] G. Vizsnyiczai, G. Frangipane, C. Maggi, F. Saglimbeni, S. Bianchi, R. D. Leonardo, *Nat. Commun.* **2017**, *8*, 15974.

[16] X. He, H. Jiang, J. Li, Y. Ma, B. Fu, C. Hu, *Small* **2021**, *17*, 2101388.

[17] X. Lyu, X. Liu, C. Zhou, S. Duan, P. Xu, J. Dai, X. Chen, Y. Peng, D. Cui, J. Tang, X. Ma, W. Wang, *J. Am. Chem. Soc.* **2021**, *143*, 12154–12164.

[18] M. Urso, C. Iffelsberger, C. C. Mayorga-Martinez, M. Pumera, *Small Methods* **2021**, *5*, 2100511.

[19] M. Pacheco, B. Jurado-Sánchez, A. Escarpa, *Angew. Chem. Int. Ed.* **2019**, *58*, 18017–18024.

[20] M. Sun, K. F. Chan, Z. Zhang, L. Wang, Q. Wang, S. Yang, S. M. Chan, P. W. Y. Chiu, J. J. Y. Sung, L. Zhang, *Adv. Mater.* **2022**, *34*, 2201888.

[21] W. Chen, H. Zhou, B. Zhang, Q. Cao, B. Wang, X. Ma, *Adv. Funct. Mater.* **2022**, *32*, 2110625.

[22] S. Zheng, Y. Wang, S. Pan, E. Ma, S. Jin, M. Jiao, W. Wang, J. Li, K. Xu, H. Wang, *Adv. Funct. Mater.* **2021**, *31*, 2100936.

[23] J. Muñoz, M. Urso, M. Pumera, *Angew. Chem.* **2022**, *61*, e202116090.

[24] Z. Xie, T. Fan, J. An, W. Choi, Y. Duo, Y. Ge, B. Zhang, G. Nie, N. Xie, T. Zheng, Y. Chen, H. Zhang, J. S. Kim, *Chem. Soc. Rev.* **2020**, *49*, 8065–8087.

[25] W. Wu, D. Mao, F. Hu, S. Xu, C. Chen, C. Zhang, X. Cheng, Y. Yuan, D. Ding, D. Kong, B. Liu, *Adv. Mater.* **2017**, *29*, 1700548.

[26] W. Piao, K. Hanaoka, T. Fujisawa, S. Takeuchi, T. Komatsu, T. Ueno, T. Terai, T. Tahara, T. Nagano, Y. Urano, *J. Am. Chem. Soc.* **2017**, *139*, 13713–13719.

[27] W. Sun, S. Li, B. Häupler, J. Liu, S. Jin, W. Steffen, U. S. Schubert, H. Butt, X.-J. Liang, S. Wu, *Adv. Mater.* **2017**, *29*, 1603702.

[28] Y. Ma, X. Li, A. Li, P. Yang, C. Zhang, B. Tang, *Angew. Chem. Int. Ed.* **2017**, *56*, 13752–13756; *Angew. Chem.* **2017**, *129*, 13940–13944.

[29] Z. Zhou, J. Song, L. Nie, X. Chen, *Chem. Soc. Rev.* **2016**, *45*, 6597–6626.

[30] C. Gao, Z. Lin, D. Lin, Z. Wu, H. Xie, Q. He, *ACS Appl. Mater. Interfaces* **2019**, *11*, 23392–23400.

[31] B. Zhao, Y. Wang, X. Yao, D. Chen, M. Fan, Z. Jin, Q. He, *Nat. Commun.* **2021**, *12*, 1345.

[32] G. S. Parkinson, *Surf. Sci. Rep.* **2016**, *71*, 272–365.

[33] P. S. Bagus, C. J. Nelin, C. R. Brundle, N. Lahiri, E. S. Ilton, K. M. Rosso, *J. Chem. Phys.* **2020**, *152*, 014704.

[34] K. Villa, F. Novotný, J. Zelenka, M. P. Browne, T. Ruml, M. Pumera, *ACS Nano* **2019**, *13*, 8135–8145.

[35] a) Y. Peng, P. Xu, S. Duan, J. Liu, J. L. Moran, W. Wang, *Angew. Chem. Int. Ed.* **2022**, *61*, e202116041; b) P. Mayorga-Burrezo, C. C. Mayorga-Martinez, M. Pumera, *Adv. Funct. Mater.* **2022**, *32*, 2106699.

[36] Y. Feng, S. Lin, S. Huang, S. Shrestha, G. Conibeer, *J. Appl. Phys.* **2015**, *117*, 125701.

[37] I. N. Reddy, N. Jayashree, V. Manjunath, D. Kim, J. Shim, *Catalysts* **2020**, *10*, 983.

[38] D. P. Singh, W. E. Uspal, M. N. Popescu, L. G. Wilson, P. Fischer, *Adv. Funct. Mater.* **2018**, *28*, 1706660.

[39] J. Zhang, F. Mou, S. Tang, J. E. Kauffman, A. Sen, J. Guan, *Appl. Mater. Today* **2022**, *26*, 101371.

[40] M. Urso, M. Ussia, F. Novotný, M. Pumera, *Nat. Commun.* **2022**, *13*, 3573.

[41] B. Dai, J. Wang, Z. Xiong, X. Zhan, W. Dai, C. Li, S. Feng, J. Tang, *Nat. Nanotechnol.* **2016**, *11*, 1087–1092.

[42] C. Chen, F. Mou, L. Xu, S. Wang, J. Guan, Z. Feng, Q. Wang, L. Kong, W. Li, J. Wang, Q. Zhang, *Adv. Mater.* **2017**, *29*, 1603374.

[43] X. Guo, Y. Wang, F. Mou, Q. Xie, S. Su, C. Chen, J. Guan, *J. Mater. Chem. C* **2022**, *10*, 5079–5087.

[44] X. Peng, M. Urso, M. Pumera, *Small Methods* **2021**, *5*, 2100617.

[45] Z. Lin, X. Fan, M. Sun, C. Gao, Q. He, H. Xie, *ACS Nano* **2018**, *12*, 2539–2545.

[46] a) Y. Chen, D. Chen, S. Liang, Y. Dai, X. Bai, B. Song, D. Zhang, H. Chen, L. Feng, *Adv. Intell. Syst.* **2022**, *4*, 2100116; b) J. Li, M. Pumera, *Chem. Soc. Rev.* **2021**, *50*, 2794–2838.

[47] M. B. Akolpoglu, Y. Alapan, N. O. Dogan, S. F. Baltaci, O. Yasa, G. A. Tural, M. Sitti, *Sci. Adv.* **2022**, *8*, eabo6163.

[48] T. Pan, Y. Shi, N. Zhao, J. Xiong, Y. Xiao, H. Xin, B. Li, *Adv. Funct. Mater.* **2022**, *32*, 2111038.

[49] A. Muñoz, D. H. Petering, F. C. Shaw, *Inorg. Chem.* **1999**, *38*, 5655–5659.

[50] M. S. Jeong, K. Yu, H. H. Chung, S. J. Park, A. Y. Lee, M. R. Song, M. Cho, J. S. Kim, *Sci. Rep.* **2016**, *6*, 26347.

Manuscript received: September 13, 2022
Accepted manuscript online: September 30, 2022
Version of record online: October 25, 2022

11. Conclusions

In summary, this thesis presents a comprehensive investigation into active microrobots and their application in sustainable environmental and biological applications. The research offers critical insights into the synthesis, characterization, and photocatalytic properties of different materials. A notable contribution of this thesis is to design more advanced microrobots in terms of i.e., higher propulsion speed, programmable collective behaviors, and response to environmental stimuli with phototaxis, which establishes a microrobotic system for water purification and cancer therapy. The primary findings are systematically categorized into three thematic parts, each addressing the key research objectives outlined in Chapter 1.

Firstly, we reported the large-scale synthesis of single-component WO_3 microrobots with active propulsion via a facile hydrothermal method, which is easily scalable, combined with calcination. The active motion and photocatalytic activity of WO_3 microrobots were applied to degrade toxic nitroaromatic pollutants, such as picric acid (PA). The microrobots degraded 70% of PA in water without any external agitation. In order to further enhance propulsion capability, Janus-structured hematite/Pt microrobots were designed with different thicknesses of Pt layers. This result demonstrates that the speed of light-powered Janus microrobots can be greatly enhanced by increasing metal layer thickness. The enhanced speed of these microrobots for the degradation of PA as a model for explosive pollutants was also tested in water. This work presents a new approach to enhance the speed of Janus microrobots based on tailoring the metal layer thickness.

Apart from photocatalytic degradation of pollutants, the exploration of biofilm removal was also investigated by designing $ZnFe_2O_4$/Pt Janus microrobots. ZFO microspheres were synthesized via a cost-effective and scalable hydrothermal method, followed by a calcination process. Subsequently, a Pt layer was deposited on the surface of the ZFO microspheres to create asymmetric Janus microrobots, enabling self-propulsion under UV light irradiation. These light-driven ZFO/Pt microrobots exhibited active locomotion with controllable "stop-and-go" motion under UV light, demonstrating effective photodegradation capabilities. These microrobots effectively eliminated Gram-negative *Escherichia coli* (*E. coli*) biofilms through a dual mechanism: photogenerated reactive oxygen species (ROS) facilitated antibacterial activity, while their light-powered active locomotion enhanced mass transfer, accelerating biofilm removal in aquatic environments. This work highlights their applicability as a robust solution to biofilm-related challenges in various industrial and environmental contexts.

Secondly, in order to further investigate the influence of microrobots shapes on their collective behaviors, hematite/Pt Janus microrobots has been demonstrated. Because of the asymmetrical dipolar moment orientation in the crystal, cubic hematite/Pt microrobots can self-assemble into regular microchains with morphologies. They exhibit different motion modes under light irradiation depending on the configuration of single microrobots. To prove the exceptional benefits of a collective behavior compared to individual microrobots, these light-powered self-assembled microchains were employed for yeast cells capture, release, and transport, for the capture and removal of suspended matter in water originated from personal care products, as well as the definitive degradation of polymeric materials. This work offers a different perspective on the collective behavior of photocatalytic microrobots with the benefits of easily batch fabrication, low-cost, and a broad range of multimodal applications.

Additionally, the treatment of micro/nanoplasctics presents a severe threat to human health due to their tiny size and persistent nature. In this regard, algae cells were selected as the platform of microrobots incorporated with Fe_3O_4 nanoparticles for precise manipulation. The algae-based microrobots exhibit collective behavior under control of external magnetic field and controllable motion to predefined location. Also, these microrobots realized 90% capture of nanoplastics and 70% capture for microplastics, which is ascribed to the reliable electrostatic interaction.

Finally, the increasing intelligence of photocatalytic microrobots was further realized by exploring the tactic behavior of dendrite-shaped microrobots. These microrobots were fabricated using a low-cost, one-step hydrothermal method, enabling efficient on-site ROS production through the photo-Fenton reaction under light illumination. The microrobots undergo negative phototactic motion under light irradiation and controllable actuation along a predefined path subjected to an external rotating magnetic field. They also demonstrated the ability to transport micro-scale targets, such as individual cells, in a non-contact manner by generating a strong fluid flow through precise manipulation of their motion. This feature allowed for controlled positioning and interaction with targeted cells. Importantly, the hematite-based microrobots exhibited excellent biocompatibility, ensuring their suitability for biomedical applications. In vitro experiments confirmed their therapeutic potential, as the ROS generated under light irradiation effectively induced apoptosis in prostate cancer cells, significantly enhancing photodynamic therapy (PDT) efficacy. These findings highlight the promise of dendrite-shaped hematite microrobots as a cost-effective and multifunctional platform for cancer therapy, combining precise manipulation, biocompatibility, and efficient ROS-based treatment mechanisms.

Looking ahead, the development of active microrobots holds tremendous promise for advancing environmental and biomedical technologies. Future research should focus on optimizing the performance of these microrobots, particularly in terms of scalability, speed, and efficiency for large-scale applications. Replacing the noble metal with other more cost-efficient strategies involved in the fabrication of Janus microrobots is of great importance for sustainable development. In addition, further exploration of new materials and hybrid systems could improve the biocompatibility, stability, and reusability of these microrobots, enabling their safe and effective deployment in real-world settings. Advances in artificial intelligence and machine learning could also contribute to the development of smarter microrobots capable of autonomous decision-making and adaptive behaviors in dynamic environments.

Ultimately, as these microrobots evolve, they have the potential to revolutionize fields ranging from environmental cleanup to personalized medicine, offering innovative solutions to some of the most pressing challenges in both sustainability and healthcare.

12. References

(1) Favere, J.; Barbosa, R. G.; Sleutels, T.; Verstraete, W.; De Gusseme, B.; Boon, N. Safeguarding the Microbial Water Quality from Source to Tap. *npj Clean Water* **2021**, *4* (1), 28. https://doi.org/10.1038/s41545-021-00118-1.

(2) Wu, J.; Cao, M.; Tong, D.; Finkelstein, Z.; Hoek, E. M. V. A Critical Review of Point-of-Use Drinking Water Treatment in the United States. *npj Clean Water* **2021**, *4* (1), 40. https://doi.org/10.1038/s41545-021-00128-z.

(3) Werber, J. R.; Osuji, C. O.; Elimelech, M. Materials for Next-Generation Desalination and Water Purification Membranes. *Nat. Rev. Mater.* **2016**, *1*, 16018. https://doi.org/10.1038/natrevmats.2016.18.

(4) Nguyen, P. Y.; Carvalho, G.; Reis, M. A. M.; Oehmen, A. A Review of the Biotransformations of Priority Pharmaceuticals in Biological Wastewater Treatment Processes. *Water Res.* **2021**, *188*, 116446. https://doi.org/10.1016/j.watres.2020.116446.

(5) Barnes, S. J. Understanding Plastics Pollution: The Role of Economic Development and Technological Research. *Environ. Pollut.* **2019**, *249*, 812–821. https://doi.org/10.1016/j.envpol.2019.03.108.

(6) Liu, S.; Gunawan, C.; Barraud, N.; Rice, S. A.; Harry, E. J.; Amal, R. Understanding, Monitoring, and Controlling Biofilm Growth in Drinking Water Distribution Systems. *Environ. Sci. Technol.* **2016**, *50* (17), 8954–8976. https://doi.org/10.1021/acs.est.6b00835.

(7) Xie, Z.; Fan, T.; An, J.; Choi, W.; Duo, Y.; Ge, Y.; Zhang, B.; Nie, G.; Xie, N.; Zheng, T.; Chen, Y.; Zhang, H.; Kim, J. S. Emerging Combination Strategies with Phototherapy in Cancer Nanomedicine. *Chem. Soc. Rev.* **2020**, *49* (22), 8065–8087. https://doi.org/10.1039/d0cs00215a.

(8) Sun, W.; Li, S.; Häupler, B.; Liu, J.; Jin, S.; Steffen, W.; Schubert, U. S.; Butt, H. J.; Liang, X. J.; Wu, S. An Amphiphilic Ruthenium Polymetallodrug for Combined Photodynamic Therapy and Photochemotherapy In Vivo. *Adv. Mater.* **2017**, *29* (6). https://doi.org/10.1002/adma.201603702.

(9) Ma, Y.; Li, X.; Li, A.; Yang, P.; Zhang, C.; Tang, B. H2S-Activable MOF Nanoparticle Photosensitizer for Effective Photodynamic Therapy against Cancer with Controllable Singlet-Oxygen Release. *Angew. Chemie - Int. Ed.* **2017**, *56* (44), 13752–13756.

https://doi.org/10.1002/anie.201708005.

(10) Jager, E. W. H.; Inganäs, O.; Lundström, I. Microrobots for Micrometer-Size Objects in Aqueous Media: Potential Tools for Single-Cell Manipulation. *Science.* **2000**, *288* (5475), 2335–2338. https://doi.org/10.1126/science.288.5475.2335.

(11) Lin, Z.; Fan, X.; Sun, M.; Gao, C.; He, Q.; Xie, H. Magnetically Actuated Peanut Colloid Motors for Cell Manipulation and Patterning. *ACS Nano* **2018**, *12* (3), 2539–2545. https://doi.org/10.1021/acsnano.7b08344.

(12) Kinbara, K.; Aida, T. Toward Intelligent Molecular Machines: Directed Motions of Biological and Artificial Molecules and Assemblies. *Chem. Rev.* **2005**, *105* (4), 1377–1400. https://doi.org/10.1021/cr030071r.

(13) Fernández-Medina, M.; Ramos-Docampo, M. A.; Hovorka, O.; Salgueiriño, V.; Städler, B. Recent Advances in Nano- and Micromotors. *Adv. Funct. Mater.* **2020**, *30* (12), 1908283.https://doi.org/10.1002/adfm.201908283.

(14) Yuan, K.; Pacheco, M.; Jurado-Sánchez, B.; Escarpa, A. Design and Control of the Micromotor Swarm Toward Smart Applications. *Adv. Intell. Syst.* **2021**, *3* (6), 2100002. https://doi.org/10.1002/aisy.202100002.

(15) Ismagilov, R. F.; Schwartz, A.; Bowden, N.; Whitesides, G. M. Autonomous Movement and Self-Assembly. *Angew. Chemie - Int. Ed.* **2002**, *41* (4), 652–654. https://doi.org/10.1002/1521-3773(20020215)41:4<652::AID-ANIE652>3.0.CO;2-U.

(16) Urso, M.; Ussia, M.; Pumera, M. Smart Micro- and Nanorobots for Water Purification. *Nat. Rev. Bioeng.* **2023**, *1* (4), 236–251. https://doi.org/10.1038/s44222-023-00025-9.

(17) Palagi, S.; Singh, D. P.; Fischer, P. Light-Controlled Micromotors and Soft Microrobots. *Adv. Opt. Mater.* **2019**, *7* (16), 1900370. https://doi.org/10.1002/adom.201900370.

(18) Xu, L.; Mou, F.; Gong, H.; Luo, M.; Guan, J. Light-Driven Micro/Nanomotors: From Fundamentals to Applications. *Chem. Soc. Rev.* **2017**, *46* (22), 6905–6926. https://doi.org/10.1039/c7cs00516d.

(19) Yang, X.; Wang, D. Photocatalysis: From Fundamental Principles to Materials and Applications. *ACS Appl. Energy Mater.* **2018**, *1* (12), 6657–6693. https://doi.org/10.1021/acsaem.8b01345.

(20) Fresno, F.; Portela, R.; Suárez, S.; Coronado, J. M. Photocatalytic Materials: Recent

Achievements and near Future Trends. *J. Mater. Chem. A* **2014**, *2* (9), 2863–2884. https://doi.org/10.1039/c3ta13793g.

(21) Shen, H.; Cai, S.; Wang, Z.; Ge, Z.; Yang, W. Magnetically Driven Microrobots: Recent Progress and Future Development. *Mater. Des.* **2023**, *227*, 111735. https://doi.org/10.1016/j.matdes.2023.111735.

(22) Eberhard, S.; Finazzi, G.; Wollman, F. A. The Dynamics of Photosynthesis. *Annu. Rev. Genet.* **2008**, *42*, 463–515. https://doi.org/10.1146/annurev.genet.42.110807.091452.

(23) Zhu, S.; Wang, D. Photocatalysis: Basic Principles, Diverse Forms of Implementations and Emerging Scientific Opportunities. *Adv. Energy Mater.* **2017**, *7* (23), 1700841. https://doi.org/10.1002/aenm.201700841.

(24) Hassaan, M. A.; El-Nemr, M. A.; Elkatory, M. R.; Ragab, S.; Niculescu, V. C.; El Nemr, A. Principles of Photocatalysts and Their Different Applications: A Review. *Springer International Publishing* **2023**, *381*, 31. https://doi.org/10.1007/s41061-023-00444-7.

(25) Costa, J. C. S.; Taveira, R. J. S.; Lima, C. F. R. A. C.; Mendes, A.; Santos, L. M. N. B. F. Optical Band Gaps of Organic Semiconductor Materials. *Opt. Mater. (Amst).* **2016**, *58*, 51–60. https://doi.org/10.1016/j.optmat.2016.03.041.

(26) Castillo-Cabrera, G. X.; Espinoza-Montero, P. J.; Alulema-Pullupaxi, P.; Mora, J. R.; Villacís-García, M. H. Bismuth Oxyhalide-Based Materials (BiOX: X = Cl, Br, I) and Their Application in Photoelectrocatalytic Degradation of Organic Pollutants in Water: A Review. *Front. Chem.* **2022**, *10* (July), 1–19. https://doi.org/10.3389/fchem.2022.900622.

(27) Dong, R.; Zhang, Q.; Gao, W.; Pei, A.; Ren, B. Highly Efficient Light-Driven TiO_2-Au Janus Micromotors. *ACS Nano* **2016**, *10* (1), 839–844. https://doi.org/10.1021/acsnano.5b05940.

(28) Villa, K. Exploring Innovative Designs and Heterojunctions in Photocatalytic Micromotors. *Chem. Commun.* **2023**, *59* (54), 8375–8383. https://doi.org/10.1039/d3cc01634j.

(29) Xu, L.; Mou, F.; Gong, H.; Luo, M.; Guan, J. Light-Driven Micro/Nanomotors: From Fundamentals to Applications. *Chem. Soc. Rev.* **2017**, *46* (22), 6905–6926. https://doi.org/10.1039/c7cs00516d.

(30) Eskandarloo, H.; Kierulf, A.; Abbaspourrad, A. Light-Harvesting Synthetic Nano- and Micromotors: A Review. **2017**, No. 607, 12218–12230. https://doi.org/10.1039/c7nr05166b.

(31) Villa, K.; Novotný, F.; Zelenka, J.; Browne, M. P.; Ruml, T.; Pumera, M. Visible-Light-Driven Single-Component $BiVO_4$ Micromotors with the Autonomous Ability for Capturing Microorganisms. *ACS Nano* **2019**, *13* (7), 8135–8145. https://doi.org/10.1021/acsnano.9b03184.

(32) Jurado-Sánchez, B.; Pacheco, M.; Maria-Hormigos, R.; Escarpa, A. Perspectives on Janus Micromotors: Materials and Applications. *Appl. Mater. Today* **2017**, *9*, 407–418. https://doi.org/10.1016/j.apmt.2017.09.005.

(33) Liang, C.; Zhan, C.; Zeng, F.; Xu, D.; Wang, Y.; Zhao, W.; Zhang, J.; Guo, J.; Feng, H.; Ma, X. Bilayer Tubular Micromotors for Simultaneous Environmental Monitoring and Remediation. *ACS Appl. Mater. Interfaces* **2018**, *10* (41), 35099–35107. https://doi.org/10.1021/acsami.8b10921.

(34) Wang, H.; Moo, J. G. S.; Pumera, M. From Nanomotors to Micromotors: The Influence of the Size of an Autonomous Bubble-Propelled Device upon Its Motion. *ACS Nano* **2016**, *10* (5), 5041–5050. https://doi.org/10.1021/acsnano.5b07771.

(35) Villa, K.; Manzanares Palenzuela, C. L.; Sofer, Z.; Matějková, S.; Pumera, M. Metal-Free Visible-Light Photoactivated C_3N_4 Bubble-Propelled Tubular Micromotors with Inherent Fluorescence and On/Off Capabilities. *ACS Nano* **2018**, *12* (12), 12482–12491. https://doi.org/10.1021/acsnano.8b06914.

(36) Mou, F.; Li, Y.; Chen, C.; Li, W.; Yin, Y.; Ma, H.; Guan, J. Single-Component TiO2 Tubular Microengines with Motion Controlled by Light-Induced Bubbles. *Small* **2015**, *11* (21), 2564–2570. https://doi.org/10.1002/smll.201403372.

(37) Wu, Z.; Si, T.; Gao, W.; Lin, X.; Wang, J.; He, Q. Superfast Near-Infrared Light-Driven Polymer Multilayer Rockets. *Small* **2016**, *12* (5), 577–582. https://doi.org/10.1002/smll.201502605.

(38) Chen, C.; Mou, F.; Xu, L.; Wang, S.; Guan, J.; Feng, Z.; Wang, Q.; Kong, L.; Li, W.; Wang, J.; Zhang, Q. Light-Steered Isotropic Semiconductor Micromotors. *Adv. Mater.* **2017**, *29* (3), 1603374. https://doi.org/10.1002/adma.201603374.

(39) Palagi, S.; Mark, A. G.; Reigh, S. Y.; Melde, K.; Qiu, T.; Zeng, H.; Parmeggiani, C.; Martella, D.; Sanchez-Castillo, A.; Kapernaum, N.; Giesselmann, F.; Wiersma, D. S.; Lauga, E.; Fischer, P. Structured Light Enables Biomimetic Swimming and Versatile Locomotion of Photoresponsive Soft Microrobots. *Nat. Mater.* **2016**, *15* (6), 647–653.

https://doi.org/10.1038/nmat4569.

(40) Niese, L.; Wang, L.; Das, S.; Simmchen, J. Apparent Phototaxis Enabled by Brownian Motion. *Soft Matter* **2020**, *16* (47), 10585–10590. https://doi.org/10.1039/d0sm01603a.

(41) Wang, J.; Xiong, Z.; Zheng, J.; Zhan, X.; Tang, J. Light-Driven Micro/Nanomotor for Promising Biomedical Tools: Principle, Challenge, and Prospect. *Acc. Chem. Res.* **2018**, *51* (9), 1957–1965. https://doi.org/10.1021/acs.accounts.8b00254.

(42) Mou, F.; Kong, L.; Chen, C.; Chen, Z.; Xu, L.; Guan, J. Light-Controlled Propulsion, Aggregation and Separation of Water-Fuelled TiO_2/Pt Janus Submicromotors and Their "on-the-Fly" Photocatalytic Activities. *Nanoscale* **2016**, *8* (9), 4976–4983. https://doi.org/10.1039/c5nr06774j.

(43) Dai, B.; Wang, J.; Xiong, Z.; Zhan, X.; Dai, W.; Li, C. C.; Feng, S. P.; Tang, J. Programmable Artificial Phototactic Microswimmer. *Nat. Nanotechnol.* **2016**, *11* (12), 1087–1092. https://doi.org/10.1038/nnano.2016.187.

(44) Pourrahimi, A. M.; Villa, K.; Manzanares Palenzuela, C. L.; Ying, Y.; Sofer, Z.; Pumera, M. Catalytic and Light-Driven ZnO/Pt Janus Nano/Micromotors: Switching of Motion Mechanism via Interface Roughness and Defect Tailoring at the Nanoscale. *Adv. Funct. Mater.* **2019**, *29* (22), 1–8. https://doi.org/10.1002/adfm.201808678.

(45) Urso, M.; Ussia, M.; Pumera, M. Breaking Polymer Chains with Self-Propelled Light-Controlled Navigable Hematite Microrobots. *Adv. Funct. Mater.* **2021**, *31*, 2101510. https://doi.org/10.1002/adfm.202101510.

(46) Anderson, J. Colloid Transport By Interfacial Forces. *Annu. Rev. Fluid Mech.* **1989**, *21* (1), 61–99. https://doi.org/10.1146/annurev.fluid.21.1.61.

(47) Xu, P.; Duan, S.; Xiao, Z.; Yang, Z.; Wang, W. Light-Powered Active Colloids from Monodisperse and Highly Tunable Microspheres with a Thin TiO_2 shell. *Soft Matter* **2020**, *16* (26), 6082–6090. https://doi.org/10.1039/d0sm00719f.

(48) Wang, W.; Duan, W.; Ahmed, S.; Mallouk, T. E.; Sen, A. Small Power: Autonomous Nano- and Micromotors Propelled by Self-Generated Gradients. *Nano Today* **2013**, *8* (5), 531–554. https://doi.org/10.1016/j.nantod.2013.08.009.

(49) Kong, L.; Mayorga-Martinez, C. C.; Guan, J.; Pumera, M. Photocatalytic Micromotors

Activated by UV to Visible Light for Environmental Remediation, Micropumps, Reversible Assembly, Transportation, and Biomimicry. *Small* **2020**, *16* (27), 1–14. https://doi.org/10.1002/smll.201903179.

(50) Hu, Y.; Liu, W.; Sun, Y. Self-Propelled Micro-/Nanomotors as “On-the-Move” Platforms: Cleaners, Sensors, and Reactors. *Adv. Funct. Mater.* **2022**, *32* (10), 32, 2109181. https://doi.org/10.1002/adfm.202109181.

(51) Lin, Z.; Si, T.; Wu, Z.; Gao, C.; Lin, X.; He, Q. Light-Activated Active Colloid Ribbons. *Angew. Chemie - Int. Ed.* **2017**, *56* (43), 13517–13520. https://doi.org/10.1002/anie.201708155.

(52) Singh, D. P.; Choudhury, U.; Fischer, P.; Mark, A. G. Non-Equilibrium Assembly of Light-Activated Colloidal Mixtures. *Adv. Mater.* **2017**, *29* (32), 1–7. https://doi.org/10.1002/adma.201701328.

(53) Zhang, Q.; Dong, R.; Wu, Y.; Gao, W.; He, Z.; Ren, B. Light-Driven Au-WO_3@C Janus Micromotors for Rapid Photodegradation of Dye Pollutants. *ACS Appl. Mater. Interfaces* **2017**, *9* (5), 4674–4683. https://doi.org/10.1021/acsami.6b12081.

(54) Wu, Y.; Si, T.; Shao, J.; Wu, Z.; He, Q. Near-Infrared Light-Driven Janus Capsule Motors: Fabrication, Propulsion, and Simulation. *Nano Res.* **2016**, *9* (12), 3747–3756. https://doi.org/10.1007/s12274-016-1245-0.

(55) Qian, B.; Montiel, D.; Bregulla, A.; Cichos, F.; Yang, H. Harnessing Thermal Fluctuations for Purposeful Activities: The Manipulation of Single Micro-Swimmers by Adaptive Photon Nudging. *Chem. Sci.* **2013**, *4* (4), 1420–1429. https://doi.org/10.1039/c2sc21263c.

(56) Zhan, Z.; Wei, F.; Zheng, J.; Yang, W.; Luo, J.; Yao, L. Recent Advances of Light-Driven Micro/Nanomotors: Toward Powerful Thrust and Precise Control. *Nanotechnol. Rev.* **2018**, *7* (6), 555–581. https://doi.org/10.1515/ntrev-2018-0106.

(57) Li, Y.; Mou, F.; Chen, C.; You, M.; Yin, Y.; Xu, L.; Guan, J. Light-Controlled Bubble Propulsion of Amorphous TiO_2/Au Janus Micromotors. *RSC Adv.* **2016**, *6* (13), 10697–10703. https://doi.org/10.1039/c5ra26798f.

(58) Kim, H.; Lee, S. Y. A Near-Infrared Light-Responsive Upconversion Nanoparticle Micromotor Propelled by Oxygen Bubbles. *Chem. Commun.* **2021**, *57* (4), 512–515. https://doi.org/10.1039/d0cc05820c.

(59) Hong, Y.; Diaz, M.; Córdova-Fteueroa, U. M.; Sen, A. Light-Driven Titanium-Dioxide-Based Reversible Microfireworks and Micromotor/Micropump Systems. *Adv. Funct. Mater.* **2010**, *20* (10), 1568–1576. https://doi.org/10.1002/adfm.201000063.

(60) Gao, W.; D'Agostino, M.; Garcia-Gradilla, V.; Orozco, J.; Wang, J. Multi-Fuel Driven Janus Micromotors. *Small* **2013**, *9* (3), 467–471. https://doi.org/10.1002/smll.201201864.

(61) Gao, W.; Pei, A.; Dong, R.; Wang, J. Catalytic Iridium-Based Janus Micromotors Powered by Ultralow Levels of Chemical Fuels. *J. Am. Chem. Soc.* **2014**, *136* (6), 2276–2279. https://doi.org/10.1021/ja413002e.

(62) Jurado-Sánchez, B.; Pacheco, M.; Rojo, J.; Escarpa, A. Magnetocatalytic Graphene Quantum Dots Janus Micromotors for Bacterial Endotoxin Detection. *Angew. Chemie - Int. Ed.* **2017**, *56* (24), 6957–6961. https://doi.org/10.1002/anie.201701396.

(63) Ussia, M.; Urso, M.; Dolezelikova, K.; Michalkova, H.; Adam, V.; Pumera, M. Active Light-Powered Antibiofilm ZnO Micromotors with Chemically Programmable Properties. *Adv. Funct. Mater.* **2021**, *31* (27). https://doi.org/10.1002/adfm.202101178.

(64) Dong, R.; Hu, Y.; Wu, Y.; Gao, W.; Ren, B.; Wang, Q.; Cai, Y. Visible-Light-Driven BiOI-Based Janus Micromotor in Pure Water. *J. Am. Chem. Soc.* **2017**, *139* (5), 1722–1725. https://doi.org/10.1021/jacs.6b09863.

(65) Xiao, Z.; Chen, J.; Duan, S.; Lv, X.; Wang, J.; Ma, X.; Tang, J.; Wang, W. Bimetallic Coatings Synergistically Enhance the Speeds of Photocatalytic TiO2 Micromotors. *Chem. Commun.* **2020**, *56* (34), 4728–4731. https://doi.org/10.1039/d0cc00212g.

(66) Wu, Y.; Dong, R.; Zhang, Q.; Ren, B. Dye-Enhanced Self-Electrophoretic Propulsion of Light-Driven TiO_2-Au Janus Micromotors. *Nano-Micro Lett.* **2017**, *9* (3), 1–12. https://doi.org/10.1007/s40820-017-0133-9.

(67) Wang, Q. L.; Wang, C.; Dong, R. F.; Pang, Q. Q.; Cai, Y. P. Steerable Light-Driven TiO_2-Fe Janus Micromotor. *Inorg. Chem. Commun.* **2018**, *91*, 1–4. https://doi.org/10.1016/j.inoche.2018.02.020.

(68) Pourrahimi, A. M.; Villa, K.; Ying, Y.; Sofer, Z.; Pumera, M. ZnO/ZnO_2 /Pt Janus Micromotors Propulsion Mode Changes with Size and Interface Structure: Enhanced Nitroaromatic Explosives Degradation under Visible Light. *ACS Appl. Mater. Interfaces* **2018**, *10* (49), 42688–

42697. https://doi.org/10.1021/acsami.8b16217.

(69) Lu, C.; Tang, Z. Advanced Inorganic Nanoarchitectures from Oriented Self-Assembly. *Adv. Mater.* **2016**, *28* (6), 1096–1108. https://doi.org/10.1002/adma.201502869.

(70) Yan, J.; Bloom, M.; Bae, S. C.; Luijten, E.; Granick, S. Linking Synchronization to Self-Assembly Using Magnetic Janus Colloids. *Nature* **2012**, *491* (7425), 578–581. https://doi.org/10.1038/nature11619.

(71) Yu, J.; Yang, L.; Zhang, L. Pattern Generation and Motion Control of a Vortex-like Paramagnetic Nanoparticle Swarm. *Int. J. Rob. Res.* **2018**, *37* (8), 912–930. https://doi.org/10.1177/0278364918784366.

(72) Breen, T. L.; Tien, J.; Oliver, S. R. J.; Hadzic, T.; Whitesides, G. M. Design and Self-Assembly of Open, Regular, 3D Mesostructures. *Science* **1999**, *284* (5416), 948–951. https://doi.org/10.1126/science.284.5416.948.

(73) Gobre, V. V.; Tkatchenko, A. Scaling Laws for van Der Waals Interactions in Nanostructured Materials. *Nat. Commun.* **2013**, *4*, 2341. https://doi.org/10.1038/ncomms3341.

(74) Miele, E.; Raj, S.; Baraissov, Z.; Král, P.; Mirsaidov, U. Dynamics of Templated Assembly of Nanoparticle Filaments within Nanochannels. *Adv. Mater.* **2017**, *29* (37), 1702682. https://doi.org/10.1002/adma.201702682.

(75) Villa, K.; Děkanovský, L.; Plutnar, J.; Kosina, J.; Pumera, M. Swarming of Perovskite-Like Bi_2WO_6 Microrobots Destroy Textile Fibers under Visible Light. *Adv. Funct. Mater.* **2020**, *30,* 2007073. https://doi.org/10.1002/adfm.202007073.

(76) Mayorga-Burrezo, P.; Mayorga-Martinez, C. C.; Pumera, M. Light-Driven Micromotors to Dissociate Protein Aggregates That Cause Neurodegenerative Diseases. *Adv. Funct. Mater.* **2022**, *32*, 2106699. https://doi.org/10.1002/adfm.202106699.

(77) Felsher, D. W. Cancer Revoked: Oncogenes as Therapeutic Targets. *Nat. Rev. Cancer* **2003**, *3* (5), 375–380. https://doi.org/10.1038/nrc1070.

(78) Dai, T.; Huang, Y.; Hamblin, M. R. Photodynamic therapy for localized infections--state of the art. *Photodiagnosis Photodyn Ther.* **2009**, 6(3-4), 170-188. https://doi.org/10.1016/j.pdpdt.2009.10.008.

(79) Agostinis, P.; Berg, K.; Cengel, K. A.; Foster, T. H.; Girotti, A. W.; Gollnick, S. O.; Hahn, S.

M.; Hamblin, M. R.; Juzeniene, A.; Kessel, D.; Korbelik, M.; Moan, J.; Mroz, P.; Nowis, D.; Piette, J.; Wilson, B. C.; Golab, J. Photodynamic Therapy of Cancer: An Update. *CA. Cancer J. Clin.* **2011**, *61* (4), 250–281. https://doi.org/10.3322/caac.20114.

(80) Juarranz, Á.; Jaén, P.; Sanz-Rodríguez, F.; Cuevas, J.; González, S. Photodynamic Therapy of Cancer. Basic Principles and Applications. *Clin. Transl. Oncol.* **2008**, *10* (3), 148–154. https://doi.org/10.1007/s12094-008-0172-2.

(81) Lucky, S. S.; Soo, K. C.; Zhang, Y. Nanoparticles in Photodynamic Therapy. *Chem. Rev.* **2015**, *115* (4), 1990–2042. https://doi.org/10.1021/cr5004198.

(82) Wang, J.; Gao, W. Nano/Microscale Motors: Biomedical Opportunities and Challenges. *ACS Nano* **2012**, *6* (7), 5745–5751. https://doi.org/10.1021/nn3028997.

(83) Jiang, W.; Niu, D.; Liu, H.; Wang, C.; Zhao, T.; Yin, L.; Shi, Y.; Chen, B.; Ding, Y.; Lu, B. Photoresponsive Soft-Robotic Platform: Biomimetic Fabrication and Remote Actuation. *Adv. Funct. Mater.* **2014**, *24* (48), 7598–7604. https://doi.org/10.1002/adfm.201402070.

(84) Li, J.; Berta, E.-F. de A.; Gao, W.; Wang, J. Micro/Nanorobots for Biomedicine: Delivery, Surgery, Sensing, and Detoxification Jinxing. *Physiol. Behav.* **2017**, *176* (5), 139–148. https://doi.org/10.1126/scirobotics.aam6431.Micro/Nanorobots.

(85) Xu, D.; Zhou, C.; Zhan, C.; Wang, Y.; You, Y.; Pan, X.; Jiao, J.; Zhang, R.; Dong, Z.; Wang, W.; Ma, X. Enzymatic Micromotors as a Mobile Photosensitizer Platform for Highly Efficient On-Chip Targeted Antibacteria Photodynamic Therapy. *Adv. Funct. Mater.* **2019**, *29* (17), 1807727. https://doi.org/10.1002/adfm.201807727.

(86) Mou, F.; Zhang, J.; Wu, Z.; Du, S.; Zhang, Z.; Xu, L.; Guan, J. Phototactic Flocking of Photochemical Micromotors. *iScience* **2019**, *19*, 415–424. https://doi.org/10.1016/j.isci.2019.07.050.

(87) Hu, Y.; Liu, W.; Sun, Y. Multiwavelength Phototactic Micromotor with Controllable Swarming Motion for “Chemistry-on-the-Fly.” *ACS Appl. Mater. Interfaces* **2020**, *12* (37), 41495–41505. https://doi.org/10.1021/acsami.0c11443.

(88) Sun, Y.; Liu, Y.; Zhang, D.; Zhang, H.; Jiang, J.; Duan, R.; Xiao, J.; Xing, J.; Zhang, D.; Dong, B. Calligraphy/Painting Based on a Bioinspired Light-Driven Micromotor with Concentration-Dependent Motion Direction Reversal and Dynamic Swarming Behavior. *ACS Appl. Mater.*

Interfaces **2019**, *11* (43), 40533–40542. https://doi.org/10.1021/acsami.9b14402.

(89) Wu, X.; Xue, X.; Wang, J.; Liu, H. Phototropic Aggregation and Light-Guided Long-Distance Collective Transport of Colloidal Particles. *Langmuir* **2020**, *36* (24), 6819–6827. https://doi.org/10.1021/acs.langmuir.0c01244.

(90) Fu, S.; Fu, D.; Xie, D.; Liu, L.; Chen, B.; Ye, Y.; Wilson, D. A.; Peng, F. Light Driven Micromotor Swarm for Tumor Photothermal Therapy. *Appl. Mater. Today* **2022**, *26*, 101348. https://doi.org/10.1016/j.apmt.2021.101348.

(91) Guo, H.; Yulaev, A.; Strelcov, E.; Tselev, A.; Arble, C.; Vladar, A. E.; Villarrubia, J. S.; Kolmakov, A. Probing Electrified Liquid-Solid Interfaces with Scanning Electron Microscopy. *ACS Appl. Mater. Interfaces* **2020**, *12*(50), 56650–56657. https://doi.org/10.1021/acsami.0c19634.

(92) Reddy, E. P.; Rojas, T. C.; Fernandez, A. Transmission Electron Microscopy and Energy-Dispersive X-ray Spectroscopy Study of V_2O_5/TiO_2-ZrO_2 Catalyst. *Langmuir* **2000**, *16*, 4217-4221.

(93) Cao, J.; Wilson, K. R. Ultrafast X-Ray Diffraction Theory. **1998**, 9523–9530.

(94) Bagus, P. S.; Ilton, E. S.; Nelin, C. J. The Interpretation of XPS Spectra: Insights into Materials Properties. *Surf. Sci. Rep.* **2013**, *68* (2), 273–304. https://doi.org/10.1016/j.surfrep.2013.03.001.

(95) Wamsley, M.; Wathudura, P.; Hu, J.; Zhang, D. Integrating-Sphere-Assisted Resonance Synchronous Spectroscopy for the Quantification of Material Double-Beam UV-Vis Absorption and Scattering Extinction. *Anal. Chem.* **2022**, *94* (33), 11610–11618. https://doi.org/10.1021/acs.analchem.2c02037.